

Forecasting seismic activity induced from hydraulic fracturing operations

James Whittaker

Geoenvironmental Research Centre

Cardiff School of Engineering

Cardiff University

Thesis submitted in candidature for the degree of Doctor of
Philosophy at Cardiff University

February 2020



Abstract

As the world transitions towards a carbon-neutral economy in order to meet the Paris climate change accords, many countries are utilising natural gas as a transition fuel while the renewable energy sector continues to develop. As part of this transition in the UK, it is the intent that the use of domestic natural gas, including gas from unconventional reservoirs such as shale, is fully realised. The extraction of natural gas from shale is not without environmental risk and seismic events induced by the hydraulic fracturing process are cited as the reason for the current suspension of hydraulic fracture operations in the UK. The reactive control approach, of which the ‘traffic light system’ procedures are part of, is the most widely used method to forecast seismic events. This ties the likelihood of a seismic event occurring to a single seismological derived parameter. There have been challenges in this approach, and newly developed probabilistic forecasting methods that are capable of predicting seismic events likely to occur in the future are still in development and yet to be the primary decision making system to control the injection schedule. The primary objective of this thesis was to research forecasting approaches that alleviates the disadvantages posed by these current methods. A software system was developed based on relating a forecasting model to real-time changes in the fracture network from the two causes of induced seismicity; an increase in pore-pressure re-activating fault lines and the transfer of stress from other seismic events. This software system analyses microseismic records using four geophysical signal analysis methods which when combined produces two maps updated in real-time; a fracture map highlighting hydraulic connections and a Coulomb stress change map. To verify the software system, the causes of a magnitude 3.9 earthquake on the 12 January 2016 from a shale gas production well in Fox Creek, Canada were retrospectively investigated and the usage of the system to forecast seismic events evaluated. The fracture map generated from the microseismic records indicated a hydraulic connection between stage 23 of the hydraulic fracture process and a legacy fault line. The input of fracture fluid increased the pore-pressure on the fault line, ultimately causing slip and the magnitude 3.9 earthquake. There was no evidence to show that static stress transfer from other seismic events in the area was affecting the triggering process. The forecast model was validated by comparing the fracture maps in the time leading up to 12 January event to the forecast model. Although numerous events were positioned to be part of a transition between the hydraulic tensile fractures to the fault line, it was not possible to analyse these events due to the low signal to noise ratio and therefore not viable to fully validate the forecast model with this case study. Further research with different case studies where the acquisition geometry is closer to the events is recommended to fully validate the forecast model before field implementation.

Acknowledgements

There are numerous people and parties whom which I must thank for their support and advice through this project and without which would not have resulted in such a successful project. I must firstly thank Professor Hywel Thomas, Dr Peter Brabham, Dr Richard Sandford and Dr Renato Zagorscak as my supervisors for their guidance, advice and ideas throughout this project. With that I must thank my friends and colleagues at the GRC for there ideas and thoughts. I am incredibly grateful for Terradat and their industrial partners for providing the industrial dataset for use with the analysis. This project used Matlab via the university license. The packages used include the CREWES package by the University of Calgary and the ISOLA package by J. Zahradnik and E. Sokos both of whom provided technical support. The Fortran packages used include the AXITRA wave-number code by Olivier Coutant and the Trabox ray-tracing software by M. Sambridge.

Finally, I must thank my family, my wife Katherine and my daughter Erin for their support over the last 4 years without which this project would not have been possible.

Contents

Abstract	I
Acknowledgements	II
Contents	III
List of Figures	VIII
List of Tables	XV
Acronyms and units	XVI
Symbols	XVIII
1 Introduction	1
1.1 Introduction	1
1.2 Research project aim and background	4
1.3 Limitations and definitions	6
1.4 Thesis overview	6
2 Literature review	8
2.1 Introduction	8
2.2 The current regulatory framework for the mitigation of seismicity induced by hydraulic fracturing processes	8
2.3 Forecasting induced seismicity	12
2.3.1 Reactive control approaches to mitigate induced seismicity . .	12
2.3.2 Induced seismicity forecast models	15
2.3.3 Evaluation of forecasting approaches	23
2.4 Mechanisms of induced seismicity from hydraulic fracturing	25

2.4.1	Fault re-activation by an increase in pore pressure from a direct hydraulic connection	25
2.4.2	Fault re-activation by the transfer of stress from other seismic events	30
2.4.3	Theoretical microseismic model to connect induced seismicity to the mechanisms	34
2.5	Discussion and detailing a new approach to forecasting	36
3	System design: review of available methods to analyse microseismic signals	38
3.1	Introduction	38
3.2	Methods to calculate a seismic event's magnitude and moment	39
3.2.1	Introduction	39
3.2.2	Relationship between source size and seismic event spectra and a review of the limitations of the method	39
3.3	Evaluation of a seismic events focal mechanism	43
3.3.1	Introduction	43
3.3.2	P- and S-wave displacement and the moment tensor	43
3.3.3	Methods to perform moment tensor inversion	45
3.3.4	Decomposition of Moment Tensor	49
3.4	Methods to measure the geometry of a seismic event from anisotropic variations of wave behaviour	55
3.4.1	Introduction	55
3.4.2	Relationship between SWS and fracture properties	55
3.4.3	Inversion workflows	57
3.5	Methods to measure the geometry of a seismic event from signal length variations	60
3.5.1	Introduction	60
3.5.2	The relationship between the source history and the radiation pattern	60
3.5.3	The relationship between the source time function and the geometric and kinematic properties of fractures	63
3.6	Calculation of the energy transfer from a seismic event	70
3.7	Calculation of stress transfer between seismic events	73
3.7.1	Introduction	73
3.7.2	Methods to model the Coulomb failure function	73
3.8	Methods to be used and planned software system	81
4	Industrial Case Study	84
4.1	Introduction	84

4.2	Location and Geological background of the Wahigan well	85
4.2.1	Geological history of the Dunvernay formation	86
4.2.2	Tectonic history of the Fox Creek area and current in-situ stresses	90
4.3	Production timeline and occurrence of the 12 January induced seismic event at the Wahigan well site	93
4.3.1	Seismic event detected on 12 January 2016	95
4.4	Microseismic data acquisition conducted at the Wahigan well	97
4.4.1	Microseismic processing conducted by the contractors at the Wahigan well	100
4.4.2	Microseismic events detected during the survey period and overview of possible causes of induced seismicity	103
4.5	Discussion	107
5	Derivation of velocity and attenuation models	108
5.1	Introduction	108
5.2	Quantitative assessment of provided velocity models	108
5.2.1	Method to be employed	109
5.2.2	Review of available data: Velocity models and microseismic records	110
5.2.3	Velocity model accuracy comparisons: fixed position events . .	114
5.2.4	Microseismic events chosen for use with the velocity model accuracy comparisons	123
5.2.5	Velocity model accuracy comparisons: variable position events	124
5.3	Development of a velocity model for use with the software system . .	130
5.3.1	Very fast simulated annealing to calibrate velocity models . .	130
5.3.2	Implementation of VFSA and changes made to the original Pei et al method	135
5.3.3	Stage 1 of velocity model development: Input model and initial constraints	138
5.3.4	Stage 2 of velocity model development: Quality control checks and additional constraints	140
5.3.5	Stage 3 of velocity model development: Final quality control checks and comparisons	146
5.4	Development of an attenuation model for use with the software system	148
5.4.1	Modelling method to be employed	148
5.4.2	Stage 1 of attenuation model development: Rise time measurements	149
5.4.3	Stage 2 of attenuation model development: 2D attenuation model derivation and verification	151

6	System Development: Implementation and testing with a single event	155
6.1	Introduction	155
6.2	Testing target	158
6.3	Software module 1: Wavelet variation to determine the rupture geometry, direction and velocity	159
6.3.1	Design and Verification	160
6.3.2	Implementation	167
6.3.3	Testing	173
6.3.4	Evaluation	175
6.4	Software module 2: Full waveform moment tensor inversion and decomposition to determine focal mechanism	176
6.4.1	Design	176
6.4.2	Implementation	180
6.4.3	Testing	188
6.4.4	Evaluation	190
6.5	Software module 3: Seismic moment and Radiated energy ratio calculations	191
6.5.1	Design	191
6.5.2	Implementation	193
6.5.3	Testing	197
6.5.4	Evaluation	198
6.6	Software module 4: Coulomb stress transfer modelling	199
6.6.1	Design	199
6.6.2	Implementation	201
6.6.3	Testing	203
6.6.4	Evaluation	206
6.7	Software outputs: Map generation	206
6.8	Discussion	209
7	System Development: Testing with the industrial case study	210
7.1	Introduction	210
7.2	Analysis of the main event	211
7.3	Mechanism 1, Hydraulic connection	213
7.3.1	Mechanism 1, fault reactivation from hydraulic stimulation: Event set	213
7.3.2	Mechanism 1, fault reactivation from hydraulic stimulation: Testing criteria	220
7.3.3	Mechanism 1: Monitoring capability tests	221
7.3.4	Conclusions, Mechanism 1	234

7.4	Mechanism 2, Stress transfer	235
7.4.1	Mechanism 2, static stress transfer from faults reactivated by hydraulic stimulation: Event set	235
7.4.2	Mechanism 2, static stress transfer from faults reactivated by hydraulic stimulation: Testing criteria	238
7.4.3	Mechanism 2: Monitoring capability tests	239
7.4.4	Conclusions, Mechanism 2	249
7.5	Forecasting induced seismicity using the software package	250
7.5.1	Mechanism 1: Forecasting induced events caused by pore-pressure changes instigated from hydraulic fracturing	251
7.5.2	Mechanism 2: Forecasting induced events triggered by static stress transfer from other microseismic events	253
7.6	Discussion	256
8	Discussion and conclusions	258
8.1	Introduction	258
8.2	Current state of forecasting induced seismicity	259
8.3	Design of a new forecasting approach and development of a software system	259
8.4	Industrial case study	260
8.5	Development and testing of the software system	261
8.6	Forecasting induced seismicity	262
8.7	Overall Conclusions	263
8.8	Suggestions for further work	264
A	Appendix - Chapter 5	267
A.1	Modification to the ray-tracing software	267
A.2	First arrival identification for the perforation shots	272
A.3	Raytracer software parameter decisions	282
A.3.1	Grid size, Z	282
A.3.2	Time Step	286
A.4	Geological Constraints for the velocity model	290
B	Appendix - Chapter 6	296
B.1	Problems with signal variation when attempting to use autopicking routines	296
B.2	Determining seismic stations installation angles	299
B.2.1	Method	299
B.2.2	Implementation	299

List of Figures

2.1	Seismic response procedure during the stimulation phase for the Basel EGS project	13
2.2	The adaptive traffic light system developed by the SED	16
2.3	Overview of induced seismic forecast models	18
2.4	Results of the stochastic seed model calibrated against observed seismicity at Basel	22
2.5	A ternary diagram showing the three components which are altered by anthropogenic activities	26
2.6	Schematic of a low-permeability reservoir with an intersecting fault	28
2.7	Causes of the Preese Hall induced seismicity	30
2.8	Coulomb stress change at the Landers fault on the San Andreas fault zone	32
2.9	A schematic map of a theoretical forecasting model based on the data provided by microseismic events	35
3.1	Calculation of A_0 from the spectral properties	40
3.2	The elemental tensors used by Křížová et al. (2013)	48
3.3	A selection of moment tensor identities and the associated focal mechanisms	51
3.4	The diamond CLVD-ISO plot with the positions of the basic component sources	52
3.5	Geometry Calculations from the slip vector	53
3.6	Workflow for inverting for rock physics parameters from SWS measurements	58
3.7	Example SWS result from Gajek et al. (2018) using the Verdon et al (2009) approach, showing the QC criteria used to assess the measurements.	59
3.8	Example of the angles used to describe equations 3.39 to 3.41	61
3.9	A example source time function for a source	62
3.10	Pulse length (ΔT) and rise time (τ) of a signal.	64

3.11	Rise time comparison	65
3.12	The frequency domain method to investigate source parameters by Tomic et al. (2009)	67
3.13	Theoretical models for different rupture types from Cesca et al. (2011)	69
3.14	The relation between the average RMS radiation pattern coefficients of P, S, SV, and SH waves as a function of the tensile angle	72
3.15	The axis system used for calculations of Coulomb stresses on optimum failure planes	75
3.16	Graphical representation of the two equations used to calculate the Coulomb stress change	77
3.17	Triggering of a 30 degree dip thrust earthquake on an adjacent patch of similar size along strike	80
3.18	Flowchart of the method to be developed	83
4.1	The location of the Wahigan well in the Alberta province, Canada	85
4.2	The stratigraphy of the Woodbend-Winterburn group of Alberta	86
4.3	The extent of the Woodbend and Winterburn group in the Western Canada Sedimentary Basin	87
4.4	Model for water circulation into the Alberta Basin as developed by Harris et al. (2018)	89
4.5	Stress trajectories for S_{Hmax} and S_{hmin} as determined from the well breakouts for the Western Canada Sedimentary Basin	91
4.6	Pressure routine applied to the formation during the hydraulic fracture operation	95
4.7	Timing and scaled magnitudes of earthquakes near Fox Creek	96
4.8	Geophone deployment in each seismic station of the surface array	97
4.9	Data quality examples	99
4.10	Velocity models provided by the industrial contact	102
4.11	A enlarged map showing the location of the well bore and events as identified by contractor A	104
4.12	A enlarged map showing the location of the well bore and events as identified by contractor B	105
5.1	Velocity models provided by the industrial contact	111
5.2	A map of the perforation shots by hydraulic fracture stage	113
5.3	The distribution of RMS error for model A and B.	115
5.4	The distribution of double difference values for all perforation shots - station pairs	116
5.5	The distribution of RMS errors along the well bore for models A and B	117

5.6	A map showing the RMS error at each station from all perforation shots using velocity model A	119
5.7	A map showing the RMS error at each station from all perforation shots using velocity model B	120
5.8	A map showing the difference in RMS error from Model B to A at each station from all perforation shots	121
5.9	The events chosen to test the velocity model accuracy as positioned by both velocity model A	124
5.10	The distribution of RMS errors for the subset of events between velocity model A and B	125
5.11	The revised position of event 76 using the Trabox ray tracer and a grid search / subdivide method with velocity model A	127
5.12	The revised position of event 76 using the Trabox ray tracer and a grid search / subdivide method with velocity model B	128
5.13	The variation in the x parameter from equation 5.3 with μ	132
5.14	The variation in the probability calculated by equation 1.4 with temperature	133
5.15	The variation in temperature with iteration using the temperature schedule set out in equation 5.6	134
5.16	The variation in temperature with iteration using the custom temperature schedule discussed above	137
5.17	Velocity model 1 as output from the optimisation process with velocity constraints as derived from the geological review.	139
5.18	A comparison of the RMS errors from the positioning of the event subset between the base velocity model and velocity model 1	141
5.19	A comparison of the RMS errors from the positioning of the event subset between the base velocity model, velocity model 1 and 3	142
5.20	Velocity model 3 as calibrated by the optimisation process	143
5.21	A comparison of the output velocity models after two runs with different initial velocity models to consider the uniqueness of the output model	145
5.22	A comparison of the RMS errors from the positioning of the event subset between the final velocity model and velocity model A and B	146
5.23	Calculation of the initial rise time from the measured rise times from event 77, nearest to station 51	150
5.24	Calculation of the initial rise time from the measured rise times from event 78, nearest to station 59	151
5.25	The median attenuation map as gridded onto a 100x100 m grid using the rise time values measured from event 78, nearest to station 59.	153

5.26	Verification of the Q_p model using event 77 showing the comparison between the measured Q_p values with the 95% confidence limits and the modelled Q_p values with the 95% confidence limits	154
6.1	The iteration prototyping model	156
6.2	The software systems flowchart	157
6.3	Data record for Event 21 with the P- (blue points) and S- (red points) wave arrivals annotated.	159
6.4	Difference between the Zollo and de Lorenzo (2001) model (red hollow points) and the measured data	162
6.5	Theoretical models for different rupture types from Cesca et al. (2011)	165
6.6	Forward modelling of the rupture time using the Cesca et al. (2011) model for a unilateral and bilateral rupture	166
6.7	Example of a seismic record from event 21 with the first arrival, risetime length and rupture length annotated	169
6.8	Flow chart for the implementation of the module	171
6.9	Display showing the measured rise times for event 21 with the modelled rise times given the outputs from the inversion process.	173
6.10	Display showing the measured rupture times for event 21 with the modelled rupture times given the outputs from the inversion process.	174
6.11	The elemental tensors used by Křížová et al. (2013).	177
6.12	The match between finite difference synthetic seismograms	178
6.13	A worked example of the preparation carried out before the generation of the Green's functions and the moment tensor inversion	183
6.14	Flow chart for the implementation of the module	186
6.15	A comparison between one of the elemental Greens Functions and the data records	189
6.16	Flow chart for the implementation of the module	196
6.17	Results from applying the Brune model to station 92 for each of the 3 channels after rotation (P, S_h and S_v) and the output magnitude compared to the two contractors.	197
6.18	A histogram of the energy ratios computed by Kwiitek and Ben-Zion (2013) and where the test event's radiative energy ratio places in this scale.	198
6.19	The parameters required for imputing a fault into the Coulomb software package	202
6.20	The Molnar model for a 2D fault with dimensions from the test event	204
6.21	The strain components for the test event modelled by the Coulomb software compared to the average strain component values as calculated by the Molnar model.	205

6.22	The Coulomb stress change for the strike-slip test event in bar.	205
6.23	The fracture and Coulomb stress change maps	208
7.1	Graph showing the empirical relationships between the earthquake magnitude, fault size and seismic moment. Image from Maxwell (2013).	212
7.2	A map showing the events during stage 22 of the injection process . .	214
7.3	A map showing the events during stage 23 of the injection process . .	215
7.4	A map showing the events during stage 24 of the injection process . .	216
7.5	A map showing the events during stage 25 of the injection process . .	217
7.6	A map showing the events during stage 26 of the injection process . .	218
7.7	The events that were chosen for subset 1 to diagnose the cause of the main event, as positioned by both velocity model A and B	219
7.8	Comparison of a poor signal to noise ratio event and a excellent signal to noise ratio event	222
7.9	Map of all events from subset 1	223
7.10	A smaller scale map of a selection of events from subset 1 where the boundaries of the plot are defined on figure 7.9.	224
7.11	A smaller scale map of a selection of events from subset 1 where the boundaries of the plot are defined on figure 7.9.	225
7.12	Map of all events from subset 1 viewed in-depth in an E-W direction	226
7.13	Fracture map generated from the software package	227
7.14	Evolution of the fracture network with time from the start of the hydraulic fracturing stage.	228
7.15	Depth view in an E-W direction of the fracture display output from the software package	230
7.16	Maps of the microseismic events fracture planes	231
7.17	Relationship between the rake angle and the fault plane, image from Alberti (2005).	232
7.18	Depth view of the wellbore, main event and a set of microseismic events with tensile angles greater than 5 degrees	233
7.19	A map of all the events detected and positioned by velocity model A	236
7.20	A map of the events positioned by velocity model A which occurred in the first 14 hours after the pumping routine started	237
7.21	Map view of stage 1 and 2 of the hydraulic fracture operations and a set of microseismic events that are part of the SW-NE fault network	241
7.22	Depth view of stage 1 and 2 of the hydraulic fracture operations and a set of microseismic events that are part of the SW-NE fault network	242
7.23	Fracture map generated from the software package	244
7.24	Depth view in an E-W direction of the fracture display output from the software package	245

7.25	Coulomb stress change for the 2.2 km depth slice and 2.4 km depth slice	247
7.26	Coulomb stress change for the 2.6 km depth slice and 2.8 km depth slice	248
7.27	Data-driven forecasting model for the first mechanism.	251
7.28	Fracture maps with time from the start of stage 23 of the hydraulic fracturing program (t0) to 7 hours prior to the main event slip (t0 + 12 hours)	252
7.29	An example of the variation in Coulomb stress with time over part of the SW-NE fault network	255
A.1	The Trabox software velocity model arrangement	268
A.2	The modified Trabox software velocity model arrangement for this site	268
A.3	The different raypaths possible in modelling in the Trabox software .	269
A.4	The new method to calculate the starting declination angle	271
A.5	Signal and noise spectrum of an example perforation shot.	273
A.6	Changes from the application of the AGC, increases the signal amplitude but also enhances low- frequency noise which could be interpreted as signal.	274
A.7	Before and after application of the processing steps to a record containing a perforation shot	276
A.8	The original record and the record after stacking all the traces in the station to form a single trace. These traces are then replicated three times for visual identification purposes	277
A.9	Semblance plot for perforation shot 20-3	278
A.10	Perforation shot 20-1, original record presented as a 3D Section with trace equalisation and T2 scaling	279
A.11	Changes to event alignment with pilot trace cross-correlation for perforation 17-1	281
A.12	Record of perforation shot 17-1	281
A.13	A figure showing the variations in the modelling outputs with the grid size in the z-direction with velocity model A	283
A.14	A figure showing the variations in the modelling outputs with the grid size in the z-direction with velocity model B	284
A.15	A figure showing the variations in the modelling outputs with the grid size in the z-direction	285
A.16	A figure showing the variations in the modelling outputs with the grid size in the z-direction	285
A.17	A figure showing the variations in the modelling outputs with time step (ms)	287
A.18	A figure showing the variations in the modelling outputs with time step (ms)	288

A.19	A figure showing the variations in the modelling outputs with time step (ms)	288
A.20	A figure showing the variations in the modelling outputs with time step (ms)	289
A.21	The variation in wave speed (m/s) for three different formations in the Alberta province with a change in overburden pressure (MPa).	291
A.22	Empirical relationship for the change in wave speed with pressure MPa for shales found in Alberta, Canada. Image from Ong et al. (2016).	292
A.23	The units within the Belloy formation. Image from the geological atlas of Canada.	294
B.1	Example of the received signals for the 14 m and 29 m geophone depths	297
B.2	Variation of the rupture time for a small change in azimuth of 20 degrees.	298
B.3	Map of the seismic array and the positions of the dynamite shots used to test the array system during installation	300
B.4	Determining the rotation for the installation axis to geographic north	301

List of Tables

1.1	Seismic events associated with hydraulic fracturing processes	2
4.1	Table of the hydraulic fracture operations conducted at the Wahigan site.	94
5.1	Initial velocity model used in the VFSA process together with the constraints for the velocity and the references used to calculate these limits.	138
6.1	Changes made during development of module 1	172
6.2	Changes made during development of module 2	187
6.3	Regional stress tensor for the Waighan site	201
6.4	Output parameters from the operation of the software system on the test event	207
7.1	Main event parameters determined from the Contractors and academics	211

Acronyms and units

- AER - Alberta energy regulator
- ATLS - Adaptive traffic light system by the SED
- Bcf/d - Billion cubic feet a day
- Bcf - Billion cubic feet
- CI - Confidence interval
- CLVD - Compensated linear vector dipole earthquake source
- DC - Double-couple earthquake source
- DFN - Discreet fault network
- EGFs - Empirical Green's functions
- EGS - Enhanced geothermal system
- EMS - European Macroseismic Scale
- ETAS - Epidemic Type Aftershock Sequence
- GIP - Gas in place
- GNM - Geomechanical-numerical model
- GUI - Graphical user interface
- ISO - Isotropic earthquake source
- ODR - Orthogonal distance regression
- OGA - Oil Gas Authority
- OLS - Ordinary least square
- MMBOE - Million Barrels of Oil Equivalent

- Mw - Moment Magnitude scale
- RMS - Root mean squared
- SED - Swiss Seismological Service
- SNR - Signal to noise ratio
- SWS - Shear wave splitting
- tcf - Trillion cubic feet
- TLP - Traffic light protocols
- TLS - Traffic light system
- VFSA - Very Fast Simulated Annealing
- VTI - Vertical transverse isotropy

Symbols

- λ - Fault rake
- ϕ - Fault strike
- δ - Fault dip
- α - Fault tensile angle
- μ_r - Random number between [0,1] used in VFSA
- τ - Rise Time
- τ_0 - Rise Time at the source
- $t_{d\alpha}$ - Rupture Time
- $t_{d\alpha 0}$ - Rupture Time at the source
- α_v - P-wave velocity for the pulse directivity method
- χ - The ratio between a unilateral to bilateral rupture
- L - The length of the rupture
- V_s - Shear velocity
- V_f - The rupture velocity of a fracture
- Q_p - The seismic quality factor (P-Wave)
- T^* - The travel time divided by seismic quality factor
- T - The travel time of a seismic wave
- C - The source specific constant for the pulse directivity method
- ϕ_r - Inclination of the ray path
- η - The station azimuth

- θ - Fracture azimuth
- \mathbf{M} - Moment tensor
- \mathbf{G} - Green Functions
- \mathbf{U} - Ground displacement
- \mathbf{E} - Elemental tensors
- M_0 - Seismic moment
- M_w - Moment magnitude
- ρ - Density
- α_Q - Attenuation along the ray path
- ω - Angular frequency
- R_v - Spherically averaged source radiation pattern
- J_c - The radiated flux
- E_p - Radiated energy, P-wave
- E_s - Radiated energy, S-wave
- σ_f - Coulomb stress change
- μ' - Effective friction (Coulomb stress change)
- τ_β - Shear stress along the plane
- σ_β - Normal stress along the plane
- ν - Poissons ratio
- μ - Shear modulus
- D - Earthquake slip
- f - Earthquake shape factor
- ϵ - Strain

Chapter 1

Introduction

1.1 Introduction

Since the ratification of the Paris climate change accords in 2016 (UN, 2016), countries around the world are transitioning towards a carbon-neutral economy in order to limit global average temperature increases to no more than 2°C above pre-industrial levels. In the UK, natural gas is considered as a transition fuel in order to reach a carbon-neutral economy while the development of the renewable sector continues and until the next generation of nuclear power plants becomes operational. The UK's offshore gas production has been in decline since the year 2000, which has meant that the UK has gone from being a net exporter of gas to importing over half of the gas supplies in 2018 (Department for Business, 2019b).

For this reason, it is the intention of the UK government to utilise fully domestic gas resources to the maximum extent and to encourage investors to explore the potential for onshore gas production from shale rock formations in the UK (Department for Business, 2019b). With regard to the potential onshore supplies in the UK, the largest potential reservoir is the Bowland basin and GIP estimates made in 2013 for this are between 822 and 2281 tcf with a median of 1322 tcf (Andrews, 2013). While this value has been recently contested by Whitelaw et al. (2019), there still exists a large potential for onshore domestic gas resources in the UK.

The process of extracting natural gas from shale rock formations and other unconventional reservoirs using hydraulic fracturing is an established process originally developed in the 1940s. It wasn't until the early 2000s when developments in drilling technology that allowed horizontal pathways to be drilled along a single formation,

this advancement, together with rising oil prices forced a new interest in unconventional reservoirs. Since this point, the US market for shale gas rapidly expanded and as of February 2018, the US became a net exporter of natural gas, reaching 5 Bcf/d in February 2019 (Dyl, 2019). Shale gas was a key part of this economical model (Smith, 2012).

The hydraulic fracturing process uses high-pressure drilling mud (water with thickening agents) with a combination of chemical and sand proppants to exceed the strain capacity of the rock, generating fractures. This process props open fractures, increasing the permeability of the reservoir and allowing gas to flow from the reservoir and up the well. This technology is not free from environmental risks and these are centred on three main topics: groundwater contamination by stray methane, uncontrolled emissions of methane to the atmosphere, and seismic activity directly or indirectly related to hydraulic fracturing (Stephenson, 2016). It is the lattermost environmental risk which is to be investigated in this research.

The process of using hydraulic fracturing to prop open fractures and increase the permeability will produce only nano to micro-scale earthquakes, unfelt at the surface. However, the presence of dormant fault lines within the subsurface and the injection of fracture fluid means that there is a risk of these fault lines re-activating due to the increase in pore-pressure and slipping generating a seismic event which is felt at the surface. These events are more substantial than the opening of hydraulic fractures and can cause disturbances on the surface. World-wide earthquakes associated with hydraulic fracturing for unconventional gas extraction and for Enhanced Geothermal Systems (EGS) projects are mainly in the minor earthquake range ($< M_w$ of 3.9) and very rarely in the light and moderate range (M_w of 4.9 and 5.9, respectively). Table 1.1 shows some representative magnitudes associated with the hydraulic fracturing process. The consequences of these earthquakes events vary significantly, for example,

Table 1.1: Seismic events associated with hydraulic fracturing processes

Site	Maximum event magnitude	Date
Basel, Switzerland (EGS)	$M_w = 3.4$	August 2006
Elmore City, Oklahoma, US (Shale gas)	$M_w = 2.9$	Jan 2011
Preese Hall, UK (Shale gas)	$M_w = 2.3$	April 2011
Fox Creek, Canada (Shale gas)	$M_w = 3.9$	Jan 2016
Sichuan Basin, China (Shale gas)	$M_w = 4.7$	Jan 2017
Pohang, South Korea (EGS)	$M_w = 5.5$	Nov 2017
Preston New Road, UK (Shale gas)	$M_w = 2.9$	August 2019

the consequence of the Basel seismic events in 2006 resulted in compensation claims of up to US\$7 million claimed (Kraft et al., 2009) and for the Preston New Road in the UK the events resulting in the process being suspended until ‘compelling new evidence’ was submitted (Department for Business, 2019a), stagnating the industry. These consequences are minor compared to the Mw 5.5 event in Pohang, South Korea associated with an EGS experiment, which resulted in injuries to 135 people and more than 1700 people displaced into emergency accommodation (Westaway and Burnside, 2019).

Mitigation of these events is a primary concern for national governing bodies and the industrial groups investing in this industry. In the UK the OGA (Oil Gas Authority) guidelines state that *“The OGA will assess any risks of seismic activity and must be satisfied that controls are in place to avoid an event altogether or, in the unlikely event that seismicity is induced, to minimise disturbance to those living and working nearby, and to reduce the risk of any damage”* OGA (2018). The control method that is in-place for hydraulic fracture operations in the UK and used throughout the world is the traffic light protocols (TLP), which was initially proposed by Bommer et al. (2006). This pragmatic approach for mitigating induced seismicity is neatly defined by Gaucher et al. (2015), by the conceptual model of, “given that the seismic events are induced by operations that force fluids into the reservoir, it should be possible to prevent any major disturbance on the surface by modifying or suspending these operations at the right moment”. This ‘right moment’ as defined by Gaucher a (in the UK, Canada and the USA) the detection of a seismic event with a magnitude exceeding a set levels and mitigatory measures include reducing the pumping pressure or suspending the program.

The challenge that these systems have faced worldwide is that even after operations were suspended using the TLS protocols, induced seismic events have continued to occur and sometimes at increasingly greater magnitudes. There are two key case studies for this. The first is Basel, Switzerland in 2006 where an Mw 2.6 event occurred setting off the amber level of alert and the injection was suspended. Four hours later an Mw 2.7 event occurred followed by an Mw 3.4 event an hour later (Kraft et al., 2009). The second case study is Preese Hall, Lancashire UK in 2011 where an Mw 2.7 event was detected during injection operations. Ten hours after operations were completed, a second event was detected at a level of Mw 1.5 (Clarke et al., 2014). In November 2019, after completion of the investigation into the Mw 2.9 event at the Preston New Road site in Lancashire, the UK Government suspended all hydraulic fracturing projects in the UK as ‘it is not possible with current technology to accurately predict the probability of tremors associated with fracking’ (Department for Business, 2019a). The ability to forecast seismic activity induced by hydraulic fracturing processes is now the singular point restricting the development

of the unconventional gas industry in the UK and requires research if the possibility of the suspension is to be lifted.

1.2 Research project aim and background

The research detailed in this thesis aims to establish the extent to which induced seismic activity from hydraulic fracturing can be forecast.

The research conducted and any developments as a result will solely utilise micro-seismic data. These are seismic recordings that are only detectable using specialist equipment (geophones) and have magnitudes less than zero. Geophysical models are used to relate the microseismic data recorded by the geophones to physical changes within the sub-surface. In a hydraulic fracturing environment, these changes are fractures propagating by all three failure modes (I, II and III).

To assist in the pursuit of this aim, contact was made with a industrial partner whom supplied a set of geophysical data collected at a shale gas extraction site in Western Canada. This dataset will be used in this research project in the following ways:

1. To ensure that the correct geophysical analysis parameters are used in any software developed, ensuring that the software package will adhere to industry acquisition standards
2. To validate models of induced seismicity against a known seismic event induced by hydraulic fracturing operations
3. To test the capabilities of any software system developed and to analysis microseismic data with industry acquired datasets

In order to achieve this aim, the following objectives were identified through the research:

1. Review and critically evaluate the current approaches to forecast seismicity associated with hydraulic fracturing.
2. Identify and review the primary mechanisms that induce seismicity from hydraulic fracturing operations.
3. Design and develop a software system to address the limitations associated with current forecast approaches.
4. Review and develop methods to appraise the positional accuracy of the geophysical models required to forecast induced seismicity

5. Evaluate the extent to which the developed software can be used to forecast induced seismicity

1.3 Limitations and definitions

The scope, limitations, and underlying assumptions of the research are listed below:

- Any software system designed will be using seismic data recorded from a shale gas extraction site as a guide for parameter choices, but aims to be applicable with any use of hydraulic fracturing, e.g. Enhanced geothermal systems and CO₂ sequestration.
- The underlying assumption of any software system is that the hydraulic fracturing operations do not occur directly into a fault line. To forecast induced seismicity on a particular fault plane, there has to be a separation between the injection point and the fault plane.
- That prediction is defined in this thesis context as a seismic event will occur in a defined time frame in a defined area.
- That forecasting is defined in this thesis context as a seismic event will occur in the near future in a defined area

1.4 Thesis overview

A brief description of the thesis structure is given below:

Chapter 2 reviews the literature surrounding the causes, consequences and means to mitigate the effects of induced seismicity. As part of this chapter, current forecasting methods are detailed and scope for a new forecasting approach is discussed. The second part of this chapter reviews the causes of induced seismicity and details the fracture network parameters required to monitor and forecast these events. Finally a set of programming requirements that a new forecasting software system must adhere to are conceived.

Chapter 3 covers the first part of the software system development, a literature review of the potential geophysical methods available to analyse microseismic signals for the purposes of identifying changes to the fracture network. Each method is reviewed with the programming requirements in mind, and are used to design a software system capable of forecasting induced seismicity. The pre-requisites for the geophysical analysis methods to be used were outlined, so as to be derived in later chapters.

Chapter 4 covers the details of a industrial case study provided to test the capabilities

of the software system. In this chapter, the dataset location, geological history, production history and geometry of the acquisition array are discussed. In addition, the first pre-requisites for the software system, the regional stress field, is derived.

Chapter 5 details the derivation of the final two prerequisites for the software system, the geophysical models describing the velocity of seismic waves during the transmission between the source and surface, and the attenuation that is applied during this transit. The chapter first contains a detailed investigation of the accuracy of two velocity models provided in the industrial dataset. Second a new velocity model is derived which is used to reposition the seismic events with a higher accuracy than the provided velocity models. The methods available to generate a attenuation model are reviewed. A attenuation model is generated given the data limitations that were in place for this industrial case study.

Chapter 6 covers the second part of the system development, implementation and the first stage of the testing of the modular software system. In this chapter, the methods outlined in chapter 3, are implemented into individual modules which are then combined into a single system. These modules are developed via an iterative prototyping approach using a single test event to evaluate the development process.

Chapter 7 details the final stage of the system development, testing of the overall system using the industrial case study for the ability to firstly monitor the evolving fracture network, and considering the extent to which the software system can forecast induced seismicity. The monitoring component of the software system is considered by retrospectively diagnosing the cause of an induced seismic event that occurred during the industrial case study. The forecasting ability of the software system is considering by comparing the forecast model established in chapter 2 to the detected microseismic events in the industrial case study.

In chapter 8, the research is summarised and compared against the original research objectives. The future potential of the use of this approach, and the software system developed, to forecast induced seismicity is evaluated. The future work required to allow this approach to be used on hydraulic fracture sites around the world is discussed.

Chapter 2

Literature review

2.1 Introduction

This literature review has two aims. The first is to review the current regulatory framework for the mitigation of induced seismicity and the current means to forecast these seismic events. Then with any knowledge gaps identified and discussed, the second part of the literature review aims to consider the mechanisms that cause induced seismicity. The fracture parameters that are linked to these mechanisms are used to address the knowledge gaps identified in the first section.

2.2 The current regulatory framework for the mitigation of seismicity induced by hydraulic fracturing processes

As part of the continued development of low permeability hydrocarbon reservoirs such as shale gas and oil fields, the process of hydraulic fracturing is routinely used to increase the reservoir permeability. This process involves using pressurised fracture fluid to extend and prop open fractures within the reservoir, thus increasing the permeability, allowing hydrocarbons to flow along the wellbore up to the surface. The consequence of this fracturing process is that ground movement is initiated within the subsurface. This ground movement should translate to the magnitudes of the sound wave within the nano- to micro-scale magnitude range. These events should only be detected using seismographs and are not felt on the surface. Existing fractures

and faults within the subsurface means that the injection of fluid can trigger a larger slip of the subsurface, translating into a seismic event that is felt and causes ground disturbances on the surface.

The consequences of these felt induced seismic events at the surface have had a negative effect on the continued efforts to utilise hydraulic fracturing in the unconventional hydrocarbon industry and other energy sectors, such as EGS and CO₂ sequestration. In the UK, after the second of two felt induced seismic events occurred at Preese Hall shale gas site, Blackpool in 2011 any further hydraulic fracturing operations in the UK were curtailed for 18 months following a governmental review (Green et al., 2012). Hydraulic fracture operations in the UK recommenced in September 2018 at the Preston New Road site, in Lancashire but operations were shut down again after a locally felt Mw 2.9 event on 26 August 2019. Hydraulic fracturing operations were then suspended through-out the UK while an investigation into a means to manage the risk of induced seismicity was conducted (OGA, 2019). Similarly the Mw 3.4 induced seismic event in Basel in 2006 (during the EGS experiment) caused non-structural damage, this experiment was immediately shut-down with compensation claims of US\$7 million claimed (Kraft et al., 2009). Both of the Preese Hall and Basel incidents resulted in international media attenuation and these incidents, as well as other injection-related induced events, are reviewed by Ellsworth (2013). While none of these incidents resulted in any injuries or deaths, the magnitude Mw 5.5 earthquake detected on 15 November 2017 in Pohang, South Korea resulted in 135 people injured along with > 1700 people displaced into emergency accommodation. This event was associated with the fluid injection at the EGS project with the final fluid injection two months prior to the 15 November earthquake (Westaway and Burnside, 2019).

To address the environmental and social consequences, and to develop the unconventional hydrocarbon industry, guidelines and recommendations have been outlined by national authorities to be applied to ensure that the effects from induced seismicity are mitigated. In the UK, the Oil Gas Authority (OGA) consolidated onshore guidance document states that for wells which are due to be hydraulic fractured, a hydraulic fracture plan must be submitted detailing how the operator will control and monitor the fracturing process. The OGA guidelines state that, “The OGA will assess any risks of seismic activity and must be satisfied that controls are in place to avoid an event altogether or, in the unlikely event that seismicity is induced, to minimise disturbance to those living and working nearby, and to reduce the risk of any damage” (OGA, 2018).

As part of these guidelines, the OGA has two policies to manage the risk of induced seismicity. The first is that “the OGA requires detailed geological studies to be

undertaken by an operator to prevent such operations taking place near geological faults, which greatly reduces the likelihood of an event”. The second policy is “the OGA requires certain controls and requirements to be adhered to by an operator, including the monitoring in advance of background seismic activity, a real-time traffic light scheme during injection, and detailed operational precautions to be incorporated in an HFP (hydraulic fracture plan) ” (OGA, 2018).

Similarly, the EU funded M4ShaleGas project aims to address the specific challenge related to understanding, preventing and mitigating the potential environmental impacts and risks of shale gas exploration and exploitation. The report by ter Heege and Cremer (2017) as part of this project devised a set of recommendations to mitigate the effects of induced seismicity. These were split into those prior to and during injection operations, with the following points to be applied prior to starting the injection of fluid:

- 1.1 Assessment of potential maximum earthquake magnitude and assessment of probability of inducing an earthquake
- 1.2 Managing the probability of inducing an earthquake
- 1.3 Accounting for uncertainty in analysis by a trial period. Compare observed and predicted response
- 1.4 Assessment of hazards and risk related to assumed maximum magnitude earthquake

The following recommendations are to be applied during injection operations:

- 2.1 Traffic light systems for ongoing operations, when observed behaviour differs from predicted behaviour
- 2.2 Optimizing hydraulic fracturing operations, leading to efficient stimulation with minimum injected fluid volume
- 2.3 Minimizing the zone of induced stress changes and affected volume of rock

With regard to hydraulic fracturing projects conducted in Canada, the AER (Alberta Energy Regulator), under subsurface order no. 2 states, “that licensees must assess the potential for induced seismicity caused by or resulting from hydraulic fracturing operations and adopt, and be immediately prepared to implement, a response plan to address potential seismic events. Licensees will be required to monitor for seismic activity in the vicinity of their hydraulic fracturing operations and follow a “traffic light” process with staged action thresholds (Parks et al., 2015)”.

Reviewing these recommendations, firstly there is a requirement from all of these

agencies to implement real-time monitoring and thresholds for mitigation measures via the “traffic light” process during operations. The second requirement is to assess the potential risk and likely hazard to cause induced seismic events during operations. These requirements, written from 2015 to 2018, are the start of a drive towards forecasting induced seismicity as a means of mitigating induced seismicity.

As of November 2019, with the completion of the investigation into induced seismic events at the Preston New Road site in the UK, hydraulic fracture operations will continue to be suspended in the UK as “it is not possible with current technology to accurately predict the probability of tremors associated with fracking” (Department for Business, 2019a) until “until compelling new evidence is provided”. Therefore the lack of research into forecasting induced seismicity is now considered as the singular point restricting the development of the unconventional gas industry in the UK. Monitoring by microseismic analysis is a key component of this and research into microseismic systems that assist in this approach is the central aim of this thesis.

2.3 Forecasting induced seismicity

The previous section explained that the aim of the current regulations, as a means to mitigate risk, is to forecast the possibility of inducing seismicity during hydraulic fracture operations. Two separate approaches are currently being researched as part of this objective. These are,

1. Linking seismological parameters to the risk of inducing seismicity from hydraulic fracture operations. These are reactive control approaches and the ‘traffic light’ system can be considered as part of this as well as efforts to monitor the fracture network development as a means to reduce the risk of induced seismicity occurring.
2. The use of forecast models to calculate the induced seismic events that are expected in the future. There are recent developments towards complete systems which aim to forecast the probability of causing a certain magnitude seismic event in near to real-time during operations and then modify the injection parameters to remove or minimise the risk of induced seismicity causing disturbances on the surface.

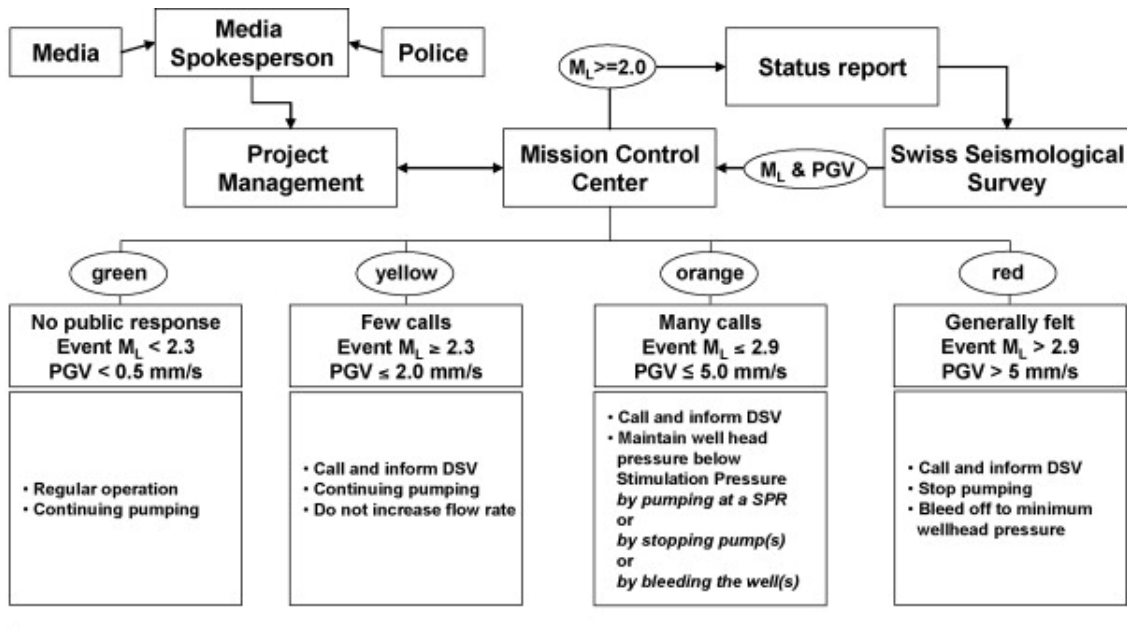
In the following section, these two approaches will be reviewed.

2.3.1 Reactive control approaches to mitigate induced seismicity

Since 2006, the primary approach to mitigating induced seismicity has been the use of reactive control approaches. This approach ties seismologically observed parameters to the current state of the fluid injection as a means to mitigate the risk of a seismic event causing a disturbance on the surface. The well known ‘traffic light’ protocols (TLP) are part of this approach and are now recognised internationally as a means to ensure that exploration and production (E&P) operators conform to set limits as a means to minimise induced seismicity.

The ‘traffic-light’ system (TLS) was initially proposed by Bommer et al. (2006) for the ‘Berlin’ geothermal project. This pragmatic approach is neatly defined by Gaucher et al. (2015), for a geothermal reservoir, by the conceptual model of, “given that the seismic events are induced by operations that force fluids into the reservoir, it should be possible to prevent any major disturbance on the surface by modifying or suspending these operations at the right moment”. There is no agreement as to when the ‘right moment’ as defined by Gaucher et al. (2015) is determined. Most systems

implemented around the world (UK, Canada, USA) utilise the magnitude of detected seismic events solely to determine if induced seismicity is progressing to the point that it will be felt. Others projects such as the EGS projects of Basel and South Korea combine seismic magnitude with peak ground velocity, and in the case of Basel, the number of phone calls made to the seismological centre. If these parameters exceed set tolerances, a range of mitigatory methods are implemented and enforced by the national or local authorities. For example, figure 2.1 shows the mitigatory methods for the different levels of induced seismicity, coloured from green to red at the Basel EGS project.



Explanation:

M_L – Local magnitude (provided by the Swiss Seismological Survey; SED)

PGV – Peak ground velocity (provided by the Swiss Seismological Survey; SED)

DSV – Drilling supervisor

Stimulation Pressure – Wellhead pressure where the first induced event occurs

SPR (Slow Pump Rate) and Stimulation Pressure to be defined in 48 hour look ahead every day

Figure 2.1: Seismic response procedure during the stimulation phase for the Basel EGS project. At green levels, magnitude levels of M_L < 2.3, the injection process carries on as normal. At yellow levels, magnitude levels of M_L > 2.3 and <2.9, pumping continues, but the flow rate remains constant. At orange levels, magnitude levels < 2.9 the well head pressure is maintained by pumping at a slower pump rate or bleeding off the well pressure. At red levels, magnitudes >2.9 pumping is immediately stopped, and the pressure is bled from the well. At all levels above green, the drilling supervisor is informed and this is communicated to project management

For such systems, real-time microseismic analysis is required to calculate the magnitude of the events. The position of events is also calculated, so as to confirm these occurred within the bounds of the site. The challenge that these systems have faced worldwide is that even after operations were suspended using the TLS protocols, induced seismic events have continued to occur and sometimes at increasingly greater magnitudes. There are two key case studies for this. The first is from Basel, Switzerland in 2006 where an Mw 2.6 event occurred setting off the orange level of alert and the injection was suspended. Four hours later an Mw 2.7 event occurred followed by an Mw 3.4 event an hour later. The second case study was from Preese Hall, Lancashire UK in 2011 where an Mw 2.7 event was detected during injection operations. After operations were completed, 10 hours later a second event was detected at a level of Mw 1.5 (Clarke et al., 2014).

The TLS is not the only layer of reactive control that is applied in hydraulic fracture operations by operators. Some E&P operators in addition to a TLS have a maximum geographic permitted extent to the hydraulic fractures generated. For example, the hydraulic fracture plan for the planned shale gas site by Third Energy at Kirby Misperton, Yorkshire, UK states that the fractures should not extend vertically into the overlying formation and horizontally the fractures should not extend beyond 400 m from the wellbore (Verdon and Harrison, 2017). Similarly for the Preston New Road shale gas site in Lancashire, there were two restrictions in place retaining to fracture growth length. The first was that fractures should not reach the faults mapped by the 3D seismic reflection survey. At this site, this minimum distance between faults and wellbore was 200 m. The second is that if hydraulic fractures do not intersect these faults, the fracture growth must not exceed site permits, which is a distance of approximately 1 km (Cuadrilla, 2018).

To consider some examples from other countries, there were restrictions in-place for the maximum fracture growth length at the Inglewood Oil Field, USA. At this site the maximum growth for a fracture filled with stimulation fluid was within the permitted site region, implying there were restrictions in place during operations (Entrix, 2012). There is still debate regarding the possibility of setting a minimum separation distance between hydraulic fractures and known faults prescribed by the national authorities, with Smythe (2019) citing a value of 850 m, and Westwood et al. (2017) citing a smaller value of 495 m. Verdon (2018) argues there are flaws in both of these calculations and that fault reactivation can occur at larger distances than both of the distances cited by these two authors. Irrespective of this debate, geometrical restrictions on fractures are used as part of a strategy to limit induced seismicity.

Both TLS and fracture length limitations can both be considered as a means to forecast seismicity caused by the hydraulic fracturing process. As discussed above

the aim of reactive control approaches is to determine ‘the right moment’ (Gaucher et al., 2015) to modify or suspend operations to prevent any major disturbances on the surface. It can then be considered that if this ‘right moment’ is reached and exceeded then seismic activity is forecast to occur in the near future.

2.3.2 Induced seismicity forecast models

Prediction models that are used to forecast induced seismicity are currently only applied in the EGS (enhanced geothermal systems) industry with the statistically-based method by Clarke et al. (2019) being suggested for the Preston New Road shale gas site in Lancashire, UK, being the sole exception. A comprehensive review of the forecast models available is presented by Gaucher et al. (2015). In the following section, key seismic prediction models and notable case studies will be reviewed together.

The aim of these forecast models, as defined by Gaucher et al. (2015), is to supply a synthetic catalogue of induced seismic events that are to be expected in the future. One of the most recent and advanced uses of these forecast models is to form the basis of an adaptive traffic light system that has been developed by the Swiss Seismological Service (SED, Wiemer et al. (2017)). This system aims to be, forward-looking, probabilistic and adaptive (Wiemer et al., 2017). The algorithmic framework for this adaptive real-time traffic light system developed by the SED is presented in figure 2.2 which shows the seismic forecast model (yellow box) as key to this algorithmic framework.

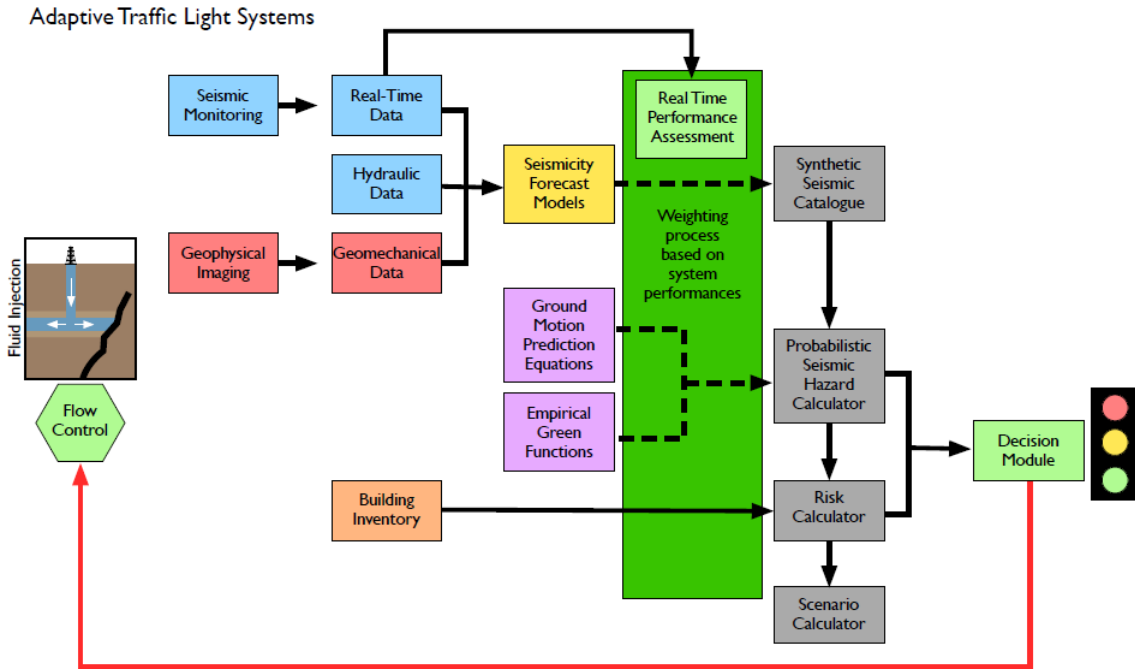


Figure 2.2: The adaptive traffic light system developed by the SED. In this system, three types of data (real-time positioning of seismic events, hydraulic data and geomechanical data from the reservoir) are brought into the seismic forecast model (yellow box). The seismic forecast model (yellow box) derives a synthetic seismic catalogue of events that are predicted to occur in the future. This catalogue and predictions of the ground motion from the magnitude of predicted seismic events are used to calculate the seismic hazard. Finally the location of buildings are used to calculate the overall risk to property and a decision is made to continue injecting fluid or to change schedule. Contrast this to figure 2.1 where this decision is based on the magnitude of a detected event. Image from Wiemer et al. (2017)

The three different modelling approaches available to predict induced seismicity are a statistical-based approach, a physics-based approach and a hybrid of both the physical and statistical methods. The workflow for all of these types of models is shown as figure 2.3 where the blue arrows follow a statistical approach, the red arrows follow a physics-based approach and the green arrows follow a hybrid approach. Gaucher et al. (2015) details that to obtain the synthetic catalogue of future induced seismic events, firstly a description of the unperturbed state of the geothermal reservoir and its seismogenic behaviour is made. For statistical-based approaches, information on the background seismicity is the minimum that is required, although flow parameters can constrain the solutions. For physical and hybrid-based approaches the reservoir structure, such as the location of any major faults, a DFN (discrete fracture network), and reservoir properties, such as the pressure and stress field are required before any modelling can begin.

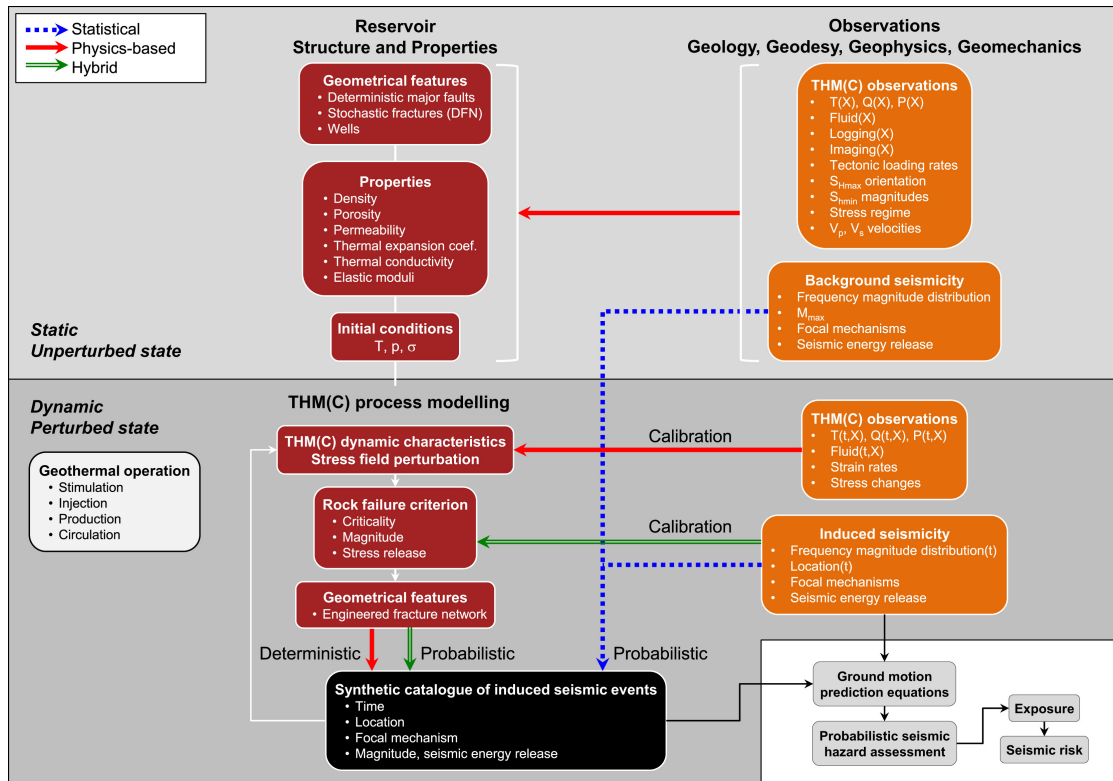


Figure 2.3: Overview of induced seismic forecast models used in the EGS industry together with the required parameters and modelling methods. This workflow highlights the static and dynamic processes that are utilised by the three different modelling approaches. For a statistical forecast model, the static processes of the observations of background seismicity are the sole inputs to predict the expected seismicity. When a physics-based model is to be considered, then the initial reservoir conditions and the thermo-hydro-mechanical(-chemical) (THMC) observations are both utilised to predict the expected seismicity. Similarly if a hybrid-approach is to be considered, then the initial reservoir conditions are used but the background seismicity is used in addition to calibrate the rock failure criterion in the reservoir. While this workflow is based on a geothermal reservoir the THMC modelling is the same modelling used to model fracture development in a hydraulically fractured unconventional gas reservoir. The different coloured arrows show the path of the different approaches taken by the statistical, physics-based and hybrid modelling approaches. Image from Gaucher et al. (2015)

There are a vast array of statistical approaches to forecasting induced seismicity, as noted by Gaucher et al. (2015), as these are inherited from the domain of statistical seismology for seismic hazard considerations. Of all of these statistical methods, a key method is by Bachmann et al. (2011) using data from the Basel EGS test. In this study, the microseismic events were retrospectively used to generate a statistical forecast model that was updated as the experiment progressed so as to simulate real-time operation. These forecast models were then compared to the observed induced seismic events. Of the 8 models tested, an ETAS (Epidemic Type Aftershock Sequence, after Ogata (1988)) model that followed the flow rate of injected fluid matched most closely to the observed data. The requirements for this system were detection and positioning of the passive seismic events in real-time. The advantage of this model to both the EGS industry and unconventional industries is that the flow rate of the fluid injection can be tied to a hazard magnitude threshold. The disadvantage of this method is while it was successful in predicting the magnitude of seismicity compared to the actual recorded induced seismic events it cannot predict the positions of where the induced seismicity may occur, nor does it predict large events or make long-term forecasts (Király-Proag et al., 2016). The reason that it cannot be used to predict large events is that the maximum possible magnitude of the events is a ‘free’ parameter for the algorithm, and choice of this parameter has an effect on the possible probabilities of exceeding a set intensity level as shown in the statistical model by Bachmann et al. (2011). This approach has recently also been applied to the Preston New Road shale gas site in Lancashire, UK (Clarke et al., 2019) where a statistical method was used in running real-time to assist in operational decisions during the hydraulic fracturing operations. The minimum required data for this model and other statistical models is a set of seismic events required to train the method.

Physics-based models, in contrast to the statistical methods, consider the underlying physical process and aim to perform better when operating conditions change, such as for the shut-in period and for long-term forecasts (Király-Proag et al., 2016). Although the seismic event information is not used in the same manner as the statistical models, the parameters determined from seismic events are utilised as either verification or as an input as initial conditions. These include the principal stress directions and magnitudes, the stress regime, and the location, geometry and extent of the fracture network. These parameters will vary with the ongoing production at the reservoir and in theory, allows the forecast model to be updated regularly as new events are detected and information added into the model.

With the initial reservoir structure and properties known, these are input into a geomechanical-numerical model (GNM). Gaucher et al. (2015) presents a list of 18 GNM codes available in 2015 together with information of the numerical method

used, the fracture network information required and the fluid flow method simulated. Of this list the fracture orientated models, which simulate pore fluid propagation in a network of rock fractures, are the most relevant to this thesis as these require the input of a DFN. From this selection, the HEX-S model by Kohl and Mégel (2007) is of interest for its ability to handle input of a DFN using either stochastic or deterministic fracture maps. This is a finite element model that solely models shear fracture slip. Each defined fracture is partitioned into slip patches, at each time step a shear criterion is evaluated separately on each slip patch. If one of these patches slips, the seismic event position is logged and the simulation continues. This method was found to be successful in simulating the induced seismicity recorded at the Soultz-sous EGS site during the GPK4 injection for the first 10 hours of the injection. During this period, the simulation correctly predicted the spatial location of the seismic events and the evolution of the seismic events in time. The required fracture network parameters for this simulation are, for each individual fracture; the positions, size, orientations and mode of fracturing (Mode I to III). These parameters can be determined either from well logs or, more pertinent to this thesis, from microseismic monitoring, which shows which fractures are active, allowing forecast models to be regularly updated during the injection process.

In-between the physically-based and statistical-based approaches are the hybrid approaches. These were introduced by Bachmann et al (2012) and Goertz-Allman and Wiemer (2013) who combined the advantages of statistical and physical models. The model by Gischig and Wiemer (2013) is a hybrid approach that uses a flow model calibrated against both the pre-stimulation and current stimulation hydraulic data to compute the transient pressure distribution. The pressure model is then used to decide whether events are triggered at so-called seed points. These triggered events positions are placed into a grid. These synthetic events are sorted by magnitude in a histogram and these are used to compute the seismic hazard expressed in terms of an EMS intensity (European Macroseismic Scale, EMS98). Observed microseismicity is used to provide calibration for the flow model and the input parameters for the seed model are manipulated until the synthetic events match the observed events in terms of both position and evolution in time. Figure 2.4 shows the successful forecasting of using this hybrid model at the EGS site in Basel, where after 1000 iterations of the model (grey area on fig 2.4) matches the observations for a 10 day period (shown as the black line on fig 2.4). This approach was extended by Karvounis et al. (2014) as part of the development towards the real-time adaptive traffic light system by Swiss Seismological Service (SED). This hybrid model extends the Gischig and Wiemer (2013) seed volume from 2D to 3D and implements a DFN with discrete fractures for the flow and in particular for EGS operations, heat transport modelling.

In this section, three different forecasting approaches were presented all which utilise

information from microseismic analysis. These included :

- A statistical model by Bachmann et al. (2011) which uses the magnitude of observed seismic events and the injection rate to predict the likelihood of an induced seismic event occurring with a specific magnitude range and of a specific time range.
- A physics-based model by Kohl and Mégel (2007) which in the definition of the input DFN utilises the position, orientation, size and class of mechanical behaviour.
- A hybrid model by Gischig and Wiemer (2013) which uses the position and occurrence time of the seismic event to calibrate the seed volume.

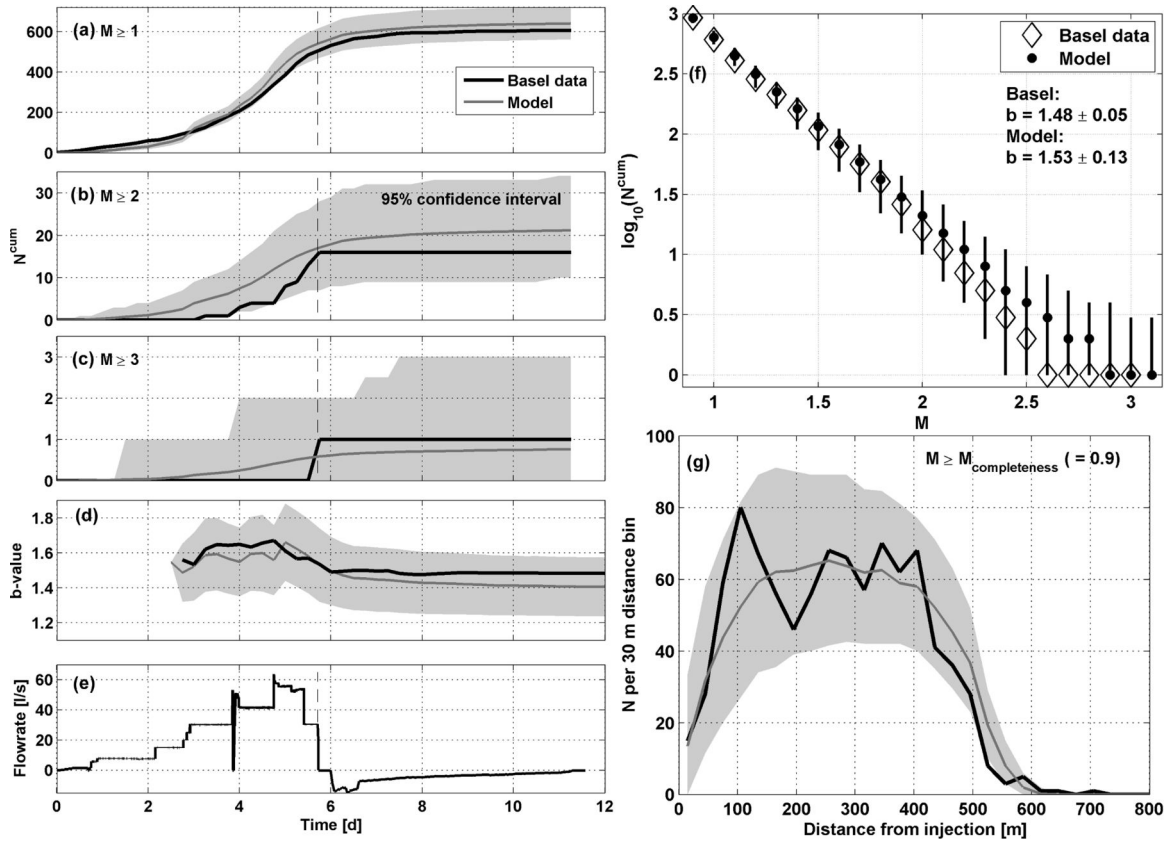


Figure 2.4: Results of the stochastic seed model calibrated against observed seismicity at Basel. (a) Cumulative number of events for $M_w > 1$. The black line represents the observations at Basel. The grey line is the mean of 1000 model realizations, the gray shading is the 95 percent confidence interval (CI) of all model realizations. (b and c) Same as in (a) for $M_w > 2$ and $M_w > 3$. (d) Temporal evolution of the b value derived from 100 events proceeding each time step. The gray shading indicates plus/minus one standard deviation about the mean. (e) Injection rate for comparison. (f) FMD of the 12 d of Basel observations and the model realizations. For the model again the mean as well as the 95 per cent CI (error bars) is shown. (g) Spatial distribution of seismicity represented as 30 m bins of distance from the injection point. Image and caption from Gischig and Wiemer (2013)

2.3.3 Evaluation of forecasting approaches

The primary approach currently used to mitigate induced seismicity from hydraulic fracture operations world-wide is to use reaction control approaches such as a TLS. Recently additional seismologically determined parameters such as the maximum hydraulic fracture extent are used in conjunction to mitigate induced seismicity. The aim of reactive control approaches is to apply mitigatory actions at the correct moment (slowing or ceasing fluid injection) so as to avert increasing seismic magnitudes which would cause a disturbance on the surface. This approach can then be considered as a forecasting tool, as if these limitations are exceeded and mitigatory actions are not implemented, then a seismic event is to forecast to occur in the near future.

The known issues of using reactive control approaches has been discussed in detail in section 2.3.1, and are summarised as :

1. Notable examples when mitigatory actions have taken place, but seismic activity continues to increase
2. Based on a simplified model that if the magnitude of seismic activity is increasing with injection, then reducing the injection rate will reduce the magnitude of seismic activity.
3. No agreement world-wide as to when mitigatory actions should take place.

The above issues have recently lead to a drive to develop systems using prediction models realised in real-time to calculate the probability of felt induced seismicity. While retrospective investigations have been conducted on numerous case studies, such as the Basel EGS experiment, which successfully predicted the seismic activity, there has yet to be a implementation where this is the primary decision making system. These types of system are still in development, with the SED trailing the adaptive traffic light system (ATLS) in the first parallel demonstration (alongside a standard TLS) in Geldinganes, Iceland in October 2019 (Personal communication, 2019). The challenges of using these predictive models currently can then be summarised as :

1. Difficulties in communicating to public as to why changes to the injection schedule are taking place
2. Computational requirements; for physically and hybrid based models these are expensive. Not all sites could handle the data requirements.
3. Difficulties in communicating to drilling teams that injections have to be ceased when no high magnitude seismic event has yet to be detected.

4. Concerns that if the choice of modelling parameters are incorrect then either the injections are unnecessarily stopped, affecting the efficiency of the process, or injections continue and seismic magnitudes increase.

To address the known issues of both of these forecasting approaches, further information is needed regarding the mechanisms that cause induce seismic activity from hydraulic fracturing operations.

2.4 Mechanisms of induced seismicity from hydraulic fracturing

In the first section of the literature review, the approaches to forecast induced seismicity were reviewed. From this review, one of the issues with a TLS, which is the primary means of mitigating induced seismicity currently, is that it is based on a simplified physics model that a continuation of the fluid injection process leads to an increase in the magnitude of seismic activity. Therefore by reducing or ceasing this process, the magnitude of detected seismic events should reduce. Unfortunately at some sites around the world, the opposite has occurred, and seismic activity with increasing magnitudes has occurred after the injection process has stopped. This section of the literature review aims to review the mechanisms responsible for inducing seismic activity from hydraulic fracture operations so as to greater understand the reasons that this occurs.

2.4.1 Fault re-activation by an increase in pore pressure from a direct hydraulic connection

A broad definition that describes the mechanism by which induced seismicity occurs is stated by McGarr et al. (2002), “Triggered or induced seismicity occurs when the mechanical state of the seismogenic crust is sufficiently perturbed to cause a fault to fail.”

Mathematically, it is commonly assumed that earthquake slip obeys the Coulomb failure criterion (Beeler et al., 2000). This criterion states that if,

$$\tau < \tau_0 + \mu(\sigma_n - p), \quad (2.1)$$

then failure does not occur, but if

$$\tau = \tau_0 + \mu(\sigma_n - p), \quad (2.2)$$

then failure occurs. In the above criterion, τ is the shear stress on the plane, μ is the co-efficient of friction, p is the pore pressure, τ_0 is the cohesion and σ_n is the normal stress on the plane.

These components can be combined into a ternary diagram as shown in figure 2.5 with the different types of induced and triggered seismicity as a way of showing the relationships between these factors.

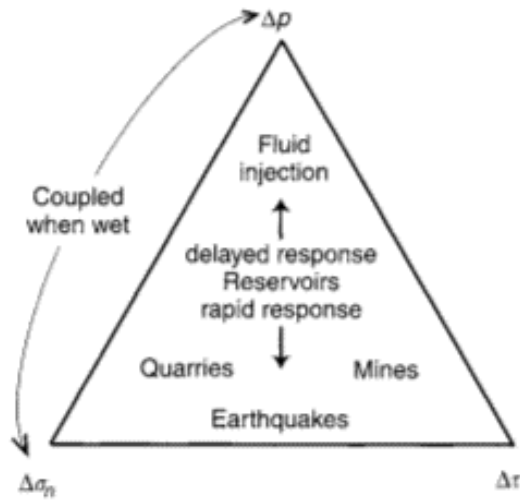


Figure 2.5: A ternary diagram showing the three components which are altered by anthropogenic activities. Surface quarries, deep mines and regional earthquakes cause an increase in seismicity primarily through modifications to the elastic stress field. Liquid injection at depth increases pore pressures. Reservoir loading of the surface can change all three of these components. Oil and gas field compaction primarily results in changes in the state of stress within the seismogenic rock mass surrounding the reservoirs. This figure references delayed responses from the anthropogenic, a point that will be returned to later. Image from McGarr et al. (2002)

In McGarr et al. (2002)'s review paper, case studies of triggered and induced seismicity from many different types of anthropogenic activities were reviewed to see whether common characteristics for each anthropogenic source could be identified. For high-pressure liquid injection, McGarr et al. (2002) summarised that seismicity tends to be triggered along pre-existing faults that are hydraulically connected with injection points. The activity is then concentrated on the portion of the fault with the highest permeability from the point of injection.

McGarr et al. (2002) also state that there is a time dependence in seismic activity. At the start of the injection process, seismicity tends to be concentrated near the injection point and as the injection proceeds the zone of influence increases. As the injection process proceeds, the upper limit of earthquake magnitudes increases and the seismic activity response to injection properties starts to lag. After the injection has ceased, the seismic activity response near the injection point stops immediately but further away from the injection, seismic activity may continue for some time afterwards.

This point is reinforced even when the fluid has been injected directly into a fault line, i.e. no time delay from transport to the fault, the failure at the fault line can lag in time compared to the injection routine, a point observed by Davies et al. (2013) from multiple case studies. This time lag was observed to be several hours between the start of pumping and fault failure at the Preese Hall site in Lancashire, UK and a time lag of 80 mins from a similar injection mechanism in Western Canada (Maxwell et al., 2009). Davies et al. (2013) concludes that this may be in part because the fault line has inherent storage and transmissibility characteristics. Lacazette and Geiser (2013) expands two of these mechanisms further. The first mechanism discussed was that slip occurs from a fluid pressure pulse and this pulse can be transmitted with or without significant fluid flow. The second mechanism is changes in the resolved shear stress on, or the fluid pressure within, a natural fracture due to “inflation”. In this mechanism, “inflation” describes the elastic deformation of the rock volume around the injection well due to the introduction of the frac fluid.

As part of the review of induced seismic activity from hydraulic fracturing, Davies et al. (2013) reviewed 198 case studies of induced seismicity from anthropogenic sources. For hydraulic fracturing operations, Davies et al concluded that four fluid pathways are possible which can increase the pore pressure and lead to fault failure (or fault reactivation). These pathways are :

1. Directly from the wellbore
2. Through new, stimulated hydraulic fractures
3. Through pre-existing fractures and minor faults
4. Through the pore network of permeable beds or along bedding planes.

These pathways are illustrated in figure 2.6.

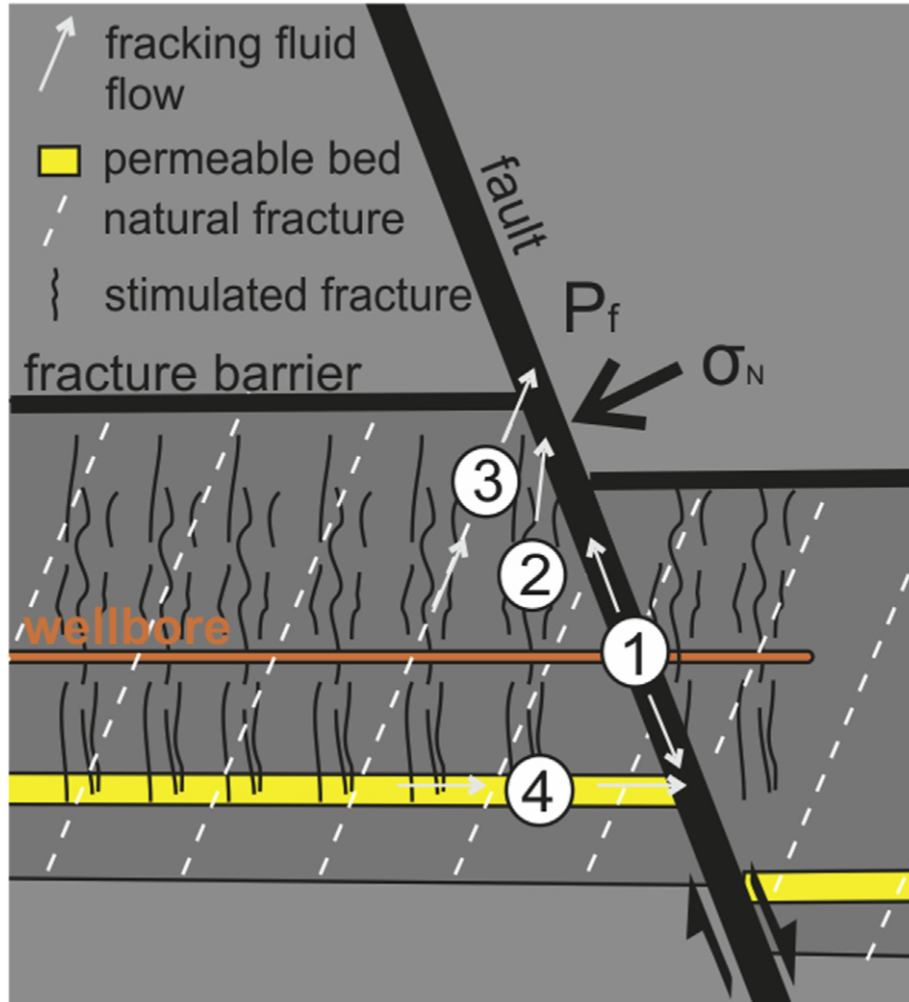


Figure 2.6: Schematic of a low-permeability reservoir with an intersecting fault and potential mechanisms for the transmission of a pore fluid pressure pulse or fluid into a fault to cause reactivation. 1) Direct connection and injection into the fault (e.g., Hulseley et al., 2010); 2) fluid flow through the stimulated hydraulic fractures into the fault (e.g., Wolhart et al., 2005); 3) fluid flow through the existing fractures; 4) fluid flow through permeable strata and along bedding planes. From Davies et al. (2013).

Expanding on this review of potential pathways, Rutqvist et al. (2015) used a 2D numerical simulation model to simulate the injection of fluid into a rock matrix with a pre-existing fault line. These simulations firstly show that the presence of a pre-existing fault line within the rock matrix increases the magnitude of the resulting seismic events. The simulation of hydraulic fracturing could cause fault rupture lengths of about 10 - 20 m which could extend to over 100 m depending on the fault permeability, the in situ stress field, and the fault strength properties. If the fault is initially nearly-impermeable, the simulations showed that only small micro-seismic events occur. Although as the fault was modelled in 2D with homogeneous properties along the length of the fault, there exists potential for parts of the faults to have varying permeabilities over the extent of the fault, leading to potentially larger magnitudes.

With regard to case studies, the operation at Preese Hall in Lancashire, UK is a key study, as it was the first documented example of notable seismicity in Europe (Clarke et al., 2014). This case study was discussed above with regard to the use of TLS. Revisiting this case study with respect to the potential for fault re-activation, two seismic events were detected at magnitudes of 2.3 Mw and 1.5 Mw on the 1 April and 27 May 2011 respectively. While the magnitude of the first event was greater than the second, the second event occurred 10 hours after completion of a hydraulic fracturing stage. The study by Clarke et al. (2014) used the microseismic signals recorded from a small number of seismometers, well logs, a 3D seismic reflection survey, image logs and fluid flow rates to interpret the sequence of events between the 1 April and 27 May. The first conclusion was that there was no indication of any faults along the vertical wellbore as seen in the image logs and from the position of the two events and subsequent aftershocks. The interpretation by Clarke et al. (2014) states that a hydraulic fracture travelled 300 m from the wellbore intersecting a pre-existing strike-slip fault during the second stage of fluid injection causing a 0.5 Mw event. After pausing the injection process, the resumption of injection resulted in a larger area of fault activation and the 2.3 Mw event on the 1 April. The fourth and fifth injection stages, on the 26 May (after a period of site suspension) reactivated the fault as flow along the hydraulic pathway established from the hydraulic fracture on the 1 April resulted in the 1.5 Mw event on the 27 May. Figure 2.7 shows Clarke et al's interpretation annotated on-top of a section from a 3D seismic reflection survey carried out in 2012 highlighting the hydraulic connection established from the fracturing process.

Another similar case study is from the Oklahoma, USA where in January 2011 a sequence of earthquakes occurred cumulating in an Mw 2.9 earthquake in close proximity to a well which was being hydraulically fractured. The study by Holland (2013) reviews the possible mechanisms which caused the sequence of earthquakes to oc-

Preese Hall - 1

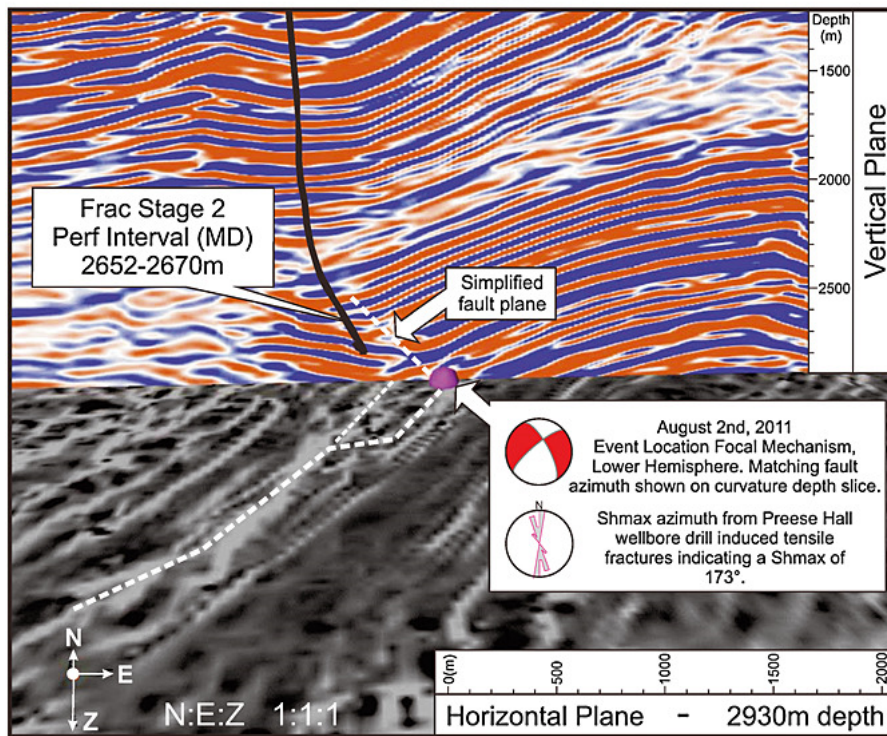


Figure 2.7: A 3-D seismic view in-depth, looking north of the Preese Hall 1 wellbore and an aftershock from the 2 August 2011 with the simplified fault plane (dashed white lines) and wellbore path (black line). From Clarke et al. (2014).

cur. With a distance of 2 km between the wellbore and earthquake locations and a time delay of 24 hours between injection and the recorded earthquakes, Holland (2013) argues that pore-fluid diffusion would not transport enough fluid to cause a pore-pressure change on the fault line. This study concludes that in the time constraints available the fluid would have to travel along a more permeable fracture or fault system, re-activating a fault line and causing the Mw 2.9 event.

2.4.2 Fault re-activation by the transfer of stress from other seismic events

The re-activation of a fault due to the increase in pore pressure (p) along natural and generated hydraulic fractures can be considered as a direct cause of seismicity from the injection of the frac fluid. In contrast, an indirect cause is one where there

is a change in the normal stress across the fault (σ) and/or a change in the shear stress or strength of the fault (τ_n) as shown in equation 2.2. McGarr et al. (2002) discusses that removal of hydrocarbons from reservoirs and subsequent compaction of the reservoir can cause induced seismicity from this process with examples referenced from the Pau basin, France, where production from a 10 km wide reservoir resulted in induced earthquakes with magnitudes ranging up to Mw 4.2. This process is most commonly seen in conventional reservoirs with high porosity and permeability but the mechanics involved, i.e. a change in the normal stress across the fault and shear stress of the fault, can be altered by the movement of other seismic activity in the area. This point is noted by McGarr et al. (2002) which states that a perturbation of the stress even as small as 0.1 bar may be sufficient to trigger seismicity.

This mechanism is analogous to the concept of stress transfer between sets of earthquakes, a concept reviewed by Stein (1999) based on a case study from the San Andreas fault. Stein (1999) showed that the occurrence of earthquakes on the San Andreas fault alters the shear and normal stresses on surrounding faults, varying the seismicity rate (a measure of the number of earthquakes per year). In this key paper, Stein (1999) uses the Coulomb failure criterion as shown as 2.3 and repeated below,

$$\tau = \tau_0 + \mu(\sigma_n - p). \quad (2.3)$$

Stein (1999) uses equation 2.3 and a spatially varying displacement field to model the change in Coulomb stress (σ_f) over the San Andreas fault zone after the Landers earthquake with the aim of seeing if the change in shear and normal stresses correspond to a spatial variation in the seismicity rate. The maps produced by Stein (1999) showed that the Landers earthquake, at a magnitude of Mw 7.3, produced a 2-bar lobe of Coulomb stress increase 40 km west of the epicentre of the Landers earthquake. This increase in Coulomb stress corresponded to the location of another high magnitude earthquake, the Big Bear earthquake at a magnitude of Mw 6.5, which occurred within 2.5 hours of the Landers earthquake. The map produced by Stein (1999), shown as figure 2.8, shows that stress can transfer from one fault zone to another, potentially causing failure.

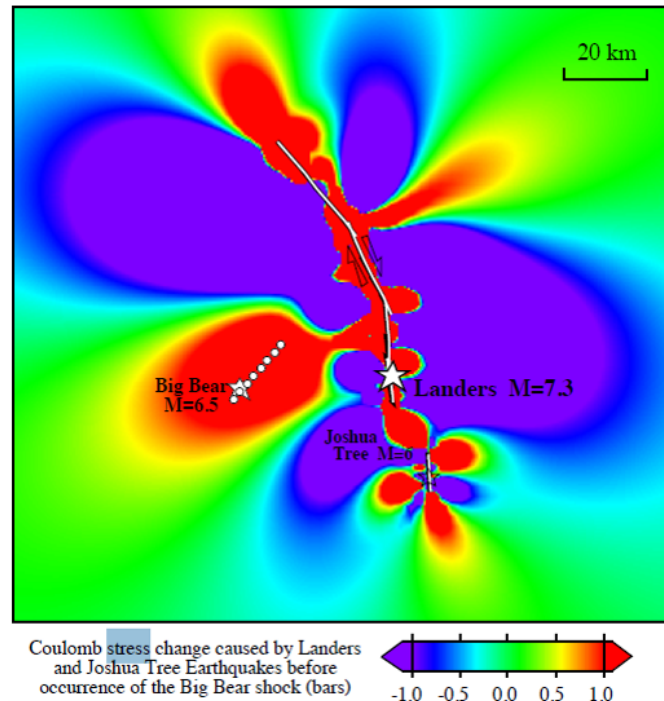


Figure 2.8: A map of the spatially varying Coulomb stress change along the San Andreas fault line. The Coulomb stress change map is modelled by firstly modelling, spatially, the displacement caused by the Landers and Joshua Tree earthquakes. The 1 bar lobe increase of Coulomb stress change is coincident of the location of the Big Bear earthquake which occurs 2.5 hours after the Landers earthquake. This shows that the slip at the Landers earthquake changes the shear and normal stresses around the area triggering the Big Bear earthquake.

While the evidence of this mechanism is from a set of earthquakes with magnitudes much greater than any observed at hydraulic fracture operations, a number of key case studies have shown that this mechanism occurs following hydraulic stimulation. The first case study is from mining-induced seismicity in a mine in the Legnica-Glogow Copper District, Poland by Orlecka-Sikora (2010). In this study, 153 recorded seismic events in the range of M_w 2.0 to 4.5 were analysed to produce the displacement model. This model was then used to retrospectively produce Coulomb stress change maps updated after each event occurs and the relationship between seismic event and increase in Coulomb stress change was compared statistically. This study indicated that new seismic events were preferentially located in areas of positive stress change exceeding 0.05 bar.

Reviewing operations that involve injection of fluid, studies by Schoenball et al.

(2012) and Catalli et al. (2013) both model the Coulomb stress change from enhanced geothermal systems from Soultz-sous Forets, France and Basel, Switzerland respectively. While the study from Schoenball et al. (2012) was not the first study to investigate the Coulomb stress change at Soultz-sous Forets, it is one of the most thorough. This study uses the focal mechanisms and positions from 715 events recorded at the site to calculate the temporal evolution of the change in Coulomb stress in 3D using an efficient computational method based on the method by Okada (1992). The Okada (1992) method models, spatially, the displacement from a set of seismic events. Using Hookes Law, these spatially varying displacements are used to calculate Coulomb stress change. This study found that the Coulomb stress change varied in the order of 10 bar and may play a minor role for injection-induced seismicity as a trigger for events after shut-in. The study by Catalli et al. (2013) advanced this investigation with the EGS experiment from Basel, Switzerland. Similar to Schoenball et al. (2012), pore pressure changes were not considered as part of the modelling so as to investigate whether elastic strains alone play a role in the triggering process. This study used 118 events with magnitudes ranging from Mw 0.7 - 3.4 with well-constrained focal mechanisms. With these events, two possible failure planes were considered for the Coulomb stress change. This study found a significant correlation between event locations and positive Coulomb stress change, implying that static stress changes from previous small-induced earthquakes are actively involved in the triggering process (Catalli et al., 2013).

2.4.3 Theoretical microseismic model to connect induced seismicity to the mechanisms

The previous sections detailed two mechanisms by which induced seismicity can occur. The first is an increase in the pore pressure by the direct hydraulic connection between the wellbore and an existing fault line, reactivating the fault. The second mechanism is the transfer of static shear and normal stresses from other seismic events. This review has shown that of the two causes, the change in pore pressure is the primary cause for failure, but as shown from the case studies from the Basel EGS experiment that if static stress changes are considered in isolation, there is evidence that this would be sufficient to trigger failure along a fault plane.

Considering the use of microseismic monitoring, if the above mechanisms can be monitored in real-time then there should be a observable change in the evolution of the fracture network that leads to a seismic event occurring. These observations can be made in real-time using arrays of geophones to record the microseismic activity over the site. By recording the microseismic signals emitted by the evolution of the fracture network, these signals can be analysed for a observable change in the fracture network. These observations can then be compared to a theoretical microseismic model to link between the real-time monitored output and the forecast of induced seismic activity. This model is based on the above literature review and is presented as a schematic in map view as figure 2.9.

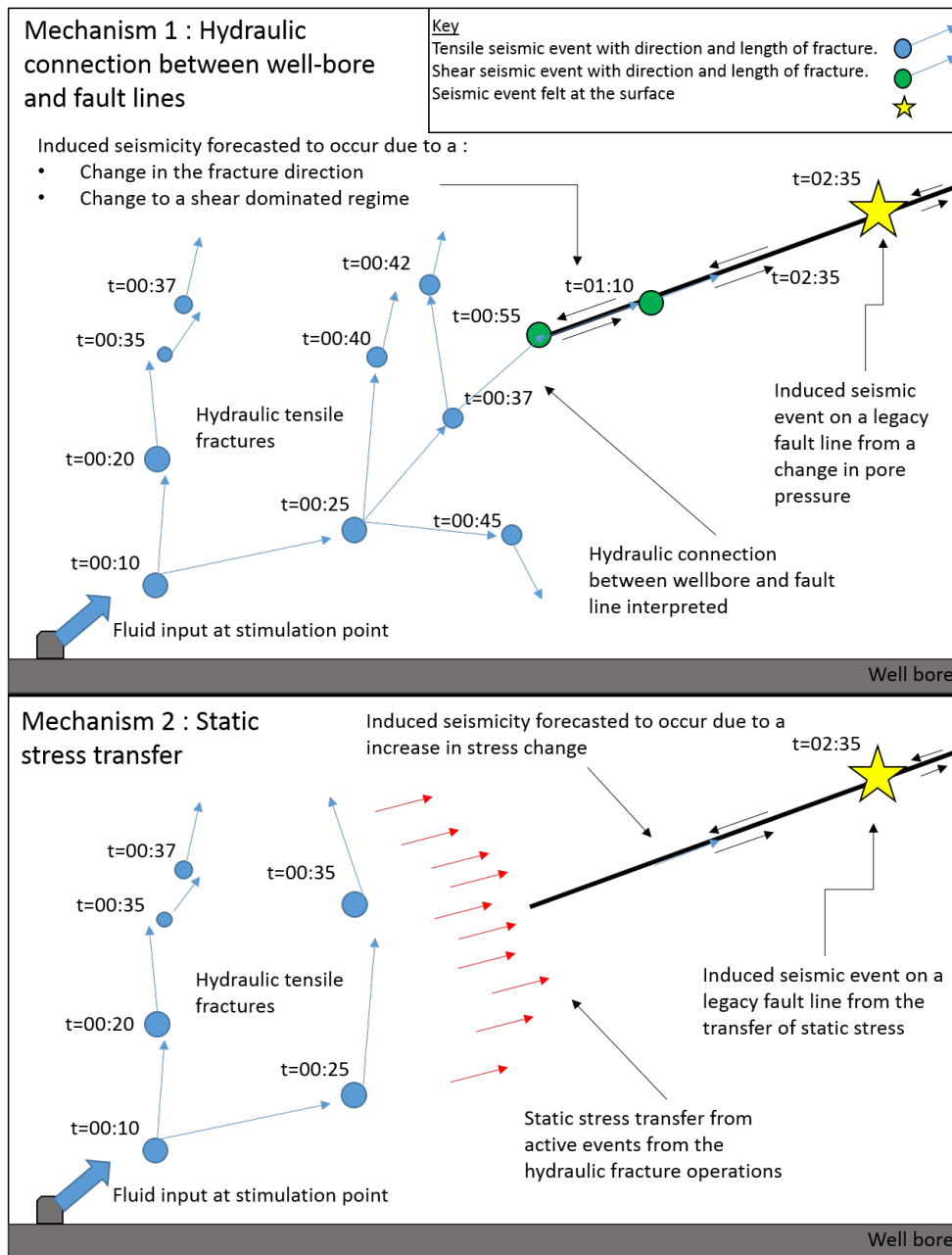


Figure 2.9: A schematic map of a theoretical forecasting model based on the data provided by microseismic events. The top window shows the first mechanism, hydraulic connections between the well-bore and fault lines. In this mechanism, tensile events extend from the wellbore and connect to a fault line. This increases the pore-pressure along a legacy fault line causing a slip. The bottom window shows the second mechanism, static stress transfer between seismic events. In this mechanism, the seismic events transfer stress towards the legacy fault line which triggers the slip.

In this model as fluid is pumped into the formation, tensile fractures open and extend away from the wellbore. With the first mechanism (top image in 2.9), there should exist a point in time when the frac fluid enters the legacy fault line. This transfer will be observed in a fracture map from two parameters, a change in the fracture direction and a change from tensile opening to shear forces. If this change is observed from the microseismic data then a future seismic event can be forecast to occur. With regard to the second mechanism, as hydraulic fractures open from fluid input this changes the normal and shear stresses in the area. If the normal and shear stresses are modelled over the site during production, there should be an observable point when these forces exceed the strain capacity of fault lines in the area triggering a seismic event. If this transfer of stress can be modelled as it develops over time then there may be a point in time when it reaches a set limit, and a future seismic event is forecast to occur.

2.5 Discussion and detailing a new approach to forecasting

In the first part of this chapter, the current regulatory frameworks to mitigate induced seismicity were reviewed and two separate forecasting approaches were identified and critically evaluated. This evaluation highlighted that currently there is only one approach available to mitigate induced seismicity and these are the reactive control approaches, which includes the TLS framework. Real-time forecast models which can predict the seismic activity from fluid injection, and would rectify the shortcomings identified from reactive control approaches, are still in trial development and are not yet ready for deployment as the primary decision making systems.

Given the current issues surrounding reactive control approaches, and the recent governmental requirements (Department for Business, 2019a) to research methods to forecast induced seismicity there is scope for a new approach to forecasting that address the issues outlined in section 2.3.3. This approach requires a system that is able to incorporate :

- Updated in real-time, so changes in the injection process can be implemented
- Rapidly implemented in the field, with reduced computational requirements compared to the GNM models used in the prediction models.
- A compliment to the existing TLS frame-work

- Easily able to communicate the reasoning behind a change in the injection schedule
- Able to incorporate the mechanisms of induced seismicity for decisions

To these ends, the theoretical microseismic model presented in section 2.4.3 from a review of the mechanisms of induced seismicity can be considered as the central model of a new forecasting approach. This approach builds upon the principles of reactive control approaches and links seismologically determined parameters to a increased risk of seismic activity occurring. Where this method differs to current approaches, is rather than using a single parameter such as seismic magnitude to make decisions, this judgement will be based on comparing the observed fracture network from the microseismicity records to the theoretical model. This directly links the current state of the fracture network to the mechanisms of induced seismicity.

Such an approach would not require computational expensive GNM models, as it is a inversion of microseismic records to the parameters of each individual fracture detected. This removes the reliance on modelling parameters, which is known to affect statistical based prediction models, and simplifies the process towards a forecast based purely on data. As the aim of this approach is to compare the outputs from real-time microseismic monitoring to a theoretical model, it is then easier to communicate the reasoning for changes in the injection schedule.

To develop a software system that follows this approach entails that both of the potential causes of induced seismicity are required to be monitored in real-time from microseismic records. To guide the development of such a system in the following chapters, the programming requirements for the software system are that it is:

- Capable of monitoring for hydraulic connections from the well bore activating fault lines
- Capable of monitoring for static stress transfers triggering seismic events
- Capable of running in real-time

The software system to be developed will be based on monitoring the microseismic events using a range of geophysical methods. The methods chosen will complement each other in order to fulfil the programming requirements and are reviewed in the next chapter.

Chapter 3

System design: review of available methods to analyse microseismic signals

3.1 Introduction

This chapter aims to review the methods available in the literature to analyse passive microseismic events for the purposes of identifying changes to the fracture network. This chapter and the software system to be developed will solely focus on signal processing methods to determine changes to the fracture network as the analysis needs to be conducted in real-time once an event is detected.

The parameters required from the analysis of the seismic events to allow a software system to monitor an evolving fracture network and make a forecast for induced seismicity are:

- The seismic event magnitude and moment
- The source focal mechanism
- The seismic event geometry
- The radiated energy emitted from seismic events
- The stress transfers between seismic events

This chapter will discuss the methods available to determine these parameters. The basic principles of each topic are reviewed together with the methods used by industry

and within academia. The final section of this chapter will detail which of these methods can be used to build into a real-time system capable of monitoring and forecasting induced seismicity and give the reasoning behind the decisions made.

3.2 Methods to calculate a seismic event's magnitude and moment

3.2.1 Introduction

Analysing the magnitude of seismic events on the surface has historically been the primary area of earthquake investigations followed by event location since the intervention of modern seismographs. The two measures of seismic magnitude most commonly used are the moment magnitude, M_w a log scaler measure of the seismic event size and the seismic moment M_0 , measured in dyn-cm. The moment magnitude is a highly important measure for monitoring hydraulic fracture operations as it is used as a constraint for continued operations at a site. In the context of forecasting induced seismicity, the magnitude of seismic events can be used as a parameter to determine if the source of the event is from a reactivated fault line or a newly opened tensile fracture, as the magnitudes for these two different types of event would differ.

3.2.2 Relationship between source size and seismic event spectra and a review of the limitations of the method

The method used to determine the seismic moment from seismic records does not vastly vary between researchers and within the industry. These all use a rupture model, usually the Brune (1970) or Boatwright (1980) models to relate the seismic spectra to the seismic moment. This relationship is detailed in a review by Eaton et al. (2014) using microseismic examples from a hydraulic fracturing project in Western Canada and is summarised below.

The relationship between the spectra from a shear slip on a circular crack and the seismic moment can be defined by the model by Brune (1970). The model relates the seismic moment M_0 to the low-frequency plateau spectral amplitude, A_0 , a value observed from the frequency domain representation of the seismic event. This is shown in figure 3.1.

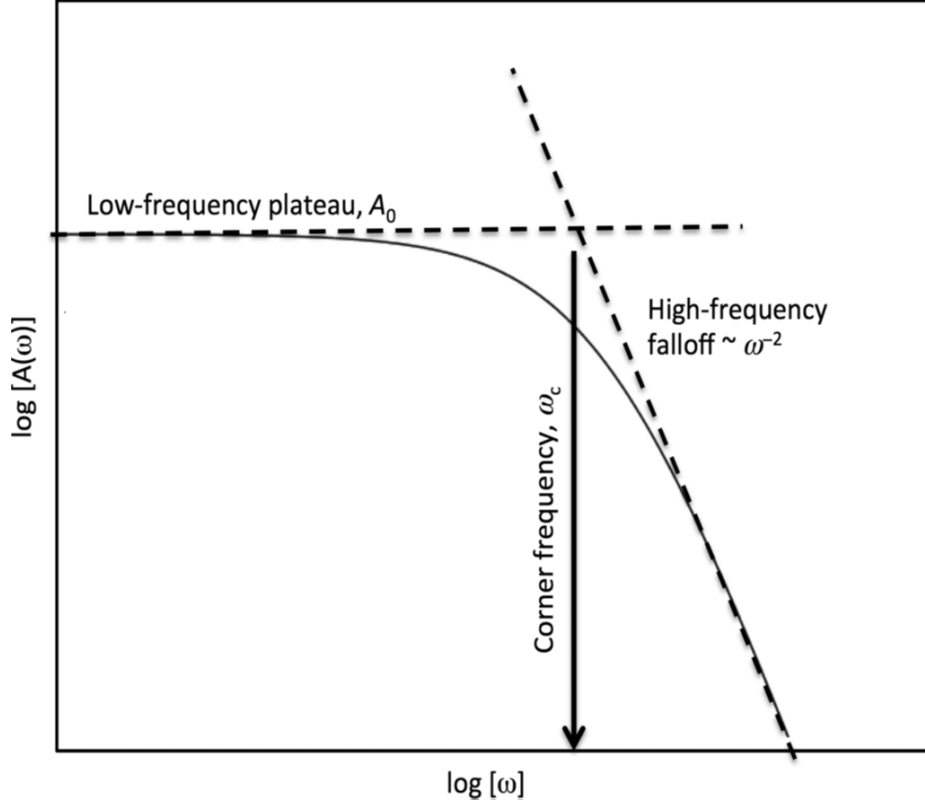


Figure 3.1: Calculation of A_0 from the spectral properties. Taken from Eaton et al. (2014)

The seismic moment M_0 relates to the low-frequency plateau A_0 via

$$M_0 = \frac{4\pi\rho c_v^3 |A_0^v| r}{R_v}, \quad (3.1)$$

where R_v is the spherically averaged source radiation pattern, r is the source-receiver distance, ρ is the density, c_v is the applicable wave speed and A_0 is the low-frequency plateau amplitude where v is the P or S wave type.

To observe the low-frequency plateau amplitude, the Brune (1970) model describes the relationship between the angular frequency (ω) and spectral amplitude as,

$$|\Omega^v(\omega, r)| = \frac{A_0^v(r) \exp(-\alpha_v r)}{1 + (\omega/\omega_c^v)^2}, \quad (3.2)$$

where α is an attenuation coefficient as given by Tonn (1991) and ω is the angular

frequency. The attenuation coefficient is given by,

$$\alpha_v(\omega) = \frac{\omega}{2c_v Q_v} \quad (3.3)$$

where c_v is the velocity of the medium, Q is the seismic quality factor, v denotes the P- or S- waves and ω is the angular frequency. A variation of the Brune (1970) model for describing the spectral relationship is given by Boatwright (1980) which states,

$$|\mathbf{\Omega}^v(\omega, r)| = \frac{A_0^v(r) \exp(-\alpha_v r)}{[1 + (\omega/\omega_c)^4]^{1/2}}. \quad (3.4)$$

With the seismic moment determined, the moment magnitude is calculated by

$$M_w = \frac{\log M_0}{1.5} - 10.73. \quad (3.5)$$

Other than using different variations on the rupture model the main service providers all use a similar approach. For example, both Schlumberger and ESG (Engineering Seismology Group) use a Brune rupture model (Maxwell et al. (2012), Schlumberger and Bosman et al. (2016), ESG).

This method has been reviewed by Stork et al. (2014) who investigated the factors which affect the robustness of measuring seismic moment. This study found that the radiation pattern used (R, in equation 3.1) can have the most significant effect on magnitude estimates. This study made a set of recommendations to follow when conducting this method. These include using at least 4 receivers to make the estimate, to use good SNR recordings of $\text{SNR} > 3$, to remove the noise spectrum from the signal spectrum before calculating the seismic moment and to use actual focal mechanisms to compute the radiation pattern correction rather than assumed focal mechanisms.

While the outputs of this process (M_0 and M_w) are key measures in the communication of the magnitude of a seismic event, these relations can be used further to derive measures of the source size and the rupture conditions. For example, the seismic moment M_0 is related to the average displacement, D , the rigidity at the source locations, μ and the rupture area S by

$$M_0 = \mu DS. \quad (3.6)$$

Moreover for tensile fractures, Eaton et al. (2014) derive a relationship between the low-frequency spectral amplitude, and the internal pressure of the fracture, P_i for P-waves and for S-waves as,

$$A_0^p = \sqrt{\frac{47}{15} \frac{P_i a^3}{2\pi\rho V_p^3 r}}, \quad (3.7)$$

$$A_0^s = \sqrt{\frac{8}{15} \frac{P_i a^3}{2\pi\rho V_s^3 r}}. \quad (3.8)$$

Where P_i is the internal pressure in Pa, ρ is the density, V_c is the applicable velocity at the source, a is the fracture radius and r is the source - receiver distance. All of these values can be used to build up a greater understanding of the conditions and extent of fault movement.

3.3 Evaluation of a seismic events focal mechanism

3.3.1 Introduction

When a seismic event occurs, the forces applied to the rock determine the type of slip, this is the focal mechanism and describe the kinematics and forces involved in an event slip.

The relationship between rock failure and the received seismic waves is underpinned by the following fundamental equation,

$$u(t) = x(t) * e(t) * q(t) * i(t), \quad (3.9)$$

where $u(t)$ is the ground displacement, $x(t)$ is the source-time function or earthquake source parameters, $e(t)$ and $q(t)$ represent the elastic and anelastic effects of the earth structure and $i(t)$ represents the instrument response of the seismometer, note that * used here describes a convolution process.

The source time function $x(t)$ contains all the information about how the rock ruptures and the other terms in the equation ($e(t), q(t)$ and $i(t)$) alter the signal between source and receiver. The source time function describes the full complex rupturing process and the only way to extract fracture properties from this function is to use an approximation. A convenient approximation for the source time function is the seismic moment tensor. This describes the focal mechanism of the source. A seismic moment tensor is represented by a 3x3 matrix, normalised to unit amplitude (Eaton and Frouhdeh, 2011). The tensor is independent of the choice of the coordinate system and describes the forces involved in the rock rupture and links it to the received seismogram as part of the source-time function $x(t)$ via the seismic moment function $\mathbf{M}(t)$. Decomposition of the moment tensor allows the focal mechanism to be determined for an individual seismic event and therefore allows the forces involved in the fracture network to be investigated.

3.3.2 P- and S-wave displacement and the moment tensor

The theoretical fundamentals of inverting for the moment tensor and then the subsequent decomposition into the events focal mechanism are described by Aki and Richards (2002) and have been summarised by numerous authors including Jost and

Herrmann (1989) and Forouhideh and Eaton (2009). This theoretical framework is summarised below.

As stated by Aki and Richards (2002), and summarised by Forouhideh and Eaton (2009) the far-field displacement for the P- and S-wave travelling in a homogeneous elastic space can be described in the spherical coordinate system as,

$$\mathbf{U}_{k(P|S)}(r, \theta, \alpha, t) = \left[\frac{1}{4\pi\rho c^3}\right] \left[\frac{\gamma_k}{r}\right] \mathbf{R}_{(P|S)}(\theta, \alpha, i, j) \mathbf{M}_{ij}(t), \quad (3.10)$$

where \mathbf{U}_k is the k th component of ground displacement for either P- or S- waves, r is the source-receiver distance, θ and ϕ are the spherical coordinate angles related to the source-receiver take-off and azimuth angles, t is the time in the seismogram after a waves first arrival time, ρ is density, c is either the P- or S-wave velocity, γ_i is the direction cosine between the direction of the maximum wave amplitude and the particular displacement component, \mathbf{R} is the radiation pattern factor for P- and S- waves for each moment tensor component (i or j), and M_{ij} is the moment tensor rate function (MTRF). If this is integrated over the source duration, τ , the following equation is obtained,

$$\mathbf{d}_{k(P|S)}(\theta, \alpha) = \int \int \int \mathbf{U}_{k(P|S)}(r, \theta, \alpha, t) = \left[\frac{1}{4\pi\rho c^3}\right] \left[\frac{\gamma_k}{r}\right] \mathbf{R}_{(P|S)}(\theta, \alpha, i, j) \mathbf{M}_{ij}(t). \quad (3.11)$$

The observed data $\mathbf{d}_{k(P|S)}(\theta, \phi)$ then has a linear connection to the source description, provided by components of the moment tensor, \mathbf{M}_{ij} . Forouhideh and Eaton (2009) then show that by using representation theorem for seismic sources from Aki and Richards (2002), equation 3.12 will take the form of

$$\mathbf{d}_n(x, t) = \int_{-\infty}^{\infty} \int_V \mathbf{G}_{nk}(x, t; r, \bar{t}) \mathbf{f}_k(r, \bar{t}) d\mathbf{V}(r) d\bar{t}, \quad (3.12)$$

where $\mathbf{d}_{n(x,t)}$ is the observed displacement at an arbitrary position x at the time t due to a distribution of equivalent body force densities f_k , \mathbf{G}_{nk} are the components of the Green's functions containing the propagation effects and V is the source volume where \mathbf{f}_k are non-zeros (Jost and Herrmann, 1989). Forouhideh and Eaton (2009) and state that the Green's functions can be expanded into a Taylor series assuming that they vary smoothly within the source volume in a range of moderate frequencies. The Taylor series expansion of the components of the Green's functions around the centroid $r=\gamma$ is,

$$\mathbf{G}_{nk}(x, t; r, \bar{t}) = \sum_{m=0}^{\infty} \frac{1}{m!} (r_{j1} - \epsilon_{j1}) \dots (r_{jm} - \epsilon_{jm}) \mathbf{G}_{nk,j1\dots jm}(x, t; \epsilon, \bar{t}). \quad (3.13)$$

If the higher order terms are neglected, then the equation simplifies to,

$$\mathbf{d}_n(x, t) = \mathbf{M}_{kj}[\mathbf{G}_{nk,j} * \mathbf{s}(t)], \quad (3.14)$$

where \mathbf{M}_{kj} is the moment tensor and $\mathbf{s}(t)$ is the source time function. Given the displacement $\mathbf{d}(x, t)$ vector is known and \mathbf{M}_{kj} is unknown then the manipulation and choice of the two remaining parameters, $\mathbf{G}_{nk,j}$ the Green's Functions and $\mathbf{s}(t)$ the source time function, dictate the extent to which the moment tensor and focal mechanism is solved for.

3.3.3 Methods to perform moment tensor inversion

There are a range of methods to determine the moment tensor and accordingly the focal mechanism. These methods all have assumptions associated with them and these have a bearing on the validity of the final output results. These methods can be broadly split by whether the input data used in the inversion is a single time sample or a continuous time series.

Single time point methods

The single-time points methods are the simplest methods to implement but also have the greatest assumptions and constraints. These methods are routinely used in the microseismic industry and have been historically applied for global seismology purposes as well.

The simplest means to determine the moment tensor using a single time point is to use the first-arrival polarity method. This doesn't determine the moment tensor directly, it determines the focal mechanism of the event with a number of assumptions. This method takes the polarity of the arrivals at receivers surrounding the events and constructs the first motion pattern. The first motion pattern is then matched to a focal pattern defined by the dip, strike, and rake angles. Since the moment tensor is not determined directly, it is assumed that the slip failure is double-couple only. This method is the simplest and quickest method to implement. Unfortunately with a small number of receivers there are a large number of possible focal mechanisms that are all valid. This method is utilised often in seismology and in the microseismic industry with an example from Rutledge and Phillips (2003) using the academic Cotton Valley dataset.

As the previous method can only interpret double-couples, a way to advance the method is by looking at the amplitudes of these points rather than just the polarity.

Eaton et al. (2014) demonstrate that the S/P amplitude ratio from an event indicates whether the event is shear or tensile failure. Similar to the polarity method this doesn't determine the moment tensor directly but allows a moment tensor to be constructed based on the focal mechanism and the balance between tensile and shear forces.

The previous two methods attempt to find the focal mechanism that provides the best-fit to the observed first motion pattern. The method by Stump and Johnson (1977) is a moment tensor inversion method solving for the moment tensor directly. This method assumes that the source time function is considered as a unit impulse function. This allows the moment tensor to be solved for using the generalised inverse and equation 3.14. By setting the source time function to a delta function reduces equation 3.14 to,

$$\mathbf{d}_n(x, t) = \mathbf{M}_{kj}[\mathbf{G}_{nk,j}], \quad (3.15)$$

where the Green functions describe the nine generalized force couples. This can be written in matrix form as,

$$\mathbf{d} = \mathbf{A}\mathbf{m} \quad (3.16)$$

where $\mathbf{d} = (a_{1p}, a_{2p}, a_{3p}, a_{1s}, a_{2s}, a_{3s})^T$ defines the observed amplitudes of the P- and S-wave direct arrivals and $\mathbf{m} = (M_{11}, M_{22}, M_{33}, M_{12}, M_{13}, M_{23})^T$ defines the independent components of the seismic moment tensor. For a single receiver, the matrix \mathbf{A} can be easily surmised from the equation 3.14 and 3.16, for additional receivers n the system can be formed by appending additional rows as required and then solving the over-determined system using the generalised inverse,

$$\mathbf{m} = \mathbf{A}^{-1}\mathbf{d} = (\mathbf{A}^T \mathbf{A})^{-1} \mathbf{A}^t \mathbf{d}. \quad (3.17)$$

This method has been implemented by numerous authors in microseismic monitoring operations with examples including Nolen-Hoeksema and Ruff (2001) from a hydro-fracturing operation in Colorado to Jechumtálová and Eisner (2008) who constrain the possible solutions for the moment tensor when only a single vertical monitoring well is available.

This method was reviewed by Eaton and Ferozideh (2011). They show caution should be exercised when using this method without a constraint as it tends to show bias towards double-couple mechanisms only. This commonly occurs when the signal to noise ratio of the microseismic records are low precluding the identification of the amplitude of certain required components. Moreover, this method was reviewed by Vavryčuk (2007) who stated that for a single monitoring well, the dipole perpendicular to the plane of both the geophones and the hypocenter cannot be resolved, as the inversion is under-determined in this axis.

Time-varying source time functions

If the moment tensor is to be resolved from a continuous time series, then the source time function $\mathbf{s}(t)$ and Green's functions \mathbf{G}_{njk} require further modelling. The source time function describes the slip routine at the event. The Green's function, in general, describe the impulse response of the Earth at a station for a force excitation and includes all wave propagation effects between source and receiver. Methods to model the Green's functions include the discrete-wavenumber method (Bouchon and Aki, 1977) and finite difference algorithms (Okamoto, 2002).

The discrete-wavenumber method introduced by Bouchon and Aki (1977) uses the reflectivity method to model the Green's Function for a known 1D layered velocity model. This method was built into the AXITRA code by Coutant (1990). Numerous authors have used the discrete-wavenumber method since it was first published for a wide variety of purposes, from seismic exploration (Dietrich and Bouchon, 1985), earthquake seismology projects (Campillo et al., 1984) and microseismicity studies with Bernard and Zollo (1989). Further information can be found in the review paper by Bouchon (2003). Modelling the source time function with the discrete-wavenumber method is conducted by assuming a time-varying function that is convolved with the Green's Functions. In Song and Toksöz (2011) a ramp function is used, but any wavelet that matches the input data can be used.

With the Green's functions and source time function modelled, an inversion strategy outlined by Křížová et al. (2013) follows. For far-field distances, equation 3.14 can be re-written as,

$$\mathbf{U}_i(t) = \sum \sum \mathbf{M}_{pq} * \mathbf{G}_{ip,q}, \quad (3.18)$$

The moment tensor can be expressed in the form of a linear combination of six elementary tensors \mathbf{M}_{pq}^i ,

$$\mathbf{M}_{pq} = \sum \mathbf{a}_i \mathbf{M}_{pq}^i. \quad (3.19)$$

This represents a convenient parametrization because in this way as the source is characterized by six scalar coefficients a_i . These elemental tensors are described as shown in figure 3.2,

$$\begin{aligned}
\mathbf{M}^1 &= \begin{pmatrix} 0 & 1 & 0 \\ 1 & 0 & 0 \\ 0 & 0 & 0 \end{pmatrix} & \mathbf{M}^2 &= \begin{pmatrix} 0 & 0 & 1 \\ 0 & 0 & 0 \\ 1 & 0 & 0 \end{pmatrix} \\
\mathbf{M}^3 &= \begin{pmatrix} 0 & 0 & 0 \\ 0 & 0 & -1 \\ 0 & -1 & 0 \end{pmatrix} & \mathbf{M}^4 &= \begin{pmatrix} -1 & 0 & 0 \\ 0 & 0 & 0 \\ 0 & 0 & 1 \end{pmatrix} \\
\mathbf{M}^5 &= \begin{pmatrix} 0 & 0 & 0 \\ 0 & -1 & 0 \\ 0 & 0 & 1 \end{pmatrix} & \mathbf{M}^6 &= \begin{pmatrix} 1 & 0 & 0 \\ 0 & 1 & 0 \\ 0 & 0 & 1 \end{pmatrix}.
\end{aligned}$$

Figure 3.2: The elemental tensors used by Křížová et al. (2013). The \mathbf{M}^1 to \mathbf{M}^5 tensors represent five DC focal mechanisms while \mathbf{M}^6 is a purely isotropic source

When equation 3.18 and 3.19 are combined together,

$$\mathbf{u}_i(t) = \sum \mathbf{a}_j \left(\sum \sum \mathbf{M}_{pq}^j * \mathbf{G}_{ip,q} \right) = \sum \mathbf{a}_j \mathbf{E}_i^j(t), \quad (3.20)$$

where \mathbf{E}_j denotes the j th elementary seismogram corresponding to the i th elementary moment tensor. This is represented in matrix notation as

$$\mathbf{u} = \mathbf{Ea}. \quad (3.21)$$

This is an overdetermined linear inverse problem and is solved via the generalised inverse by the least-squares method. This paper concludes with an example from two Mw 4.9 earthquakes in Greece. With regard to microseismic examples, a variation of this method has been applied by Song and Toksöz (2011) who invert for the source parameters for both the near and far-field distances from a single observation well.

The inversion method as implemented by Okamoto (2002) combines 3D finite-difference modelling for the Green Functions and an inversion strategy that solves for both the moment tensor and the source position. The challenge with generating Green Functions with a finite-difference method is the large computational expense. This is compounded by solving for the position as well as the minimum of five Green's Functions that are required at each source position. Okamoto (2002) handles this by using only 2.5D dimensions in the finite-difference operation and a 'reciprocal' method that can generate the required Green's Functions for only three finite difference calculations per single station.

The disadvantages of these methods over the single time point methods are that the velocity model has to be accurate, as each Green Function defined is, at its simplest, a fully synthetic copy of the field data with a known source mechanism. Moreover, signal to noise issues will also hinder the inversions using this method.

Methods currently of use in industry

The current methods utilised by the microseismic industry are outlined on a company by company basis below for three service providers:

- Microseismic Inc. Microseismic inc utilises single amplitude points from the P-wave arrival to solve for the full moment tensor (Stanek and Eisner, 2013).
- Schlumberger. Schlumberger utilises a single amplitude point method in the frequency domain to solve for the full moment tensor. The velocity model for this can be a layered homogeneous model or a layered VTI model (Leaney and Chapman, 2010).
- Magnitude, a Baker Hughes company. Magnitude uses a single amplitude point method matched to a focal mechanism (Zhang et al., 2014)

3.3.4 Decomposition of Moment Tensor

With the moment tensor solved for, there are a number of different ways that the moment tensor can be used to determine the focal mechanism and accordingly the mechanisms that caused the seismic event.

The first step to determining the focal mechanism is to discern the type of source for the seismic event. This is then used to guide the model choice to calculate the relevant focal mechanism. Knopoff and Randall (1970) proposed decomposing the moment tensors into three elementary parts: the isotropic (ISO), double-couple (DC) and compensated linear vector dipole (CLVD) components. These components describe the source type. For example, the double-couple (DC) component describes the forces involved in a shear fault, as present in the vast majority of seismic events. The second component is the isotropic source (ISO) which describes the forces involved with a volume change, associated with explosive and implosive ruptures, such as nuclear bomb testing. The final component used by Knopoff and Randall is the CLVD component which describes a set of three dipoles that are compensated with one dipole -2 times the magnitude of the others (Steith, 2003). These components

together with their associated focal mechanism display patterns or 'basketball' plots are shown as figure 3.3.

Moment tensor	Beachball	Moment tensor	Beachball
ISO $\frac{1}{\sqrt{3}} \begin{pmatrix} 1 & 0 & 0 \\ 0 & 1 & 0 \\ 0 & 0 & 1 \end{pmatrix}$		$-\frac{1}{\sqrt{3}} \begin{pmatrix} 1 & 0 & 0 \\ 0 & 1 & 0 \\ 0 & 0 & 1 \end{pmatrix}$	
DC $-\frac{1}{\sqrt{2}} \begin{pmatrix} 0 & 1 & 0 \\ 1 & 0 & 0 \\ 0 & 0 & 0 \end{pmatrix}$		$\frac{1}{\sqrt{2}} \begin{pmatrix} 1 & 0 & 0 \\ 0 & -1 & 0 \\ 0 & 0 & 0 \end{pmatrix}$	
$\frac{1}{\sqrt{2}} \begin{pmatrix} 0 & 0 & -1 \\ 0 & 0 & 0 \\ -1 & 0 & 0 \end{pmatrix}$		$\frac{1}{\sqrt{2}} \begin{pmatrix} 0 & 0 & 0 \\ 0 & 0 & -1 \\ 0 & -1 & 0 \end{pmatrix}$	
$\frac{1}{\sqrt{2}} \begin{pmatrix} -1 & 0 & 0 \\ 0 & 0 & 0 \\ 0 & 0 & 1 \end{pmatrix}$		$\frac{1}{\sqrt{2}} \begin{pmatrix} 0 & 0 & 0 \\ 0 & -1 & 0 \\ 0 & 0 & 1 \end{pmatrix}$	
CLVD $\frac{1}{\sqrt{6}} \begin{pmatrix} 1 & 0 & 0 \\ 0 & -2 & 0 \\ 0 & 0 & 1 \end{pmatrix}$		$\frac{1}{\sqrt{6}} \begin{pmatrix} -2 & 0 & 0 \\ 0 & 1 & 0 \\ 0 & 0 & 1 \end{pmatrix}$	
$\frac{1}{\sqrt{6}} \begin{pmatrix} 1 & 0 & 0 \\ 0 & 1 & 0 \\ 0 & 0 & -2 \end{pmatrix}$		$-\frac{1}{\sqrt{6}} \begin{pmatrix} 1 & 0 & 0 \\ 0 & 1 & 0 \\ 0 & 0 & -2 \end{pmatrix}$	

Figure 3.3: A selection of moment tensor identities and the associated focal mechanisms. Image from Dahlen and Tromp (1998) modified by Steith (2003)

In order to decompose and then classify the source type from the moment tensor, the eigenvectors and eigenvalues of the moment tensor can be used as shown in the following equations from Vavryčuk (2001) and Linzer (2005). For the isotropic component

$$ISO\% = \frac{100tr(\mathbf{M})}{|tr(\mathbf{M})| + \sum_{i=1}^3 |m_i^*|}, \quad (3.22)$$

where m_i are the ordered eigenvalues according to the magnitude and the trace is computed by summing the eigenvalues together, for example

$$tr(\mathbf{M}) = m_1 + m_2 + m_3. \quad (3.23)$$

Similarly for the DC component,

$$DC\% = \frac{m_3^*(1 - 2F)}{|m_3^*(1 - 2F)| + |2m_3^*F|} (100 - \%ISO), \quad (3.24)$$

where

$$F = m_1^*/m_3^* \quad (3.25)$$

and

$$m_i^* = m_i - 1/3tr(\mathbf{M}). \quad (3.26)$$

Finally for the CLVD component,

$$CLVD\% = 2\epsilon(100\% - |ISO\%|), \quad (3.27)$$

where

$$\epsilon = -\frac{m_3^*}{|m_1^*|} \quad (3.28)$$

Taken from Vavryčuk (2001) and Linzer (2005).

Decomposition of the moment tensor into these three separate components as discussed by Vavryčuk (2001) is well-defined and unambiguous by equations 3.22 to 3.28 but it is also mathematically based and yields poor information on the physical processes at the source. Figure 3.4 shows the three basic components as described by the Knopoff and Randall (1970) decomposition.

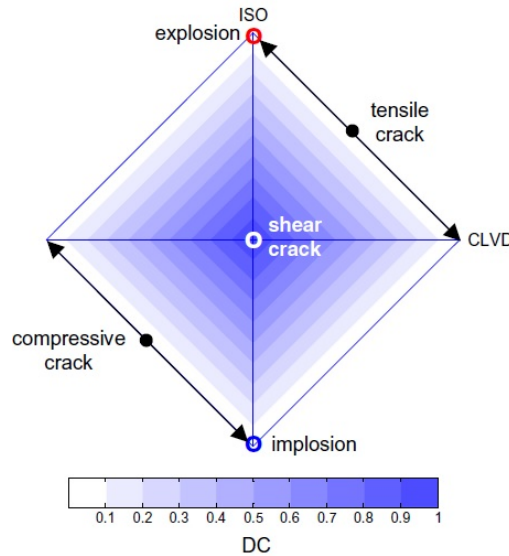


Figure 3.4: The diamond CLVD-ISO plot with the positions of the basic component sources. The arrows indicate the range of possible positions of moment tensors for tensile and compressive cracks. From Vavryčuk (2005)

With the type of source discerned from the decomposition, an appropriate model for the source needs to be applied. For DC sources (shear crack) this is well documented and Steith (2003) covers this topic. The set of three angles, dip, strike, rake relate to the slip vector \mathbf{u} , determined from the eigenvectors of the moment tensor, and describe the failure mechanics fully. A schematic of a fault and these angles are shown as figure 3.5

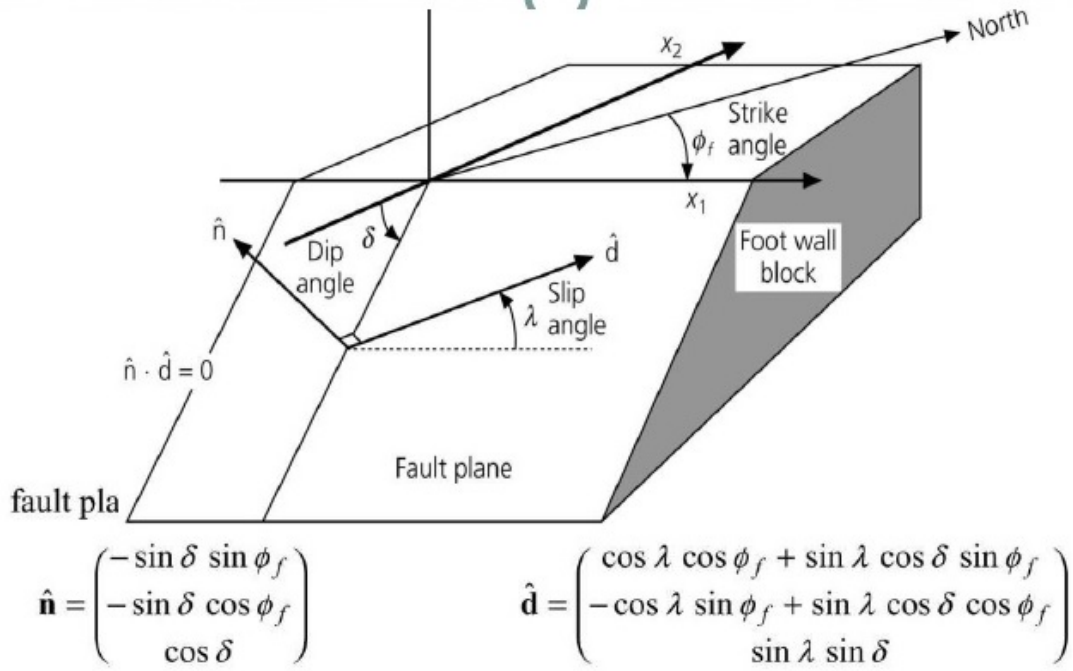


Figure 3.5: Geometry Calculations from the slip vector. Image from Steith (2003)

Unfortunately the symmetric nature of a moment tensor means that there is an element of ambiguity involved in this mechanical description. This ambiguity is that the fault plane and auxiliary plane, which are perpendicular, are mathematically equally valid for a given moment tensor. In this situation it is common to use external data to determine which of the two models is correct.

The following moment tensor model can be used to describe sources where tensile forces dominate (shown in figure 3.4 as tensile cracks) :

$$\mathbf{M} = M_0 \begin{bmatrix} \lambda + \mu & 0 & 0 \\ 0 & \lambda & 0 \\ 0 & 0 & \lambda \end{bmatrix} \quad (3.29)$$

Where the eigenvalues for this model are $m_1 > m_2 = m_3$. Vavryčuk (2001) proposed a more specific decomposition to take into account this fracture type. This method entails inclusion of an angle, α , into the standard shear crack model of dip, strike, and rake. This is calculated by using the eigenvalues, m_1 to m_3 (ordered appropriately)

and calculated by,

$$\sin\alpha = \frac{m_1 + m_3 - 2m_2}{m_1 - m_3}. \quad (3.30)$$

The results of this calculation provide clear information on the mechanics involved: an α of 90 degrees is a pure tensile event; -90 degrees is a pure compressional event and 0 degrees is a pure shear event. Another similar method was presented by Ohtsu (1991) who looked at the ratios of DC, CLVD, and ISO and created a classification system based on this to classify between shear and tensile events.

It would be useful to determine the fluid flow directions for these tensile fractures from the moment tensor. This is still a area of ongoing research and in the model presented above, the T axis from the moment tensor defines the crack opening vector with the P axis defining the fluid flow. Unfortunately, the ambiguity in this model stems from the fact that the eigenvalues for the P and B axis are the same, meaning it is impossible to know which of these two is the P axis and therefore fluid direction. For this reason, it is usual to represent this model as two discs pulling apart as shown in Ohtsu (1991). Other models applied to determine the fluid flow direction through fractures from the moment tensor is the expanding cylinder model used in geothermal and volcanology research Nakano and Kumagai (2005).

3.4 Methods to measure the geometry of a seismic event from anisotropic variations of wave behaviour

3.4.1 Introduction

The presence of fractures within a rock frame and the properties of these fractures (alignment and fluid fill) alter the velocity and amplitude of waves travelling through this rock frame. These anisotropic variations of velocity and amplitude with direction can be used to determine fracture properties, of which shear wave splitting is a readily used property.

Shear wave splitting (SWS) occurs when the shear wave travels through an anisotropic region and splits into two orthogonally polarized waves, one of which will travel faster than the other. The polarisation of the fast wave and the time lag between the arrivals of the fast and slow wave can be measured on 3-component geophones and used to characterize the splitting along the raypath. By using these parameters, the fracture alignment and fill, can be calculated and used in part to diagnose if induced seismicity is occurring.

3.4.2 Relationship between SWS and fracture properties

The fundamentals of using SWS to solve for fracture properties are described by Verdon et al. (2009). First, as the shear waves can travel in any direction, any model used must compute the full $3 \times 3 \times 3 \times 3$ stiffness tensor C . Since compliance is the inverse of stiffness, then $S = C^{-1}$.

The overall compliance tensor can be considered as a combination of the compliance of the fractures ΔS and the rock frame compliance S^r as

$$\mathbf{S} = \mathbf{S}^r + \Delta \mathbf{S}. \quad (3.31)$$

The compliance for a rock frame with VTI symmetry is,

$$\mathbf{S}^r = \begin{bmatrix} C_{11}^r & C_{11}^r - 2C_{66}^r & C_{13}^r & 0 & 0 & 0 \\ C_{11}^r - 2C_{66}^r & C_{11}^r & C_{13}^r & 0 & 0 & 0 \\ C_{13}^r & C_{13}^r & C_{13}^r & 0 & 0 & 0 \\ 0 & 0 & 0 & C_{44}^r & 0 & 0 \\ 0 & 0 & 0 & 0 & C_{44}^r & 0 \\ 0 & 0 & 0 & 0 & 0 & C_{66}^r \end{bmatrix}^{-1}, \quad (3.32)$$

where $C_{11} > C_{33}$ and $C_{66} > C_{44}$. The strength of the shear wave anisotropy caused by the VTI system is given by Thomsen's 1986 parameters defined as :

$$\gamma = \frac{C_{66}^r - C_{44}^r}{2C_{44}^r} \quad (3.33)$$

and

$$\delta = \frac{(C_{13}^r + C_{44}^r)^2 - (C_{33}^r + C_{44}^r)^2}{2C_{33}^r(C_{33}^r + C_{44}^r)}. \quad (3.34)$$

The compliance from a set of vertical, aligned fractures can be considered as :

$$\Delta \mathbf{S} = \begin{bmatrix} B_n & 0 & 0 & 0 & 0 & 0 \\ 0 & 0 & 0 & 0 & 0 & 0 \\ 0 & 0 & 0 & 0 & 0 & 0 \\ 0 & 0 & 0 & 0 & 0 & 0 \\ 0 & 0 & 0 & 0 & B_{Tv} & 0 \\ 0 & 0 & 0 & 0 & 0 & B_{Th} \end{bmatrix} \quad (3.35)$$

Where B_n is the normal compliance of the fracture and B_{th} and B_{tv} are the shear compliances in the vertical and horizontal planes. The equation in 3.35 is aligned along the x_1 axis, this is rotated to give fractures in different strike directions. Verdon et al detail that only if VTI anisotropy is significant then B_{th} and B_{tv} will differ with a change in rotation. Using an idealised fracture geometry of a penny-shaped fracture (Hudson, 1981) and a low-frequency end-member then, B_n , B_{tv} and B_{th} are given by,

$$B_n = \frac{4}{3} \left(\frac{\gamma}{C_{66}^r} \right) \frac{C_{11}^r}{C_{11}^r - C_{66}^r} \quad (3.36)$$

$$B_{Th} = \frac{16}{3} \left(\frac{\gamma}{C_{66}^r} \right) \frac{C_{11}^r}{3C_{11}^r - 2C_{66}^r} \quad (3.37)$$

$$B_{Tv} = \frac{16}{3} \left(\frac{\gamma}{C_{44}^r} \right) \frac{C_{11}^r}{3C_{11}^r - 2C_{44}^r} \quad (3.38)$$

The above equations link the elastic stiffness of a rock, the matrix C , to a horizontally layered sedimentary rock with VTI with a fabric strength γ and δ , with a set of vertical fractures included within the volume with a density of γ and strike of α .

3.4.3 Inversion workflows

While this method is applied as a matter of course in global seismological studies (Kendall et al., 2006) application of this type of method to microseismic datasets is limited, with the majority of studies being conducted using the method by James Verdon from the University of Bristol as reported in Verdon et al. (2009) and Verdon and Kendall (2011). For these reasons, the workflow that has been established by Verdon is briefly discussed.

The workflow by Verdon uses the Christoffel equation to compute σ and δV_s for each shear wave arrival with a specific azimuth (θ) and inclination(ϕ). A surface is computed that covers the extent of the events used in the inversion. The σ and δV_s are modelled and compared to the observed data set with a rms misfit. This rms misfit is then minimised by the grid search process. This workflow is summarised in figure 3.6 from Verdon et al. (2009).

An example of an SWS result and the QC steps applied is shown in figure 3.7 by Gajek et al. (2018) from a hydraulic fracturing site in Poland monitored using a down-hole monitoring well.

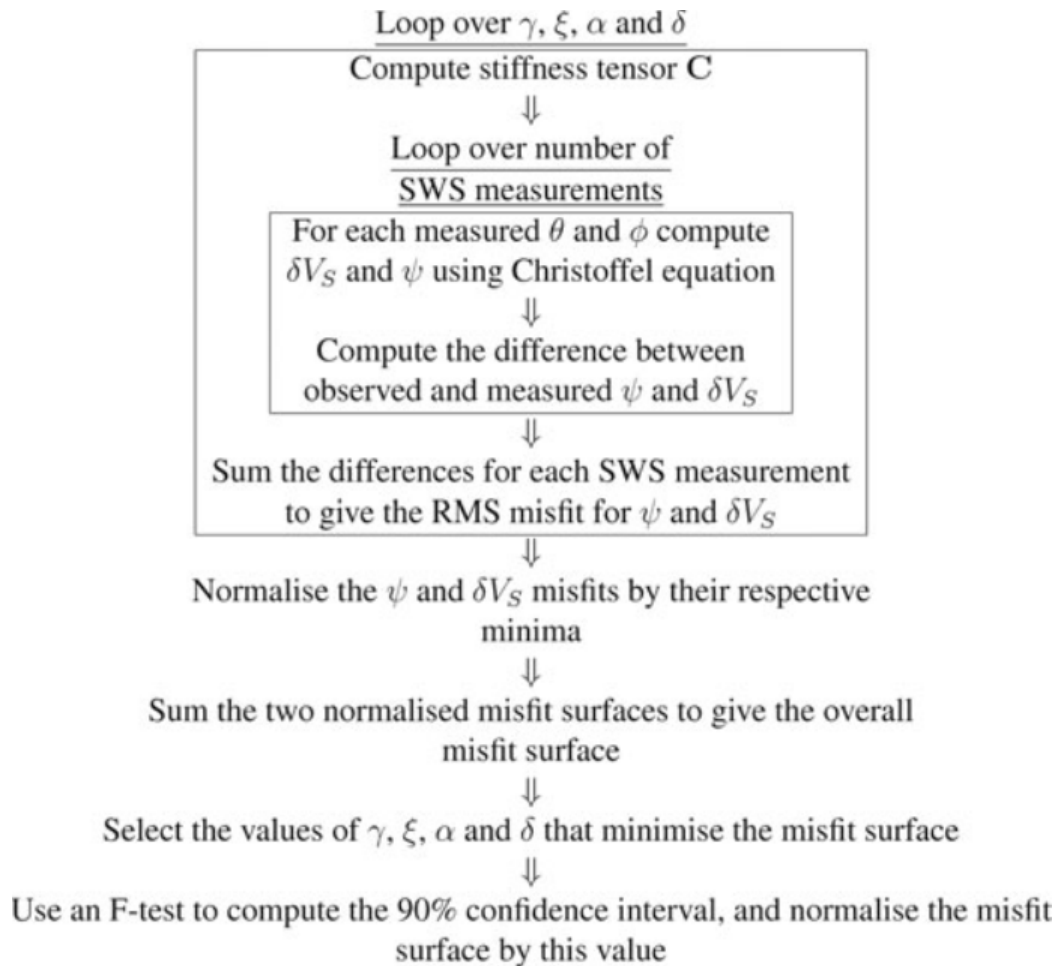


Figure 3.6: Workflow for inverting for rock physics parameters from SWS measurements, Verdon et al. (2009)

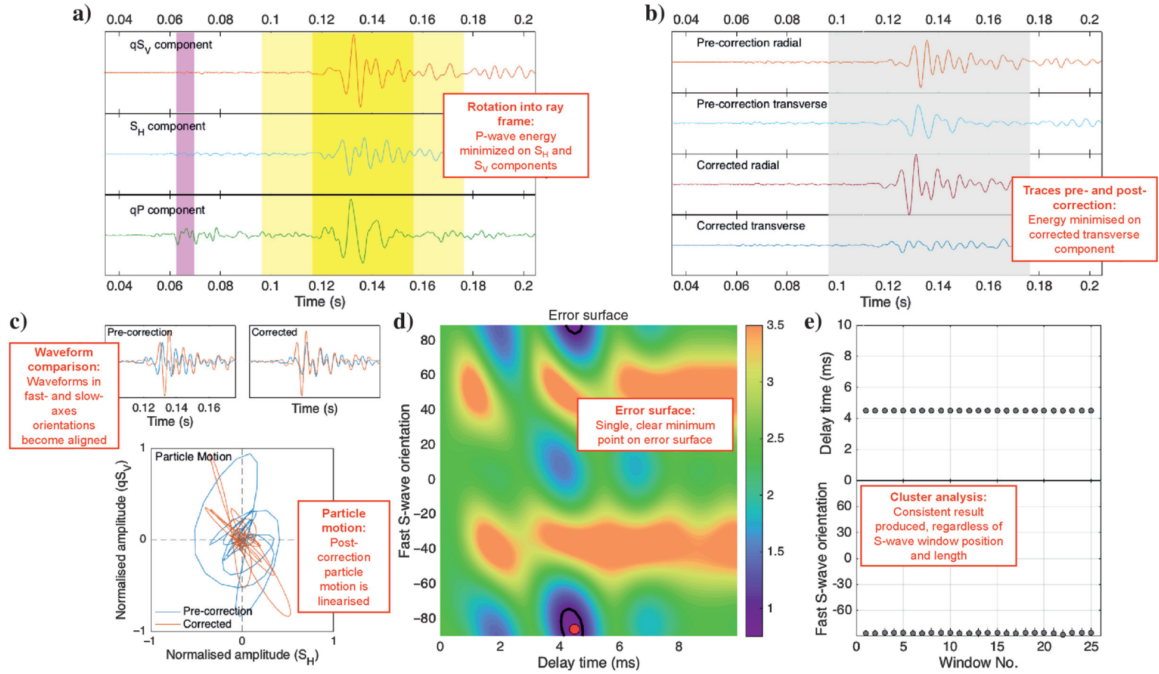


Figure 3.7: Example SWS result from Gajek et al. (2018) using the Verdon et al. (2009) approach, showing the QC criteria used to assess the measurements. In (a), the recorded waveforms are plotted in the ray-frame coordinates rotated to ensure that P-wave energy is minimized on the qSH and qSV components. In (b), the radial and transverse components prior to and after the SWS correction have been plotted: the SWS correction should minimize energy on the transverse component. In (c), the S-wave arrivals in the SWS fast- and slow-orientation coordinates, and the pre and post-correction particle motion are plotted. After correction, two matching waveforms should be found, resulting in a linearisation of the particle motion. In (d), an error surface of the correction method is plotted. This surface is a function of delay time and fast direction, normalized such that the 95% confidence (highlighted in bold) interval is one: A single, clear minimum point should be produced. In (e), the SWS results are plotted with a variation in the analysis window choice taken from the bands in (a). A good result should be consistent regardless of the choice of analysis window. Summarised from Gajek et al. (2018).

3.5 Methods to measure the geometry of a seismic event from signal length variations

3.5.1 Introduction

When a seismic event occurs and the rock mass slips, this movement is expressed by the source time function. The modelling of the source time function allows parameters such as the length of the fracture, velocity and the direction of the fracture opening to be determined from the data records. These parameters can be used to determine the direction and extent of a propagating fracture network.

3.5.2 The relationship between the source history and the radiation pattern

To determine geometric and kinematic parameters such as length, rupture velocity and direction from seismic events a relationship between the P- and S- wave arrivals and these parameters are required. The radiation pattern emitted by a finite length seismic source moving along a path with a direction differs from a point source radiation pattern emitted by an explosive seismic source. This radiation pattern varies with direction and the far-field displacement is then given, in the spherical coordinate system, as,

$$u_R = \frac{P_0}{12\pi\beta} \left(\frac{\beta}{\alpha}\right)^3 \frac{F}{R} \left[\frac{g(t_\alpha) - g(t_\alpha - t_{d\alpha})}{t_{d\alpha}} \right] \quad (3.39)$$

$$u_{ih} = \frac{P_0}{24\pi\beta R} \frac{\delta F}{\delta i_h} \left[\frac{g(t_\beta) - g(t_\beta - t_{d\beta})}{t_{d\beta}} \right] \quad (3.40)$$

$$u_{\phi h} = \frac{P_0}{24\pi\beta R \sin(i_h)} \frac{\delta F}{\delta \phi_h} \left[\frac{g(t_\beta) - g(t_\beta - t_{d\beta})}{t_{d\beta}} \right]. \quad (3.41)$$

Where R is the distance between source and receiver, P_0 is the source potency, β is the S- wave velocity, α is the P- wave velocity, F is the radiation pattern for a shear failure, i_h is the angle from the vertical axis and ϕ_h is the angle from the horizontal x_1 axis, $g(t)$ is the source time function, $t_{d\alpha}$ and $t_{d\beta}$ are the duration of the P- and S-wave signals at the observation point respectively and t_α and t_β is the time arrival for the P- and S-waves respectively. Equation 3.39 to 3.41 requires the source potency, P_0 as

$$P_0 = \bar{U} L W, \quad (3.42)$$

$$t_\alpha = t - \frac{R}{\alpha} \quad (3.43)$$

and

$$t_{d\alpha} = \frac{L}{V_f} \left(1 - \frac{V_f}{\alpha} \cos(\theta)\right), \quad (3.44)$$

where t is the time vector \bar{U} is the dislocation, L is the length of the fracture, W is the width of the fracture, V_f is the velocity of the rupture and θ is the angle between the observer and point of fracture initiation. These angles used in equation 3.39 to 3.41 are illustrated in figure 3.8.

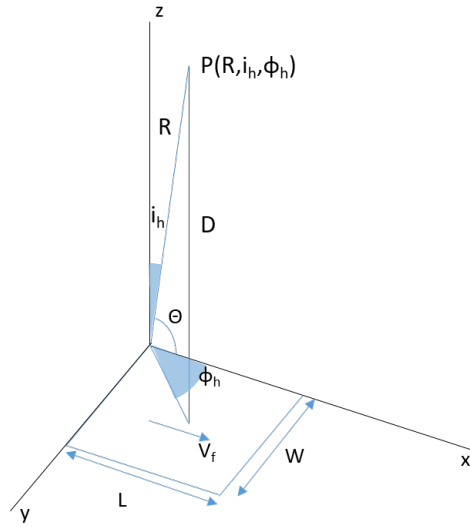


Figure 3.8: Example of the angles used to describe equations 3.39 to 3.41. A fracture of length, L and width, W moving at a velocity of V_f moving at an angle θ transmitting a wave that is recorded at an observation point, P , at a distance R . Modified from Ben-Menahem and Singh (2012).

An example of the source time function, $g(t)$ when $t_{d\alpha} < \tau$, the rise time, is shown as figure 3.9.

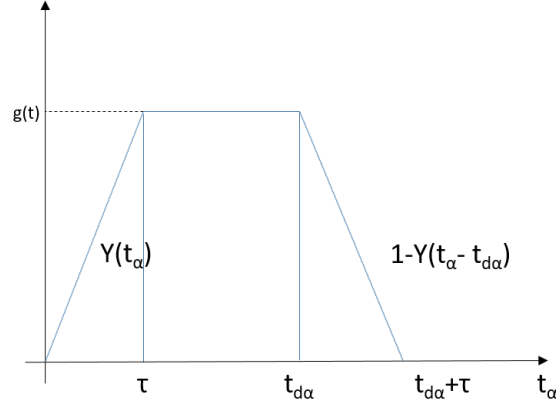


Figure 3.9: A example source time function $g(t)$ for a source when τ , the rise time, is less than the rupture duration, $\tau_{d\alpha}$. Modified from Ben-Menahem and Singh (2012).

The rise time, τ , is the time required for the slip to end the acceleration phase during the movement. The P- and S- wave duration times or rupture times, are given by

$$t_{d\alpha} = \frac{L}{V_f} \left(1 - \frac{V_f}{\alpha} \cos\theta\right), \quad (3.45)$$

$$t_{d\beta} = \frac{L}{V_f} \left(1 - \frac{V_f}{\beta} \cos\theta\right). \quad (3.46)$$

where L is the length of the fracture, V_f is the rupture velocity, α and β are velocities for the P- and S- wave arrivals and θ is the horizontal angle of the fracture.

Using equation 3.39 for two diametrically opposite points 180 degrees apart the P wave amplitudes are different by a factor of,

$$\frac{u_R(R, i_h, \phi_h)}{u_R(R, \pi - i_h, \pi + \phi_h)} = \frac{t_{forward}}{t_{backward}} = \frac{1 + (V_f/\alpha)\cos\theta}{1 - (V_f/\alpha)\cos\theta}. \quad (3.47)$$

The duration of this forward field is less than the duration of the backward field by an amount

$$t_{forward} - t_{backwards} = (2L/\alpha)\cos\phi. \quad (3.48)$$

Therefore waves arriving at a seismograph in the direction of the fracture have a higher frequency, shorter wavelengths, and higher amplitudes than the arrivals diametrically opposite to the fracture direction. It is this observation which allows a relationship to be derived to determine the fracture properties from these measurable parameters.

3.5.3 The relationship between the source time function and the geometric and kinematic properties of fractures

In the previous section, relationships between frequency and amplitude content of the received wavefield and the properties of the seismic source were established. In this section, the methods currently used to model this relationship are explored. From a thorough review of literature and of best practices by industrial service providers for microseismic monitoring, methods using these relationships are currently constrained solely to academic investigations.

The methods used in academia currently are based on either measuring the change in frequency content or a change in the wavelet time length, as a measure of the variation in source time function in the time domain. The academic investigations into seismic events are mainly focussed on events which have a high magnitude. The reasoning is that these have higher signal to noise ratios and the attenuation structure between source and receiver will not dominate the calculations of rupture direction, length and velocity. The methods highlighted here showcase those which have been applied to seismic events in the small to microseismic range ($M_w < 2$) in both the time and frequency domains.

A method utilising variations in the wavelet time length measured in the time domain

This method is based on the work by Aldo Zollo, of the Università di Napoli Federico II, Naples and Salvatore de Lorenzo of the Università di Bari, Italy. The method introduced by Zollo and de Lorenzo (2001) involves determining the source parameters and the attenuation structure from the measured rise and the rupture times from a set of synthetic events. A schematic of how the measured values of the rise time and rupture time are taken from a data record is shown in figure 3.10.

The scheme used by Zollo and de Lorenzo (2001) involves solving for the attenuation structure and the source parameters by two equations (3.49 and 3.50). The first relationship is :

$$\tau = \tau_0 + \gamma(L, c, \theta) \frac{T}{Q} + \lambda(L, c, \theta), \quad (3.49)$$

where τ is the measured rise time at the receiver, τ_0 is the rise time at the source, T is the travel time of the ray, Q is the attenuation applied to the ray path, γ and λ are functions depending on the length L of the source, the P-wave velocity c and θ a function of the dip and strike angles of the rock.

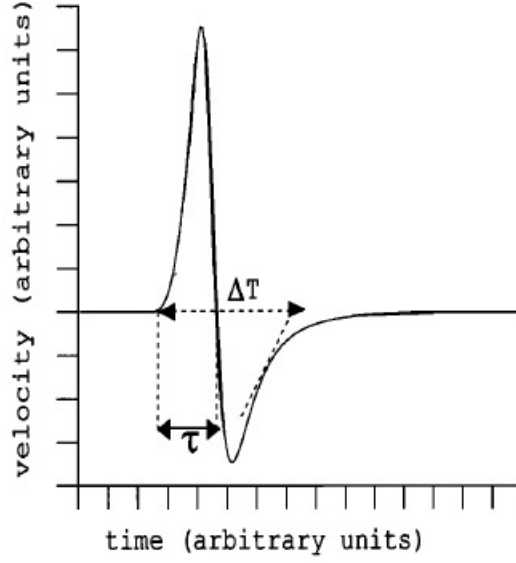


Figure 3.10: Pulse length (ΔT) and rise time (τ) of a signal. Taken from De Lorenzo and Zollo (2003)

The second relationship used is :

$$\Delta T = \Delta T_0 + C \frac{T}{Q}. \quad (3.50)$$

Where ΔT is the measured rupture time at the receiver, ΔT_0 is the rupture time at the source, C is a source-specific constant, T is the travel time of the ray and Q is the attenuation applied to the ray path. The function for γ is given by :

$$\gamma(L, c, \theta) = \gamma_1 \frac{L}{c} \sin \theta + \gamma_2, \quad (3.51)$$

where L is the length of the fracture, c is the rupture velocity, θ is a function of the dip and strike angles of the rock and γ_1 , γ_2 are constants to be estimated separately. The function for λ is given by

$$\lambda(L, c, \theta) = \lambda_1 \frac{L}{c} \sin \theta + \lambda_2, \quad (3.52)$$

where L is the length of the fracture, c is the rupture velocity, θ is a function of the dip and strike angles of the rock and λ_1 , λ_2 are also constants to be estimated separately.

The method used by Zollo and de Lorenzo (2001) to invert for the source parameters and the attenuation structure using equation 3.49 requires the functions of equations

3.51 and 3.52 to be calibrated to the velocity model of the study area. This calibration process consists in computing, for different source parameters and Q_p values a set of synthetic seismograms. These synthetic seismograms detail the wave-field radiating from a rupture and propagating through an anelastic medium. Using these synthetic seismograms, the rise times are computed through an automatic picking code and γ_1 , γ_2 , λ_1 and λ_2 are estimated through a regression analysis, minimizing the misfit between these synthetic rise times and those predicted in equation 3.52. An example of these comparisons between the synthetic and predicted rise times are shown as figure 3.11.

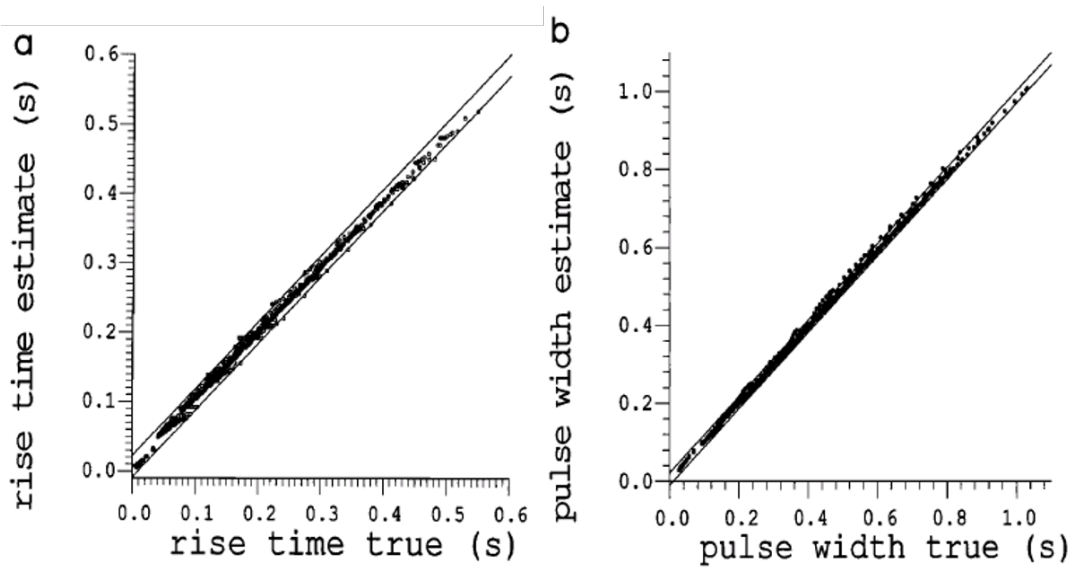


Figure 3.11: The Zollo and de Lorenzo (2001) method to calculate both the source parameters and attenuation structure. (a) Comparison between the estimated values of the rise time as deduced by equation 3.49 and those measured from the synthetic seismograms.(b) Comparison between the values of the rupture width as deduced by equation 3.50 and those measured from the synthetic seismograms. Image from Zollo and de Lorenzo (2001)

With equations 3.51 and 3.52 calibrated using values of γ_1, γ_2 , λ_1 and λ_2 the non-linear equations of 3.49 and 3.50 are solved using a global optimization technique the ‘simplex downhill method’. To utilise the global optimization technique a misfit parameter is required,

$$\sigma = \sum \sum [W_{\tau_{ij}}(\tau_{i,j_{obs}} - \tau_{i,j_{est}})^2 + W_{\Delta T_{i,j}}(T_{i,j_{obs}} - T_{i,j_{est}})^2] \quad (3.53)$$

where τ and ΔT are the estimated and observed rise time and rupture lengths.

This method has been applied in De Lorenzo et al. (2004) using a set of 260 micro-earthquakes with magnitude ranges between Mw 0.6 to Mw 3.5 in south-eastern Sicily. The main assumption for this method is that the rupture velocity is set to 0.9 times the shear wave velocity. This assumption is based on laboratory experiments as discussed by Madariaga (1976) which showed that the rupture velocity varies between 0.6 to 0.9 times the shear wave velocity. The other assumption is that the failure of the fault is based on the circular crack model by Sato and Hirasawa (1973). The other consideration with this method is that this process solves for both the source parameters and the attenuation structure. De Lorenzo et al. (2004) state that the quality factor, Q is strongly dependent on both V_p and V_r (and hence V_s from the rupture velocity assumption) at the seismic source. Therefore if the velocity model at the source is poorly constrained, then the estimates of the source model and seismic quality factor will be affected.

Methods utilising variations in the frequency content

The first method discussed is by Tomic et al. (2009) who investigated source parameters and the rupture velocity of small induced earthquakes generated by the variation of water level in a water reservoir. The method involves using small earthquakes as empirical Green's functions (EGFs) to remove the site and path effects to the analysis of six earthquakes chosen for the analysis. The six earthquakes to be studied and all the small earthquakes to be used as EGFs are firstly analysed in the frequency domain to determine the corner frequency, f_c , the long period amplitude ω_0 , Q the attenuation along the ray path. The spectra calculated from this analysis are then used to calculate spectral ratios between each of these six study events and each of the corresponding EGFs. The spectral ratios are then averaged to obtain a mean spectral ratio for each of the six events. This method is shown in figure 3.12

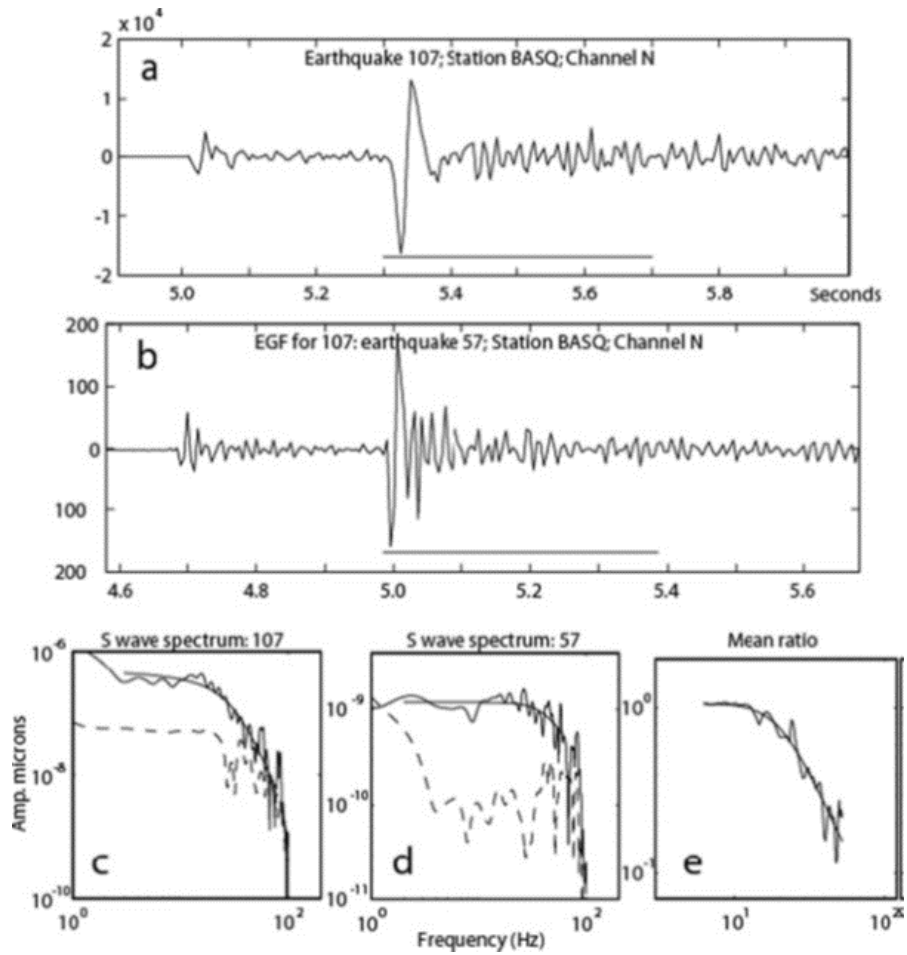


Figure 3.12: The frequency domain method to investigate source parameters by Tomic et al. (2009). In panel (a) the north component of the seismogram for a seismic event in the time domain. In panel (b) the north component of the seismogram for a seismic event in the time domain used as a EGF. In panel (c) and (d) the frequency domain representation of (a) and (b) with the noise spectrum as a dotted line. Panel (e) shows the spectral ratio using all suitable EGF's

This spectral ratio is deconvolved from the six events and the spectra are transformed back into the time domain where the duration of the source time function is calculated by taking the time duration between the first to second zero crossing. Using these measurements, directivity and rupture velocity was modelled with the path and site effects (attenuation) removed. This study found that the rupture velocity of these small induced earthquakes was at least 0.6 times the shear wave velocity, in-line with the laboratory experiments in Madariaga (1976). The assumptions within this method are clear, with this method it is not possible to analyse all of the 286 events that the author had access to, as the majority of these events are used to create the EGFs to remove the path effects in the modelling. A study by Kane et al. (2013) investigates small events at Parkfield, California along the San Andreas Fault and uses a similar method to Tomic et al. (2009) to remove the path and local effects from the spectral modelling. By clustering sets of small events together, the effects of scattering and attenuation are assumed to be similar along all the same paths. All the events are transformed into the spectral domain and the site and path effects are iteratively removed from each of the 20 clusters of events. The corrected P-wave displacement spectra are then modelled with the following equation,

$$f_{c,app} = f_c \frac{1}{1 - \frac{V_r}{c}} \cos\theta \quad (3.54)$$

where $f_{c,app}$ is the apparent corner frequency of the source spectrum, f_c is the true corner frequency, V_r is the rupture velocity, c is the seismic wave velocity and θ is the angle of rupture. By using this method, 450 directivity estimates were made, from 2263 recorded events. Similar to the Tomic et al. (2009) method all events cannot be analysed individually as the events require clustering to remove the path effects.

The final method highlighted is an automated method used to determine the direction of earthquake slip by Cesca et al. (2011). This algorithm was built to assist in the determination of ground motion and to reduce the risks from earthquake damage. The method utilises the source inversion method by Cesca et al. (2010) which generates a set of Green's functions for a range of Earth models, source depths and epicentral distances. These Green's Functions are then matched to the amplitude spectra of the data records. These amplitude spectra are inverted using as a base, the relationship between rupture length and direction, length and rupture velocity as specified in equation 3.45. This relationship is then extended to include bilateral and asymmetric ruptures into the following relationship,

$$\Delta t(\phi) = \text{Max}[t_r + L_1/v_R - (L_1/v_p)\cos(\phi), t_r + L_2/v_R + (L_2/v_p)\cos(\phi)]. \quad (3.55)$$

An example of these different types of ruptures is shown as figure 3.13.

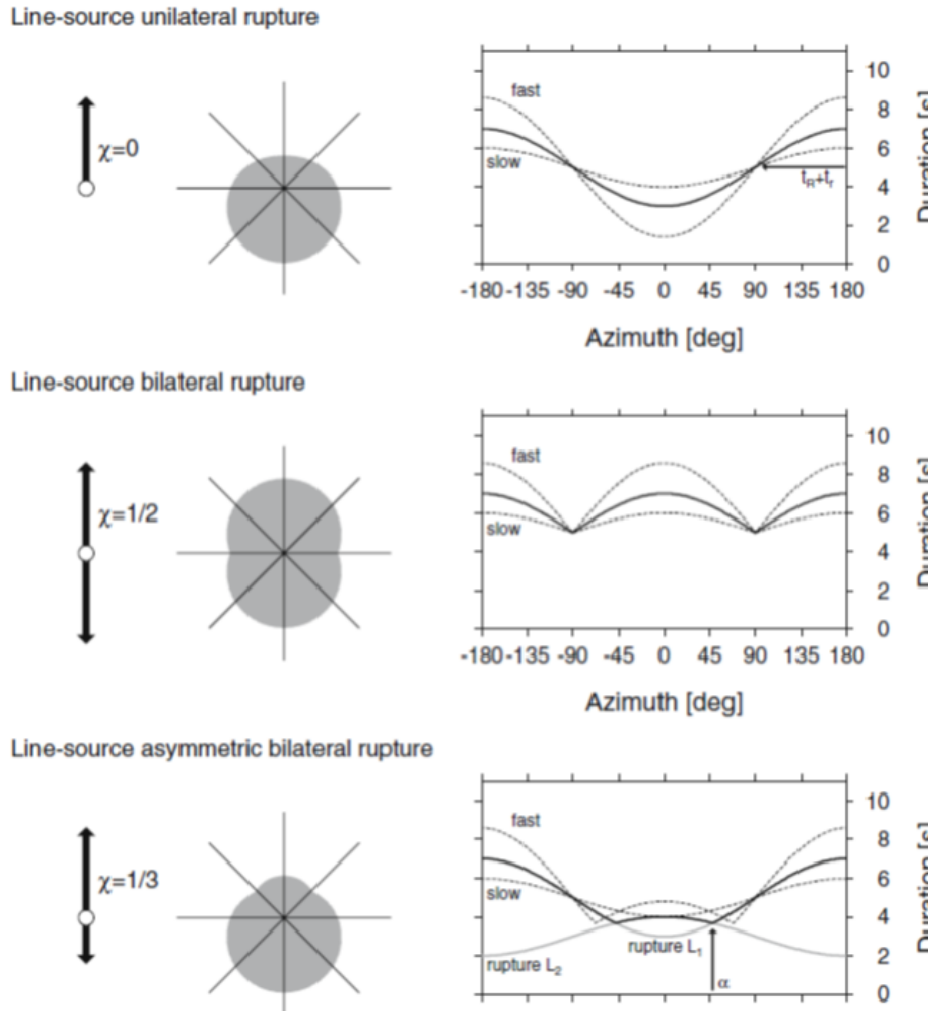


Figure 3.13: Theoretical models for different rupture types from Cesca et al. (2011) with (top) pure unilateral rupture, (centre) pure bilateral rupture and (bottom) asymmetric bilateral rupture. Left hand side shows the movement on the fault and the radiation pattern emitted. Right hand side images show the rupture time models for each of these rupture types.

This method is computationally efficient, with an inversion only taking a couple of minutes to converge on a solution and that by using theoretical Green Functions based on a Earth's response model rather than empirical Green's functions path effects can be compensated for without the use of clusters of events or additional smaller events. This method has been applied to two large Mw 6 earthquakes in Greece but has not been applied to any seismic events in the small to microseismic range.

3.6 Calculation of the energy transfer from a seismic event

When rock slip occurs, the strain energy built up inside the fault is converted into heat, kinetic, and elastic energy. This energy is radiated out into the surrounding rock. The energy released differs depending on the failure type and used to ascertain the type of failure. A useful measure from this type of investigation is the ratio between the radiated energy in the P- and S- waves. This ratio can be used to indicate the existence of tensile components in a seismic event, a parameter that can be used to determine if the seismic event is caused by a reactivated fault line or a newly opened tensile fracture.

After a thorough review of literature and of the publicly available information from microseismic monitoring service companies, analysis of energy transfers from microseismic events has currently only been applied in academic investigations. Of these academic investigations some, such as Boroumand and Eaton (2012), utilise seismology methods to calculate the radiated energy. For example, Boroumand and Eaton (2012) use a simple empirical relationship with the seismic moment to calculate radiated energy from a microseismic survey of a hydraulic fracturing operation. This is built into an energy balance with the input energy derived from an integration of the surface treatment pressure and injection rate at each hydraulic fracturing stage. Another method used on microseismic surveys used by Oye et al. (2005) is to use the integrated velocity spectrum by,

$$E_{rad} = 4\pi\rho\beta S_{v2}, \quad (3.56)$$

where ρ is the density, β is the velocity and S_{v2} is the integrated velocity spectrum. Both of these methods do not take into account the radiation pattern emitted from the slip and the effect that a tensile or shear failure has on the radiated energy.

The method used by Kwiatek and Ben-Zion (2013) is a modification of the method by Boatwright and Fletcher (1984) used to measure radiated energy from small

shear/tensile earthquakes and takes into account the different radiation patterns emitted from shear or tensile events. This method states that to measure the radiated energy from microseismic records the radiated energy flux from a seismic source may be calculated using :

$$J_c = \frac{1}{\pi} \int [\omega \Omega(\omega)]^2 d\omega \quad (3.57)$$

where ω is the angular frequency and $\Omega(\omega)$ is the root mean squared (RMS) ground displacement spectrum for either the P or S waves and can be determined from using either the Brune (1970) or Boatwright (1980) models as discussed in equations 3.4 and 6.27 in the earlier section. The energy flux at a given position on the focal sphere depends strongly on the radiation pattern, directivity and rupture velocity. If the directivity and rupture velocity are neglected, Boatwright and Fletcher (1984) state the energy recorded at a given station that is radiated by a given wave type from a seismic source can be expressed as :

$$E_c = 4\pi\rho V_c < R_c >^2 (R/R_c)^2 J_c, \quad (3.58)$$

where ρ is the rock density, V_c is the wave velocity and $< R_c >$ is the P or S wave average radiation pattern correction coefficient, R_c is the correction for the radiation pattern of either P or S waves at a particular station and R is the source-receiver distance. To solve the integral for the energy flux, J_c given in 3.57 the following equation is used :

$$J_c = 2 \int_{f_{min}}^{f_{max}} [u_c(f) \exp \frac{\pi f R}{V_c Q_c}]^2 df. \quad (3.59)$$

In equation 3.59, u_c is the raw ground velocity spectrum of either P or S waves, V_c and Q_c are the velocity and seismic quality factor respectively. To calculate the average radiation pattern correction coefficient, the method as specified in Boore and Boatwright (1984) can be used when the seismic source is a pure shear rupture. This can be altered if the rupture is caused by a combination of tensile forces as well as shear forces using a method by Ou (2008). The variation of the average radiation pattern correction coefficient with the tensile angle for an example fault is shown as figure 3.14. This method was applied to 539 seismic events that occurred after an Mw 1.9 event from a deep South African mine and show that the E_s/E_p ratios for the events are relatively low <5 indicating that a significant number contain a tensile component in the failure.

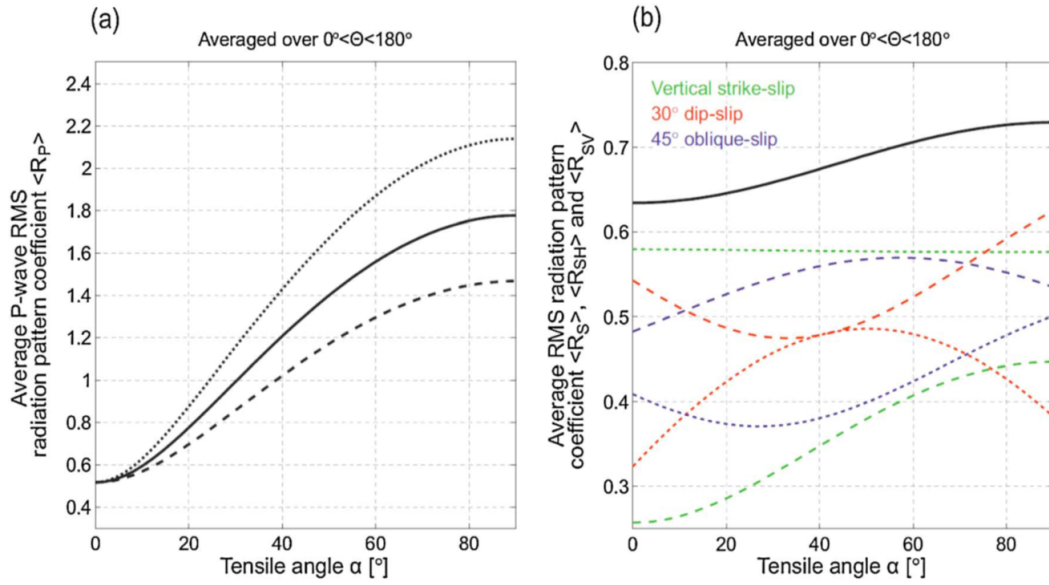


Figure 3.14: The relation between the average RMS radiation pattern coefficients of P, S, SV, and SH waves as a function of the tensile angle. The RMS radiation pattern coefficients were averaged over the whole focal sphere. (a) The RP coefficient is plotted for three values of Poisson's ratio (0.20, 0.25, and 0.29, drawn with dashed, solid, and dotted lines, respectively). The RP coefficient is appropriate for an arbitrary focal mechanism as it is averaged over the whole focal sphere. (b) The RS coefficient is plotted using black solid line and is independent of the focal mechanism. The average RMS radiation pattern coefficients of SH and SV phases, R_{SH} and R_{SV} , are shown using dotted and dashed red/blue/green lines, corresponding to the different focal mechanisms. Taken from Kwiatek and Ben-Zion (2013)

3.7 Calculation of stress transfer between seismic events

3.7.1 Introduction

The transfer of static normal and shear stresses between seismic events can alter the likelihood of failure at potential nearby faults. This is a cause of induced seismicity as was discussed in chapter 2. By spatially modelling the Coulomb failure function after each seismic event occurs, the extent to which seismic activity is altering the normal and shear stresses on a fault plane can be quantified, and areas where seismicity may occur next, could be avoided. In this section, the methods by which this is modelled will be reviewed.

3.7.2 Methods to model the Coulomb failure function

The Coulomb failure criterion (eq 2.2) as defined in chapter 2 stated that if $\tau_0 + \mu(\sigma_n - p)$ exceeds to the shear stress (τ) then failure on a plane occurs. Equation 2.2 can be considered in terms of the change in Coulomb stress (σ_f) or Coulomb failure function (ΔCFF , from Lin et al. (2011)) due to a change in either the normal stresses (σ_β), the shear stresses (τ_β) on the plane, the friction coefficient on the plane (μ) or the pore pressure P , where

$$\sigma_f = \tau_\beta - \mu(\sigma_\beta - P), \quad (3.60)$$

assuming the cohesion (τ_0) remains constant. The subscript β is used to detail the orientation of the failure plane to the σ_1 axis.

If the normal and shear stresses on the fault plane are known then expression 3.60 can be used to determine if slip at a fault is more or less likely to occur from the sign of the Coulomb failure function (σ_f) where a negative number means a failure is less likely to occur and conversly a positive number indicates that a failure is more likely to occur.

To use equation 3.60 as a means to quantify the likelihood of triggering a earthquake slip in a specific area from the transfer of normal and shear stresses from previous seismic events, these stresses need to be firstly modelled into spatially varying fields. An established methodology by Stein et al. (1992) as built into the Coulomb 3 software by Lin et al. (2011) and Toda et al. (2005) uses the Okada (1992) model to calculate a displacement and strain field based on a supplied grid and a set of fault parameters (position and focal mechanism). These spatially varying fields are converted into

stress tensors by simple Hooke's law using pre-defined Young's modulus (E) and Poisson's ratio (ν) values for an isotropic material as,

$$\sigma_{xx} = \frac{E}{(1 + \nu)} \left(\frac{\nu V}{1 - 2\nu} + \epsilon_{xx} \right) \quad (3.61)$$

$$\sigma_{yy} = \frac{E}{(1 + \nu)} \left(\frac{\nu V}{1 - 2\nu} + \epsilon_{yy} \right) \quad (3.62)$$

$$\sigma_{zz} = \frac{E}{(1 + \nu)} \left(\frac{\nu V}{1 - 2\nu} + \epsilon_{zz} \right) \quad (3.63)$$

$$\tau_{xy} = \frac{E}{2(1 + \nu)} (\epsilon_{xy} + \epsilon_{yx}) \quad (3.64)$$

$$\tau_{xz} = \frac{E}{2(1 + \nu)} (\epsilon_{xz} + \epsilon_{zx}) \quad (3.65)$$

$$\tau_{yz} = \frac{E}{2(1 + \nu)} (\epsilon_{yz} + \epsilon_{zy}), \quad (3.66)$$

where ϵ_{ij} is the strain in the i by the j direction as specified and V is the sum of the strains in the three Cartesian directions (xx,yy and zz).

Other authors in this field of study use slightly different means to calculate the stress tensors such as Cianetti et al. (2005) who use a finite element modelling procedure to model the stress changes and surface deformations over the 1992 Landers and 1999 Hector Mine earthquakes. Another example is Broichhausen et al. (2015) from Midland Valley who implemented elastic dislocation modelling into the Move software suite.

With the normal and shear stress fields calculated in the Cartesian coordinate system, consideration must be taken of the angle of the fault plane for which is to be studied. For equation 3.60 to be valid, King et al. (1994) states the value of τ_β must always be positive. Resolving stresses onto a plane may result in positive or negative values depending on whether the potential for slip is in a right- or left-lateral direction. So the sign of τ_β must, therefore be chosen appropriately. King goes on to say that if the failure plane is orientated at β to the σ_1 axis the stress components applied to it in terms of the principal stresses are :

$$\sigma_\beta = \frac{1}{2}(\sigma_1 + \sigma_3) - \frac{1}{2}(\sigma_1 - \sigma_3)\cos 2\beta \quad (3.67)$$

$$\tau_\beta = \frac{1}{2}(\sigma_1 - \sigma_3)\sin 2\beta, \quad (3.68)$$

where σ_1 is the greatest principal stress and σ_3 is the least principal stress. If equations 3.67 and 3.68 are substituted into 3.60 it becomes :

$$\sigma_f = \frac{1}{2}(\sigma_1 - \sigma_3)(\sin 2\beta - \mu \cos 2\beta) - \frac{1}{2}\mu(\sigma_1 + \sigma_3) + \mu p. \quad (3.69)$$

To orientate the stresses calculated from the elastic half space modelling from a Cartesian coordinate system into the principal stress directions for use with equation 3.69 the following set of equations are used,

$$\sigma_{11} = \sigma_{xx} \cos^2 \psi + 2\sigma_{xy} \sin \psi \cos \alpha + \sigma_{yy} \sin^2 \psi \quad (3.70)$$

$$\sigma_{33} = \sigma_{xx} \sin^2 \psi + 2\sigma_{xy} \sin \psi \cos \psi + \sigma_{yy} \cos^2 \psi \quad (3.71)$$

$$\tau_{13} = \frac{1}{2}(\sigma_{yy} - \sigma_{xx}) \sin 2\psi + \tau_{xy} \cos 2\alpha. \quad (3.72)$$

Where ψ is the angle of the plane from the x-axis and σ_{ij} and τ_{ij} are the stresses calculated from the elastic half-space modelling described in equations 3.61 to 3.66. This geometry is illustrated in figure 3.15.

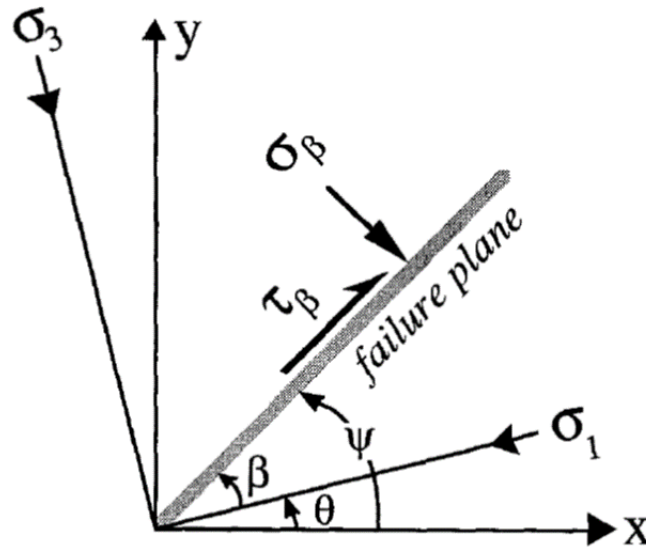


Figure 3.15: The axis system used for calculations of Coulomb stresses on optimum failure planes. Compression and right-lateral shear stress on the failure plane are taken as positive. The sign τ_β is reversed for calculations of left-lateral movement. Taken from King, 1994

With stresses orientated in the principal stress directions, to calculate the change in Coulomb stress for a vertical strike-slip fault, the change of Coulomb stress for right-lateral σ_f^R and left-lateral σ_f^L motion on planes orientated at ψ with respect to the x-axis are,

$$\sigma_f^R = \tau_{13}^R + \mu' \sigma_{33} \quad (3.73)$$

$$\sigma_f^L = \tau_{13}^L + \mu' \sigma_{33}, \quad (3.74)$$

where μ' is the effective coefficient of friction defined by,

$$\mu' = \mu(1 - B) \quad (3.75)$$

and B is the Skempton coefficient and varies between 0 and 1 and represents the pore-pressure. The results for this calculation are shown visually in figure 3.16 and show that to the North and South of the fault line there is a increase in the Coulomb stress change. This kind of investigation would be suitable for segments along a known strike-slip fault, e.g. the San Andreas fault as the regional stress field or preexisting stress fields from other events are not required.

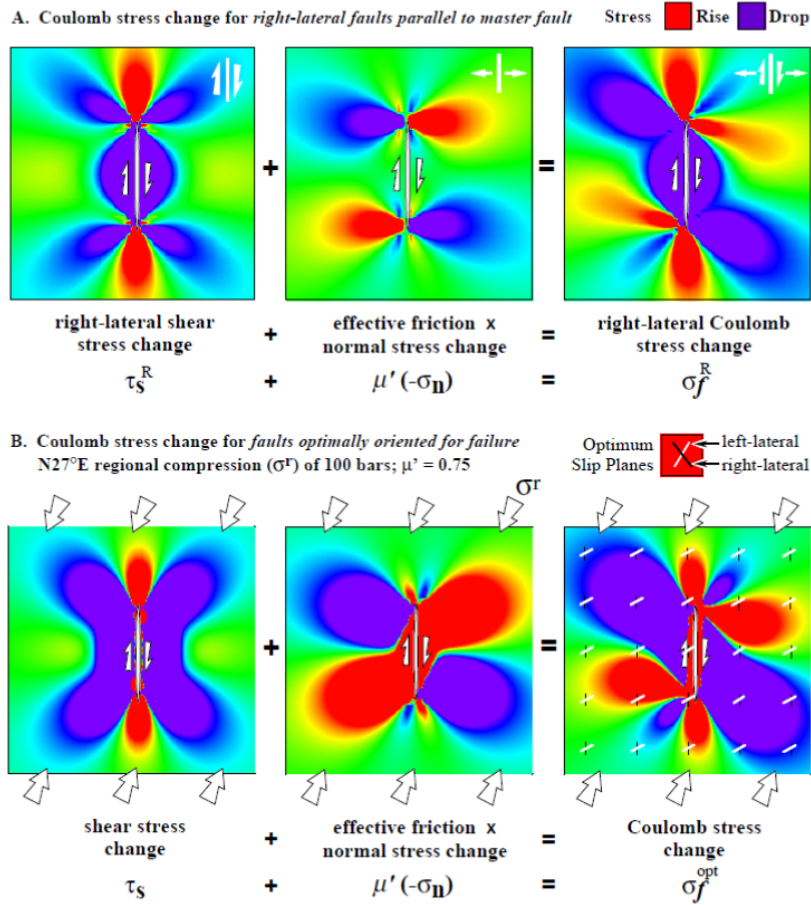


Figure 3.16: Graphical representation of the two equations used to calculate the Coulomb stress change, A) a source-receiver combination of faults and B) optimally orientated faults. The regional stress field in this situation alters the magnitude of the Coulomb stress change. Taken from King, 1994

It would be more useful in the context of hazard prediction to calculate the Coulomb failure function for possible future failures at unspecified orientations. The method by which King et al. (1994) handles this is to consider that the maximum Coulomb stress changes occur along the axis of the master fault line. There is a presumption that there exists a sufficient number of small faults with all possible orientations at all locations, and that once the maximum stress occurs one of these small faults, which is optimally orientated to the master fault direction, will then slip. The optimum directions are determined not only by the stress change due to one earthquake but also the regional stress direction. These terms can be combined into the following to

give the total stress σ_{ij}^t ,

$$\sigma_{ij}^t = \sigma_{ij}^r + \sigma_{ij}^q, \quad (3.76)$$

where σ_{ij}^r is the regional stresses and σ_{ij}^q stress from the earthquakes. The orientation of the principal axes resulting from the total stress is therefore derived using,

$$\theta = \frac{1}{2} \tan^{-1} \left(\frac{2\sigma_{xy}^t}{\sigma_{xx}^t - \sigma_{yy}^t} \right), \quad (3.77)$$

where θ is the orientation of one principal axis to the x-axis and the other is at $\theta + 90$ degrees. From these two directions, the angle of greatest compression θ_1 must be chosen and the optimum failure angle α_0 is given by $\theta_1 \pm \beta$. With the optimum failure angle determined from the total stress σ_{ij}^t the normal and shear stress changes on the planes are determined only by the earthquake stress change, σ_{ij}^q component of equation 3.76. The Coulomb stress change calculations then become,

$$\sigma_{33} = \sigma_{xx}^q \sin^2 \alpha_0 - 2\sigma_{xy}^q \sin \alpha_0 \cos \alpha_0 + \sigma_{yy}^q \cos^2 \alpha_0 \quad (3.78)$$

$$\tau_{13} = \frac{1}{2} (\sigma_{yy}^q - \sigma_{xx}^q) \sin 2\alpha_0 + \tau_{xy}^q \cos 2\alpha_0 \quad (3.79)$$

which are substituted into the Coulomb stress change equation as

$$\sigma_f^{opt} = \tau_{13} - \mu' \sigma_{33}, \quad (3.80)$$

where μ' is the effective coefficient of friction defined in equation 3.75.

Figure 3.16 shows the 2D Coulomb stress change for these two scenarios, the first a receiver fault aligned parallel to the master fault and the second optimum slip planes with a regional compression of 100 bar. This figure shows that the regional stress field doesn't change the arrangement of the lobes of stress rise or drop but serves to increase the magnitude of the stress change. The optimally orientated planes implies that failure is increasingly likely to occur in the areas of stress rise following one of the two optimum slip plane directions.

In the previous calculations the assumptions are that the faults involved are vertical on a 2D horizontal slice. This means that the stress components of σ_{zz}, σ_{xz} and σ_{yz} were neglected. Once this calculation moves to a 3D dimensional case and strike-slip and dip-slip faults are taken into account the ratio of stress magnitudes must be taken into account. As detailed by King et al, the parameters required are 1) the relative magnitude of the vertical stress σ_{zz}^r relative to the horizontal regional stresses and 2) the ratio of the vertical to horizontal stresses. An example of this interaction by dip-slip faults and the calculated Coulomb stress change is shown as figure 3.17 for a thrust fault. This shows that for a square source (a L/W ratio of 1) there is a

1-bar increase of stress increase over a similar size adjacent patch and that if the fault geometry changes to a rectangular fault this is spread over a larger area.

These calculations form the basis for the Coulomb 3 software. The required information to be entered for this software package are 1) the geometry of each fault including slip distance, 2) the focal mechanism for each fault, 3) the regional stress components including the vertical and horizontal stress gradients and 4) the elastic parameters for the study area.

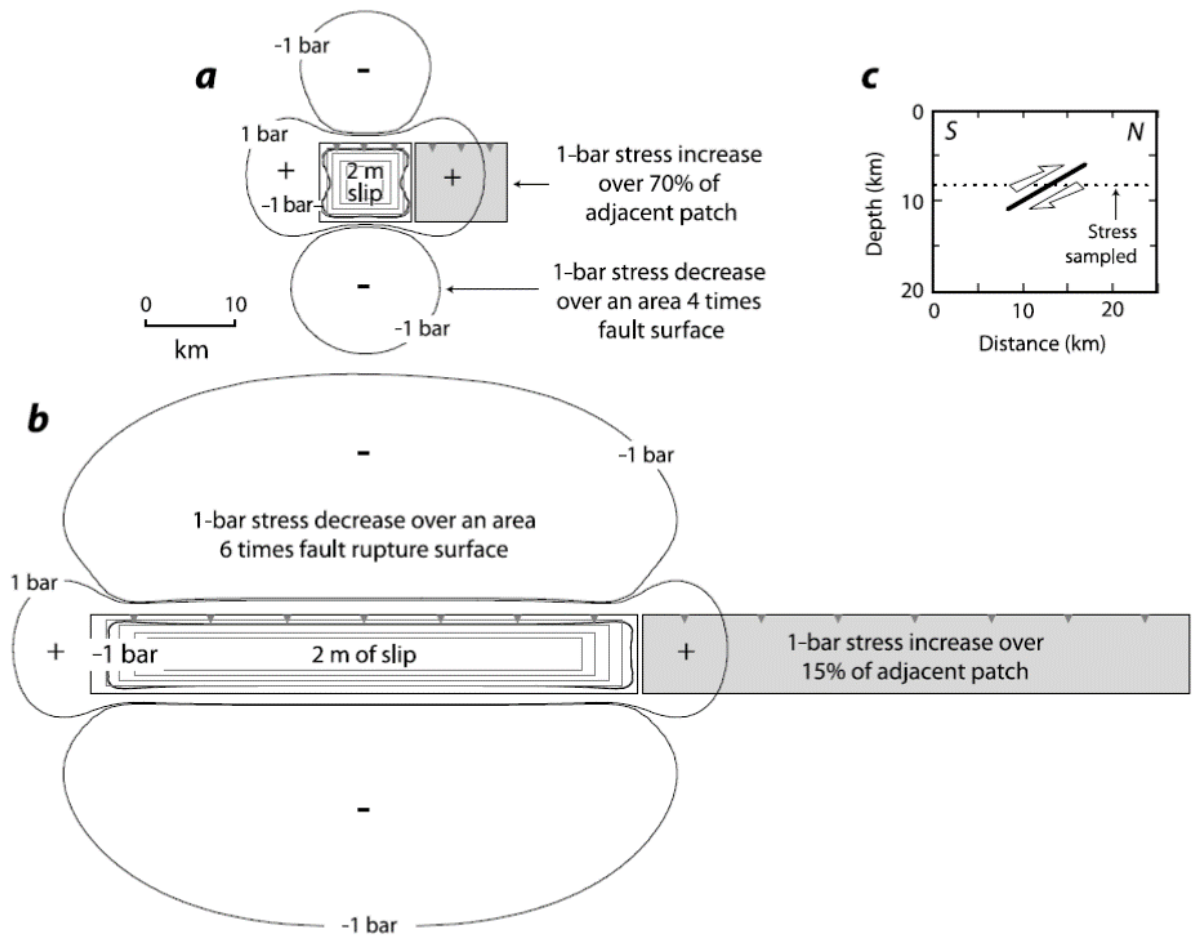


Figure 3.17: Triggering of a 30 degree dip thrust earthquake on an adjacent patch of similar size along strike. A) for a square source with a stress drop of 60 bar increases the stress adjacent to the earthquake by 1 bar for a similar size patch. B) for a rectangle event with a stress drop of 47 bar, only a area 15 m² of the adjacent similar size patch experiences the 1 bar stress increase. C) shows the cross-section this slice is taken from. Taken from Lin et al. (2011)

This software has been used in many seismic hazard studies including Toda et al. (2005) who created animations of the evolution of the stress transfer for a 17 year period on the San Andreas fault using Coulomb 3 for the purposes of forecasting earthquakes $M_w > 5$ in the period 2003-2015 and Xu and Xu (2012) who used it to model the triggering potential caused from the Bam (M_w 6.6) and Wenchuan earthquakes (M_w 7.9). For scales closer to the microseismic level, this approach has been used in mining-induced seismicity in Orlecka-Sikora (2010) which showed that stress transfer can accelerate the mining-induced seismicity generation. The underlying assumptions with this approach and software are, 1) uniform elastic properties, 2) pore pressure change is proportional to the fault-normal stress with the Skempton coefficient B , 3) uniform regional stress components over the study area. An example from hydraulic fracturing operations was from Schoenball et al. (2012) who develop a method based on the King et al. (1994) calculations of optimum orientated fault planes to analytically compute the coseismic change of Coulomb stress at the Soultz-sous EGS project. None of these above software solutions strays from the assumption of pore pressure proportionality to the fault-normal stress. While Kettlety et al. (2018) use variations of the Skempton coefficient to vary the significance of the pore pressure component to model injection-related induced seismicity this is still a uniform static value which doesn't vary with time (and therefore drainage variations). The study by Cocco and Rice (2002) implemented a Skempton tensor for analysis of the anisotropic variation in the pore pressure.

3.8 Methods to be used and planned software system

This chapter has focussed on reviewing the methods from literature used to analyse microseismic signals to determine parameters of a fracture network. To build a software system that can forecast induced seismicity, a combination of the methods outlined in this review will be used. The requirements for the system as discussed in the previous chapter are that they should be :

1. Capable of monitoring for hydraulic connections from the well bore activating fault lines
2. Capable of monitoring for static stress transfers triggering seismic events
3. Capable of running in real-time

To fulfil requirement 2, the Coloumb failure function will be calculated on an event by event basis as each event is detected, in part similar to the method shown in Toda

et al. (2005). In order to do this, the focal mechanism, source geometry and slip magnitude for each event are required. Therefore an inversion to the full moment tensor is required for both requirements 1 and 2. Inverting for the full moment tensor requires either using a method which is based on the amplitude of a single time sample of the P- and S- wave arrivals or making full use of the waveform. The issues with solving for the moment tensor using only single amplitude points as discussed in section 3.3.3 preclude using this type of method, so for this reason a full waveform inversion method will be utilised. The problems with the mathematical ambiguity, when the moment tensor is decomposed, can be resolved by using the directional information provided from the pulse variations methods to eliminate one of the two possible solutions. As a verification check as to the kinematics involved in the event slip, the P to S wave energy ratio shown by Kwiatek and Ben-Zion (2013) will be used to determine the tensile/shear forces involved in the rupture.

Of the methods discussed in this review, the one type of method that cannot be used in this type of software system is shear wave splitting methods, as this method cannot be implemented in real-time. Shear wave splitting methods as detailed in section 3.4 rely on sets of data points, rather than a point by point basis, which are then inverted for a set of fracture parameters for an area. While there is potential to discern fracture directions from opening fractures that are otherwise undetectable, as more and more events are recorded the output result will vary as the monitoring period continues. This requirement also means that frequency domain based methods that use variations in the pulse length to determine fracture direction, those by Tomic et al. (2009) and Kane et al. (2013), also cannot be used as these use smaller, or clusters of, events to remove attenuation effects from the calculations. For these reasons a method similar to that operated by Zollo and de Lorenzo (2001) will be utilised to determine fracture direction.

To conclude, figure 3.18 shows the work-flow of the software system. The established information and systems required for this software to work in the field in real-time are 1) that the velocity and attenuation models have already been determined and 2) that the microseismic event has already been detected and positioned by a separate system.

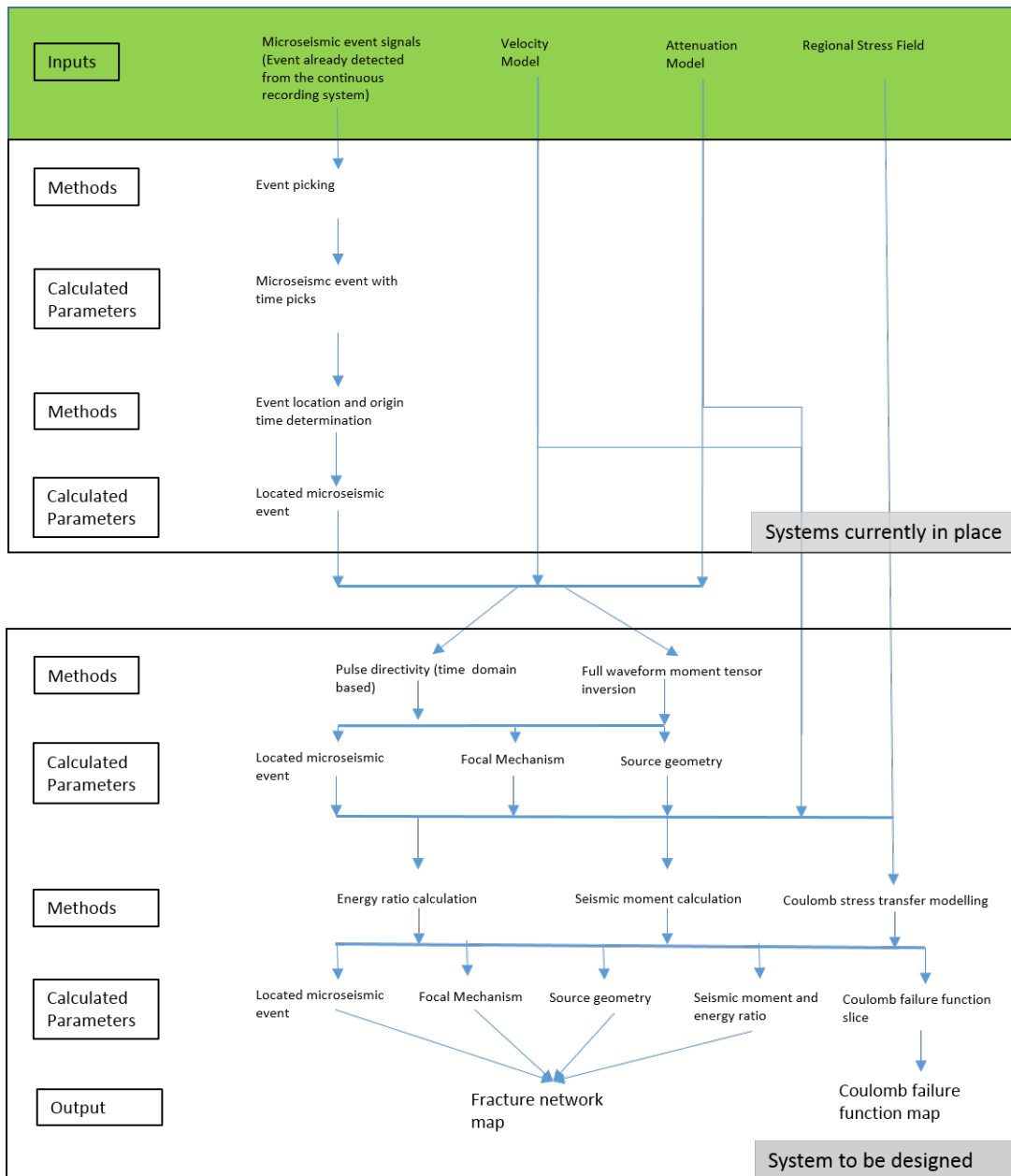


Figure 3.18: Flowchart of the method to be developed. The systems currently in place are those used by microseismic service companies to detect and position seismic events.

Chapter 4

Industrial Case Study

4.1 Introduction

For the development of a viable software system to investigate in real-time if seismicity caused by hydraulic fracture operations can be forecast using microseismic analysis, a real world case study where seismicity has been attributed to the well operations is required. Ideally, such a microseismic dataset will have acquired microseismic signals prior to the start of hydraulic process, until after the felt induced event occurs such that the ability of a software solution to forecast induced seismicity can be tested.

To this end, a micro-seismic dataset was supplied by an industrial contact from a production shale gas site in Fox Creek in the Alberta Providence, Canada. This dataset consists of microseismic readings acquired during production of a single horizontal well, the Wahigan well, which was suspended on 12 January 2016 due to detection of an Mw 4.8 magnitude seismic event located within 5 km of the well site. After investigations by multiple authors (Schultz et al., 2017) and Wang et al. (2016) and the regulatory authority (AER), it was considered that production at the Wahigan well was the cause of this event. The aim of this chapter is to fully review the background of this site, including the geological and production history of the well and the microseismic survey that was conducted at the site at that time.

4.2 Location and Geological background of the Wahigan well

The Wahigan well is located 54 km west of Fox Creek in the Alberta Providence, Canada at 54° 25' N, 117° 18' W . This location is shown as figure 4.1.

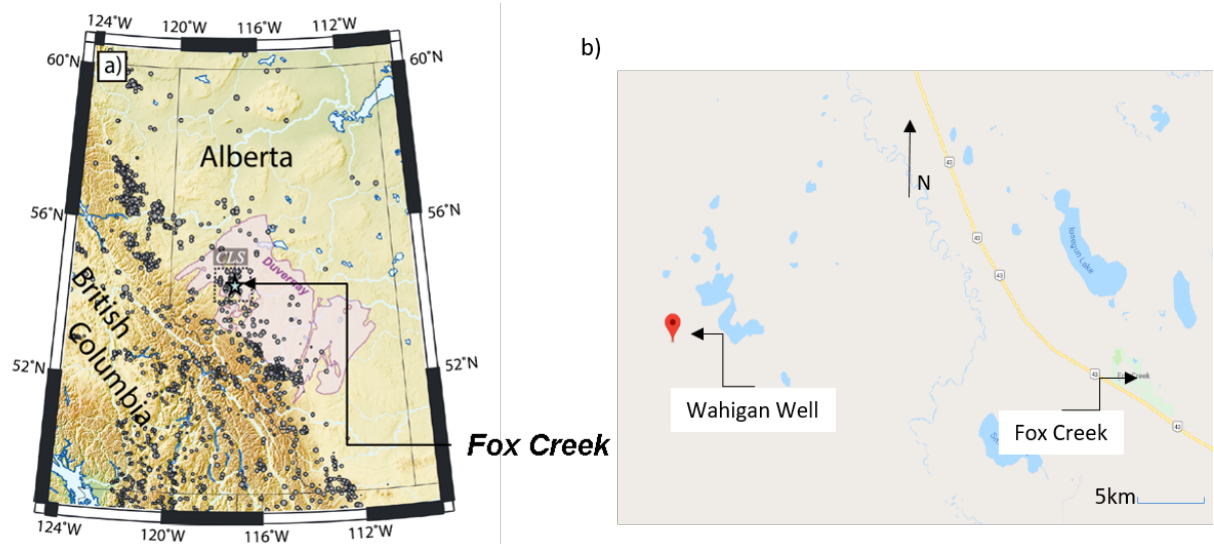


Figure 4.1: The location of the Wahigan well in the Alberta province, Canada and the extent of the Dunverney formation. Left image from Schultz et al. (2017). Right image from Google 2019

The drilling target for the Wahigan well is the Dunverney formation, within the Western Canada Sedimentary Basin. This is an organic-rich shale that is a proven source rock for conventional oil and gas reservoirs (Stoakes and Creaney, 1984). This formation is considered to be Alberta's foremost unconventional shale resource (Preston et al., 2016) with proven remaining reserves of 354 MMboe and probable reserves of 395 MMboe as of December 2016.

4.2.1 Geological history of the Dunvernay formation

The Dunvernay formation is a siliceous to calcareous, organic-rich mudstone that is a depositional unit within the Woodbend-Winterburn group (Switzer et al., 1994). The Woodbend-Winterburn group stratigraphy is shown as figure 4.2.

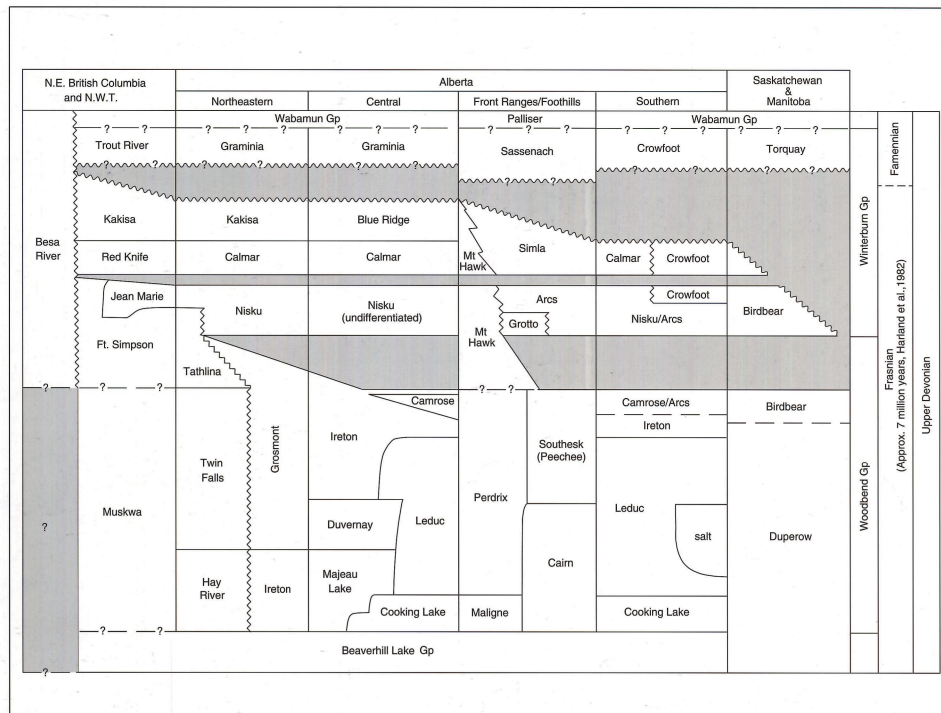


Figure 4.2: The stratigraphy of the Woodbend-Winterburn group of Alberta. Image from Switzer (1980)

The geographical extent of the Western Canada Sedimentary basin and the generalized thickness of both the Woodbend and Winterburn parts of the group in this basin, as determined by a set of control wells, is shown as figure 4.3.

During the early phases of the Woodbend group deposition in the Frasnian, late Devonian period, the Western Canada Sedimentary basin underwent gradual deepening. This deepening resulted in the deposition of a thick aggradational succession of carbonates. At the end of the Woodbend deposition, during periods of a reduced rate of subsidence and/or sea-level fall, most of the basin was filled by mudstones (Switzer et al., 1994). This process occurred within the Frasnian stage, part of the upper Devonian period. As noted by Switzer et al. (1994) the accumulation rate into this basin at this time was the highest compared to all other Paleozoic periods as a result

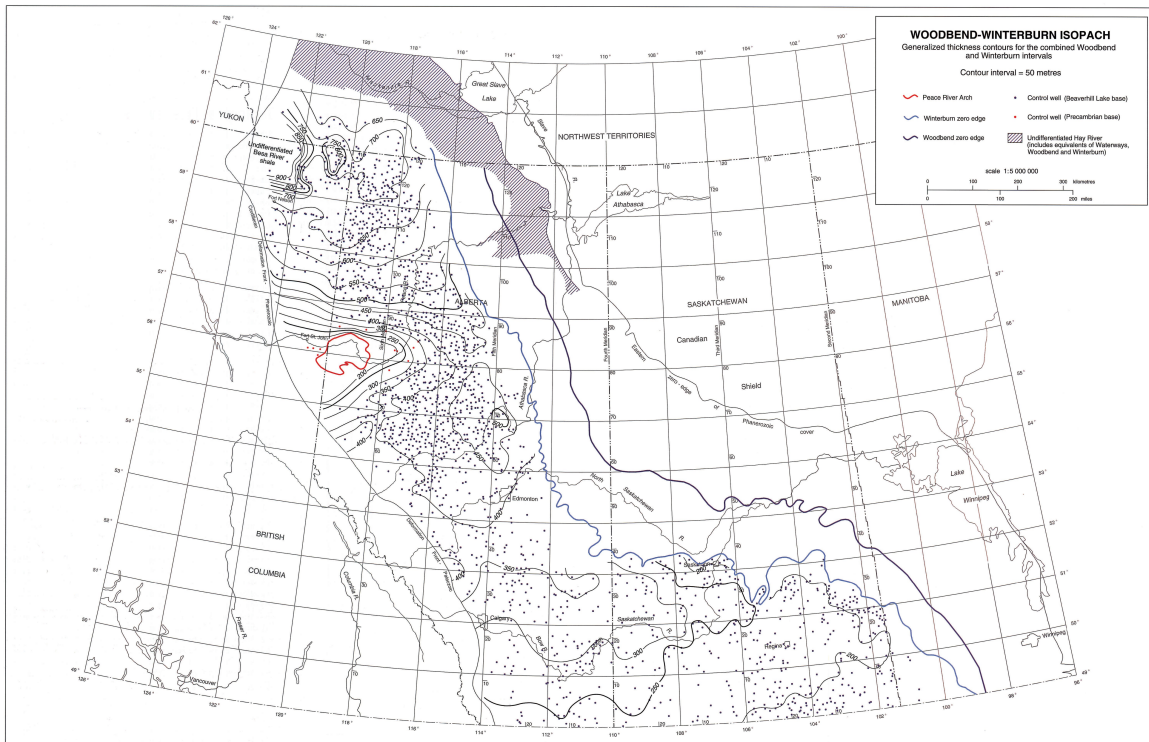


Figure 4.3: The extent of the Woodbend and Winterburn group in the Western Canada Sedimentary Basin. Image from Switzer (1980)

of the interplay between the eustatic sea-level changes, rapid sedimentation and basin subsidence.

As stated by Switzer et al. (1994) and Harris et al. (2018) the deposition of the Duvernay interval is as a result of profound change in the depositional environment in the basin as a cause of a major rise in sea level. The sequence is characterized by extensive basinal deposits, synchronous with a significant stage of Leduc reef growth similar to the underlying Majeau lake interval. The Dunvernay formation differs to the Majeau Lake formation as it consists of dark brown bituminous shale and limestone rather than the greenish-grey and brown shales. This difference in shale type represents a period of high accumulation rates in the basin and the preservation of the organic carbon, a factor influencing the hydrocarbon prospectivity of this formation. Switzer et al. (1994) associates this to a change in the stratification and oxygenation of basal waters during the maximum transgressive stage of the Woodbend group.

An investigation by Harris et al. (2018) developed a model for the accumulation of the organic carbon which ultimately leads to the hydrocarbon prospectivity of the

Dunvernay formation. Harris showed that the sea level rise at the beginning of the Duvernay deposition allowed an influx of nutrient-rich upwelled water to flow from the shelf into the basin when prior to this these organic mudstones were restricted to parts of the continental shelf. A model for the water circulation for the Alberta basin by Harris is shown as figure 4.4.

The conclusion of the deposition of the Duvernay formation ended this period of marine transgression with the sea level deepening to allow a stratified water column to develop over the entire basin. At this point the Ireton formation began to deposit, starting a period of basin shallowing and associated deposition of marine carbonates such as the Wabamun formation.

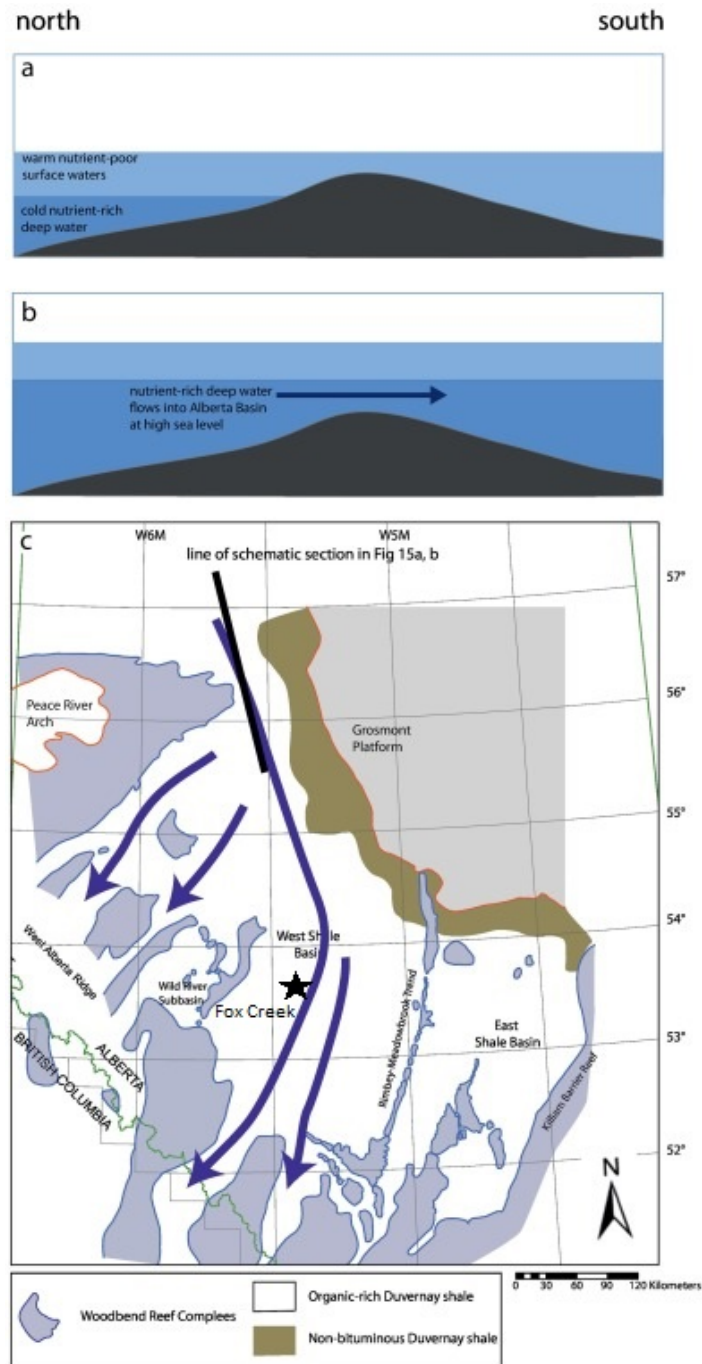


Figure 4.4: Model for water circulation into the Alberta Basin as developed by Harris et al. (2018). At low sea level (a), circulation of nutrient-charged cold deep water is blocked from entering the Alberta Basin. At higher sea level (b, c), cold deep water can cross a bathymetric sill between the Peace River Arch and the Grosmont Platform, stimulating bio-productivity in the Alberta Basin. Taken from Harris et al. (2018). The approximate location of the site is annotated on c).

4.2.2 Tectonic history of the Fox Creek area and current in-situ stresses

If the regional extent and geological timings of faults within the area are understood then this information can be used to conclude that hydraulic fracturing could potentially re-activate these faults resulting in felt seismicity on the surface. Unfortunately, there is little information regarding the faulting within the Fox Creek region.

Of the information available, a 3D regional structural geology model by Weides et al. (2014) covering a 90 x 70 km area centred 220 km to the north of Fox Creek in the Peace River area was developed using sets of 2D seismic lines and associated well information. While this model was not within the confines of the site, this structural model identified 9 fault zones. In particular, one normal fault, the ‘Tangent’ fault by Richards et al. (1990), extended from the Banff formation right through into the basement including the Ireton formation (the overlying formation to the Duvernay in the Fox Creek area). The existence of a fault of this age within the Western Canada Sedimentary basin indicates the possibility of posteriori structural movement projected within the Fox Creek region. Within the Fox Creek area an interpretation of a confidential 3D seismic dataset using the horizon slicing technique identified sets of lineaments within an interval just above the Duvernay. These lineaments couldn’t be categorised as faults as Chopra et al. (2017) notes as they are not visible on the seismic sections. This point is agreed by Eaton et al. (2018) who also note that while lineaments are visible along horizon slices on a different 3D seismic volume acquired from another confidential location near Fox Creek, these do not correlate to visible features on the seismic data. Although these features are not seen on the seismic data, Chopra et al. (2017) emphasis the point that the seismic acquisition set-up, e.g. bin size, may have a bearing on the ability to resolve small faults and these faults could still be reactivated from the hydraulic stimulation process.

A review of the current in-situ stress fields for the Western Canada Sedimentary Basin has been carried out by J.S. Bell (1994) using a collection of many techniques including well breakouts, hydraulic fracture orientations and over-coring measurements modelled the stress trajectories for the basin. This is shown graphically as figure 4.5.

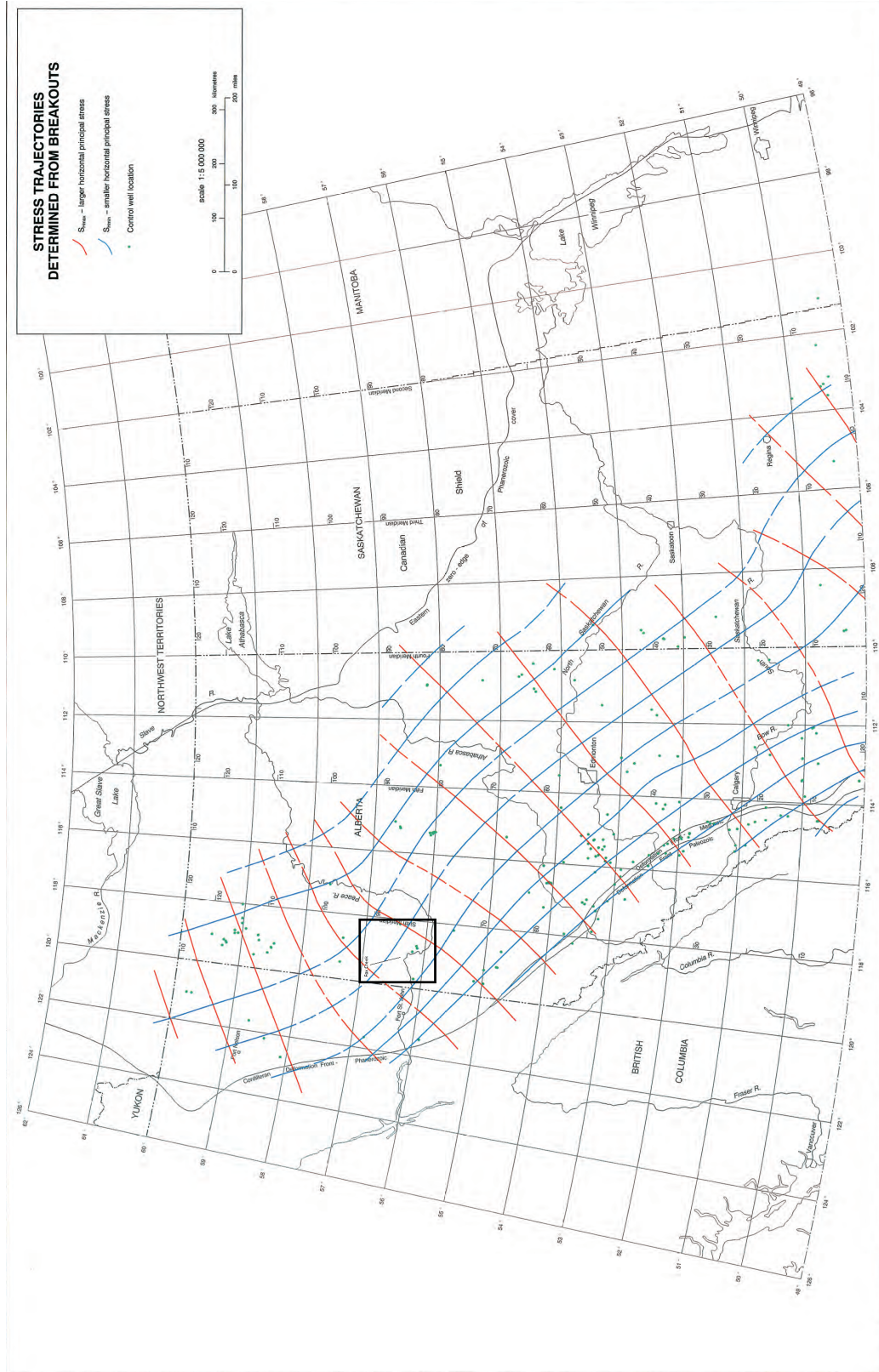


Figure 4.5: Stress trajectories for S_{Hmax} and S_{Hmin} as determined from the well breakouts for the Western Canada Sedimentary Basin. The Fox Creek area is annotated. Image from J.S. Bell (1994)

With reference to figure 4.5, the stress trajectory for SHmax varies gradually over the basin from 30 to 70 degrees and over the Fox Creek area, this figure is closer to 45 degrees. A paper by Shen et al. (2019) looks more closely at the Fox Creek area. Within this study, a model was developed to calculate the full stress tensor over the Duvernay formation in a 150 x 150 km grid centred on Fox Creek from the analysis of 20 borehole image logs. Using this information Shen et al. (2019) then calculates the magnitude of the three Andersonian stress vectors, SHmax, Sh, Sv and the pore pressure component Pp. This study found that “The observed PP all substantially exceed those anticipated from a normal hydrostatic (water) gradient of 9.8 kPa/m that assumes continuous hydraulic conductivity from depth to the surface; and, indeed, even exceed the expected wellbore fluid pressure Pw with gradients bounded below 14 kPa/m due to high mud densities reported (Shen et al., 2019)”. This report also found that the tangent gradients of the horizontal stresses are higher than the stress-to-depth ratios in this area. These values, and the pore pressure component, in particular, indicate that the balance of forces on fault lines within the Duvernay formation could be reactivated by further increases to pore pressure, invoked by hydraulic fracturing.

These results were gridded into surfaces over the full study area of 150 x 150 km allowing the principal stress directions and magnitude to be calculated for any latitude and longitude within this area of which the Wahigan site resides. Since a pre-requisite for the software system is knowledge of the regional stress directions and magnitudes, these were determined from this study for the Wahigan site and are listed below :

1. SH direction, 40 degrees azimuth, SH magnitude 110×10^5 Pa
2. Sh direction, 130 degrees azimuth, Sh magnitude 32×10^5 Pa
3. Sv direction, 90 degrees azimuth / 90 degrees plunge, Sv magnitude 58×10^5 Pa

4.3 Production timeline and occurrence of the 12 January induced seismic event at the Wahigan well site

This section reviews the production timeline of the Wahigan well from the pilot well to the production horizontal well along with parameters of the pressure and frac fluid used in the hydraulic fracturing operations. Finally, this section will detail the reported facts accompanying the 12 January 2016 induced seismic event with a comparison to other induced events reported around the world.

Drilling started for pilot well (Talisman HZ WAHIGAN 15-7-22-63) on the 14 August 2014 (Spud date) and completed on 20 September 2014. The well was drilled vertically to a final depth of 3465 m TVD and wire line logged on 2 September 2014. Wireline surveys included sonic, density, resistivity and spontaneous potential tools.

Three horizontal wells were drilled from this vertical well bore designated well pad 10-06. Horizontal drilling started on the well of interest, 15-25-62-23, on 9 October 2015 and completed on the 17 November 2015. This was wire line logged on the 12 November 2015.

A total of 30 hydraulic fracture stages were planned, starting on 4 January 2016. First the well bore was perforated at the appropriate stage using three perforation guns and plugged with a packer. Once perforated, frac fluid was pumped through this perforation at an average flow rate of 8 m³/min and an average pressure of 59,500 to 71,300 kPa. The solid component of the frac fluid was a combination of sand and HYDROPROP, a ceramic proppant and from stage 2 of the process, these components weighed 5,146 kg and 145,850 kg respectively. The fluid component of the frac fluid comprised of, using stage 2 as an example, 1350 m³ of clean fluid with 8 m³ of 15 % hydrochloric acid. Table 4.1 and figure 4.6 show the pumping times for each of these stages and the flow rate applied to the formation at each stage respectively.

Table 4.1: Table of the hydraulic fracture operations conducted at the Wahigan site.

Hydraulic Fracture Stage	Start Date/Time	End Date/Time
Stage 1	04/01/2016 18:02	04/01/2016 20:47
Stage 2	05/01/2016 04:13	05/01/2016 07:33
Stage 3	05/01/2016 12:00	05/01/2016 02:56
Stage 4	05/01/2016 20:35	05/01/2016 23:28
Stage 5	06/01/2016 03:31	06/01/2016 06:30
Stage 6	06/01/2016 10:21	06/01/2016 13:13
Stage 7	06/01/2016 16:39	06/01/2016 19:50
Stage 8	06/01/2016 23:19	07/01/2016 02:02
Stage 9	07/01/2016 21:33	08/01/2016 00:25
Stage 10	08/01/2016 03:34	08/01/2016 06:23
Stage 11	08/01/2016 09:30	08/01/2016 12:23
Stage 12	08/01/2016 15:30	08/01/2016 18:16
Stage 13	08/01/2016 21:23	09/01/2016 00:00
Stage 14	09/01/2016 02:55	09/01/2016 05:40
Stage 15	09/01/2016 16:52	09/01/2016 20:14
Stage 16	09/01/2016 23:31	10/01/2016 02:09
Stage 17	10/01/2016 05:33	10/01/2016 08:20
Stage 18	10/01/2016 11:02	10/01/2016 13:43
Stage 19	10/01/2016 16:20	10/01/2016 19:05
Stage 20	10/01/2016 21:47	11/01/2016 00:43
Stage 21	11/01/2016 07:17	11/01/2016 09:55
Stage 22	11/01/2016 12:25	11/01/2016 15:06
Stage 23	11/01/2016 17:37	11/01/2016 20:18
Stage 24	11/01/2016 22:45	12/01/2016 01:11
Stage 25	12/01/2016 04:21	12/01/2016 06:55
Stage 26	12/01/2016 09:53	12/01/2016 11:34

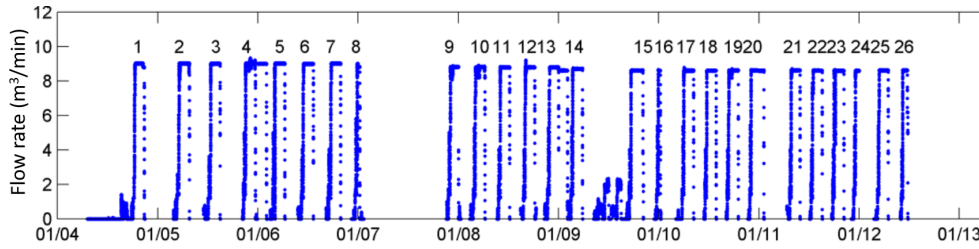


Figure 4.6: Pressure routine applied to the formation during the hydraulic fracture operation. Image from microseismic processing report (Contractor B, 2016)

4.3.1 Seismic event detected on 12 January 2016

During the hydraulic fracturing stage 26 on the 12 January at 18:27, a large seismic event was detected by the teams on site, at a level of Mw 4.8, within 5 km of the well and felt on-site by company personal (Mageau, 2016). This exceeded the limit of seismicity as set by the AER (Alberta energy regulator) of Mw 4.0 (Subsurface Order No. 2, Parks et al. (2015).

In accordance with Subsurface Order No. 2, operations were suspended at the site. The frac fluid used during the current stimulation stage was shut in and the wellbore was flushed with 51m³ of fluid. The hydraulic fracture and wireline drilling equipment was removed from the borehole and operations suspended pending approval from the AER to continue.

The magnitude of this event, as reported to the AER, was later revised down from Mw 4.8 to Mw 4.1 (Schultz et al., 2017). This event was the largest induced seismic event detected since the start of the extraction of shale gas from this formation in June 2010 (Schultz et al., 2017). This event is shown on a distribution of seismic magnitudes compared with date detected as figure 4.7. Some of the seismic events detected shown in figure 4.7 have been grouped together by the different hydraulic fracture sites operating at the time, with the Waighan well assigned to group SS17, highlighting the context of this event in comparison to other events detected in the area.

In comparison with other induced seismic events worldwide, this event is in the top 50% of induced seismicity magnitudes for shale gas extraction, with the lowest being the events associated with the Preese Hall operations in Blackpool, UK at Mw 2.3 (Clarke et al., 2014) in 2012 followed by operations conducted in south-central Oklahoma, USA (Ellsworth, 2013) at Mw 2.9. The largest magnitude event associated with shale gas extraction is from the Sichuan Basin, China where five events exceeded Mw 4 with the highest at a level of Mw 4.7 (Lei et al., 2017).

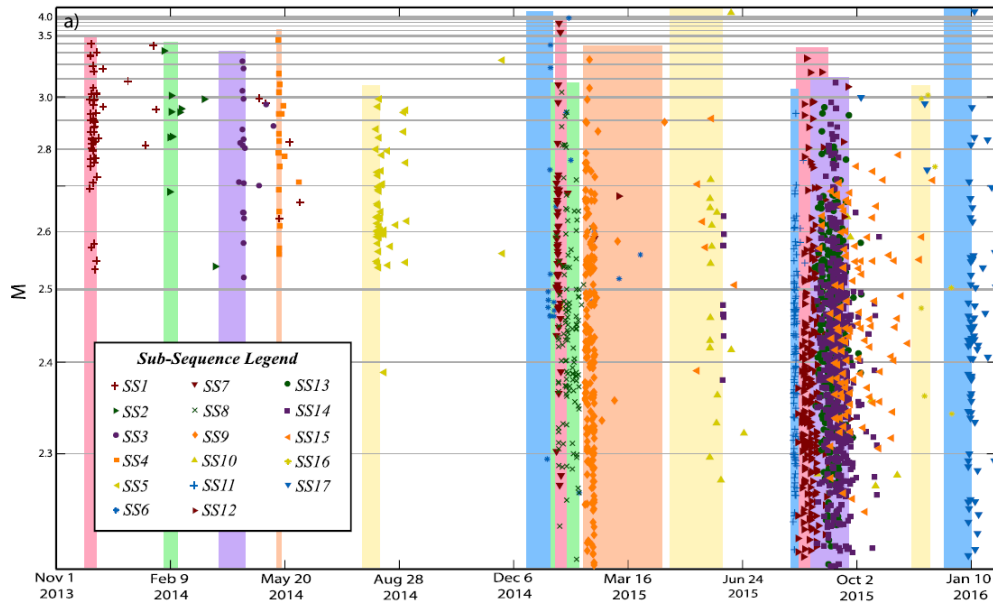


Figure 4.7: Timing and scaled magnitudes of earthquakes near Fox Creek with colour coded groupings associated with hydraulic fracture operations in the area. Image from Schultz et al 2017

4.4 Microseismic data acquisition conducted at the Wahigan well

The microseismic data at this site were acquired using a 96 station surface array. The majority of these stations consisted of a 30 m deep borehole with a permanent installation of orthogonal three-component geophone assembly fixed at the bottom of the borehole and two shallow single component geophones deployed above. A schematic of the geophone installation is shown below as figure 4.8, note the steel rebar fixing the deepest geophone in place and rope linking the other geophones together.

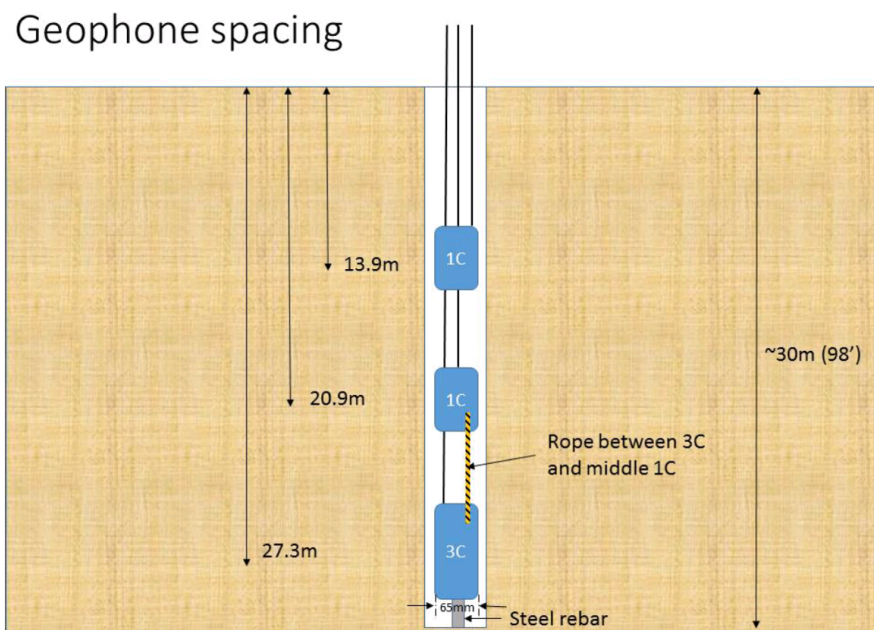


Figure 4.8: Geophone deployment in each seismic station of the surface array

While the majority of geophone stations consisted of this borehole geometry, 5 stations were fitted with different geometries, consisting of a set of geophones placed on the surface which were summed together to form a single trace. Stations 37, 38 and 49 had a single geophone close to the borehole and a set of 12 geophones placed at 1.5 m intervals alongside the boreholes with geophone 6 centre on the borehole. Stations 58 and 61 had two sets of 12 geophones at 1.5 m intervals either side of the boreholes. Station 88 had 24 geophones placed at 0.75 m intervals along one side of the borehole. The traces were summed together to form a single trace recorded in the data file.

The polarity of the array was designed to meet the SEG standard, with a physical tap to the sensor from the bottom on the vertical component and on the back of the horizontal component resulted in a negative first break on the recording system and a negative number in the recorded file. The geophones used in the array were the GS-One 592 geophones by Geospace Technologies. A poles and zeros file describing the instrument effect for the GS-One 592 geophone was also available.

The microseismic surface array acquired signals from the period of 29th December 2015 to 15th January 2016. Contractor A processed the microseismic data from the period 5th to 14th January 2016. Contractor B processed the microseismic data from the period from January 04, 2016 to January 12, 2016. Neither contractors processed the data in real-time, contractor A processed the data between February - May 2016 and contractor B completed the processing of the data a year later on the 2nd May 2017. Both contractors provided processing reports, seismic event catalogues, velocity models and interim reports as part of the data package provided.

Data quality was variable from this case study. It was difficult to identify the first arrivals on some events due to a low signal to noise ratio. Other events had a much higher signal to noise ratio and the first arrivals were clearly identifiable. These records are shown in figure 4.9.

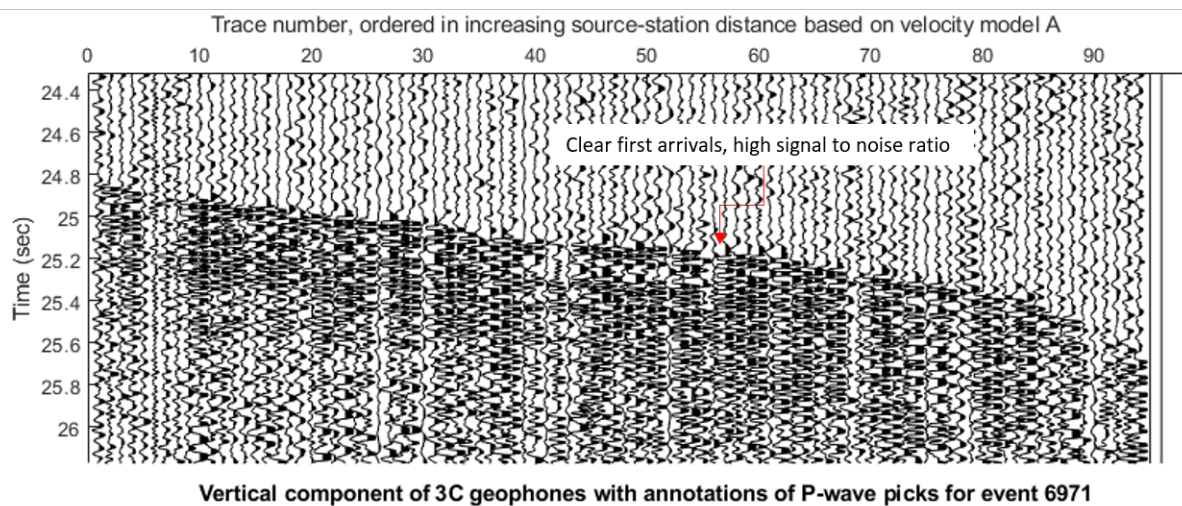
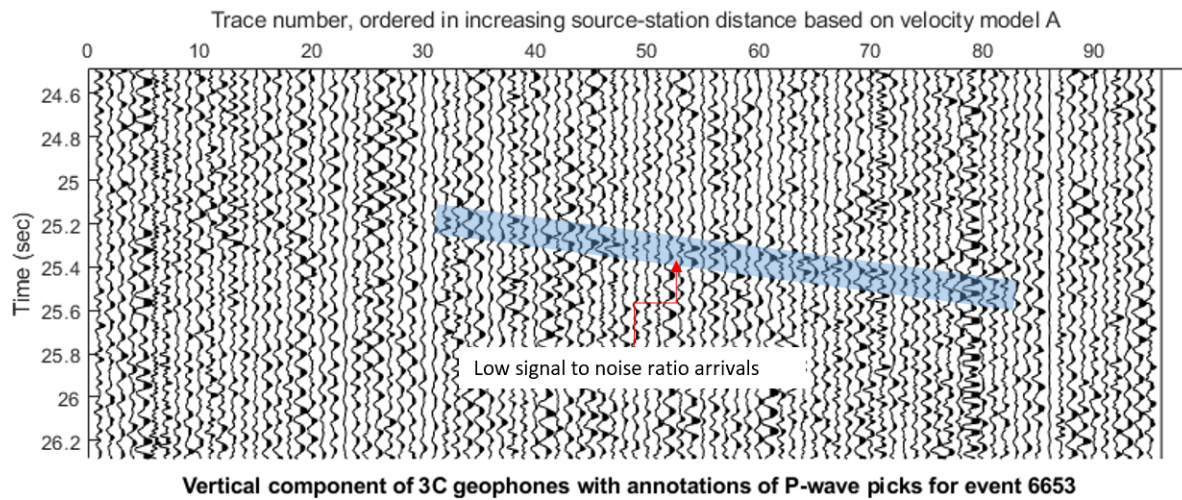


Figure 4.9: Data quality examples from the microseismic acquisition. Top, a poor signal to noise ratio event where the first arrivals are visible on a few stations. Bottom, a high signal to noise ratio event where the first arrivals are visible on all the stations.

4.4.1 Microseismic processing conducted by the contractors at the Wahigan well

The contractors processed the data using their own proprietary software, but fundamentally both software packages are designed using similar principles. Both packages are designed to automatically detect and position the microseismic events within the data acquisition time window.

Contractor A used an approach described as template relative migration. Bardainne et al. (2016) details that the migration operation is undertaken via cross-correlation with one (or several) template event(s) recorded. On this dataset five events were picked as the templates, these templates are then adjusted using the velocity for each possible point within a defined search space. The raw input data is then correlated with these template picks adjusted for each point in space. If the correlated raw data is stacked and exceeds a certain threshold, an event candidate is identified at the defined location (Bardainne et al., 2016). No individual picks for each channel are recorded during this process.

The algorithm used by contractor B is a model-based, scanning algorithm that searches the continuous data for the times and locations of microseismic events. The travel-times for every point on the grid are forward modelled using the chosen velocity model to create a travel time look-up table. The raw data was then stacked with all possible positions at an interval of 10 seconds with an overlap of 1s using the travel time corrections as determined from the travel time look-up table. If this stacked point exceeds a certain value then it is registered as an event at that position and time, again no individual picks for each channel are recorded during this process. Further details of this can be found in Kao and Shan (2004). The differences between these methods are that Contractor A minimises the amount of processing to be undertaken by comparing the raw data to the template picks and then searching in space close to the nearest template event. Contractor B, on the other hand, calculates the possible position and origin time for every event by looking at every possible space coordinate.

Both contractors utilise the sonic velocity log measured from the vertical borehole (15-7-22-63). To smooth the sonic velocity log, contractor A used a long averaging window in the region of 250 m compared to the smoothing function applied by Contractor B with a window of 50 m. During the velocity model development process and positioning, contractor A found that the position of the perforated shots deviated from the known well log positions. To remedy this, contractor A uses the theoretical ray-traced times from the templates compared to the picked arrival times and calculated the average adjustment to the velocity model required to best fit these 5 templates

to the data. This was a factor of 6.5%. Application of this factor reduced the positional error on the perforation shots to $dX = 6.68$ m, $dY = 26.81$ m and $dZ = 25.62$ m. Contractor B in comparison did not alter the velocity model from what was measured by the logging tool. Figure 4.10 shows the two velocity models used in the processing.

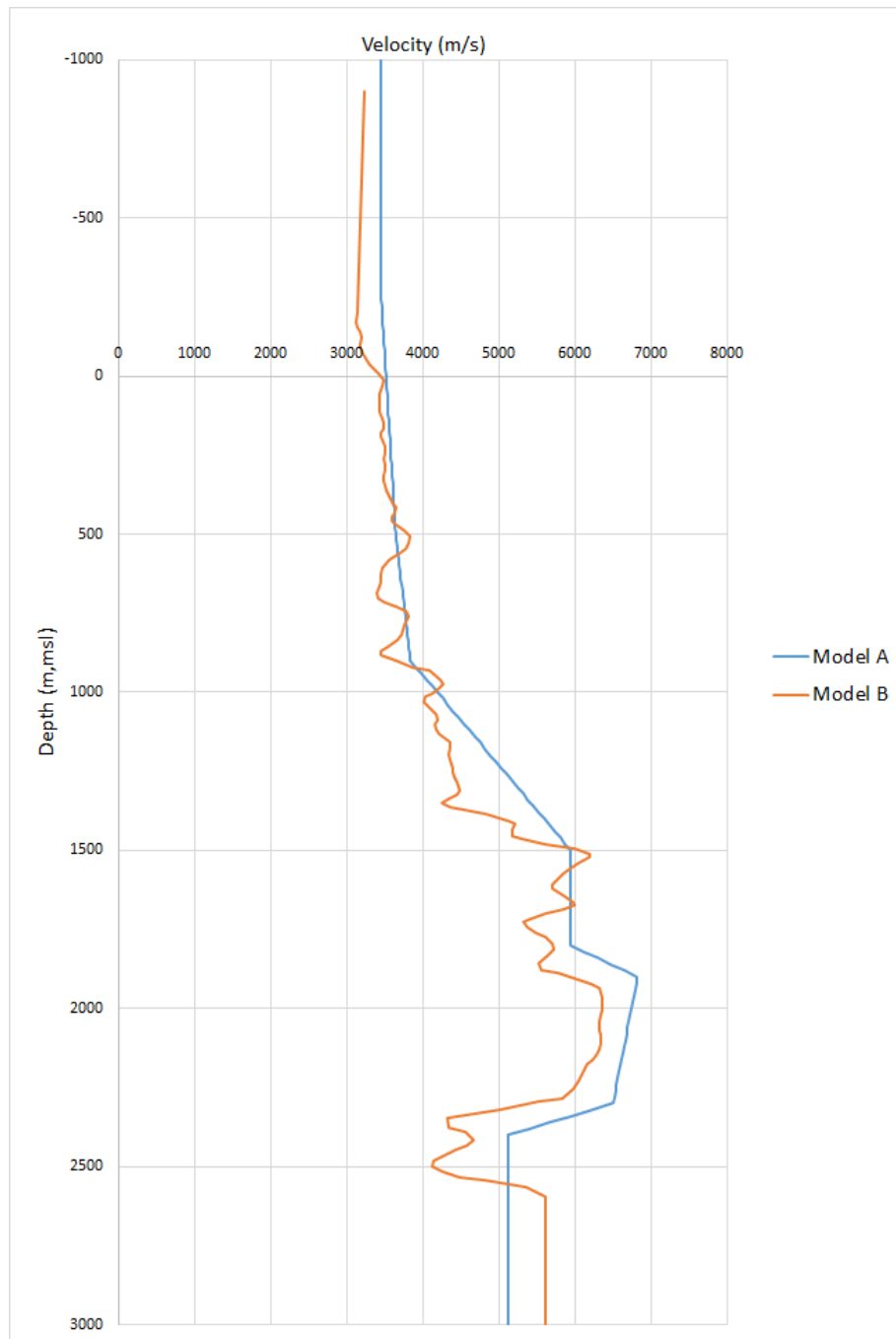


Figure 4.10: Velocity models provided by the industrial contact, note the difference in the smoother operator between both velocity models and the velocity shift applied in Model A

4.4.2 Microseismic events detected during the survey period and overview of possible causes of induced seismicity

To identify if the two mechanisms for induced seismicity occurred at the site (re-activation from pore pressure changes and the transfer of stress), all of the events from the events catalogues were placed onto a map and coloured by the pumping day from the first hydraulic fracturing stage on January 4th. These maps annotated with the main event position, regional stress direction and additional areas of interest are shown for both velocity model A and B as figures 4.11 and 4.12.

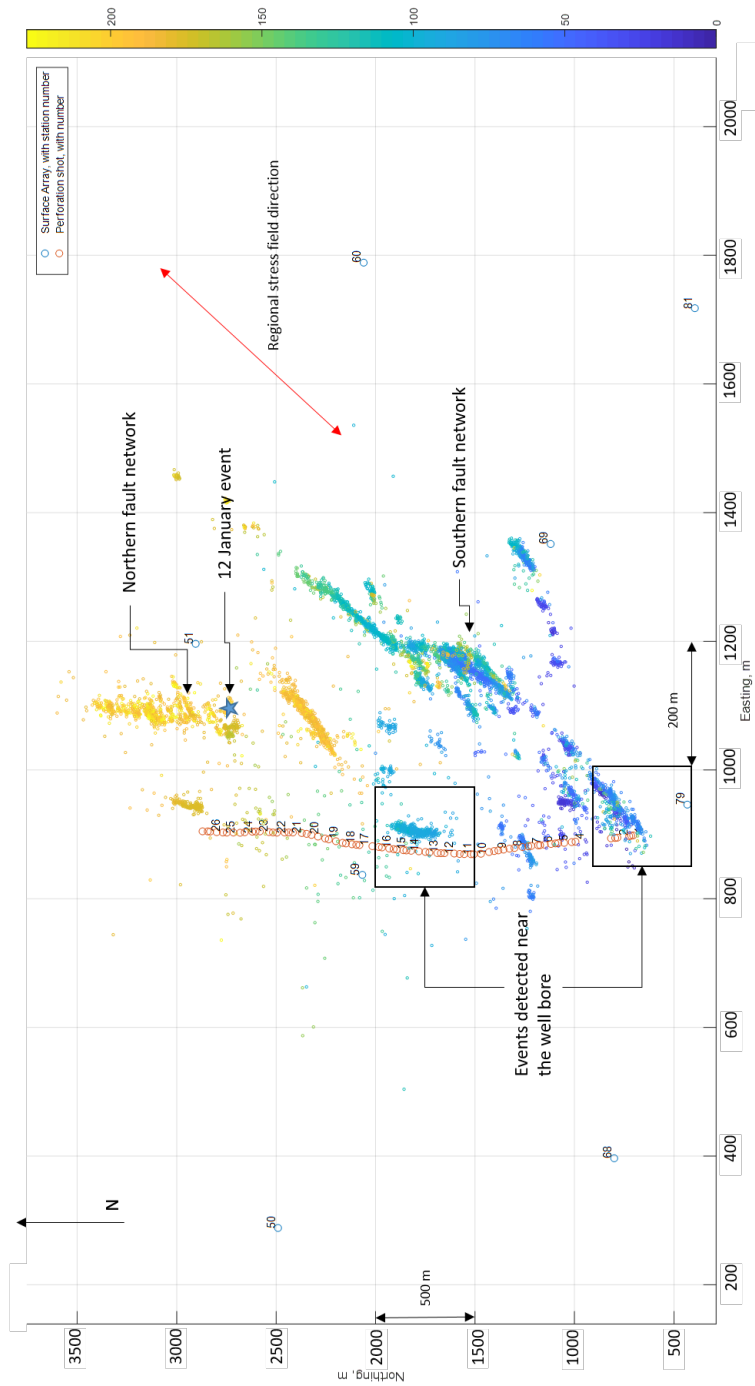


Figure 4.11: A enlarged map showing the location of the well bore and events as identified by contractor A. The colour of the event points varies with occurrence time in hours from the start of injection at the site.

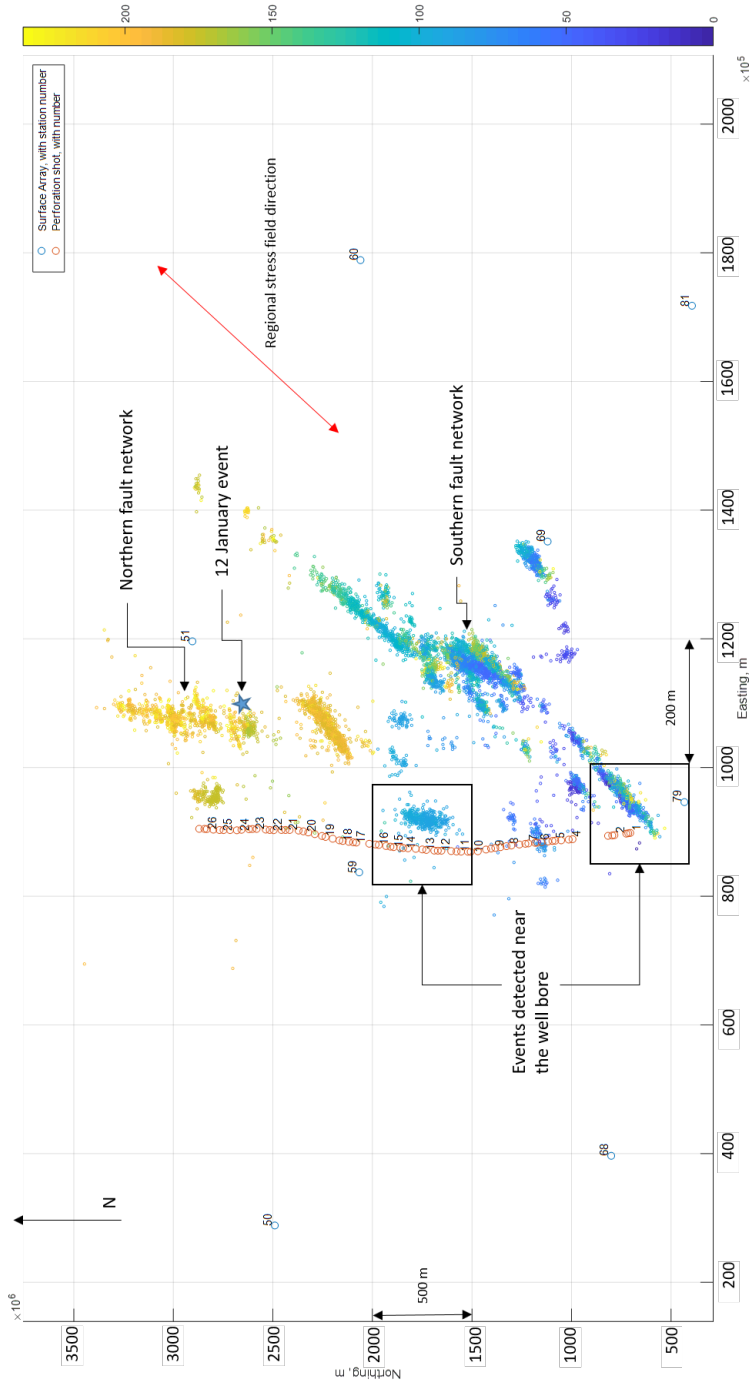


Figure 4.12: A enlarged map showing the location of the well bore and events as identified by contractor B. The colour of the event points varies with occurrence time in hours from the start of injection at the site.

The maps in figure 4.11 and 4.12 show that other than hydraulic fracture stages 1 to 4 and 12 to 16 there are relatively few events detected near the well bore. The vast majority of events detected are up to 500 m away from the well bore. These events are aligned with the regional stress field direction (taken from the J.S. Bell (1994) indicating these events are movement along fault lines. These faults can be separated, into two different networks, as judged from the direction and occurrence time of the events. The first fault network starts at the southern end of the site near stage 1 of the hydraulic fracturing process and trends in a north-easterly direction. The faults on this network are active at different times during the microseismic survey, with the most southerly faults active during day 1 of the survey and the most north-easterly faults active from day 5 to 7. The second fault network comprises of events trending in a north-south direction north of the location of the main event. These events were detected later in the survey, after the occurrence of the main event. This implies that the slip from the main event has altered the stress state in this area, resulting in fault movement northwards along the fault line.

With regard to the two broad causes of induced seismicity, the existence of microseismic events to the north of the survey that occur after the movement at the main event implies that the stress field has changed. To examine if there is a potential hydraulic connection for frac fluid between the well bore and main event position (shown by the star on the maps in figure 4.11 and 4.12, a closer review on a stage by stage basis is required as well as a review of the velocity model accuracy before further conclusions can be drawn.

4.5 Discussion

In this chapter, the geologic background of the prospectivity of Dunvernay formation was reviewed together with a review of the current regional in-situ stresses calculated to the formation as context to understanding the predominant hydraulic fracture direction. The production history of the site and the operator parameters for the hydraulic fracture operation were also reviewed. As part of this review, the timeline of the site operations leading up to the 12 January seismic event (therein, main event) and subsequent site suspension was summarised.

In the context of a review of the microseismic data quality, the placement and installation of the microseismic monitoring surface array were reviewed and as well as a thorough review of the processing carried out at the time by the two contractors (A and B) to automatically detect and position the microseismic events captured by the surface array. Finally, an overview of the microseismic events detected by the stations was conducted.

Chapter 5

Derivation of velocity and attenuation models

5.1 Introduction

In this chapter, the final two requisites for implementing the software system are derived. These are the velocity and attenuation models. The velocity model is a crucial component in microseismic analysis, as the accuracy of the position and timing of the detected passive events are wholly dependent on the model. The attenuation model is required to correct the change in frequency content, due to the loss of energy from heat losses and scattering which will affect the results obtained from the analysis.

5.2 Quantitative assessment of provided velocity models

The first of the pre-requisites for the software system is the site velocity model. Two velocity models were provided as part of the data package by the industrial contact and the source of these velocity models has been discussed in depth in chapter 4. The first step was to decide which of the two velocity models provided the greatest positional accuracy. The motivation for this investigation is that there is a 350 m discrepancy in depth positioning of the main event between the two different contractors. This may be attributable to the different velocity models used.

5.2.1 Method to be employed

To assess the positional accuracy of the two velocity models, a method based on the work by Pei et al. (2009) and later updated by Jiang et al. (2016) was applied. The method as detailed by Pei and Jiang is to calculate the RMS error between the observed arrival times of the primary seismic waves in the observed records and modelled travel times calculated by the ray-tracing process.

As passive seismic events are recorded onto a continuous recording system, the exact origin time of the events are not known. To tie the modelled travel times to the observed times, the double-differencing concept for station pairs is utilised as per Zhang et al 2010. In Jiang et al's work a single reference station, based on using the highest amplitude arrival is utilised to tie the observed time to the modelled times. These modelled and observed arrival times are subtracted from the arrival time at the reference station resulting in two sets of single difference times, one for the observed and one for the modelled travel times. These times are then subtracted from each other, resulting in a set of double difference times for each receiver. Pei and Jiang both then use equation 5.1 to calculate the RMS error from the double-difference values,

$$E(V) = \sqrt{\frac{1}{n} \sum_{i=1}^n \delta\Delta t_i^2}. \quad (5.1)$$

Where n is the number of source-receiver pairs, $\delta\Delta t_i$ is the double difference times in seconds.

To calculate the modelled travel times, a means to calculate the travel times for a given velocity model is required. For this purpose, a seismic ray tracer was utilised. After reviewing a number of packages the Trabox software package by Sambridge and Kennett (1990), last modified in 2001. This ray tracer uses a time step method to trace rays through a heterogeneous 3D velocity medium at either a set time step or a variable time step depending on the user preference. The velocity model is represented by a 3-D mesh of knots and uses a Cardinal spline interpolation to calculate the velocity and derivatives of velocity in-between each knot. At each time step, the declination and azimuth of the ray path are re-calculated by the derivatives of the velocity model taken from the Cardinal splines, therefore as velocity varies from cell to cell, the ray will refract or reflect accordingly from cell to cell of the path to the receiver location. The final component of the ray tracer is a configurable horizontal boundary between the two different velocity models which uses Snell's law to calculate ray direction after the ray path is incident on the surface.

The Trabox raytracing system was designed with large scale seismology in mind so modifications were made to ensure it ran reliably at this scale. The key modification was designing a new method to solve for the initial angles of azimuth and declination to ensure that a path can be traced between source and receiver. While this was already solved for as part of the original code, the reliability was a concern, especially in the presence of strong velocity contrasts. A new system using an iterative method was designed and implemented, which ensures that the final traced ray is from a direct raypath solely. Further details of this modification can be found in the appendix.

5.2.2 Review of available data: Velocity models and micro-seismic records

Velocity models provided

The velocity models provided by the industrial contact were from two different contractors. Both contractors use the sonic log data from the vertical pilot well and both contractors smooth the 1D sonic log into a 1D velocity field. The difference between the contractors processing was the length of averaging applied and any statics shifts in velocity as determined for calibration methodology reasons. Contractor A applied a longer space smoothing operator of the order of 350 m. Contractor A also applied a shift of 6.5% to the velocity model based on the misfit between the modelled timing from the perforations shots and those identified by their software package. Contractor B, on the other hand, applied a short smoothing operator of the order of 50 m on the sonic log. Further details of these process can be found in chapter 4. Both of these models are shown as figure 5.1.

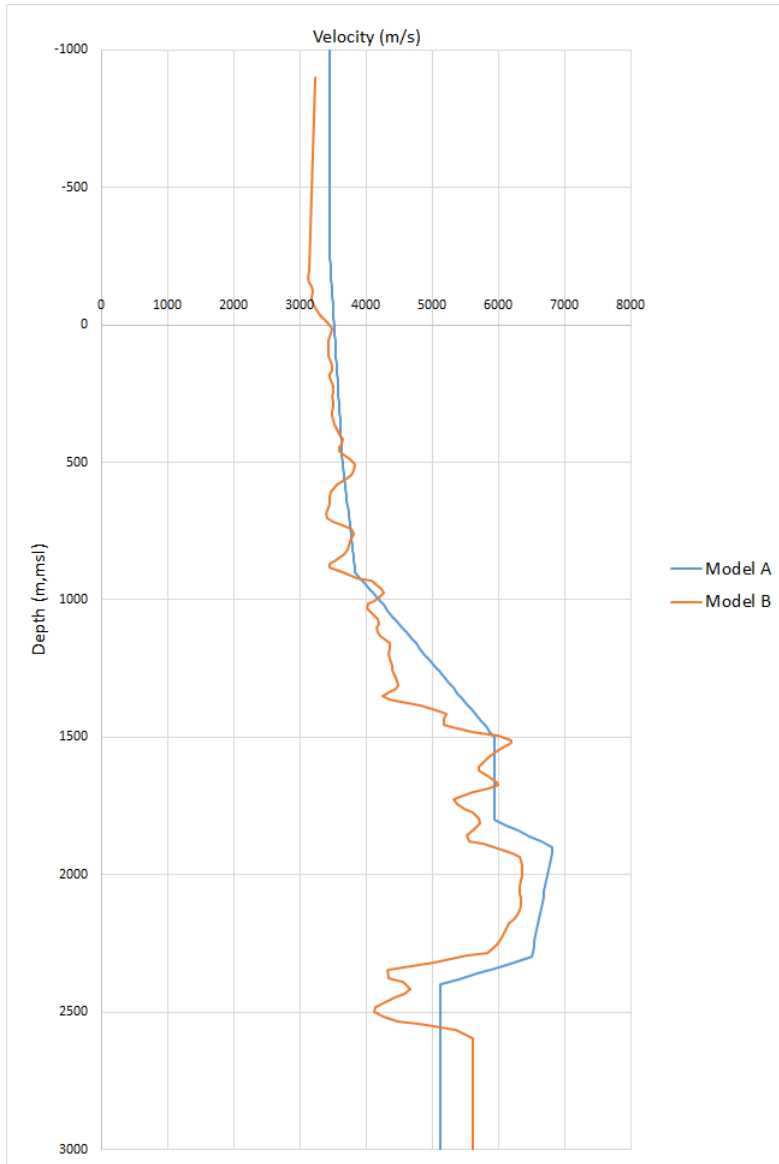


Figure 5.1: Velocity models provided by the industrial contact, note the difference in the smoother between both velocity models and the velocity shift applied in Model A

Microseismic records

To gauge the accuracy of the two velocity models, there are two sets of travel time data that are available. The first set of travel time data used were the p-wave arrival times determined from a set of fixed-position sources, the perforation shots through the casing. These were used to calculate the RMS error for each perforation shot. The advantage of using perforation shots is that it removes the variable of unknown position from the comparison between different velocity models. The disadvantages are that these events have low signal to noise ratios. These events were distributed in a north to south arrangement with limited distribution in the east-west direction. A map of the of these perforations shot locations along the borehole is shown as figure 5.2.

The second set of travel time data available was the P-wave arrival times from the passive seismic events detected during the 9-day microseismic survey. The advantage of using these events is that for the majority of the events in the subset, the signal to noise ratio is higher than the perforation shots so that the signal can be seen at all offsets and all travel times can be used in the RMS calculation. The disadvantages with these events are that the position of these events is unknown and as the number of events detected is greater than 9000, with no first arrival picks information available, the number of events had to be filtered down to a smaller subset of events to allow efficient testing of the method.

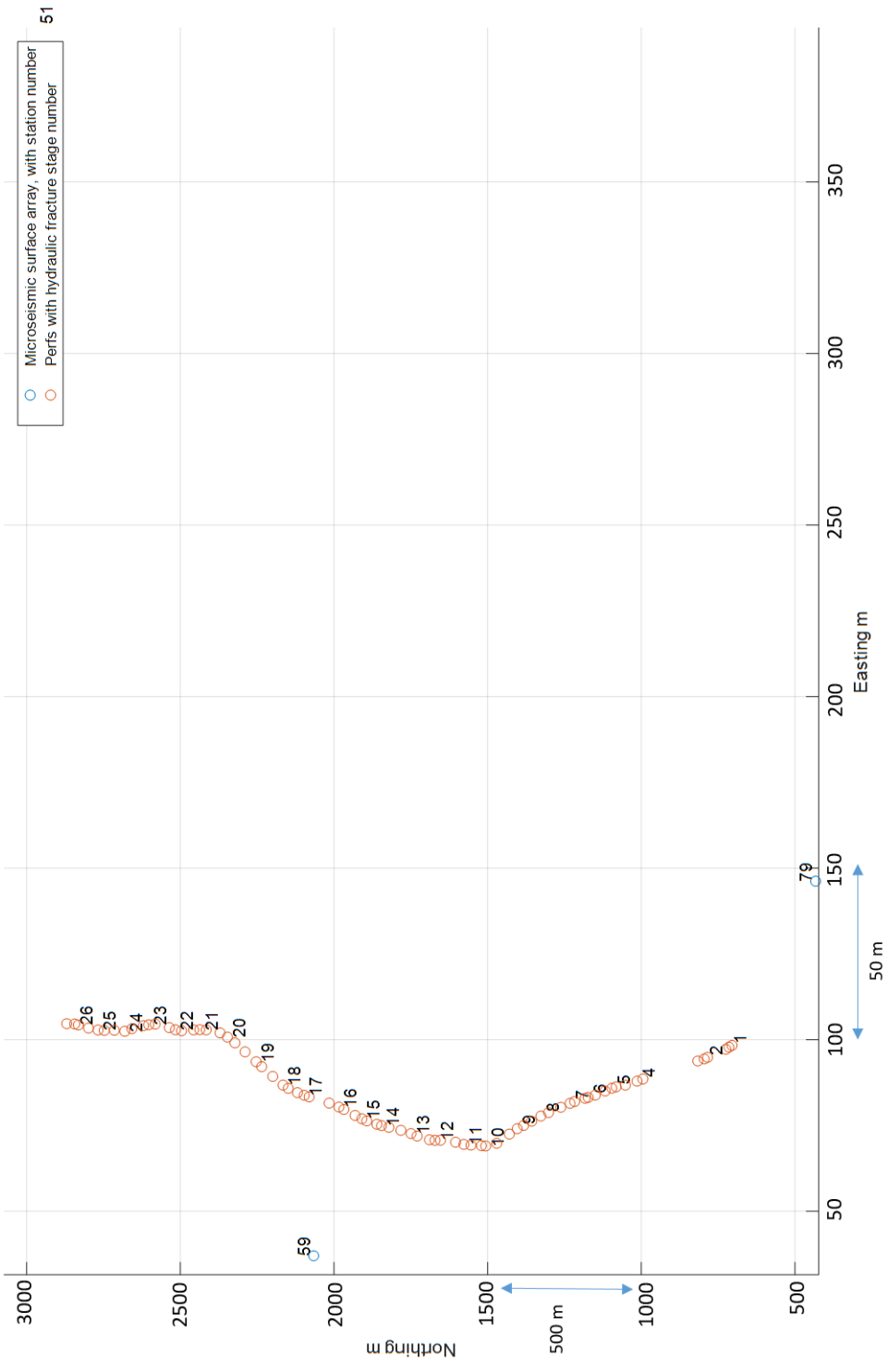


Figure 5.2: A map of the perforation shots by hydraulic fracture stage

5.2.3 Velocity model accuracy comparisons: fixed position events

All the seismic data were recorded continuously onto 30-second SEG-D records. Records were taken when the perforation shots were fired, but these timings were from a 2 minute time window, so these cannot be used to time the event arrivals accurately. The perforation shots employed at this site consisted of three explosive shots fired in quick succession through the casing.

The seismic data was converted from SEG-D to SEG-Y using the Seaseis software and a T^2 scalar was applied. In order to improve the signal to noise ratio, all three vertical channels from each station were summed together, with manual timing adjustments as calculated from dynamite shots fired near the surface. To further narrow down the search window for the perforation shots, a semblance based method with a linear moveout equation was utilised. After manual identification, an automated cross-correlation method was applied based on the work by De Meersman et al. (2009). This used a window size of 0.0150 seconds with a limit of 5 iterations. Further details of the testing of the picking method can be found in the appendix.

With the raytracing software, set-up and the first arrivals identified, parameter testing was conducted on the raytracing environment to ensure that the parameters chosen have a minimal effect to the ray output but balanced against processing time and memory limits. Parameter testing was conducted by comparing the fixed position arrival times with the ray-traced times. This process found that a 50x50x10 m grid, with a time step of 2 ms (matching the input data) provided consistent travel times and used the smallest practical computational resources. Further details of the parameter testing for the ray-tracing software can be found in the Appendix A.

With the first arrivals identified for the perforation shots and the ray-tracing software setup, the RMS error for the perforation shots was calculated. This was conducted in Matlab with a custom script where the ray tracer is instigated for each perforation shot position, which then calculates the double-difference times and the RMS error as per the method outlined by Pei et al. (2009) and Jiang et al. (2016).

The RMS error for all perforation shots for model A and B is 0.0841 s and 0.0859 s respectively. As this difference is minor, it is worth considering a couple of other statistical methods to consider the significance of this value. The first measure was to take the RMS errors for each individual perforation shot and plot these in a distribution plot. This is shown as figure 5.3.

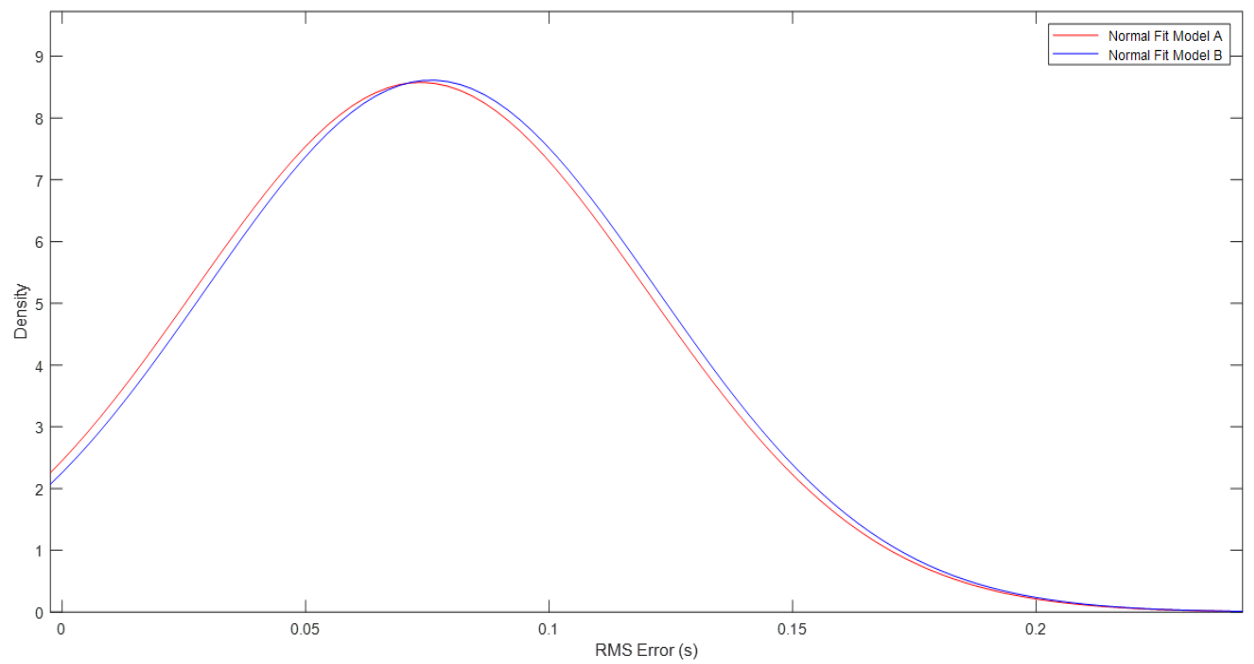


Figure 5.3: The distribution of RMS errors for model A and B. The differences are minor but the median RMS error for model A is shifted more towards zero than for model B

This shows that the distribution curve for model A trends closer to zero than model B and agrees with the overall RMS error for all points discussed above. As this plot is based on the RMS error from 72 perforation shots, it would be useful to see the distribution of misfits before any sort of averaging has taken place. Figure 5.4 is a distribution plot of 4009 double-difference values for models A and B.

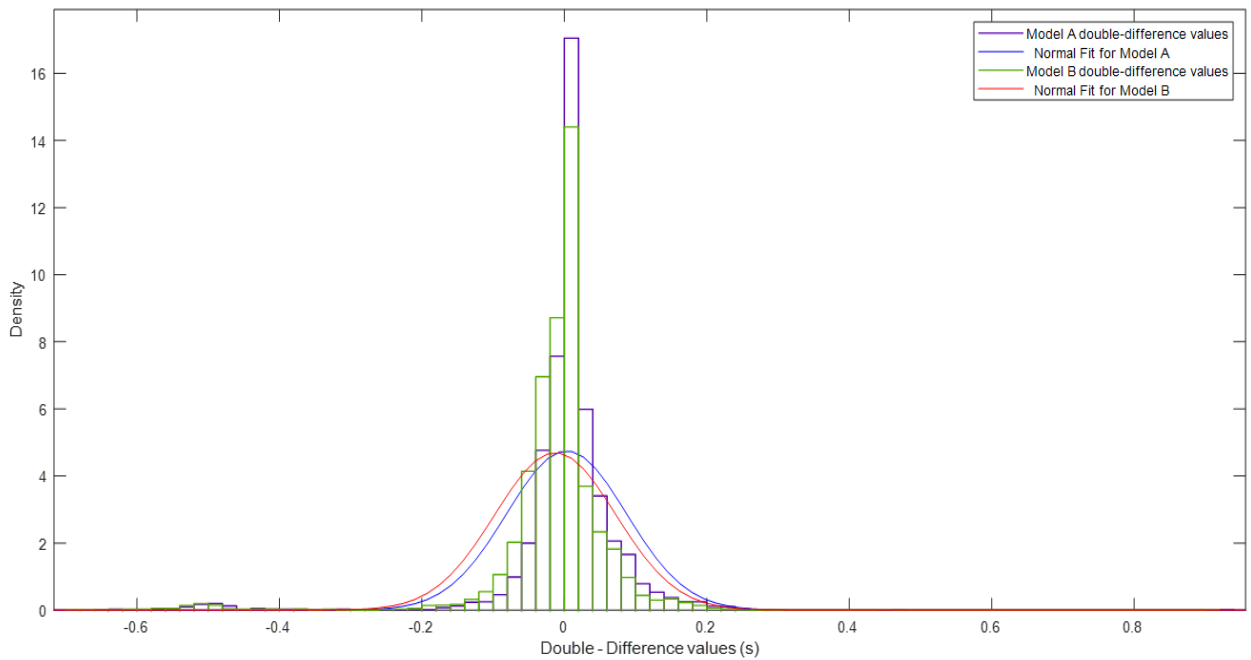


Figure 5.4: The distribution of double difference values for all perforation shots - station pairs. Using this plot the differences between model A and B are clearer than from using RMS error alone, and show the normal curve for model A is distributed closer to zero than model B

Figure 5.4 is useful as it shows the distribution of all the double-difference values, particularly highlighting the outlying RMS values. If the velocity model was a perfect match this would equate to a standard deviation of zero. As is the case the standard deviations for model A and B are 0.0840 s and 0.0850 s respectively. This shows that model A not only has a lower RMS error overall but the double difference values are distributed around zero more than for model B.

It is useful to consider the spatial variations of RMS error from these velocity models. Figure 5.5 shows a map of the RMS errors for model A and B for each perforation shot.

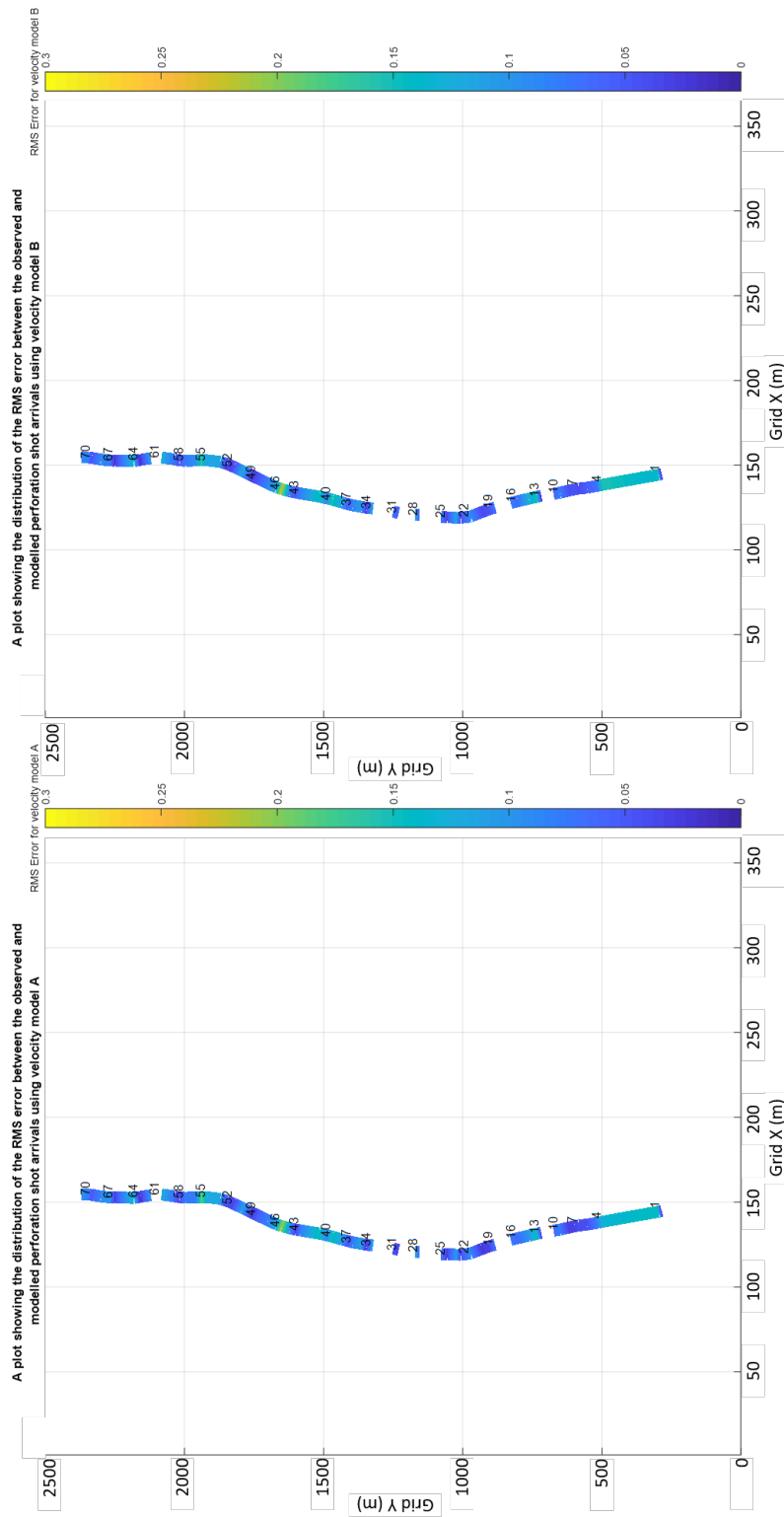


Figure 5.5: The distribution of RMS errors along the well bore for models A and B. Overall model A has a smaller misfit than model B, except near the well bore heel at perforation 72 where the unaltered sonic log is a closer match to the velocity model there

Figure 5.5 shows that velocity model B is a more robust match for the perforation shots nearing the well heel, perforation shots 60 to 72, than model A which has an overall lower error for all the other perforation shots. This is likely due to velocity model B being a simple smoothing of the sonic log whereas velocity model A has had a static shift of velocity applied to the model ensuring a greater fit along all of the perforation shots.

The final maps (figure 5.6, 5.7 and 5.8 shown overleaf) highlights the station by station RMS error, by calculating the RMS error for all perforations shots which occur at each station.

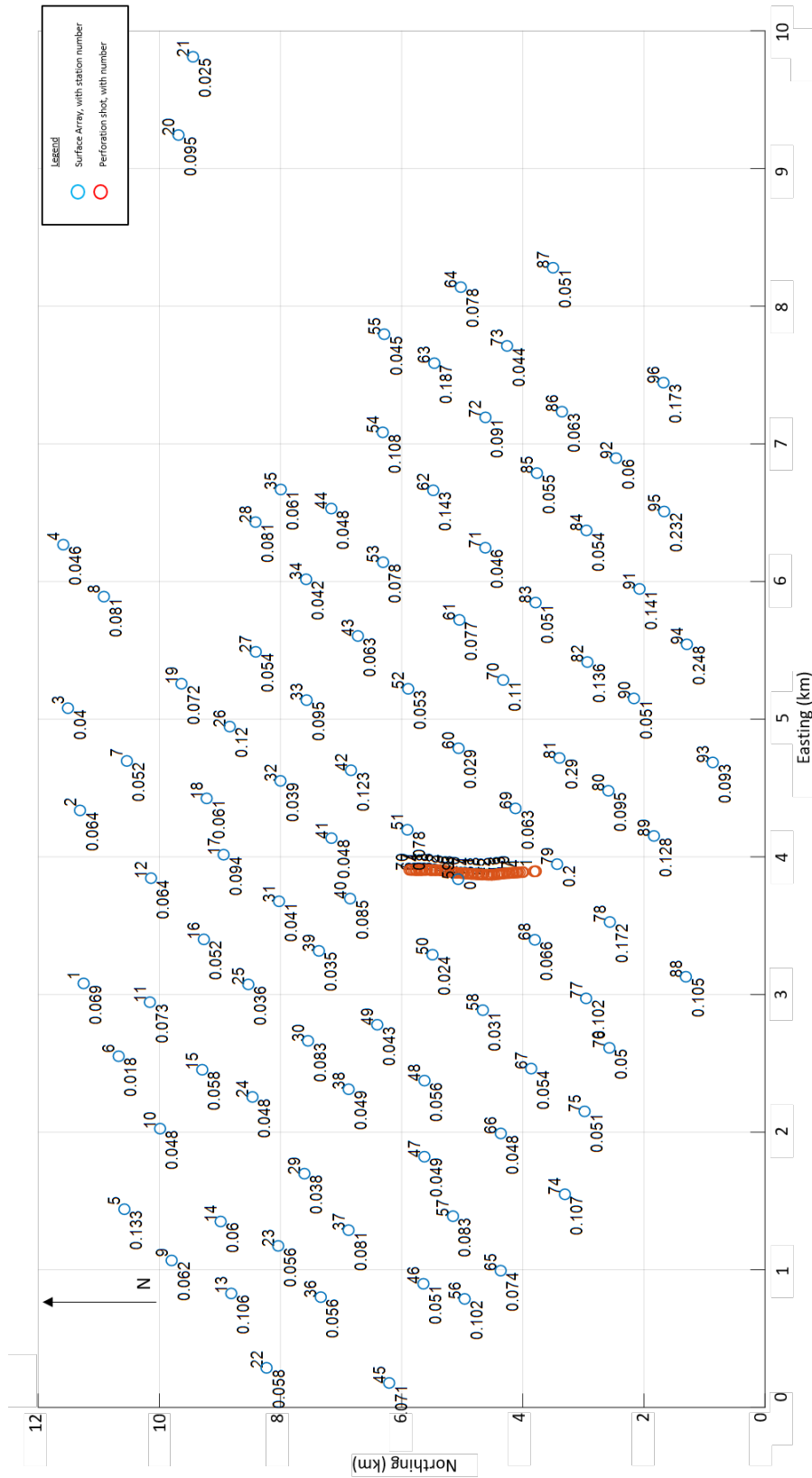


Figure 5.6: A map showing the RMS error at each station from all perforation shots using velocity model A. The grid size for this run is 100x100x10 m with a variable time step starting at 0.002 s to 0.060 s.

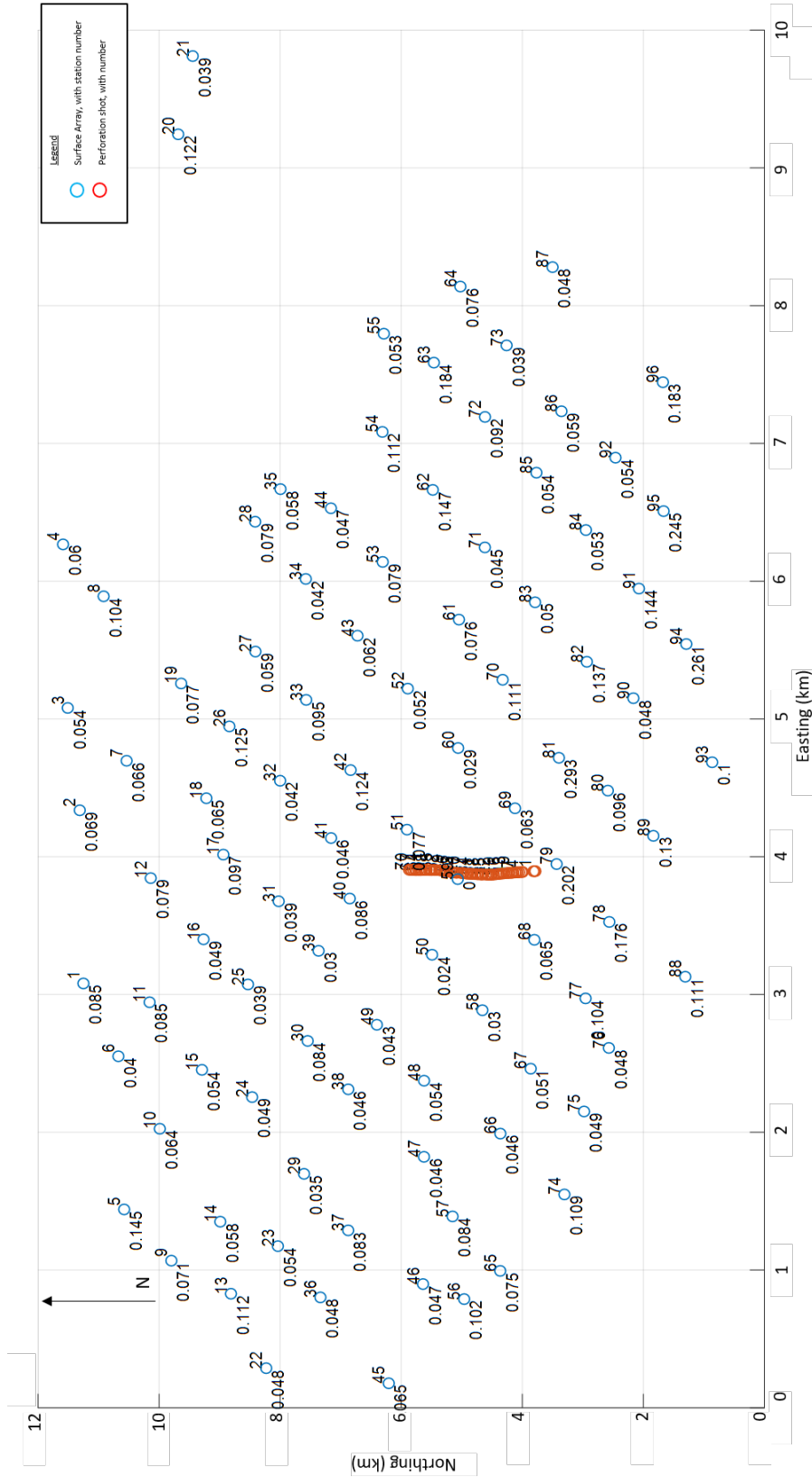


Figure 5.7: A map showing the RMS error at each station from all perforation shots using velocity model B. The grid size for this run is 100x100x10 m with a variable time step starting at 0.002 s to 0.060 s.

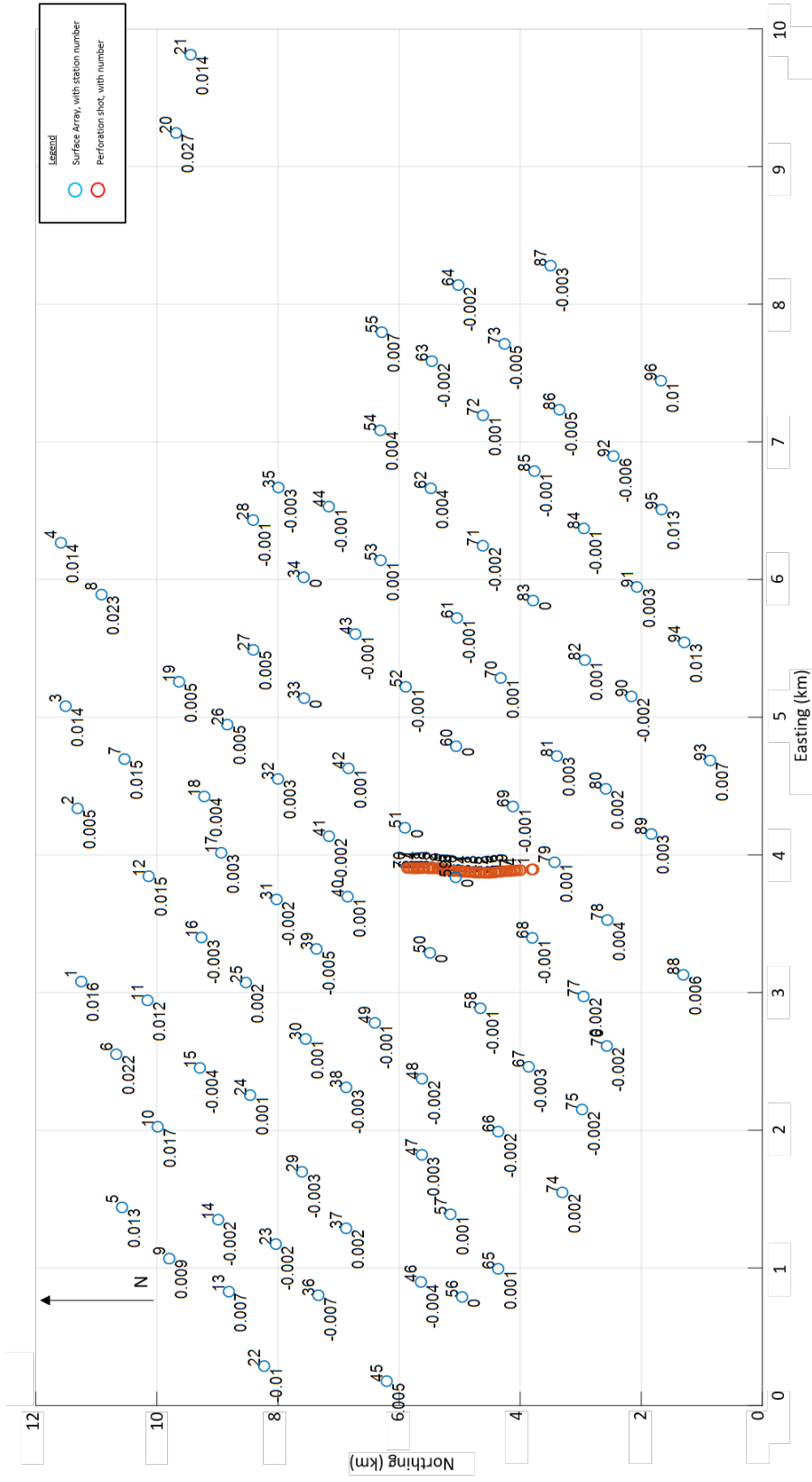


Figure 5.8: A map showing the difference in RMS error from Model B to A at each station from all perforation shots. A positive number indicates where the error from velocity model B is greater than model A. The grid size for this run is 100x100x10 m with a variable time step starting at 0.002 s to 0.060 s.

The maps in figure 5.6 and 5.7 both show that the distribution of errors is variable with the northern section exhibiting the highest RMS errors. The map in figure 5.8 shows the change in RMS error from Model B to A. This highlights that the velocity increase applied to Model A results in an higher accuracy for ray paths at the furthest distances and in particular the northern section of the survey.

All of this information supports a choice that for the perforation shots, velocity model A is a closer fit to the true velocity model than model B.

5.2.4 Microseismic events chosen for use with the velocity model accuracy comparisons

With the comparisons completed for the fixed position events, the perforation shots, the variable position events are now considered. There were more than 9000 events detected during the 9-day survey. As first arrival times were not available, it is not possible to consider large numbers of events in this work with the resources that were available. A sub-section of events that correspond to the two causes of induced seismicity were considered.

The previous section concluded that velocity model A has a higher accuracy than model B when the fixed position events were considered, so to filter the events down to a subset of events, the positions as determined by velocity model A were used. As the choice of event is based on the mechanisms of hydraulic fracturing, the discussion regarding the choice of events is detailed fully in chapter 7. For the purposes of this review of the velocity model accuracy, a total of 12 events were taken from the 174 events chosen to describe the mechanisms of induced seismicity. These 12 events cover both the area closest to the well-bore path and areas further away from the well-bore. Within this list, the main event and two events that were close to stations 59 and 51 for use with the attenuation modelling to be considered later in the chapter were included. With regard to the map positional differences between the two velocity models for these events, the average differences for the easting and northing coordinates are 15 m and 80 m respectively for these test events. While these map position differences are minor, the average differences in depth for these test events is 186 m, emphasising the variability in depth between these velocity models.

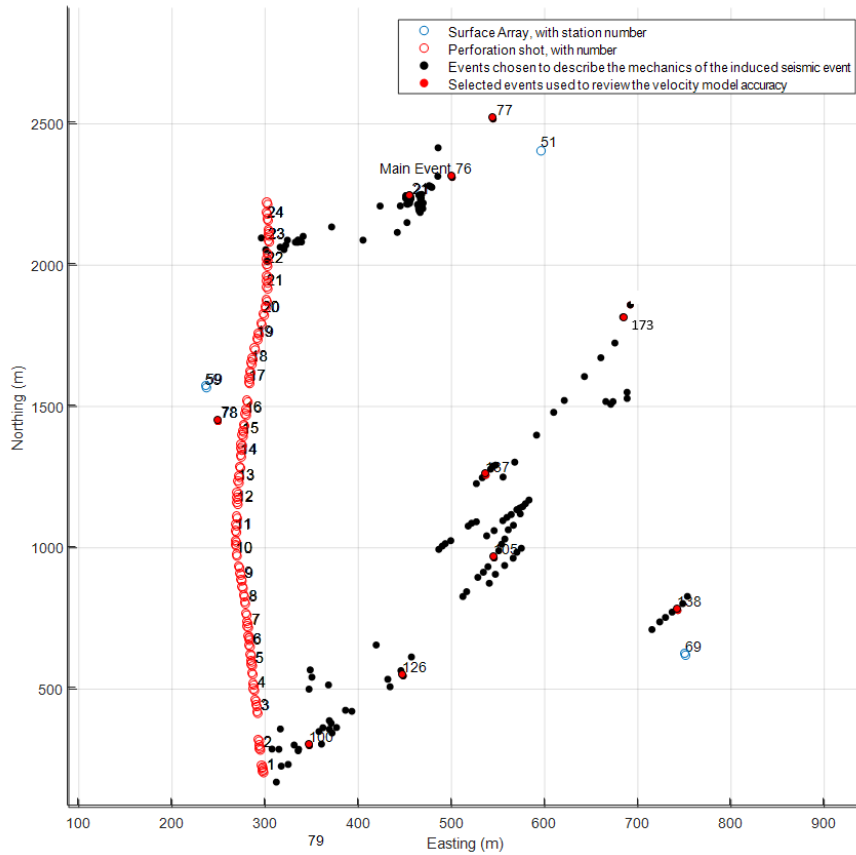


Figure 5.9: The events chosen to test the velocity model accuracy as positioned by both velocity model A

5.2.5 Velocity model accuracy comparisons: variable position events

Similar to the fixed position events, these records were subject to the same processing flow from SEG-D to SEG-Y as the perforation shot records. If required these records were summed together to improve the signal to noise ratio. Using the ray tracer and each position as provided by the contractors, the travel times were ray-traced through the respective velocity model. After each ray trace, the double-difference times and RMS error is calculated as per the method outlined by Pei et al. (2009) and Jiang et al (2016). A graph of the RMS errors between both contractor's velocity models is shown as figure 5.10.

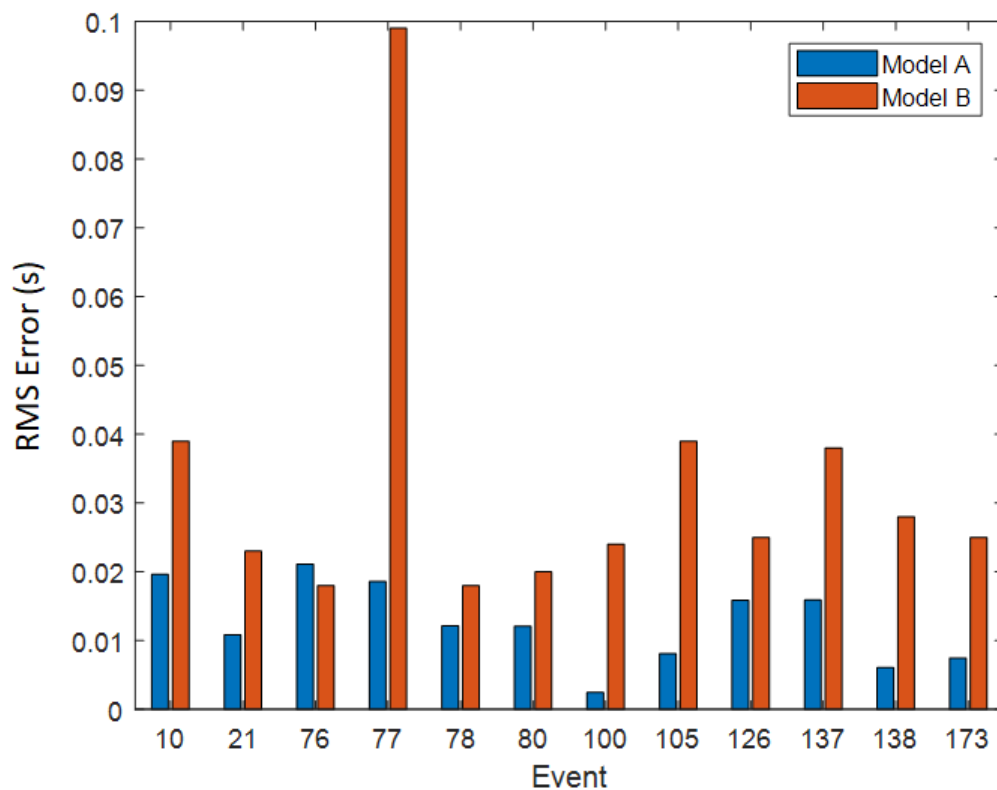


Figure 5.10: The distribution of RMS errors for the subset of events between velocity model A and B

Comparing the RMS errors between the different velocity models using the set of 12 events in figure 5.10 shows that the accuracies have improved using velocity model A. The only event where the RMS error is increased from using velocity model A rather than model B is the main event. The differences in RMS error for the main event were 0.0212 s and 0.0184 s for model A and B respectively. This change while minor in terms of RMS represents a depth position change of 350 m.

To ensure that this difference is purely down to the velocity model, a validation check was conducted. This check consisted of positioning the main event (for both velocity models) using a custom-built MATLAB algorithm that invokes the ray tracer and reviews the output RMS error and subsequent positions. If the discrepancy in depth is still present after repositioning the event, then the influence of the type of ray tracing to the discrepancy can be removed. To conduct this positioning, a grid search/subdivision method was written in Matlab. This method is a grid search

algorithm that involves splitting the grid into multiple sections and ray tracing a position within each of these sections. The RMS errors for these sections are then ordered and the section with the lowest RMS error is subdivided multiple times to a value set by the user.

To ensure this algorithm ran efficiently and could reliably find the smallest RMS error in the model, the initial grid is limited to 5 km x 7 km surrounding the well bore. This boundary is the limit for all the events as positioned by both contractors, so is a reasonable assumption that the events occurred within this region. The distribution of stations on the surface allows a precise measure of position in the x and y direction to be obtained. For this reason, the grid is always subdivided in the x and y direction and the depth position is always set at the same four steps. This ensures that a local minimum does not alter the overall result. Once nine iterations of this method have been completed, the x and y positions are held constant and a grid search in depth of 15 m increments is conducted from 1500 m to 3950 m depth.

The following figures show the output of this process as figure 5.11 and 5.12.

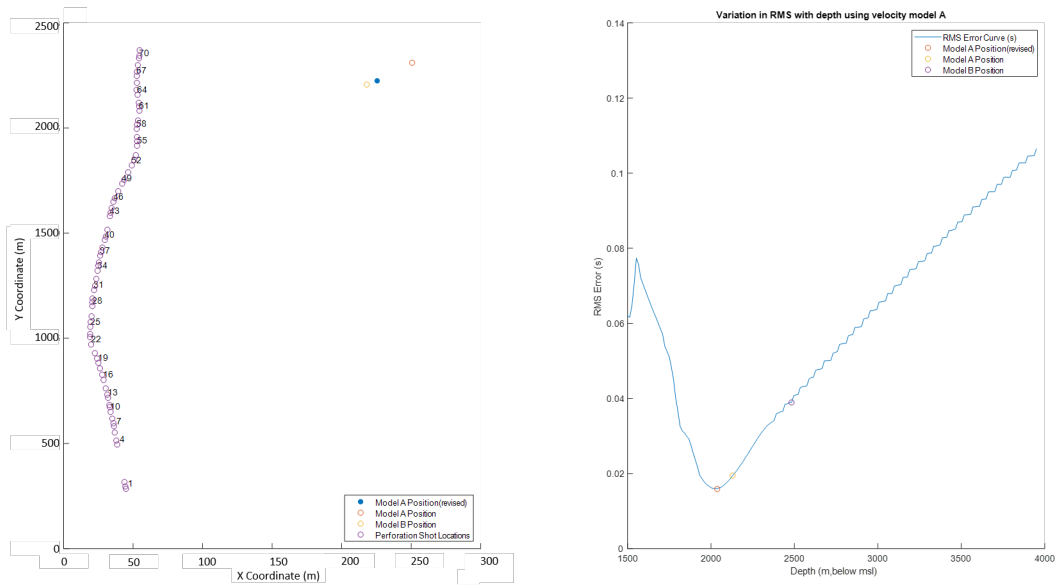


Figure 5.11: The revised position of event 76 using the Trabox ray tracer and a grid search / subdivide method with velocity model A. The revised location is 25 m to east, 85 m to the south and 90 m shallower than the original supplied location. Without the original picks used in the positioning by the contractor, this cannot be refined down closer to the original supplied location.

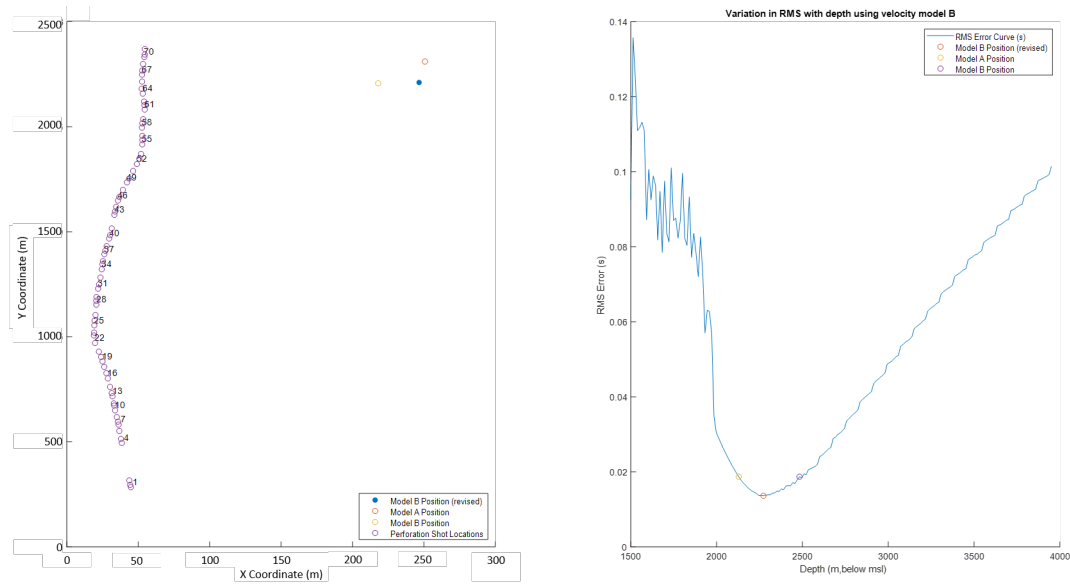


Figure 5.12: The revised position of event 76 using the Trabox ray tracer and a grid search / subdivide method with velocity model B. The revised location is 29 m to the west, 4 m to the north and 213 m shallower than the original supplied location. Without the original picks used in the positioning by the contractor, this cannot be refined down closer to the original supplied location.

Figure 5.11 and 5.12 show that by repositioning this event with two different velocity models, there is still a difference in depth of 213 m between the two events and that model B has greater accuracy for this event as shown by the RMS errors of 0.0158 s and 0.01362 s respectively. By repositioning the events with the first arrival picks independently identified away from any influence of the contractors, removes this potential source of error and highlights the maximum differences in error are purely due to using different velocity models.

This difference in accuracy can be attributed to the static shift applied to model A as determined in the positional calibration process by contractor A. This shift was intended to improve the fit for the entire length of the well bore positions. The main event position regardless of the velocity model used is 300 m away to the east from the well bore position, highlighting that the velocity model has been over-fitted to the training data which is only present in a north-south distribution.

The caveat to this conclusion is the choice of reference time to calculate the double-difference times. In this algorithm, this is set as the arrival time at the nearest station to the events original position. It is not known how the contractor's software chooses this reference time, either if it set at a single station throughout the process, or as a best-fit station that minimises the misfit between modelled travel times and identified arrival times. This factor may have a bearing on the positions and the contractor's own accuracy determinations.

5.3 Development of a velocity model for use with the software system

In the prior section, the velocity models provided by contractors A and B were reviewed for the positional accuracy. This found that velocity model A once calibrated, improved the positional accuracy of the fixed position events by a average of 2%. This process had a detrimental effect to the accuracy of the main event as determined by the RMS values. In order to move forward and develop the software system, a velocity model which improves on the positional accuracy of all the variable positions events is required. To these ends, a new 1D velocity model was calculated by calibrating the sonic log using an optimisation method, Very Fast Simulated Annealing (VFSA, as referenced by Ingber, 1989).

5.3.1 Very fast simulated annealing to calibrate velocity models

Simulated annealing algorithms such as VFSA are search algorithms that seek the global minimum of an objective function in a given model space. The main advantage of this method over matrix inverse methods, as discussed by Jiang et al (2016) is that there are no large matrix equations to solve, constraints can be added easily and it is not dependent on the initial starting value.

The algorithm flow is controlled by a ‘temperature’ parameter that varies according to a schedule linked to an iteration number. The temperature parameter controls the potential range of random numbers used to generate the perturbations to the model parameters and also controls the acceptance criteria for each parameter. With an increase in iteration number, there is a reduction in temperature. If the temperature is reduced slowly enough, the solution will always converge onto the global minimum (Pei et al, 2009). The VFSA method has been used by other authors most notably, Jiang et al (2016) and Pei et al (2009) whom both used this method to calculate a new velocity model for microseismic event location. The difference between VFSA and Simulated annealing is the temperature schedule is an exponential relationship, allowing the solution to iterate quickly to a global minimum.

To calculate the perturbation to the model parameter, a random number between [-1,1] is derived by,

$$x = \text{sgn}(\mu_r - 0.5)T_k[(1 + \frac{1}{T_k})^{2|\mu_r - 1|} - 1]. \quad (5.2)$$

Where sgn is the signum function, T_k is the current temperature and μ_r is a random number from $[0,1]$. The model parameter vector is then updated individually by,

$$V_i^{k+1} = V_i^k + x S_{fact} (V_i^{max} - V_i^{min}). \quad (5.3)$$

In equation 5.3, x is defined as a random number controlled by the temperature T , S_{fact} is a control parameter introduced by Jiang et al (2016), V_i is the velocity at the vector index i at a given iteration k and $V_{max} - V_{min}$ is the range allowed within the constraints for the particular model parameter. The S_{fact} parameter introduced by Jiang et al (2016) is a factor which reduces the step size of each perturbation and in this thesis, this was set to 0.1. This differs from the work by Pei et al. (2009) which doesn't use this parameter. Instead, the V_{min} and V_{max} are constrained more tightly meaning the step size for each perturbation is limited.

As the temperature reduces within the algorithm, the factor x given in equation 5.3 reduces significantly with temperature, therein reducing the maximum possible change made at each iteration. So for a value of μ_r equalling 0.6 the x parameter starts at 0.2 at a temperature of 10 but at a temperature of 1E-9 this value drops significantly to 2.78E-13. This variation is shown graphically in figure 5.13 which shows the variation in the x parameter with temperature and the random number μ_r .

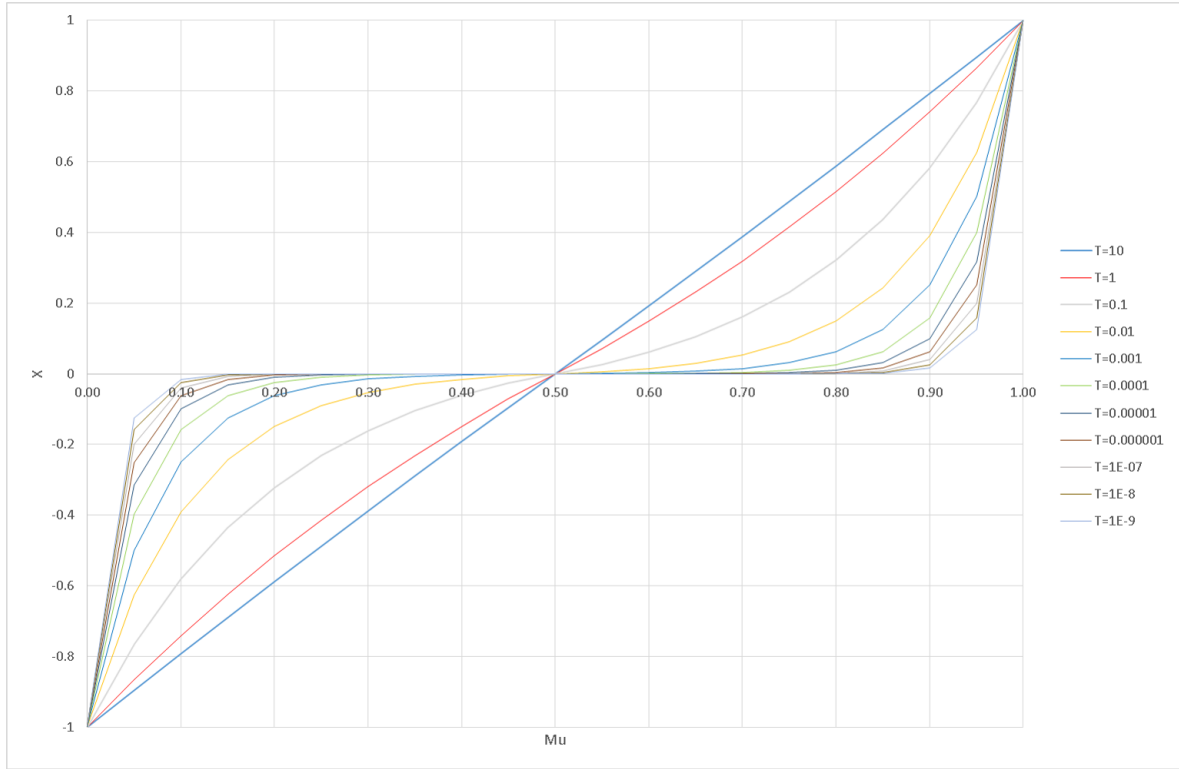


Figure 5.13: The variation in the x parameter from equation 5.3 with μ , a random number in the range $[0\ 1]$ and temperature T_k . With a decrease in temperature, the parameter x significantly reduces, therein reducing the maximum perturbation that is possible at that temperature.

With a new parameter determined from equation 5.3, the objective function is calculated. The objective function is the same RMS error function as defined in section 5.2.1 by

$$E(V) = \sqrt{\frac{1}{n} \sum_{i=1}^n \delta\Delta t_i^2}, \quad (5.4)$$

where the double-difference values ($\delta\Delta t_i^2$) are calculated from the difference between the measured travel times and the modelled travel times. The values are referenced to the arrival time by using a pre-determined reference trace to circumvent the lack of an origin time in the data.

If the objective function is less than the previous objective function the program moves onto the next model parameter. If the objective function is greater than the previous objective function then the parameter is accepted with an acceptance

probability,

$$P(V \rightarrow V') = \exp\left[\alpha \frac{E(V) - E(V')}{T}\right]. \quad (5.5)$$

Where α is a parameter which alters depending on the number of perturbations which fail to meet the acceptance criteria divided by the number of perturbations which met the acceptance criteria.

This acceptance criterion varies significantly with the temperature control parameter. As the temperature reduces the probability calculated from equation 5.5 reduces. This change is shown below as figure 5.14 below, which shows that as the temperature reduces by two orders of magnitude the probability value reduces from 9.8 to 8.2E-02 for an objective function 0.0001 greater than the RMS.

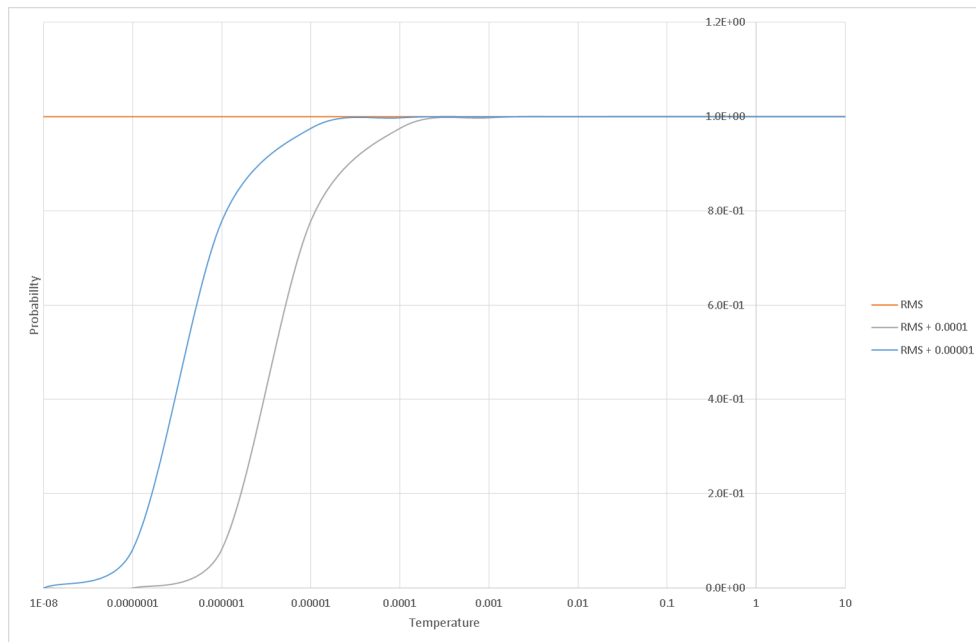


Figure 5.14: The variation in the probability calculated by equation 1.4 with temperature. As the temperature reduces, the probability calculated for objective functions which have increased (RMS + 1E4 and RMS + 1E5), reduces with an exponential relationship. This effectively creates an acceptance cut-off at certain temperatures as the chance that the comparison random number is less than this number is statistically unlikely.

With all the model parameters accepted, the temperature is reduced slightly and the algorithm moves onto the next iteration. The temperature schedule is given by,

$$T_k = T_0 \exp(-ck^{1/2N}), \quad (5.6)$$

where T_k is the temperature at an iteration k , T_0 is the starting temperature, c is a constant (set at 0.5 for both Pei and Jiang's work) and N is the number of model parameters. As the temperature schedule is an exponential function, there can only be a limited number of iterations before the temperature reduces to the point where the perturbations are insignificant and the number is too small to be represented in an 8-byte real number. Figure 5.15 shows the temperature curve for a 10 initial temperature, a 0.5 value for the c constant showing that after 10 iterations the temperature parameter drops to $1e-271$.

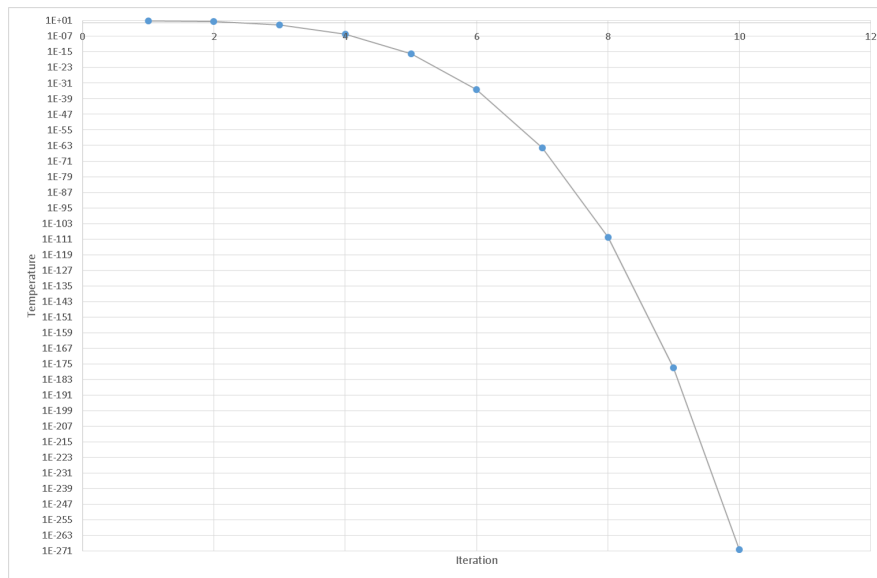


Figure 5.15: The variation in temperature with iteration using the temperature schedule set out in equation 5.6. For this relationship, c equals 0.5, with N equalling 10 with a starting temperature of 10.

To summarise the algorithm flow, the steps are as follows:

1. Calculate initial objective function
2. Using the starting temperature to calculate the perturbation to the model parameters
3. Calculate the objective function
4. Compare the objective function against the previous objective function
 - (a) If the objective function is an improvement, alter the model vector to the new value.
 - (b) If the objective function is not an improvement, calculate the probability function shown in eq 5.5.
 - (c) If the probability function is greater than a random number then the model vector is updated, if not a perturbation is generated and the process loops until the objective function or the probability function meet the above criteria.
5. Once the final model parameter has been optimised, the iteration number increases by 1 and the temperature is lowered by the relationship as shown in equation 5.6.

5.3.2 Implementation of VFSA and changes made to the original Pei et al method

To implement VFSA for this dataset, the global optimisation toolbox within MATLAB was used to control the VFSA process with MATLAB running an external script to call the ray-tracing software, Trabox, to calculate the objective function. The ray-tracing settings were maintained from the velocity accuracy calculations in section 5.2.1. The global optimisation toolbox in Matlab contains base scripts to run simulated annealing. These were subsequently modified to conform with the equations as detailed in Jiang and Pei.

There were four changes made to the algorithm from the described method by Pei et al. (2009), these were :

1. Modification of the temperature to probability function equation to improve algorithm process speed
2. Opposing polarity perturbations at each model calculation

3. Alterations to the temperature schedule to allow the solution to reach a global minimum
4. Addition of velocity layer width to the model

With regard to the modification of the temperature to probability function, this change was made as even though the variable α in equation 5.5 is a factor based on the number of failed models compared to successful models. The number of failed models required to allow an objective function to pass the criteria at the lowest temperatures was so large that processing time multiplied to be unmanageable. By increasing the temperature increments by 2 at each failed model, a model will eventually meet the criteria therein improving the algorithm runtime without duly affecting its ability to reach the global minimum

The second addition to the algorithm is to consider the opposite polarity perturbation before recalculating the model. This allows the method to try two different perturbations at that temperature before moving to a different temperature therein improving the algorithm runtime.

The third change was to alter the temperature schedule to allow the solution to more readily reach the global minimum. The initial temperature was set to 10 with a constant, c of 0.5 used in equation 5.6. This would lead to a limit of 10 iterations before the temperature decreased below a temperature that was representable with an 8-byte real number. To ensure that the global minimum was reached, after 10 iterations the temperature was raised back up to 10 and the iteration process starts again. This ensures the solution doesn't settle in a local minimum. The downside of this is that the processing time increases with further iterations. A graph of this temperature schedule is shown as figure 5.16.

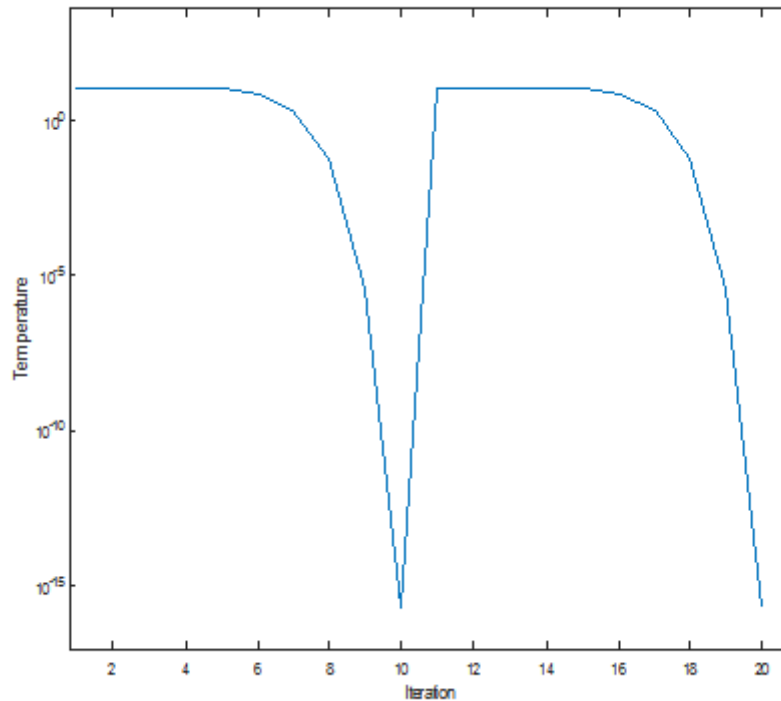


Figure 5.16: The variation in temperature with iteration using the custom temperature schedule discussed above. For this relationship, c equals 0.5, with N equalling 18 with a starting temperature of 10.

The final change to the algorithm compared to the original method as outlined by Pei et al. (2009), is to consider the thickness of each velocity layer in the 1D model. Under the assumption of no tectonic activity, the layers thickness may vary compared to the measured thicknesses next to the well. By varying the velocity and thicknesses of the layers as part of the optimisation algorithm, an additional improvement could be made to the RMS error. To incorporate this into the algorithm, these changes to layer depth are considered as layer thickness within the algorithm, with an consequent additional set of variables. To build the velocity model during this process, at each perturbation, the layer width variables are used to calculate the depths of the velocity model. The thickness of the final layer in the velocity model is widened or shortened where required to ensure a final depth of 5000 m. By introducing these variables into the algorithm, this doubles the number of variables required to be processed, with an according increase in algorithm runtime, but this allows the models to be calibrated where the geological layering varies over the site.

Table 5.1: Initial velocity model used in the VFSA process together with the constraints for the velocity and the references used to calculate these limits.

Formations	Layer	Start Depth (-868 msl)	End Depth (-868 msl)			Min/Max Velocity		Reference
				Thickness	Velocity	Min	Max	
		m	m	m	m/s	m/s	m/s	
Recent to Upper Cretaceous	1	0	1229	1229	3328.1	2000	3500	Mavko et al 2001
Lea Park Formation	2	1229	1677	448	3543.0	3022	4110	Hans 1986
Second White Spec shale	3	1677	2335	658	4144	3200	4200	Martinez and Schmitt (2016)
Montney and Belloy	4	2253	2447	112	5185	4075	7000	Hans 1986
Mississippi	5	2447	2657	211	6037	4500	6347	Miller and Stewart (1990)
Banff	6	2657	2855	197	5608	5500	7000	Davies (1974)
Wabamun	7	2855	3271	417	6242	5500	7000	Davies (1974)
Ireton	8	3271	3448	177	4340	4250	6500	Davies (1974)
Duvernay and Majeau Lake	9	3448	3509	61	4058	3500	5250	Ong et al 2015
Top Carboniferous	10	3509	5000	1491	5633	5500	7000	Davies (1974)

5.3.3 Stage 1 of velocity model development: Input model and initial constraints

The starting point for developing the velocity model was to average the sonic log into a series of layers which could be entered as individual variable inputs into the VFSA process. The 15 formation tops provided were used to split and average the sonic log into a set of 15 layers. These 15 layers were then averaged down to 10 layers by assuming a minimum layer thickness of 50 m to simplify the optimisation process, resulting in a set of 20 variables. For each of these 20 variables, a set of constraints are required for the VFSA process. Constraints for the variables were based on geological processes rather than arbitrary values. As the optimisation process alters the velocity and width of each layer and therefore depth, overburden pressure was decided to be the dominant process which alters the velocity over the site. Other parameters that alter the velocity over a site scale are porosity, fluid content and mineral content.

To calculate these constraints a geological literature review was carried out for each formation to find relationships for velocity with respect to pressure, porosity, fluid and mineral content. Table 5.1 shows the input velocity model with the minimum and maximum velocities and the references used to calculate these limits. Further details of the geological models used to define these constraints are in the appendix.

Two additional constraints were considered in this process. This first was that the velocity of layer 1 has to be less than layer 2 velocity so as to replicate the trend of an increase of velocity with depth. The second constraint was to hold the velocity of the base layer constant during the optimisation process. This was to ensure that convergence was always reached during the ray tracing process. With the initial variables and constraints decided, these were input into the VFSA algorithm and the process was run for 20 iterations. The model run time on a server-based architecture using a parallel processing scheme was around 60 hours. The output objective function for this algorithm run was 0.0363 s from an initial objective function of 0.04408 s. The velocity model was output and labelled as velocity model 1 for future reference. This model is shown below as figure 5.17.

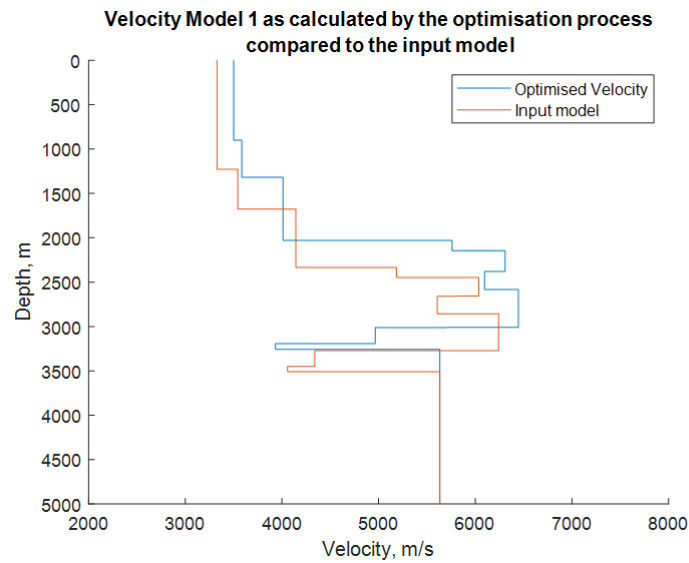


Figure 5.17: Velocity model 1 as output from the optimisation process with velocity constraints as derived from the geological review.

5.3.4 Stage 2 of velocity model development: Quality control checks and additional constraints

There are two considerations to be made while considering the output of the optimisation process. These are model uniqueness and potential over-fitting to the training data. These two factors were checked for on velocity model 1, and if required additional constraints were applied before re-running the algorithm.

Overfitting

The concept of over-fitting is when a model calculated by a set of training data only fits the training data. This is a key concern with regard to this dataset where the training data occupies a north-south transect and events which occurred away from this transect may be mispositioned. This problem was diagnosed in section 5.2.5 where contractor A applied a 6.5% shift to the velocity model to improve the fit to the perforation shots. In doing so this shifted the depth of the main event by 300 m compared to the velocity model used by contractor B, with a corresponding reduction in accuracy as calculated by the RMS errors.

To review the over-fitting issue, a subset of 12 events from the full data catalogue were repositioned using the base velocity model described in section 5.3.3. The events were repositioned again using velocity model 1 and the RMS errors were compared. This comparison is shown graphically in figure 5.18.

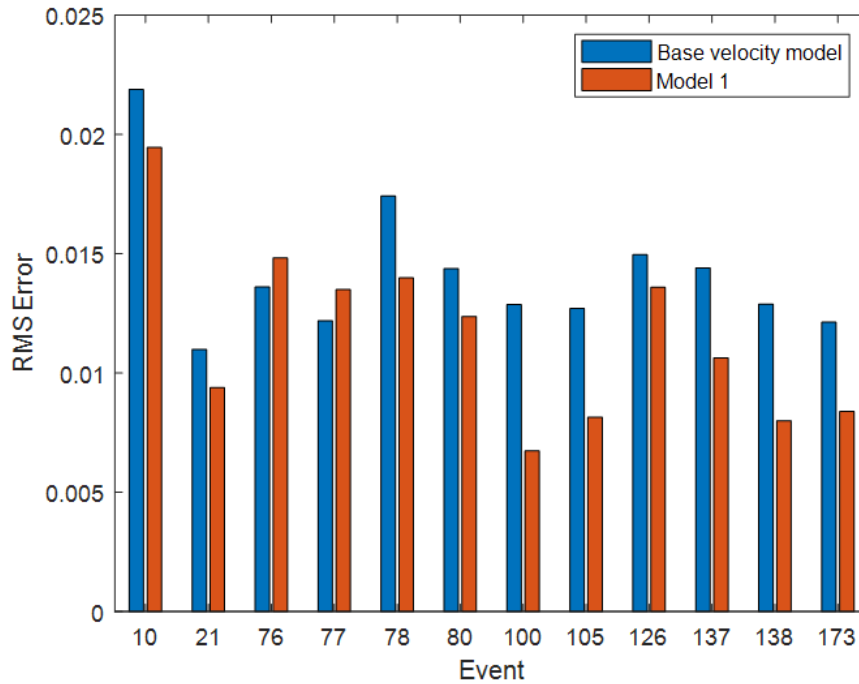


Figure 5.18: A comparison of the RMS errors from the positioning of the event subset between the base velocity model and velocity model 1

While it is clear from figure 5.18 that there has been an improvement to the accuracy of the vast majority of events using the optimised velocity model, there is a problem with the main event (Id 76). The RMS for this event changes from 0.0136 s to 0.0148 s. This minor change in RMS corresponds to a significant change in depth from 2247 m (msl) to 1938 m (msl), a variation of 315 m. As the main event is the end-point for the induced seismic activity the main event position compared to the other events has significant implications for understanding the mechanisms that caused the event.

To solve the over-fitting problem, the earlier velocity model constraints were reconsidered. As mentioned above, contractor A applied a 6.5% static shift to the velocity model to allow a more accurate fit to the perforation shots, therefore it can be said that to fit the perforation shots, a faster overall velocity is required. This is opposite to positioning the main event. To improve the positional accuracy for the main event, the top constraint for the velocity was moved closer to the initial velocity model. Two different constraints were considered, a 3% maximum velocity variation compared to the initial velocity model and a 0.5% maximum velocity variation. The algorithm was

run again with these two constraints to produce two new velocity models (Velocity Model 2 and 3).

Velocity models 2 and 3 were used to reposition the main event resulting in an RMS error of 0.01393 s and 0.01345 s respectively. Both of these constraints are an improvement compared to model 1 at an RMS error of 0.0148 s. Of the two models, model 3 was preferred as the RMS error for this model is less than the error for the base velocity model of 0.0136 s.

To check how this constraint affects the positional error for the other events, velocity model 3 was used to reposition all the events chosen in the subset. The RMS errors from the base velocity model, velocity model 1 and 3 were compared using the bar chart in figure 5.19 below.

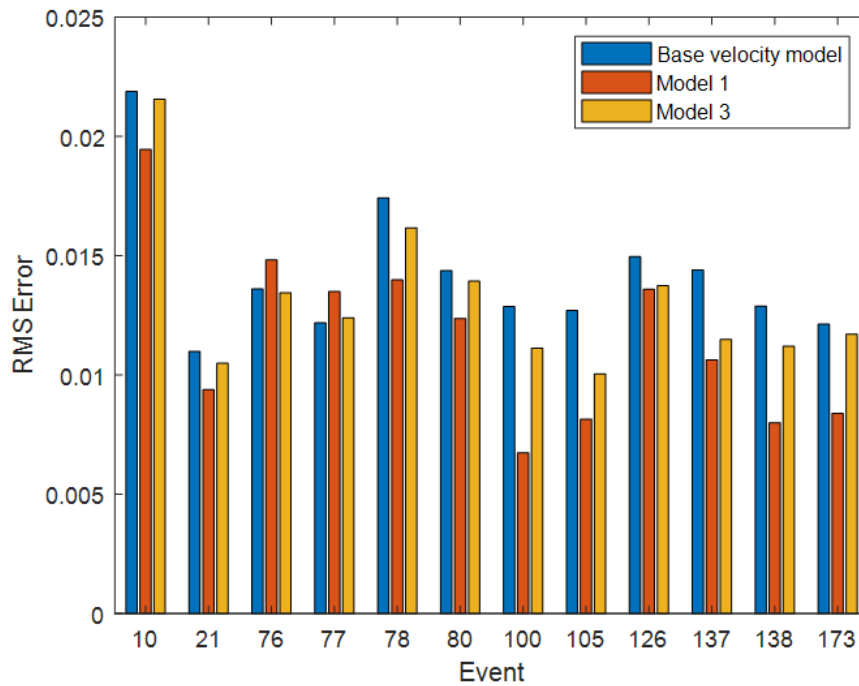


Figure 5.19: A comparison of the RMS errors from the positioning of the event subset between the base velocity model, velocity model 1 and 3

Figure 5.19 shows that constraining the maximum velocity restricts the improvement in RMS error for the majority of events but these all show an improvement in the RMS error compared to using the base velocity model. There is one event, id 77, where the base velocity model is smaller than the RMS error than either of the optimised velocity models. In this event, model 3 is closest in accuracy compared to the base velocity model. Given this, and the improvement to the main event, model 3 is to be used as the velocity model for the next performance check, uniqueness. This velocity model is shown below as figure 5.20.

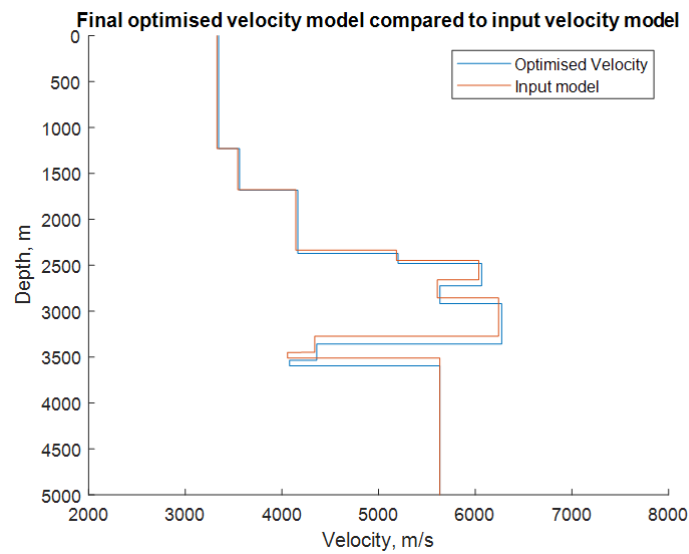


Figure 5.20: Velocity model 3 as calibrated by the optimisation process

Model Uniqueness

As the VFSA process relies upon a Monte Carlo approach, the global minimum may not be reached within the process and it may settle at a different local minimum depending on the run. While steps were taken to minimise this by setting a temperature schedule that resets back to the initial temperature half-way through the process, further mitigation steps may have to be considered. This is reviewed by running the VFSA process multiple times with changes made to the initial velocity model to see if the same velocity model can be reached regardless of the initial velocity model. Figure 5.21 shows the process after it has been run twice with these changes.

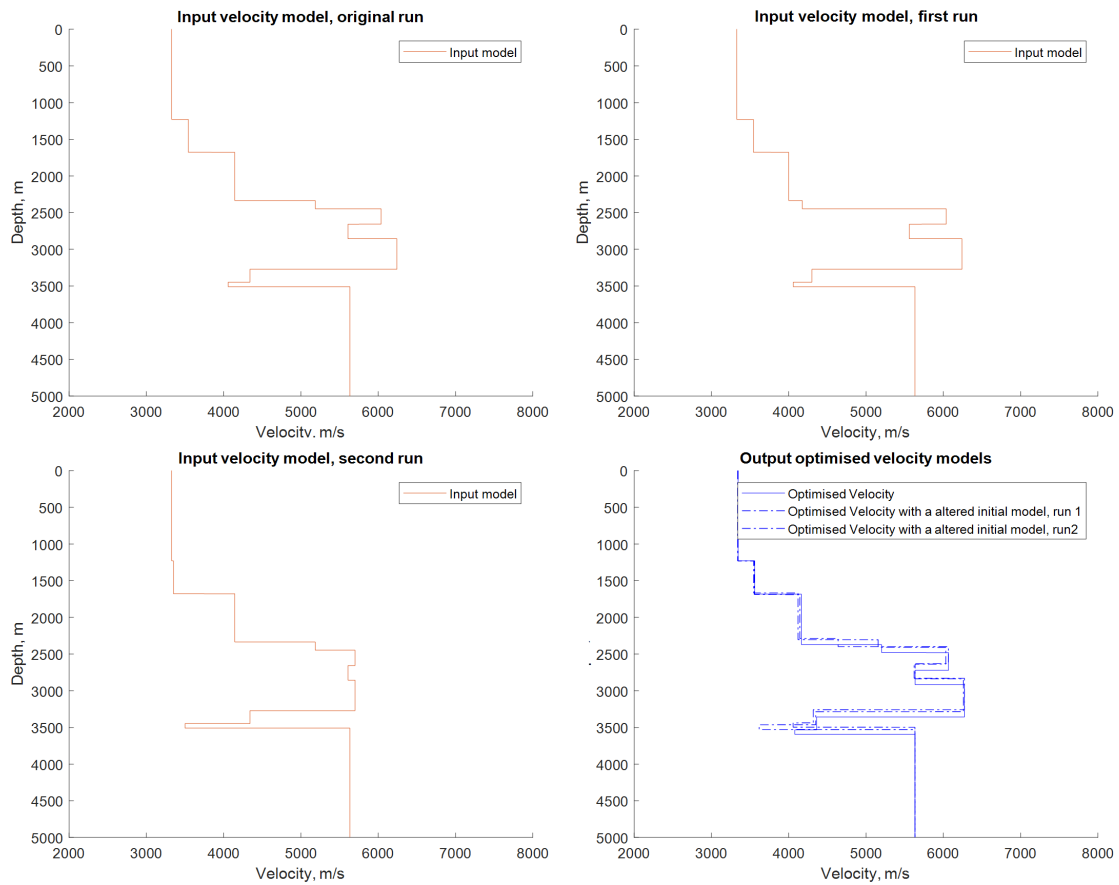


Figure 5.21: A comparison of the output velocity models after two runs with different initial velocity models to consider the uniqueness of the output model. The output models are similar especially layers 5 to 8 at model depth 2250 to 3000 m, showing that the combination of source-receiver paths and the temperature schedule enable the method to reach a global minimum

As shown in figure 5.21, there is little change in the optimised models from the different runs especially layers 5 to 8 at depths 2500 m onwards. This shows that the model fitting process is outputting a unique velocity model given the constraints and input parameters and this velocity model should be considered as final from the VFSA process.

5.3.5 Stage 3 of velocity model development: Final quality control checks and comparisons

The RMS error from the positioning of the events using the final velocity model is compared to RMS errors from positioning using velocity models A and B in the bar chart below.

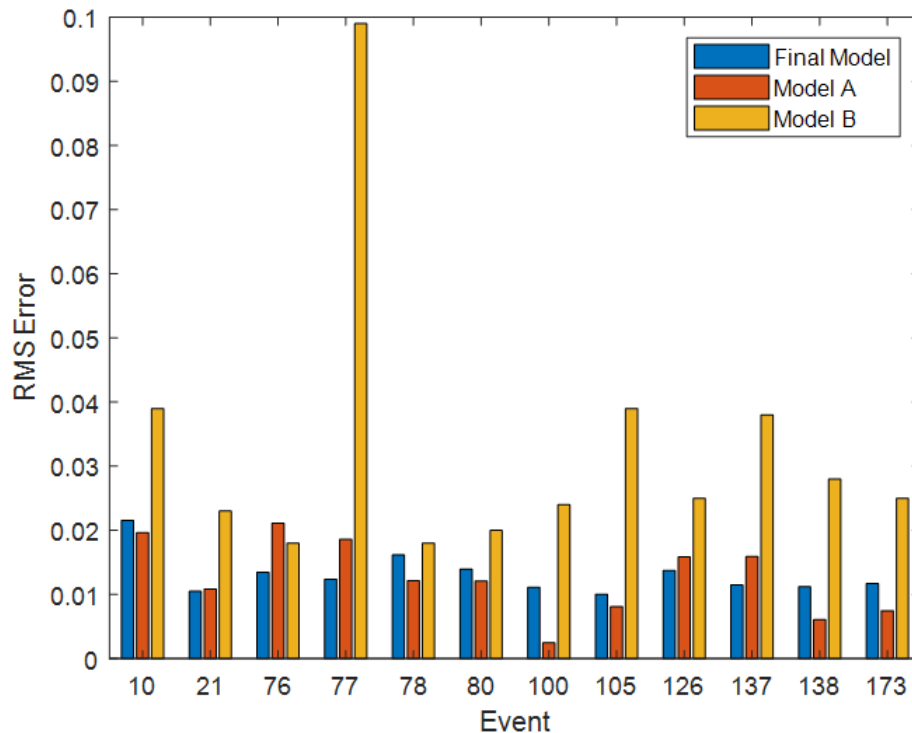


Figure 5.22: A comparison of the RMS errors from the positioning of the event subset between the final velocity model and velocity model A and B

The bar chart in figure 5.22 shows that the final velocity model has successfully improved the error for the main event and 5 of the other test events compared to

both velocity models provided by the contractors. All of the events positioned using the final velocity model has an RMS error lower than those positioned using velocity model B, unaltered from the original well log. These comparisons show that the new velocity model is suitable for use with the software system as it has improved the main event accuracy and the positions of the majority of events around the site.

5.4 Development of an attenuation model for use with the software system

The second of the pre-requisites for the software system is an attenuation model. The attenuation model is required to compensate for the loss of energy from intrinsic (Q_{int}) and scattering losses (Q_{app}) between the source and receiver. This loss of energy alters the received signal to the extent that it needs to be compensated for during the application of the software system. This section details the model used to generate the attenuation model required for the software system.

5.4.1 Modelling method to be employed

Method to calculate Q_p from microseismic signals

The methods used to calculate attenuation from seismic data were reviewed by Tonn (1991). Of these methods, the rise time method as detailed by Gladwin and Stacey (1974) will be used as this method does not require source information. This method is based on measuring the change in the rise time, the time between the start of the wavelet and the tangent of the point of maximum slope, and the relation,

$$\tau = \tau_0 + C \int_0^t Q^{-1} dt. \quad (5.7)$$

In equation 5.7, τ is the rise time, τ_0 is the rise time at the $t=0$, C is a source-specific constant, and Q is the assumed frequency-independent attenuation. This method differs from the spectral ratio method by Tonn (1991) which requires a spectrum close to the source to be captured. As this microseismic survey was acquired using a surface array there is no opportunity to capture the spectrum close to the source as the minimum distance between the sources and receivers exceeds 2100 m. The rise time method was expanded by Tselentis et al. (2010) using tomographic concepts, to generate a 3D model of both Q_p and Q_s variation over the Rio Antirrio straits area.

The method detailed by Tselentis et al. (2010), considers equation 5.7 with constant Q_p and V_p as,

$$\tau = \tau_0 + \frac{CT}{Q}. \quad (5.8)$$

For each passive seismic event used to generate the attenuation model the rise time at each receiver is measured. These rise times are plotted against the travel time of

the raypath and the initial rise time τ_0 is calculated using linear regression to find the y-axis intercept. With the initial rise time known from linear regression, equation 5.8 can be rearranged to find Q for that raypath.

Derivation of Q_p model

When deciding on the method used to generate a model from the attenuation values, the number of dimensions to be modelled was considered. As the seismic data is acquired in a surface array and as the majority of the seismic events are within a band of 2000 - 2600 m there is no meaningful relationship that can be derived for Q_p between the surface and 2000 m as the variations in Q with depth cannot be separated from the lateral variations of Q. This means that a 2D attenuation model that varies laterally would be a logical choice.

To generate a 2D model of the attenuation values for this site two passive seismic events were used. The events chosen for this purpose were ones which positioned laterally as close as possible to the seismic stations 51 and 59. This ensures that the measured attenuation values for these stations can be considered constant for this grid cell.

5.4.2 Stage 1 of attenuation model development: Rise time measurements

The first stage in the modelling was to calculate the attenuation from the microseismic signals for the two chosen events. The P-wave arrival times for these events (Ids 77 and 78) were identified and these were repositioned using the velocity model generated in section 5.3. Following the method by Tselentis et al. (2010), these two events are low magnitude to ensure that rise time directivity effects are minimal, and have a high signal to noise ratio to assist clarity while picking.

With the first arrivals picked and events repositioned, the rise time values were identified within Matlab. Firstly the record was resampled to a 1 ms sampling interval from the original 2 ms sampling interval. Secondly, to ensure repeatability, the start of the wavelet was identified by taking a 200 ms time window around the first arrival point and using an autopicker to pick when the wavelet starts. This autopicker from the CREWES toolbox is based on an average magnitude method and the picking point was set to occur when the ratio of maximum amplitude to sample average amplitude exceeded 10. The rise time end-point was set at the first zero-crossing point following Tselentis et al. (2010) as the picking point as set out by Gladwin and Stacey (1974)

cannot be reliably picked on data where scattering and secondary arrivals interfere with the signal. All three vertical channels available were used to measure the rise time lengths which were then averaged using a median filter.

To calculate the initial rise time τ_0 , linear regression was utilised within Matlab using the median averaged risetime values and the travel times as identified from the start of the wavelet minus the origin time. Figure 5.23 and 5.24 show the resulting graphs from this process which identify the initial rise time to be 0.013 ± 0.004 and 0.012 ± 0.003 for events 77(nearest to station 51) and 78 (nearest to station 59) respectively. Using the initial rise time values and the measured rise times the attenuation values were calculated together with the 95% confidence limits.

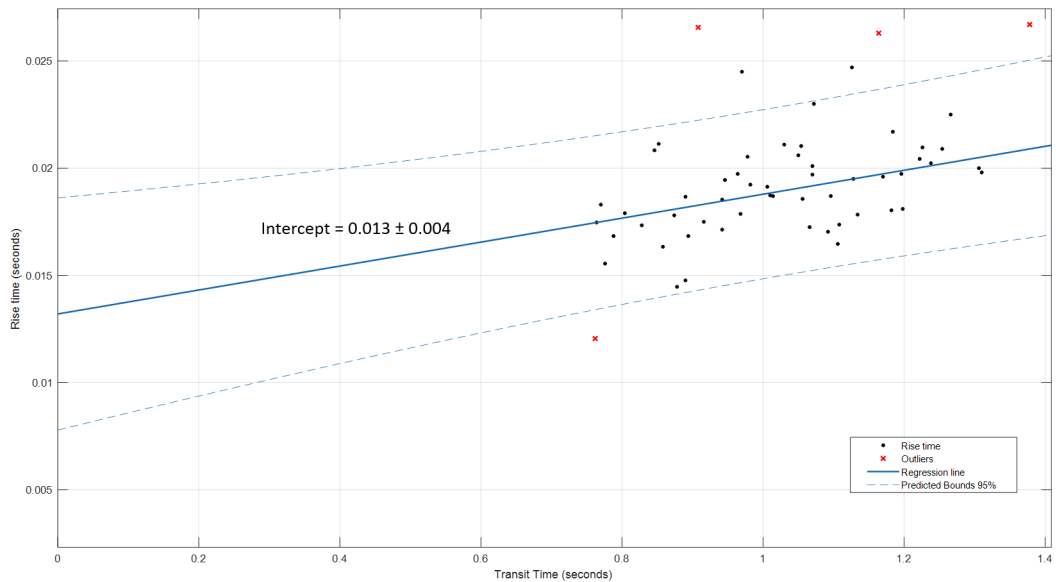


Figure 5.23: Calculation of the initial rise time from the measured rise times from event 77, nearest to station 51. The initial rise time for this event is calculated to be 0.013 ± 0.004 seconds

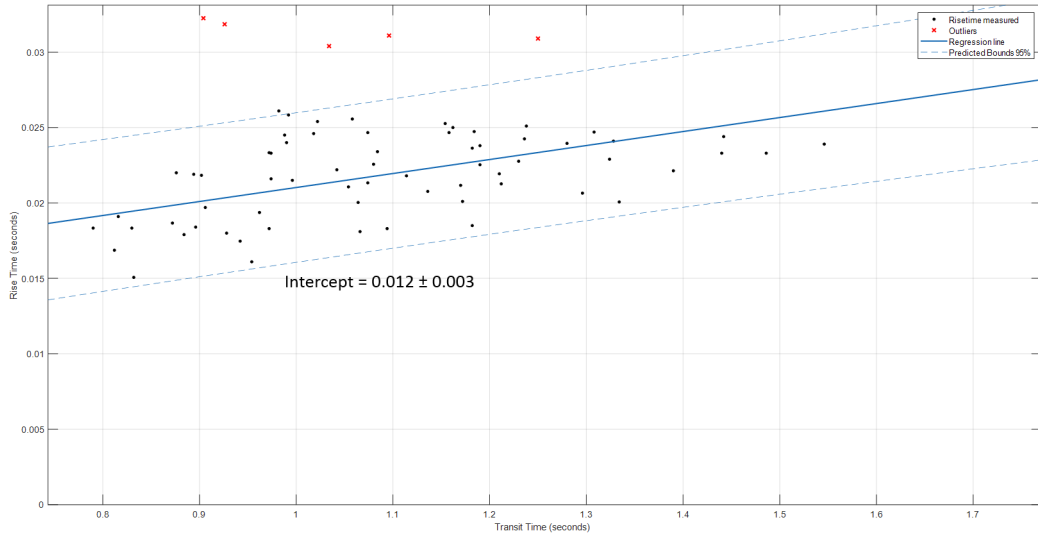


Figure 5.24: Calculation of the initial rise time from the measured rise times from event 78, nearest to station 59. The initial rise time for this event is calculated to be 0.012 ± 0.003 seconds

5.4.3 Stage 2 of attenuation model development: 2D attenuation model derivation and verification

To generate a 2D model from the attenuation values, one event was used to derive the model and the second event was used for verification purposes. Event 78 which was closest to station 59 was utilised to generate the 2D model, as this positioned in the centre of the survey grid.

The first step was to use the travel times to each station and generate a travel time map from the source to all stations using the scattered interpolant function within Matlab, regularised onto a 100 x 100 m grid using the ‘natural’ regularisation method. Secondly, the calculated Q_p values were used together with the travel times to calculate the T^* for each station. This was also gridded using the scattered interpolant function and regularised onto the same grid using the same regularisation method. In order to avoid extrapolation of the Q_p values to excessively large or small values, the corner points of the grid were set a Q_p value of 200 to ensure that in areas of no data, the Q_p values linearly increases up to a maximum of 200. These two maps were then divided together on a grid cell by grid cell basis to calculate Q_p . This process was repeated for the minimum and maximum Q_p values as decided by the 95 % confidence

limits from the regression of the initial rise times. The median attenuation map is presented as part of figure 5.25.

To verify the attenuation model, the Q_p measurements made on event 77 were used. The measured Q_p values were compared to the model Q_p values. The modelled Q values were calculated by taking the ray-traced path and summing T/Q_p values along the path between source and receiver, where T is the sampling interval for the ray trace in time and Q is the attenuation that is applied at that point along the path taken from the model.

These values are compared in figure 5.26 which shows that the modelled Q_p are within the error bounds of the measured Q_p values. This comparison shows that the attenuation model is suitable, given the acquisition geometry, for use with the software system.

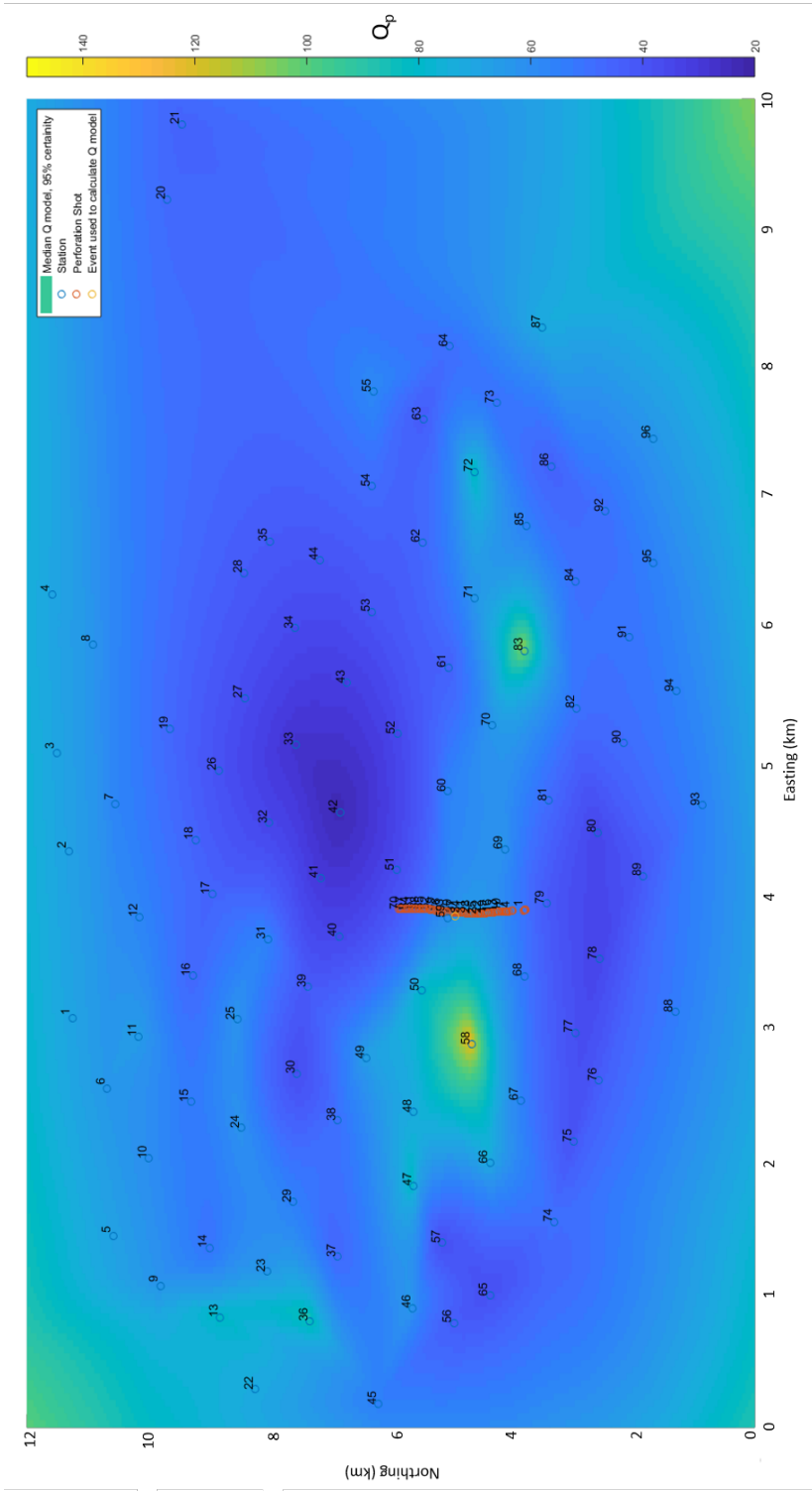


Figure 5.25: The median attenuation map as gridded onto a 100x100 m grid using the rise time values measured from event 78, nearest to station 59.

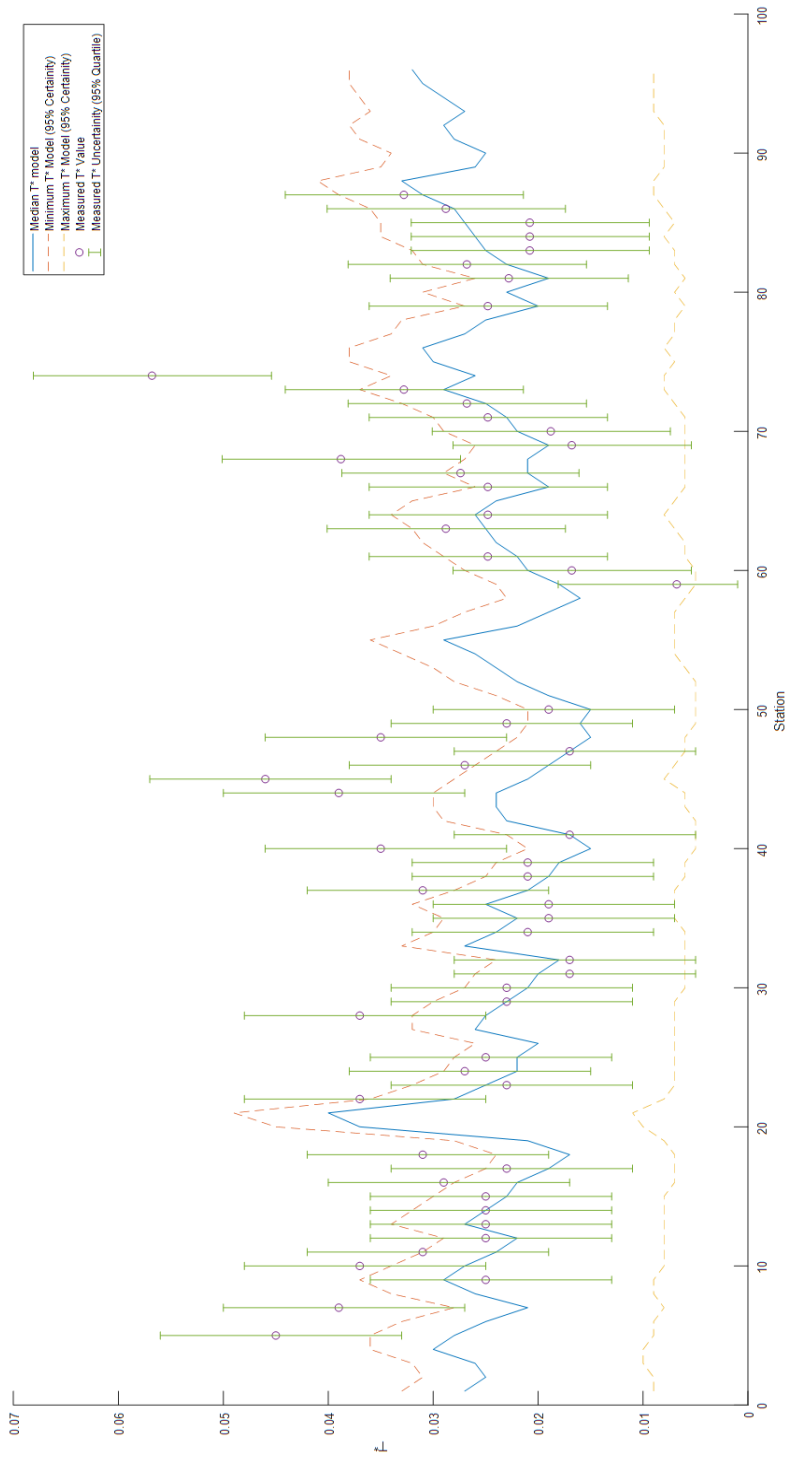


Figure 5.26: Verification of the Qp model using event 77 showing the comparison between the measured Q_p values with the 95% confidence limits and the modelled Q_p values with the 95% confidence limits

Chapter 6

System Development: Implementation and testing with a single event

6.1 Introduction

This chapter documents the implementation and testing of the software system given the three programming requirements as detailed in chapter 2, the methodology as decided upon in chapter 3 and using the pre-requisites derived in chapter 5. The programming requirements were:

1. The capability to monitor for hydraulic connections from the wellbore activating fault lines
2. The capability to monitor for static stress transfers triggering seismic events
3. The capability of running in real-time.

The software system is split into separate modules and each module was developed using an iterative software prototyping approach. In this approach, the software design and implementation were iterated until the software module reached functionality as judged compared to a set of functionality tests. A flow chart of this approach is shown as figure 6.1 and shows the cyclic nature of design, implementation, testing and appraisal.

There are four separate modules in this system and these are shown on a flowchart of the system design as figure 6.2 with the inputs, intermediate outputs and final

outputs. The final outputs for the software system are two maps updated in real-time, a fracture map showing the evolving fracture network with fluid injection and a Coulomb stress change map.

This chapter will outline, for each module, the software design based on the theoretical relationships established in chapter 3 with the validity of using such a method at the microseismic scale. Secondly, the implementation of the software design is detailed and this programming is verified with details from the testing programming.

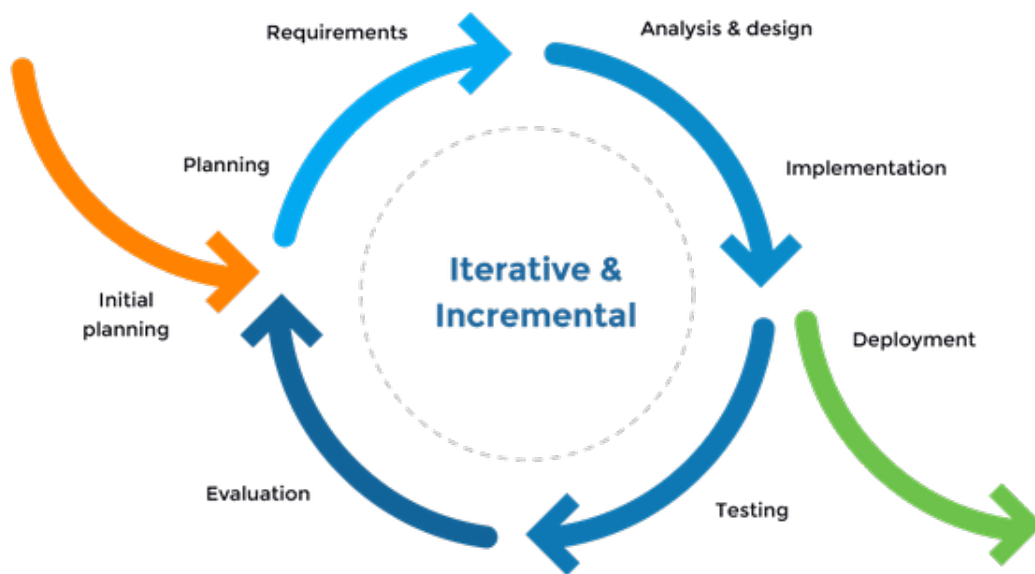


Figure 6.1: The iteration prototyping model. This model is split into design, implementation, testing and evaluation

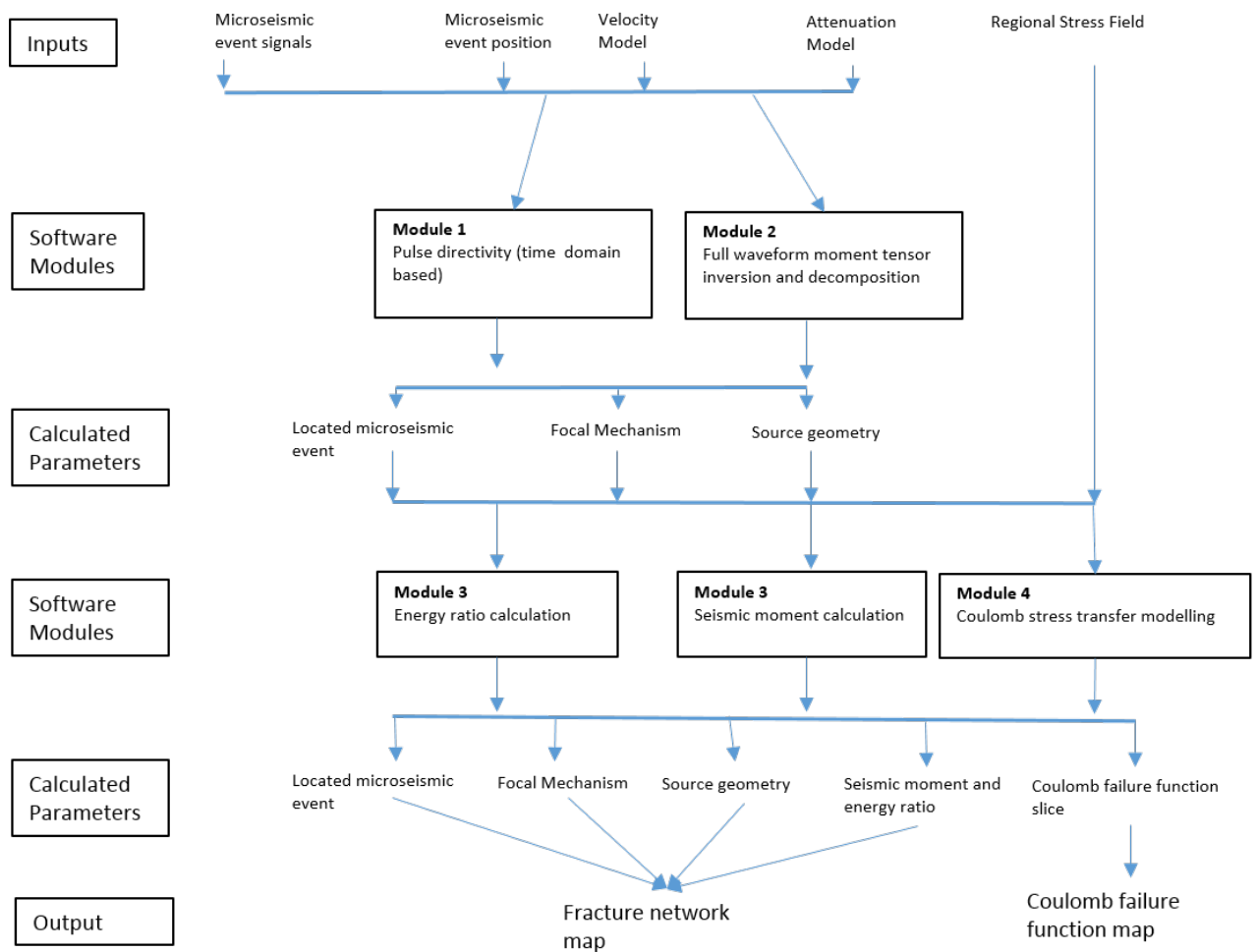


Figure 6.2: The software systems flowchart. There are four modules in this system, Pulse directivity, Moment tensor inversion and decomposition, Seismic moment and energy ratio calculation and Coulomb stress failure modelling

6.2 Testing target

Development of these modules started before the industrial dataset was made available. During this time, initial testing was conducted using, forward models, synthetic events and a single event from the Cotton Valley academic microseismic dataset. The purpose of this initial testing was to gain a deeper understanding of the way the methods operated, allowing these methods to be extended to be applied in an automated manner. This initial testing allowed a focussed testing plan, concerned with the conditions associated with industrial datasets, could be implemented once the Waighan dataset was made available.

To ensure that testing and development with the Waighan dataset was efficient, a single event was utilised. This enabled an efficient prototyping methodology, minimising the processing between iterations of the module development. For this testing, a single event, ID 21, as identified in the previous chapter was used. This event is the first event where the signal to noise ratio is sufficient to clearly see the signal wavelet. While the main event (ID 76) could have been used for this testing, the signal is clipped on the majority of channels, frustrating the prototyping process and potentially leading to poor processing decisions when compared this to the other events in the case study.

The details of event 21 at the start of the processing sequence is :

- Position (re-calculated using new velocity model and referenced to the well position): 102.2 m, 808.7 m, 2692.246 m
- Magnitude Mw (Contractor A) : -0.94
- Magnitude Mw (Contractor B) : 0.75

An example of the data record for event 21 showing the P- and S- wave arrivals are shown as figure 6.3.

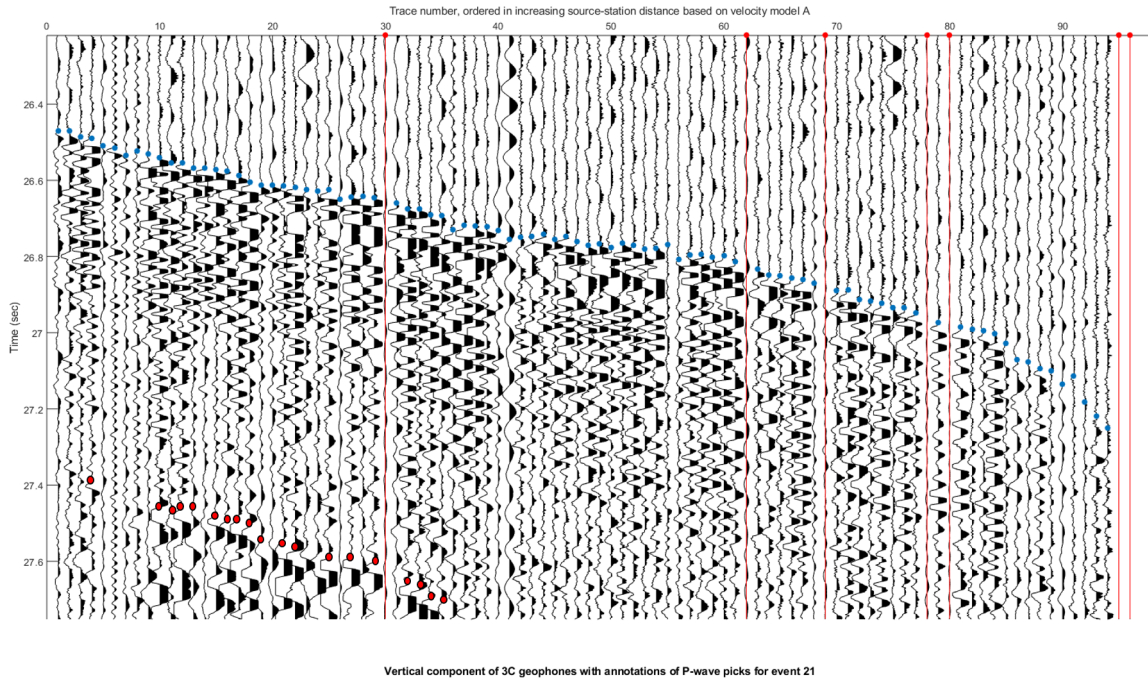


Figure 6.3: Data record for Event 21 with the P- (blue points) and S- (red points) wave arrivals annotated.

6.3 Software module 1: Wavelet variation to determine the rupture geometry, direction and velocity

The first module of the software system which to be developed uses the relationship between the duration of the seismic signal to the geometry, direction and velocity of a fault or fracture. This information is part of the solution for requirements 1 and 2 of the software system requirements. To ensure that the module follows requirement 3, capable of running in real-time, a time-domain methodology was implemented due to the reasons discussed in chapter 3.

The starting basis for this method is the model by Zollo and de Lorenzo (2001), as this calculates a result on an event by event basis in the time domain. The method by Zollo and de Lorenzo (2001) uses a series of relationships to determine the Q model as well as the required rupture parameters. In this implementation the Q model has been separately defined, simplifying the method by removing free parameters from

the calculations.

Prototyping for this module began before the Waighan dataset was made available and forward models, synthetics and the Cotton Valley dataset were used to test the developing method in the interim. It was only after the Waighan dataset arrived and module development was focussed on the challenges retaining to the industrial dataset that clear programming objectives set to programming iterations could be established. These challenges required four distinct iterations of the module development. Rather than describing the design, implementation and testing of each individual iteration, the final iteration is described in this chapter. Details of the implementation changes made after iteration are detailed in table 6.1 within the implementation section.

6.3.1 Design and Verification

Theory and initial design

The key formulation used in this module relates the P-wave duration time, $t_{d\alpha_0}$, to the direction and geometrical parameters of the fracture as shown in Ben-Menahem and Singh (2012) as,

$$t_{d\alpha_0} = \frac{L}{V_f} \left(1 - \frac{V_f \cos\theta}{\alpha_v}\right), \quad (6.1)$$

where L is the length of the fracture, V_f is the rupture velocity, α_v is the velocity for the P- wave arrival and θ is the horizontal angle (strike) of the fracture. The P-wave duration time is calculated as the time between the start of the wave and the second zero-crossing on particle velocity data.

This equation is based on the assumption that the receivers and source are on the same plane. To take account for the vertical angle and for an independent fracture azimuth (θ) compared to receiver azimuth (η), equation 6.1 is modified to,

$$t_{d\alpha_0} = \frac{L}{V_f} \left(1 - \frac{V_f \cos(\phi_r) \cos(\eta - \theta)}{\alpha_v}\right), \quad (6.2)$$

Given the input variable, the P-wave duration time ($t_{d\alpha_0}$) and the constants of P-wave velocity (α_v), receiver azimuth (η) and inclination (ϕ_r) there are three output variables, fracture length, velocity and direction. As there are three output variables, it would be sensible to incorporate another data point and accordingly another equation into the design of this module. This is managed by using the equation for

risetime. Risetime is a measure of the start of the wavelet to, according to the convention set by Zollo and de Lorenzo (2001), the first zero crossing point of the wavelet on particle velocity records. The risetime relates to the length and velocity of the rupture by,

$$\tau_0 = \frac{L}{V_f} \left(1 - \frac{V_f \cos(\phi_r)}{\alpha_v}\right), \quad (6.3)$$

where ϕ_r is the inclination angle of the ray from the horizontal axis.

Microseismic scale validation of the initial design

As part of their study, Zollo and de Lorenzo (2001) tested this method on a 3.1 magnitude seismic event. This is categorised as a minor earthquake. The size of the test event and of the other events detected in the survey are at the micro-scale, of which the maximum moment magnitude is 0 with a minimum of -4 (Euzen, 2011).

The theoretical equations as defined from Menahem and Singh for rupture time and rise time do not signify there is a scaling limit at when the above method could not be applied, therefore the only restrictions are on the ability of the sample rate of the seismographs to record such variations. For example, if the test event is considered with a fracture length of 1 m and 100 m and a rupture velocity of 2.7 km/s this would correspond to a variation in rupture time with azimuth from 0.4 ms to 40 ms respectively. Similarly, with regard to the rise time, this would correspond to a variation with inclination from 0.1 ms to 14 ms for a fracture of length 1 m and 100 m respectively. To measure both the rupture time and rise times for these two models, an appropriate sampling rate must be utilised to ensure the rupture time and rise times are sampled correctly. Following the Nyquist-Shannon theorem, the sampling interval used needs to represent the smallest possible rupture time and rise time to be modelled. In these two models, this corresponds to a minimum rupture time of 0.17 ms and 17 ms and for the rise time of 0.13 ms and 13.1 ms. So to theoretically measure the rupture times and rise times for these models a sampling interval of 0.08 ms and 8 ms respectively would theoretically allow both the rupture time (equal to the periodicity of the wave) and the rise time (half the periodicity of the wave) to be measured in the time domain.

In this case study, the sampling interval is 2 ms, meaning the smallest possible rupture duration that can be sampled at this sampling rate is 4 ms. With the Zollo and de Lorenzo (2001) model and the geometry for the test event, this corresponds to a minimum rupture length of 23.2 m. For the rise time, which is half the periodicity of the wave, this is 2 ms and equates to a corresponding rupture length of 16 m.

Final design

Equations 6.2 and 6.3 were used as stated for the first two iterations of the development. However, the resulting outputs from iteration 2, highlighted that the Ben-Menahem and Singh (2012) model could not sufficiently model the rupture time compared to the measured data. This is shown in figure 6.4, where the modelled curve, using outputs from the separate calculation for the risetime, is smaller than the measured values. Moreover, there is no clear peak or trough in the measured data which is predicted from the Menahem and Singh model.

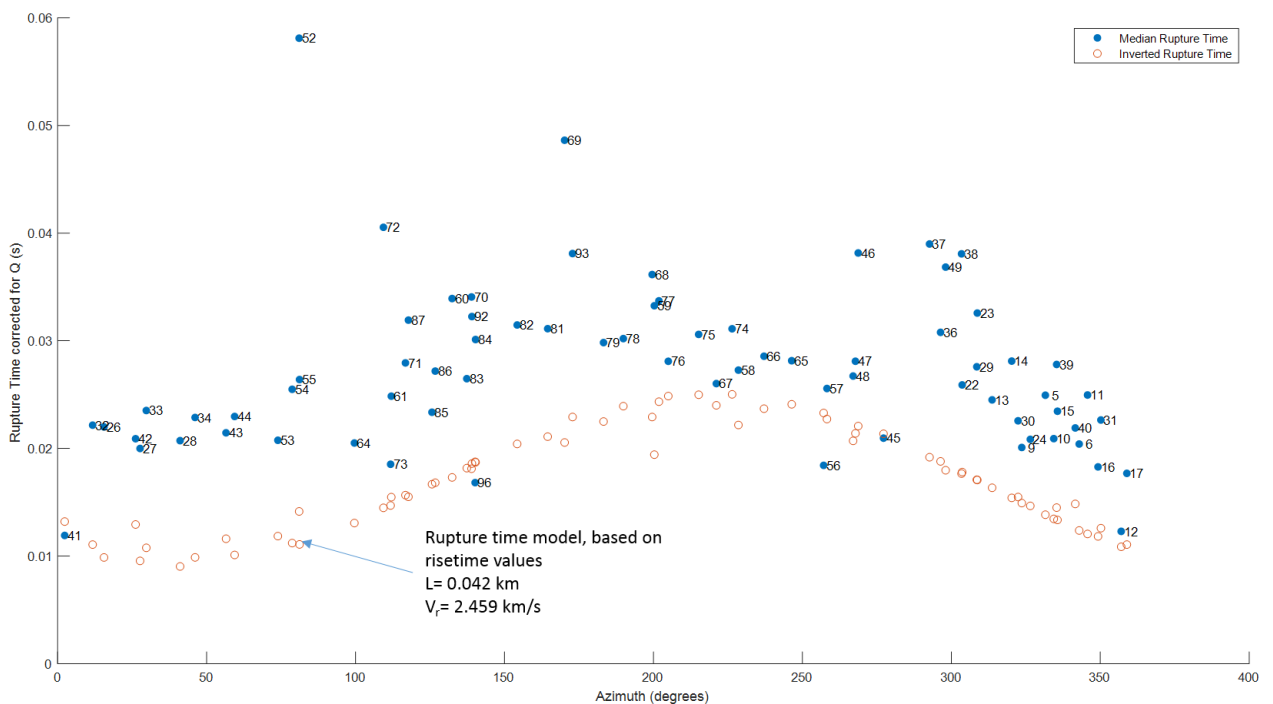


Figure 6.4: Difference between the Zollo and de Lorenzo (2001) model (red hollow points) and the measured data. The Zollo and de Lorenzo (2001) model here is based on the results from the analysis of the measured rise times using equation 6.3. The measured points do not follow a simple sinusoidal model as predicted by the Zollo and de Lorenzo (2001) model, highlighting that this model is not the correct choice for this data.

To resolve this problem, the model by Cesca et al. (2011) was utilised. This is an evolution of the Menahem and Singh model and considers bilateral, asymmetric

bilateral and unilateral ruptures. The different rupture types as outlined by Cesca et al. (2011) are shown as figure 6.5.

The equation used to define the rupture time for the Cesca et al. (2011) model is,

$$\Delta t(\phi_r) = Max[\tau_0 + L_1/v_f - (L_1/\alpha_v)\cos(\phi_r), t_r + L_2/v_f + (L_2/\alpha_v)\cos(\phi_r)], \quad (6.4)$$

where L_1 and L_2 are the lengths in the two opposing directions. Equation 6.4 essentially uses equation 6.1 to define the rupture time for two opposing directions and then uses the maximum rupture time as defined by the MAX function to calculate the resulting ‘apparent’ source duration. The term ‘apparent’ is used as this time is defined from the frequency domain meaning that it also includes the rise time parameter, a parameter not required in the definition of rupture time in the time domain. Given the above model and changes made to define equation 6.2 from the base equation in 6.1, the following equation defines the rupture time for a bilateral to unilateral rupture in the time domain as,

$$t_{d\alpha_0} = Max\left[\frac{(1-\chi)L}{V_f} - \left(\frac{(1-\chi)L.\cos(\phi_r)\cos(\eta-\theta)}{\alpha_v}\right), \frac{\chi L}{V_f} + \left(\frac{\chi L.\cos(\phi_r)\cos(\eta-\theta)}{\alpha_v}\right)\right], \quad (6.5)$$

where χ is the ratio between the shortest segment and the entire rupture length.

The system design will implement equations 6.3 and 6.5 together.

Microseismic scale validation, final design

Moving from the Zollo and de Lorenzo (2001) model to the Cesca et al. (2011) model for the rupture time means that the minimum fault size has to be verified again to ensure that this method can be applied to this case study.

The minimum rupture time that is possible with the Cesca et al. (2011) matches the same minimum rupture time for the Zollo and de Lorenzo (2001). The challenge with the Cesca et al. (2011) model is the range of rupture times is smaller compared to the Zollo model and the variation with azimuth may not be resolvable for bilateral ruptures ($\chi=0.5$). This consideration is shown in figure 6.6 from using a forward modelling approach.

The above consideration is assuming there is no attenuation applied between source and receiver. Attenuation will always increase the apparent rupture and rise times

causing (assuming the attenuation between source and receiver is known) the minimum resolvable fault length to increase. So for the test event the minimum and maximum correction for attenuation, the T^* variable used in this method, is 6 ms and 19 ms respectively. The relationship between the measured and source rupture and rise times is an additive relationship so the presence of attenuation means that the minimum rupture time has to be simply greater than the attenuation correction.

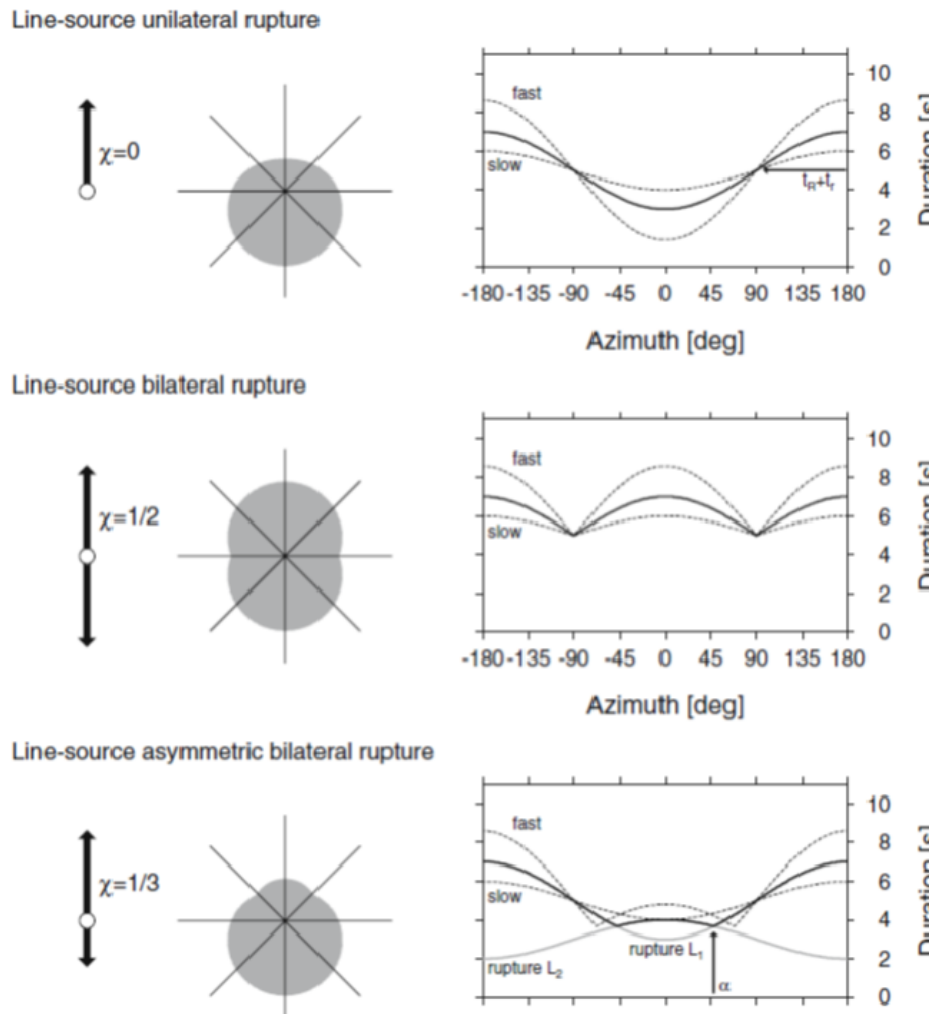


Figure 6.5: Theoretical models for different rupture types from Cesca et al. (2011) with (top) pure unilateral rupture, (centre) pure bilateral rupture and (bottom) asymmetric bilateral rupture. The left-hand side image shows the movement on the fault and the radiation pattern emitted. The right-hand side image shows the rupture time models for each of these rupture types.

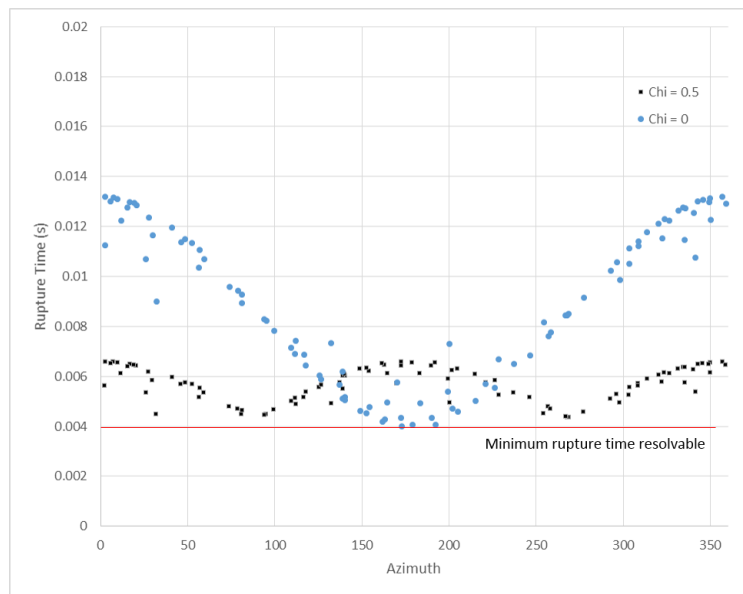


Figure 6.6: Forward modelling of the rupture time using the Cesca et al. (2011) model for a unilateral and bilateral rupture, with the minimum resolvable rupture time without attenuation for a sampling rate of 2 ms.

6.3.2 Implementation

This central part of this module is programmed in MATLAB with ancillary functions running in Python. The starting point for this module is to load the relevant data into memory. For this module, this consists of the data records, first arrivals, velocity and attenuation models, station position, and event position which are retrieved from data storage.

Implementation stage 1: First arrivals, rise time and rupture time identification

The first stage in implementing the method is to set-up a clear consistent methodology to identify (1) the first arrivals (2) the rise times and (3) the rupture time. With regard to (1) although as part of this system's overall progress, the first arrivals have already been identified in a previous stage, the accuracy of these picks needs to be consistent throughout the record. Similarly, with regard to (2) and (3), the time identification for these values is crucial as the variation in risetime and rupture time with inclination and azimuth is 10 ms and 30 ms respectively for a 75 m long fracture.

To these ends, the seismic signal is firstly re-sampled down to 1 ms from 2 ms to improve the picking accuracy. With this completed, an autopicker is used to identify a consistent first arrival. This autopicker uses the ratio of maximum amplitude to sample average amplitude to determine the first arrival and is part of the CREWES toolbox. A time window of 100 ms is used, centred around the origin time point.

While the risetimes and rupture times should be automatically measured from the data records in a real-time system, this case study, in particular, showed a number of data quality limitations which precluded this. Testing of iteration 1 of this module with automated algorithms to determine risetime and rupture time showed that the picking accuracy was extremely variable leading to a null output. This inaccuracy was due to variations in the polarity of the first break and local wave effects in the way the geophones channels were installed. To manage the first issue, manual verification of all traces is firstly carried out before any identification of the first arrivals, rise times or rupture times is conducted.

The risetimes are calculated by firstly identifying the smallest amplitude sample in the 100 ms time window after the wave arrives. With this point manually identified, the first zero-crossing is calculated automatically. To ensure that this is accurate as possible, the amplitude samples either side of the zero-crossing are taken and are interpolated to a 0.1 ms sampling interval. This process is conducted on all three

channels within each station, a total of 288 possible traces. The values for each station are median filtered to form a single value for each station.

With regard to measuring the rupture time, during the testing of iteration 1, the rupture lengths measured from the geophone channels installed at 20.9 m and 13.9 m in each station borehole were significantly different than the models for rupture lengths indicate for the small additional distance travelled from the 27.9 m geophone. For this reason, only the deepest channel at 27.9 m was used to identify the rupture length. This identification process was conducted manually as there were still local wave effects which stopped the automated algorithm from functioning efficiently. These issues are documented as part of the overall iteration changes log in table 6.1 at the end of this section and as a series of figures in the appendix. In all the rupture time models, the time should gradually increase or decrease with a change in azimuth. To ensure that the identification of the rupture time is consistent with these models and there are no sharp drops, the traces are ordered and measured primarily by azimuth and then by inclination.

As an example, these three picks are shown on a data record shown in figure 6.7.

Implementation stage 2: Calculating the average attenuation and velocity applied to each raypath

During passage of the wave between the source and receiver, attenuation as described by the seismic quality factor, Q_p will extend the wavelet length and the measured risetimes (τ) and rupture times ($t_{d\alpha}$) will be in error unless attenuation is compensated for. To compensate the measured risetimes for attenuation the following relationship is used as,

$$\tau = \tau_0 + C \frac{T}{Q_p} \quad (6.6)$$

and for the rupture times a similar relationship is used as,

$$t_{d\alpha} = t_{d\alpha 0} + C \frac{T}{Q_p}, \quad (6.7)$$

where C is a source-specific constant, T is the travel time, Q_p is the seismic quality factor, and where τ_0 and $t_{d\alpha 0}$ are the risetimes and rupture times at the source.

There are two parameters that are required for these equations, C the source-specific constant and Q_p the seismic quality along the raypath. With regard to the source-specific constant, C, this has been experimentally determined from ultrasonic acoustic pulses (Gladwin and Stacey, 1974) to be 0.5. For the case of small events, a C value of

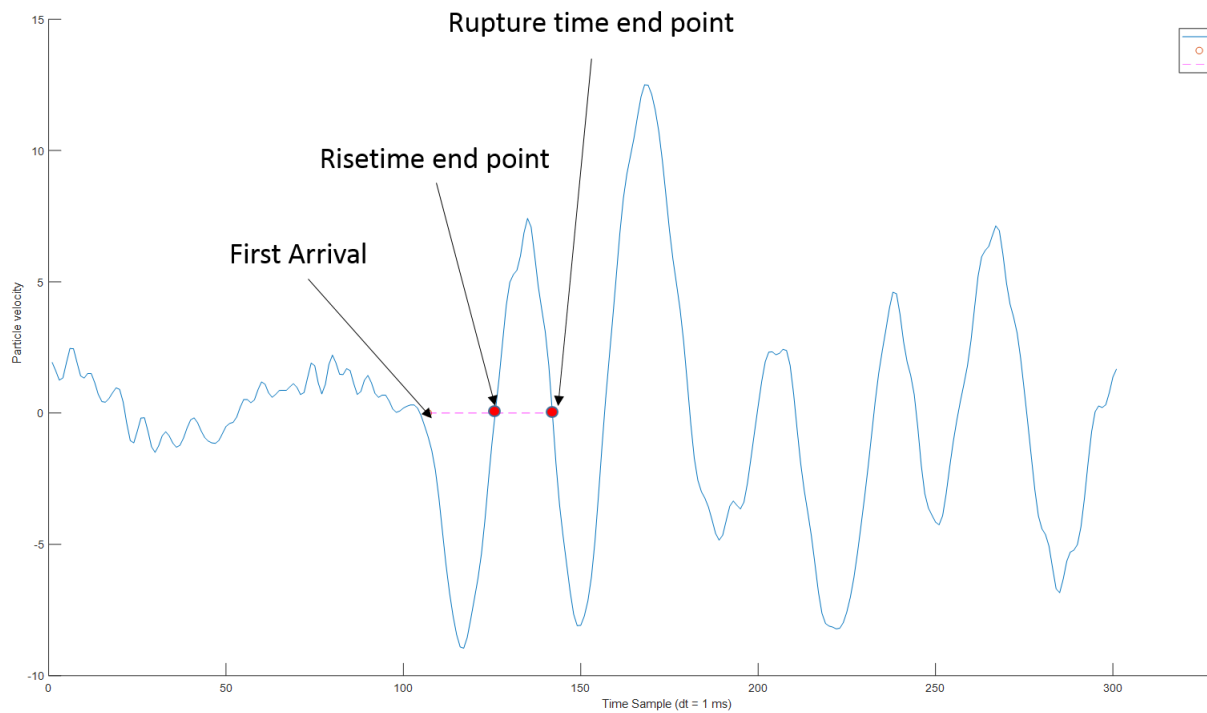


Figure 6.7: Example of a seismic record from event 21 with the first arrival, risetime length and rupture length annotated

0.5 corresponds to an impulsive displacement function is commonly used (De Lorenzo and Zollo, 2003). The seismic quality factor that is used for each receiver is determined from a ray trace through the 2D Q_p model. At each time step of 2 ms, the T^* value (T/Q_p) is calculated. These are summed to calculate the attenuation applied to each ray and can be used to remove the attenuation from the measured risetimes and rupture times when required.

Implementation stage 3: Non-linear equation solver

With a set of risetimes and rupture times measured, and the velocity and attenuation parameters calculated, equations 6.5 and 6.3 can be solved for rupture length, velocity and direction. The method established, after iterating through four evolutions of this module, is to solve for the fracture length and velocity from the risetimes first and use the output for fracture velocity as a held parameter to solve for fracture length,

the ratio of segment sizes χ and the fracture direction from the rupture times.

Before any computation is conducted, an additional data filtering step is applied. To ensure that risetimes and rupture time are taken only from stations where the Q_p model has correctly compensated for attenuation, the risetimes are compensated for Q_p using equation 6.6 and the median Q_p model. Any risetimes which are negative or greater than the nearest station to the source are flagged to be removed during the computations. This flag persists through the rupture time calculations.

To solve equations 6.5 and 6.3 and compensate for attenuation, these two equations are firstly substituted into the relevant Q_p compensation equations, equations 6.6 and 6.7. Both of these equations are solved using orthogonal distance regression (ODR) in Python based on the Fortran code originally by Boggs et al. (1989). Ordinary least square (OLS) regression procedures treat the data for explanatory variables as fixed, i.e. not subject to error of any kind (Boggs et al., 1989). ODR lifts this restriction and errors can be propagated through both the ‘independent’ and ‘dependent’ variables. This is key in this situation as the regression is solved based on the inclination and azimuths as the dependent variables for the risetime and rupture time respectively but the main source of error for both of these calculations is the Q_p value, an ‘independent’ variable. There is also scope for expansion with additional error estimates on the other ‘independent’ variable of velocity. Using such an approach also allows the 95% quartile results to be calculated as part of the computation.

Error estimates are described in the ODR algorithm as a set of variances, one for each ray path calculated from 95% quartile range from the Q_p model. An initial estimate of the output results is also required for ODR. For the risetime calculation, this is a fracture length of 0.2 km and a fracture velocity of 2.5 km/s. For the rupture time calculations, these are a fracture length of 0.2 km and a fracture direction based on the azimuth from the minimum rupture time. The χ parameter that defines the segments for the unilateral/bilateral rupture was a sensitive parameter and was decided on a case by case basis following the example models in figure 6.5 with values 0.1, 0.2, 0.3 and 0.4 trailed until an acceptable fit was acquired.

To implement such code in MATLAB, all required data (including ray-by-ray variances for the Q_p model) are imported into Python, whereupon the ODR flow is instigated and the output results together with the 95% quartile range, exported back into Matlab. In Matlab the output results are used to forward model the risetimes and rupture times accordingly and these are overlaid on a figure together with the original measured data. This implementation is described in the flow chart in figure 6.16 and the iteration changes made during this development process detailed in table 6.1.

Source geometry module

Method : Variations in rise and rupture time with inclination and azimuth.

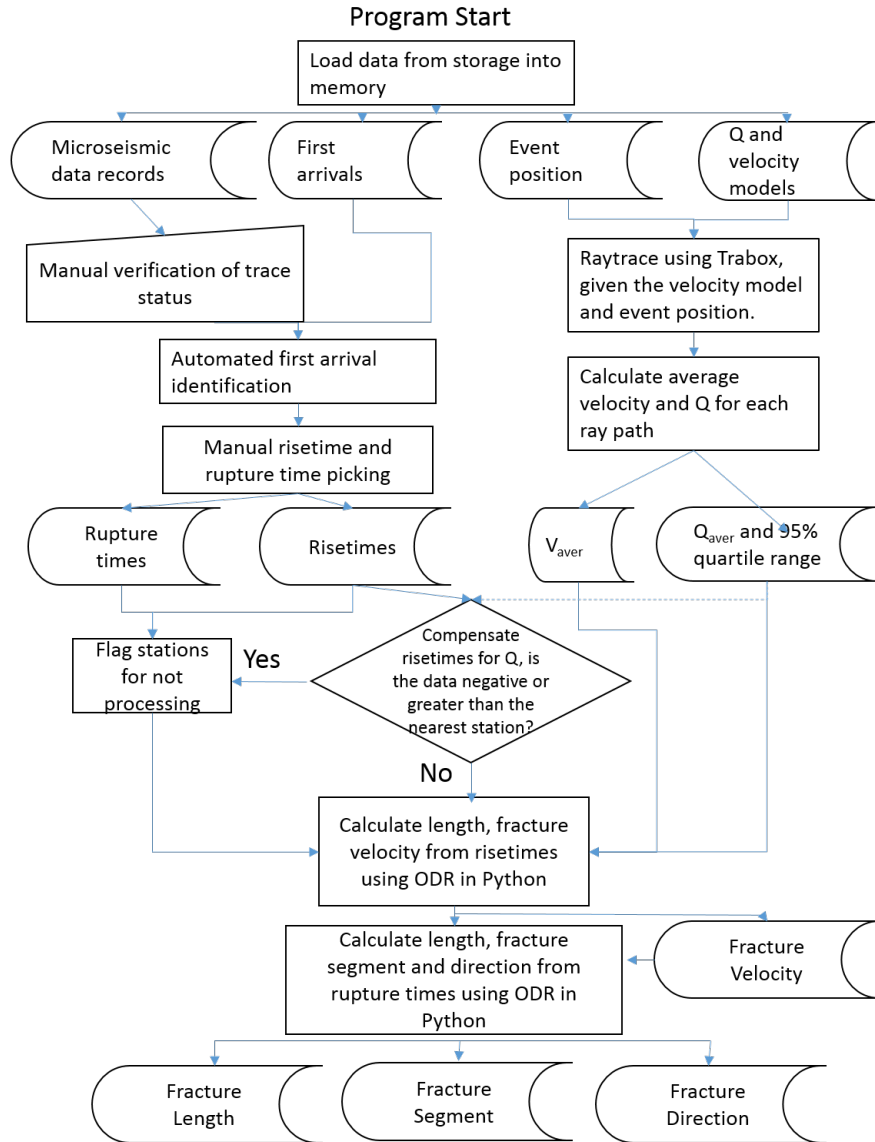


Figure 6.8: Flow chart for the implementation of the module

Table 6.1: Changes made during development of module 1

Iteration	Current functionality	Outputs	Comments	Changes to be made for next iteration
1	Automated identification of rise time and rupture time; Menahem and Singh model for rupture time	Null Output	Polarity changes confuse rise time autopicker; Variation in the shallow channels end points for the rupture time Local wave effects alter the second zero crossing timing;	Manual verification of all traces used in program; Manual identification of the rise time and rupture time end points
2	Manual identification of rise time and rupture time; Menahem and Singh model for rupture time	Rise Time outputs : Vr= 2.45 km/s, L = 0.042 km; Rupture Time outputs : Vr=1.10 km/s, L = 0.028 km;	Difference in the fracture velocity outputs. Higher confidence in the rise time output as fits into recognised theory. Modelled rupture times poorly fit the measured rupture times.	Measured data has no clear peak, implies bilateral movement on the fault, switch to the Cesca et al (2011) model. Use and hold the fracture velocity parameter from the rise time calculation during the rupture time computation
3	Manual identification of rise time and rupture time; Cesca et al model for rupture time	Rise Time outputs : L = 0.065 km; Rupture Time outputs : L = 0.044 km;	Fracture lengths differ by 0.02 km; Modelled rupture times fit the measured rupture times; Inaccuracies not taken into account	Implement inaccuracies from the Q model
4	Manual identification of rise time and rupture time; Cesca et al model for rupture time; Inaccuracies from the Q model taken into account by using ODR;	Rise Time outputs : L = 0.065 ± 0.022 km; Rupture Time outputs : L = 0.044 ± 0.01 km;	Fracture lengths differ by 0.02 km; Modelled rupture times fit the measured rupture times; Inaccuracies taken into account	Implementation fulfilled requirements, no additional iterations required

6.3.3 Testing

The verification of the programming in this module was based on the judgement from three different items of information determined using the test event,

1. Modelled times matching the measured times
2. Output results being physically valid, and within logical bounds deemed from literature
3. Output results, where possible, agreeing with the two different equations used

The final iteration of the module computes the following displays which allow item 1 of the list above to be verified. Figure 6.9 shows the modelled rise time and measured rise times together with the error bars as defined from the inaccuracies from the Q model. This figure shows that the fracture length and velocity as inverted from the rise times using the ODR process bears a close resemblance to the measured values. The length of the error bars for the output model varies with inclination from 1 ms between minimum and maximum at 30 degrees to less than 4 ms for the nearest trace at an inclination of 90 degrees. This highlights the sensitivity of the nearest trace to the overall model parameters.

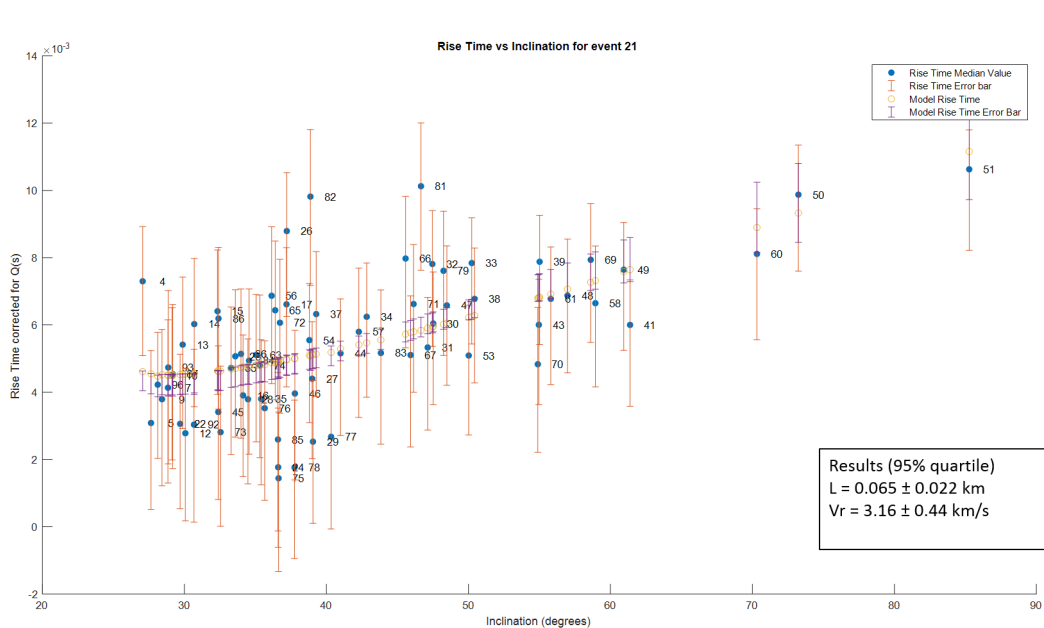


Figure 6.9: Display showing the measured rise times for event 21 with the modelled rise times given the outputs from the inversion process.

Figure 6.10 shows the modelled rupture times using the Cesca et al (2011) model as well as the measured values. This figure shows that the parameters as inverted from the rupture times using ODR bear a close resemblance to the measured values as the vast majority of the modelled rupture times are within error of the measured rupture times.

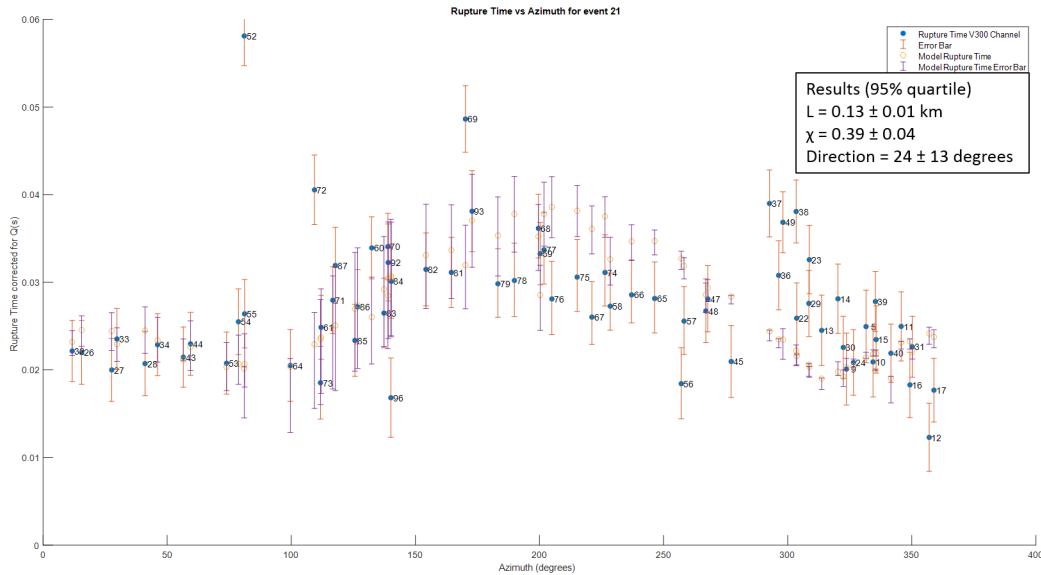


Figure 6.10: Display showing the measured rupture times for event 21 with the modelled rupture times given the outputs from the inversion process.

Concerning item 2 of the testing judgements, the calculated fracture velocity is firstly compared to other velocities found in the literature. The fracture velocities as inverted from the risetimes for the test event is 3.16 ± 0.51 km/s. Source studies reported in Causse and Song (2015) show that the rupture velocity generally varies between $0.65V_s$ and $0.9V_s$. Supershear rupture velocities, those exceeding the shear velocity, have been simulated in dynamic rupture simulations and supported by several observations (Bouchon et al. (2001) and Yue et al. (2013)) although only seven occurrences of it have been reported so far.

Given that the rupture velocity of 2.72 km/s from the $0.9V_s$ ratio and a shear wave velocity as determined from the well log at this depth, highlights that the calculated median rupture velocity of 3.16 km/s exceeds the range as reported by Causse and Song (2015). This is not as concerning as could be, as the 95% quartile range for this result ranges from $2.65 - 3.67$ km/s and is within error of these empirical relationships.

Concerning item 3 of the testing judgements, the fracture lengths can be compared between the rise time and rupture time inversion methods. The fracture length as inverted from the rise time measurements was $L = 0.065 \pm 0.022$ km and the fracture length as inverted from the rupture time measurements was, when the segment ratio χ is taken into account, $L = 0.044 \pm 0.01$ km. These results compare favourably and are both within error of each other.

6.3.4 Evaluation

This module, developed using an iterative prototyping approach has been successful as deemed from the testing criteria, in relating the variation in the wavelet size to the rupture geometry, velocity and direction. Comparing this back to the original requirements of real-time processing, there are still challenges regarding the operational time of this module. These challenges stem from data issues in the case study. The microseismic data records from this case study are recorded by three geophones installed in a 30 m deep borehole. The base geophone at 27 m is held in place with steel rebar and the two shallow geophones are held in place with rope. This means that the records from the shallow geophones have large variations in the wavelet size that are substantially different from the models due to secondary reflections and scattering within the borehole. With a different dataset, these issues may be removed, meaning that the automated procedures for identifying the rise time and rupture time can be implemented and the module can be run in real-time.

6.4 Software module 2: Full waveform moment tensor inversion and decomposition to determine focal mechanism

The second module of the software system to be developed will use moment tensor inversion to invert for the focal mechanism of the fracture. This information is part of the solution for the software systems requirements 1 and 2.

The design of this module will be to use a full waveform method based on Křížová et al. (2013) for the moment tensor inversion, rather than a single point based moment tensor inversion. The use of such a method removes the bias towards double-couple mechanisms as discussed in chapter 3. The decomposition is based on the Vavryčuk (2001) methods. This module implements both of these methods in a real-time automated processing flow.

Prototyping for this module (as described in iterations 1 to 3) was conducted before the Waighan dataset was made available using synthetic seismograms and the Cotton Valley dataset. This development continued (iterations 4 and 5) using the test event from the Waighan dataset once available. Details of the implementation changes made after each iteration are detailed in table 6.4.2 within the implementation section.

6.4.1 Design

Theory

The full waveform moment tensor inversion method used is based on the method by Křížová et al. (2013). In this strategy, the ground displacement $\mathbf{U}_i(t)$ can be written as the sum of the moment tensor, \mathbf{M}_{pq} convolved with the Green Functions, $\mathbf{G}_{ip,q}$ as

$$\mathbf{U}_i(t) = \sum \sum \mathbf{M}_{pq} * \mathbf{G}_{ip,q}, \quad (6.8)$$

The moment tensor can be expressed in the form of a linear combination of six elementary tensors \mathbf{M}_i ,

$$\mathbf{M}_{pq} = \sum a_i \mathbf{M}_{pq}^i. \quad (6.9)$$

This represents a convenient parametrization because, in this way, the source is characterized by six scalar coefficients a_i . These elemental tensors are described as shown in figure 6.11,

$$\begin{aligned}
\mathbf{M}^1 &= \begin{pmatrix} 0 & 1 & 0 \\ 1 & 0 & 0 \\ 0 & 0 & 0 \end{pmatrix} & \mathbf{M}^2 &= \begin{pmatrix} 0 & 0 & 1 \\ 0 & 0 & 0 \\ 1 & 0 & 0 \end{pmatrix} \\
\mathbf{M}^3 &= \begin{pmatrix} 0 & 0 & 0 \\ 0 & 0 & -1 \\ 0 & -1 & 0 \end{pmatrix} & \mathbf{M}^4 &= \begin{pmatrix} -1 & 0 & 0 \\ 0 & 0 & 0 \\ 0 & 0 & 1 \end{pmatrix} \\
\mathbf{M}^5 &= \begin{pmatrix} 0 & 0 & 0 \\ 0 & -1 & 0 \\ 0 & 0 & 1 \end{pmatrix} & \mathbf{M}^6 &= \begin{pmatrix} 1 & 0 & 0 \\ 0 & 1 & 0 \\ 0 & 0 & 1 \end{pmatrix}.
\end{aligned}$$

Figure 6.11: The elemental tensors used by Křížová et al. (2013). The \mathbf{M}^1 to \mathbf{M}^5 tensors represent five DC focal mechanisms while \mathbf{M}^6 is a purely isotropic source

When equation 6.8 and 6.9 are combined together,

$$\mathbf{u}_i(t) = \sum \mathbf{a}_j \left(\sum \sum \mathbf{M}_{pq}^j * \mathbf{G}_{ip,q} \right) = \sum \mathbf{a}_j \mathbf{E}_i^j(t), \quad (6.10)$$

where \mathbf{E}_j denotes the j th elementary seismogram corresponding to the j th elementary moment tensor. This is represented in matrix notation as

$$\mathbf{u} = \mathbf{E} \mathbf{a}_i, \quad (6.11)$$

where \mathbf{a}_i are the six scalar coefficients that describe the moment tensor and \mathbf{E} are the six elemental tensors convolved with a Green Function, thus becoming the elemental seismograms. This is an overdetermined linear inverse problem and \mathbf{a}_i is solved for via the generalised inverse by the least-squares method. To determine the moment tensor from the linear combination of the scalar coefficients the following set of simple equations are used, note that the moment tensor is symmetrical over the diagonal so only 6 unique terms are required to describe the full moment tensor.

$$\begin{aligned}
\mathbf{M}_{1,1} &= -\mathbf{E}_4 + \mathbf{E}_6 \\
\mathbf{M}_{1,2} &= \mathbf{E}_1 \\
\mathbf{M}_{1,3} &= \mathbf{E}_2 \\
\mathbf{M}_{2,2} &= -\mathbf{E}_5 + \mathbf{E}_6 \\
\mathbf{M}_{2,3} &= \mathbf{E}_3 \\
\mathbf{M}_{3,3} &= \mathbf{E}_4 + \mathbf{E}_5 + \mathbf{E}_6
\end{aligned} \quad (6.12)$$

Design

To solve the inverse problem, the elementary seismograms, \mathbf{E} , are modelled using the AXITRA wave-number code by Coutant (1990) with a 1D velocity model and a known source time function. Simply put the inversion software ISOLA seeks to find a combination of the six scalar coefficients a_1 to a_6 which fully describes the data records by comparing these mathematically to the set of six elemental seismograms. So, for example, a set of data records with a moment tensor described by M^1 in figure 6.11 should, assuming the source time function and velocity model used to model the elemental seismograms match the data records, result in a_1 equalling 1. This is shown in figure 6.12, with a comparison between a finite-difference synthetic seismogram with a moment tensor matching M^1 from the elemental tensors in figure 6.11 to the equivalent elemental seismogram modelled from the AXITRA code, from the ISOLA software suite. This emphasises the importance of the elemental seismogram modelling and ensuring the data records match the character and timing as closely as possible.

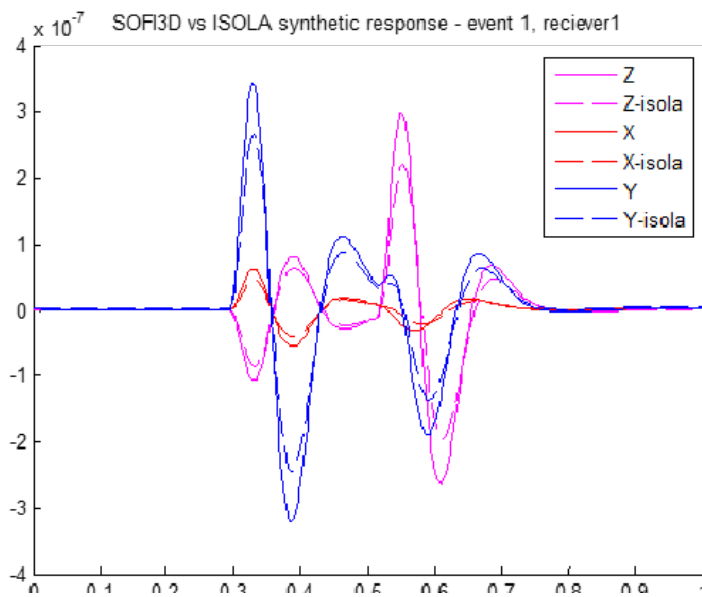


Figure 6.12: The match between a finite difference synthetic seismogram with a moment tensor matching M^1 from the elemental tensors from figure 6.11 matching the equivalent elemental Green function.

The original code by Zahradnik and Sokos calculates the Greens Function using a 1D velocity model with inputs of the P- and S- wave velocities in a layer cake configuration

using the AXITRA code initiated from the ISOLA Gui in Matlab. Testing of this method started before the Waighan case study was available and a key change to the design of this software module was implemented from testing and experimentation using finite difference synthetics and an academic dataset, the Cotton Valley dataset. This testing found that the timing of the wavelet arrivals is key to improving the misfit between synthetic elemental functions and the data records as measured by the cross-correlation value. A 1D velocity model, especially in areas of highly heterogeneous velocity changes can only model the arrivals to a certain level of accuracy. If the arrival is early or later by a couple of milliseconds, the wavelets will misalign and increase the misfit and accordingly reduce the confidence in the output solution. To counteract this problem and to evolve the system into a system that can handle 3D velocities, for all of the receivers to be modelled, a separate velocity for each ray path is calculated for the P- and S- waves. Rather than in the original configuration, where AXITRA calculates the Greens Functions for all the receivers based on the same 1D velocity model. AXITRA is now run for each receiver with a new velocity model based on the P- and S- wave ray velocities for each receiver. This will have an additional computational cost associated with it but with modern parallel processing architectures, these costs can be reduced.

With the moment tensor inversion conducted, the moment tensor is decomposed into the focal mechanism. This process and the methods used to decompose the moment tensor have been reviewed in chapter 3. In this design, the Vavryčuk (2001) method of decomposition is used. In this method, an additional angle is determined to the standard set of dip, strike and rake. This angle is the tensile angle which describes the opening or closure of the fracture in and out of the fault plane. An angle of 90 degrees describes a fracture opening under tensile forces and an angle of -90 degrees describes an open fracture closing from a compressional force.

The relationships between the moment tensor and these four angles, dip (δ), strike (ϕ) and rake (λ) are for the fault normal n as,

$$n_1 = -\sin\delta\sin\phi \quad (6.13)$$

$$n_2 = \sin\delta\cos\phi \quad (6.14)$$

$$n_3 = \cos\delta, \quad (6.15)$$

and for the dislocation direction ν as,

$$\nu_1 = (\cos\lambda\cos\phi + \cos\delta\sin\lambda\sin\phi)\cos\alpha - \sin\delta\sin\phi\sin\alpha \quad (6.16)$$

$$\nu_2 = (\cos\lambda\sin\phi + \cos\delta\sin\lambda\cos\phi)\cos\alpha + \sin\delta\cos\phi\sin\alpha \quad (6.17)$$

$$\nu_3 = -\sin\lambda\sin\delta\cos\alpha - \cos\delta\sin\alpha \quad (6.18)$$

where the normal and dislocation vectors are expressed in terms of the eigenvectors (e_1 , e_2 and e_3) and eigenvalues (M_1 , M_2 and M_3) of the moment tensor \mathbf{M} are,

$$n = \sqrt{\frac{M_1 - M_2}{M_1 - M_3}}e_1 + \sqrt{\frac{M_3 - M_2}{M_3 - M_1}}e_3 \quad (6.19)$$

$$\nu = \sqrt{\frac{M_1 - M_2}{M_1 - M_3}}e_1 - \sqrt{\frac{M_3 - M_2}{M_3 - M_1}}e_3 \quad (6.20)$$

As can be seen in equations to , the angles of strike and dip can be derived solely from the normal vector and the tensile angle and rake angle can only be derived from the dislocation direction.

Microseismic scale validity

As with module 1, the module design is validated to ensure the method can be employed at microseismic scales. This method, based on the strategy by Křížová et al. (2013) has been used on minor earthquakes in Greece. This method has also been applied to microseismic events in two case studies, Lorenzo et al. (2017) and Agurto-Detzel et al. (2017), showing that use of such a method on microseismic scales is not novel and there are no minimum scales where such an approach can be applied. This point is reinforced by the theoretical review presented by Aki and Richards (2002). The only factor which could limit the ability to analyse a micro-size event is the sampling interval. This point was addressed when discussing the validation for module 1, and attenuation will always extend the wavelet meaning the minimum fault size resolvable is not wholly dependent on the sampling interval. Other than data issues such as a poor signal to noise ratio or local scattering of the signal reducing the wavelet clarity, there is nothing theoretical that invalidates using such design to analysis microseismic faulting.

6.4.2 Implementation

This implementation of this module is split into two parts, the inversion of the data records to the moment tensor and the second part decomposing the moment tensor into the focal mechanism. The implementation must also follow requirement 3 of the software system, that it can operate in a real-time automated processing flow. The two parts of the implementation are:

1. The inversion part of this module is based on the ISOLA code by Zahradník and Sokos. The ISOLA code is a set of Fortran programs linked to a Matlab GUI which sets up, models the elemental seismograms, runs the inversion and provides the means to validate the results. For the implementation of this module, the elemental seismograms modelling an inversion parts of the system were utilised to solve for the moment tensor and a new MATLAB front end link used. This would allow the software to be run in real-time.
2. The moment tensor decomposition part of this module is based on the Vavryčuk (2001) method and uses the Matlab script by Vaclav Vavrycuk.

The starting point for this software module is to load the relevant data into memory in Matlab. For this module, this consists of the data records, times for the P and S wave arrivals, station position, and event position which are retrieved from data storage.

Implementation stage 1: Setting up the source files for the Greens functions calculation and inversion

This first stage of the implementation is concerned with two tasks, (1) setting up and preparing the data records for the inversion and (2) preparing a set of data files for the synthetic elemental seismogram modelling.

To prepare the data records, the first task is to ensure that the recording orientation of the 3-C geophones matches that of the elemental seismograms. The elemental seismograms as generated by AXITRA are aligned in N-S, E-W, vertical orientations for the three channels. To match this, the data records are rotated from the installation directions to these orientations. The original installation azimuths were not recorded so a method of determining the installation angles was devised from the P-wave magnitudes for a set of dynamite seismic test shots. Further details of this process can be found in appendix B2. The data channel is then rotated to cardinal directions using,

$$U_e = \cos(tool)h_1 + \sin(tool)h_2 \quad (6.21)$$

$$U_n = -\sin(tool)h_1 + \cos(tool)h_2, \quad (6.22)$$

where *tool* is the angle of the H2 channel direction from North.

Next, to reduce data noise and improve the misfit, the data records were simplified. Essentially this means that any seismic information that is not part of the first wave period (e.g. a single peak/trough combination) are set to zero. This is conducted by placing a Margrave window around the first wave period on both the P- and S-

wave arrivals to graduate the signals to zero reducing ringing but also cutting out any noise in the data. The records are also shifted so that the origin of the source starts at sample 1.

To prepare the data files for the synthetic elemental seismogram, first the P- and S-wave arrival times and event position were used to calculate, on a ray-by-ray basis, the velocities required for a P- and S- wave to arrive at that time. The P-wave times were taken from the previous modules identification procedure but as only P-waves were considered in that module, the S-wave arrival times were manually identified in this instance. The end result for this was a text file with the velocity models required for all the receivers to be modelled. So for example, for station 92, the P- and S- wave velocities are 4.55 km/s and 2.36 km/s respectively and for station 42 the P- and S- wave velocities are 4.46 km/s and 2.19 km/s respectively. With the timing of the P- and S- wave arrivals managed, the source time function needs to be considered. Following the second iteration of the module development, it was found that although the Q model varies the wavelet size of the arrivals in the synthetic modelling, there were still wavelet size differences between the synthetic model and real data that altered the overall misfit. To counter this, rather than using the Q model which despite the best intentions cannot exactly model the 3D attenuation structure due to the geometry constraints discussed in chapter 5, a unique wavelet time length for each station P-wave arrival is taken from the data records and used as input for the source-time function in the AXITRA modelling. To this end, the length of the wavelet in time for each active receiver is taken and saved into a file for AXITRA to use with the Green Functions modelling.

The application of these tasks is shown on a working example in figure 6.13.

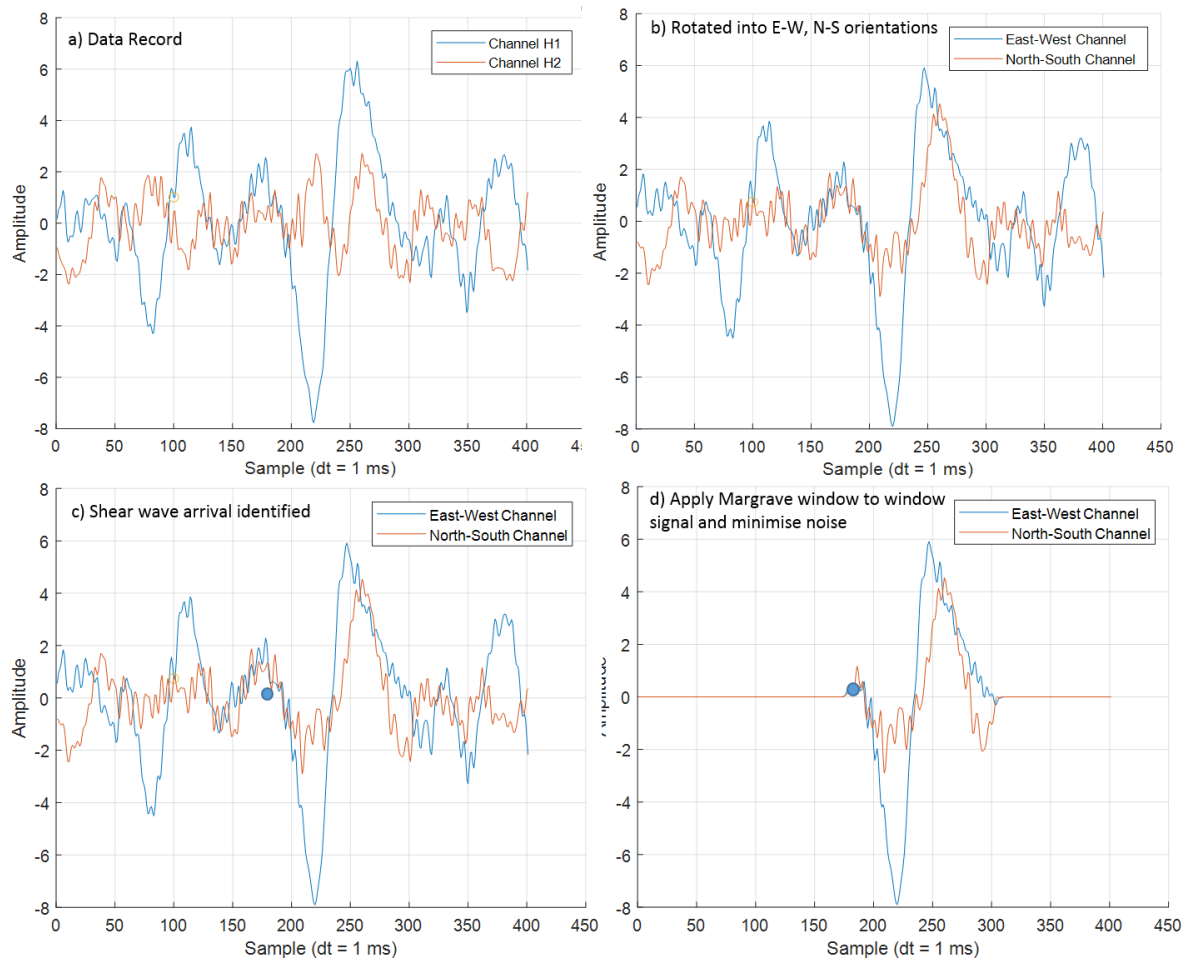


Figure 6.13: A worked example of the preparation carried out before the generation of the Green's functions and the moment tensor inversion. In b) the data record from a) is rotated into the E-W and N-S orientations using the installation directions. Next, the S-wave arrival is identified (blue point). This point is used to calculate the Shear wave velocity for this particular station. Finally, a Margrave window is applied to the data record to minimise noise and improve the match with the Greens Functions.

Implementation stage 2: Calculation of the Greens functions in 3D

The velocity models file and wavelet size file are copied to a server-based computer. AXITRA is then run for each receiver in parallel where possible. This improves the efficiency of the overall process. These files are then copied back to the Windows PC and in Matlab these individual files are re-combined into a single file containing all the elemental seismograms.

Implementation stage 3: Moment tensor inversion

To run the inversion, the ISOLA Fortran module is run from Matlab using the elemental seismograms and data records. Originally the moment tensor inversion varies the timing of the data records compared to the seismograms to minimise the misfit. With the 3D velocity model method, this is now redundant as the match should be optimised without any changes to the timing. A frequency filter is also applied to the data and elemental seismograms to improve the misfit. In this case study, this was set at 5-10-80-85 Hz. Once the inversion is completed, the moment tensor is output in terms of the 6 elemental seismograms, E_i as described in figure 6.11. This is converted into the moment tensor terms by the following set of equations,

$$\begin{aligned}M_{1,1} &= -E_4 + E_6 \\M_{1,2} &= E_1 \\M_{1,3} &= E_2 \\M_{2,2} &= -E_5 + E_6 \\M_{2,3} &= E_3 \\M_{3,3} &= E_4 + E_5 + E_6\end{aligned}\tag{6.23}$$

Implementation stage 4: Moment tensor decomposition

In this implementation, equations 6.4.1 to 6.14 are solved using the MATLAB moment tensor decomposition script by Vaclav Vavryčuk. This script firstly decomposes the moment tensor into the eigenvectors and eigenvalues and calculates the two solutions for dip and strike. For the tensile angle, both solutions are exactly the same, as observed by Vavryčuk (2001), so this is solved by using,

$$\sin\alpha = \frac{M_1 + M_3 - 2M_2}{M_1 - M_3}.\tag{6.24}$$

For the rake angle, equation is solved given both possible solutions for dip and strike and the tensile angle calculated above. The outputs from these equations are automatically plotted on a diamond plot and the results saved to data storage ready for the next event.

Implementation: Flow chart and iteration changes during module development

Overall, the implementation of this module is described in a flow chart in figure 6.16.

Focal mechanism module
 Method : Inversion of data records to moment tensor and subsequent decomposition

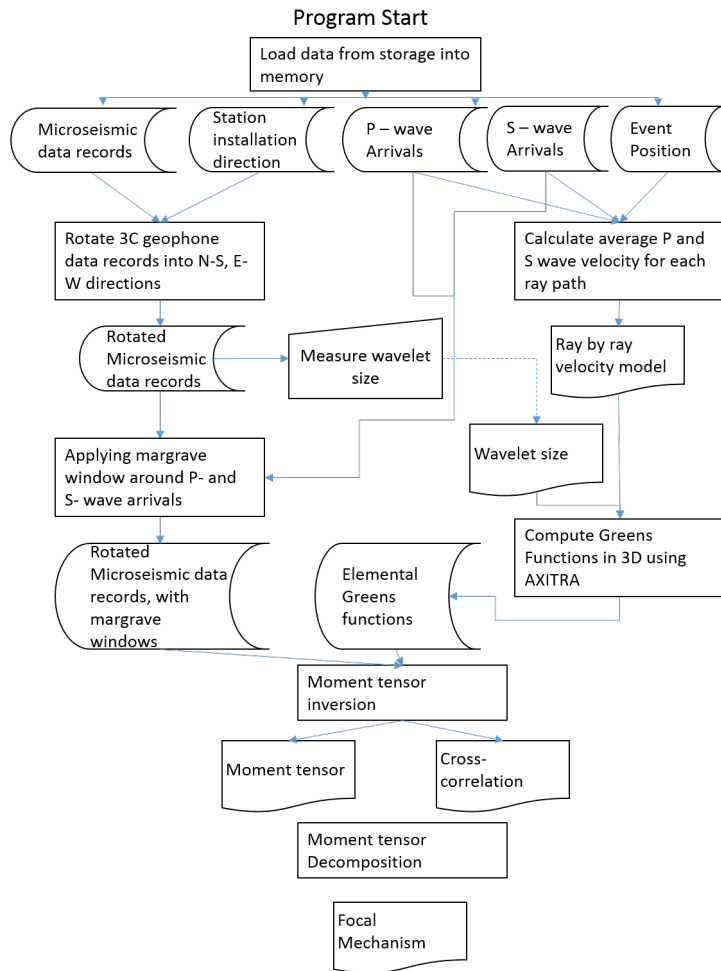


Figure 6.14: Flow chart for the implementation of the module

Table 6.2: Changes made during development of module 2

Iteration	Dataset	Functionality challenge	Quantifiable parameters	Comments	Changes to be made for next iteration
1	Cotton Valley	AXITRA : P and S waves misalignment between data records and synthetic seismograms	P to S wave time differs by a average 11 ms compared to data records, minimum and maximum time difference is 4 ms and 181 ms respectively	Clear visual misfit	Implement a ray based velocity method to generate elemental seismograms
2	Cotton Valley	AXITRA : P and S waves misalignment between data records and synthetic seismograms	P to S wave time differs by a average 7 ms compared to data records, minimum and maximum time difference is 0 ms and 85 ms respectively	Improvement on all receivers by using individual velocity models for each receiver	Use ideal ray path velocities to ensure wave arrives at the exact time
3	Cotton Valley	AXITRA : P and S waves misalignment between data records and synthetic seismograms	No difference from the P- to S- wave arrivals time	Clear match between the elemental seismograms and data records	Testing with this dataset is complete
4	Waighan	AXITRA : Length of arrivals differs between data records and elemental seismograms.	Cross-correlation of 0.13	Elemental seismograms longer than that of the data records	Remove Q-model dependencies, use individual wavelet size for source time function
5	Waighan	AXITRA : Length of arrivals differs between data records and elemental seismograms.	Cross-correlation of 0.25	Improved match between the elemental seismograms and data records	Specific challenge completed

6.4.3 Testing

The processing in this module is split over two parts, the first is the moment tensor inversion and accompanying synthetic modelling and the second is the decomposition of the moment tensor into the focal mechanism. This section describes the judgement criteria and results from the test event used to verify the implemented programming.

The testing and development of the moment tensor inversion part of the module started before the Waighan dataset was made available. During this time, experimentation was conducted on synthetics and then later the Cotton Valley academic dataset. A key program iteration was made during this period to move from using a single 1D velocity model to a ray-by-ray velocity model. The functionality of this change was verified quantitatively by considering the P- to S- wave timing between the synthetic elemental seismograms and the recorded data.

With a programming solution to timing issues resolved in the previous dataset, the current industrial dataset contained an issue not originally identified in the academic dataset pertaining to a misfit in the shape and length of the wavelet between the synthetic elemental seismograms and the data records. This was resolved by using a wavelet specific to the station as part of the Green's functions calculation. The functionality of such a solution was verified by (1) judging visually the match between the synthetic elemental seismogram and the data record and (2) using whole trace cross-correlation.

The final iteration of the software module as applied to the test event is shown as a comparison between one of the synthetic elemental seismograms and the data records for station 92 in figure 6.15.

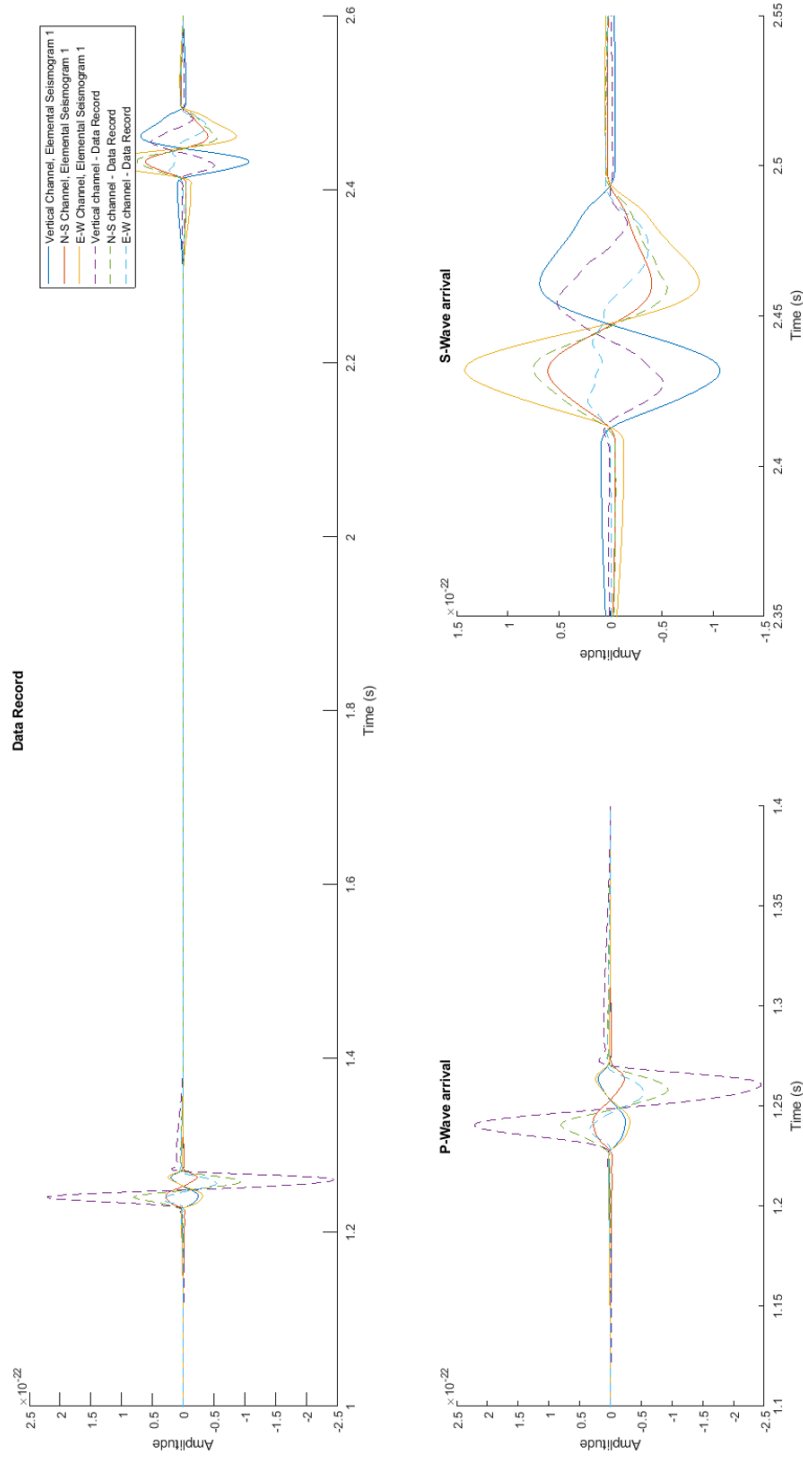


Figure 6.15: A comparison between one of the elemental Green Functions and the data records. This elemental Green Function is a double-couple source with a moment tensor as specified in the text

The moment tensor for this elemental Green Function for the comparison is,

$$\begin{bmatrix} 0 & 1 & 0 \\ 1 & 0 & 0 \\ 0 & 0 & 0 \end{bmatrix}. \quad (6.25)$$

This figure shows that for station 92 with the pre-inversion filter applied, the shape and timing between the elemental seismogram and data records match. The differences between the polarity of the elemental seismogram and the magnitudes of the P- to S- waves are due to the differences between the sources moment tensor to the known moment tensor for the elemental seismogram. If the moment tensor for event 21 is as described in 6.25, then the polarity and magnitude between the P- to S- waves would also match. When the cross-correlation is computed for all the viable stations for this event, this results in a cross-correlation misfit of 0.25.

For the second part, the moment tensor decomposition, there was very little required to confirm the validity of the programming used as the implementation required adding an open-source Matlab script by Vaclav Vavrycuk into the processing flow and adding one equation (eq 6.24) to determine the tensile angle.

To judge that the overall output is valid, the final results for the fault strike from the analysis of the test event can be compared with the results from module 1. The two solutions available from the moment tensor decomposition for the fault strike are 281° and 99° . The second solution (99°) compares reasonably with the output result from module 1 where the strike direction was determined to be $24 \pm 32^\circ$.

6.4.4 Evaluation

This module, developed using an iterative prototyping approach has been successful in determining the focal mechanism from microseismic data records using a full waveform moment tensor inversion and decomposition approach. This approach originally by Křížová et al. (2013), was improved in three key aspects :

- Moving from the generation of the synthetic elemental seismograms using a 1D velocity field to a 3D velocity field improving the match between data records and elemental seismograms
- Applying Mangrove windows around the seismic signals in the data records to isolate the arrivals and minimise the noise
- Using station by station wavelet lengths to specify the source time functions widths, removing the dependencies of the Q-model.

With regard to the processing speed of the module, even with a parallel processing approach to generating the Green's functions, further optimisation is still required before this module can be run in real-time. With regard to manual operations, this approach currently uses the P-wave arrivals and wavelet length from the operation of the previous module to enable more rapid processing. As the previous module only considers the P-wave arrivals, the S-wave arrival time and length of the signal, in this current version, still require manual identification. These are the only manual operations that remain before it can be considered a real-time automated procedure.

6.5 Software module 3: Seismic moment and Radiated energy ratio calculations

The third module of the software system to be developed calculates the seismic moment of the event and the radiated energy ratio for the S- and P-waves from the source automatically from the detected seismic event. The seismic moment and the magnitude which is derived from this are key parameters in any microseismic monitoring operations. The S- to P- wave radiative energy ratio is a measure of the compressional to tensile forces that occur at the source and is used to ratify the focal mechanism determined in module 2. These output parameters from this module are required as part of the software systems requirements 1) and 2).

The prototyping and implementation of this module differ from the approach in modules 1 and 2 as it involves implementing two established methods from literature that have already been applied at this scale without any major changes. The prototyping required in this case was ensuring that these methods can be run in an automated manner and free of programming errors. This section then details the two methods, implementation into an automated process and testing to ensure this is free of errors.

6.5.1 Design

This module is split into two parts, the calculation of the seismic moment and the calculation of the P to S wave radiative energy ratio. The broad design is that the data records are set-up first, then the seismic moment is calculated before applying the second part of the module.

Design part 1: Seismic moment calculations

The method used for this module follows the now-standard approach of using a model relating the spectral components of the seismic wave to the seismic moment such as the Brune (1970) or Boatwright (1980) models. With regard to potential difficulties encountered with handling signals at the microseismic scale, the approaches by Eaton et al. (2014) and the guidelines by Stork et al. (2014), as reviewed in chapter 3, are both taken into account.

The established method determines the seismic moment by firstly fitting a model to the spectra of the received seismic signal. These free parameters in these models are the corner frequency and the low-frequency asymptotic limit. This low-frequency asymptotic limit A_0^v is then substituted into the following to calculate the seismic moment as,

$$M_0 = \frac{4\pi\rho c_v^3 |A_0^v| r}{R_v}, \quad (6.26)$$

where R_v is the spherically averaged source radiation pattern, r is the source-receiver distance, c_v is the applicable wave speed and A_0 is the low-frequency plateau amplitude where v is the P or S wave type.

For this module, the formulation by Walter and Brune (1993) was used. This is a Brune model extended to include the effects of attenuation. This formulation describes the variation of the spectra (Ω) with angular frequency (ω) and distance (r) as

$$|\Omega^v(\omega, r)| = \frac{A_0^v(r) \exp(-\alpha_v Q r)}{1 + (\omega/\omega_c^v)^2}, \quad (6.27)$$

where $\alpha_v Q$ is an attenuation coefficient as given by Tonn (1991), ω is the angular frequency and $A_0^v(r)$ is the low-frequency asymptotic limit of the displacement amplitude. The attenuation coefficient is given by,

$$\alpha_v Q(\omega) = \frac{\omega}{2V_v Q_v} \quad (6.28)$$

where V_v is the velocity of the medium, Q_v is the seismic quality factor, v denotes the P- or S- waves and ω is the angular frequency.

Design part 2: Energy ratio calculations

The method used in this module follows the approach by Kwiatek and Ben-Zion (2013). In this method the radiated flux from a seismic source is measured from the

integral of the P- and S- wave spectra by

$$J_c = 2 \int_{f_{min}}^{f_{max}} [u_c(f) \exp \frac{\pi f R}{V_c Q_c}]^2 df. \quad (6.29)$$

In equation 6.29, u_c is the raw ground velocity spectrum of either P or S waves, V_c and Q_c are the velocity and seismic quality factor respectively, R is the source-receiver distance.

The radiated energy is then calculated using,

$$E_c = 4\pi\rho V_c \langle R_c \rangle^2 (R/R_c)^2 J_c, \quad (6.30)$$

where ρ is the rock density, V_c is the wave velocity and $\langle R_c \rangle$ is the P or S wave average radiation pattern correction coefficient, R_c is the correction for the radiation pattern of either P or S waves at a particular station and R is the source-receiver distance.

With the radiated energy ratio calculated, this can be compared to the failure mode. For a pure shear slip on a circular fault, the Sato and Hirasawa (1973) model gives a E_s/E_p ratio of 24.4 for a rupture velocity of $0.9V_s$ which drops to a ratio of 17.8 for rupture velocities less than $0.7V_s$. In contrast, the ratio for a circular tensile crack model by Sato (1978) has the ratio range from 0.9 to 1.15 for a range of rupture velocities. Kwiatek and Ben-Zion (2013) handles this by setting a lower bound for shear cracks to be 4.5 based on a stationary source from a model from Boore and Boatwright (1984). Any E_s/E_p ratios that are less than 4.5 are indicative of tensile components of faulting.

6.5.2 Implementation

The processing in this module is split into the two parts, with the first part concerning the calculation of the seismic moment and the second part the calculation of the radiated energy ratio.

This module is run solely in Matlab. Within the system structure, this module follows modules 1 and 2. Therefore in addition to the ‘standard’ data loaded from storage such as the seismic data records and positional data (event and stations) the focal mechanism as determined in module 2 is loaded into memory.

Implementation stage 1: Determination of the radiation pattern

The first step in calculating the seismic moment and as recommended by Stork et al. (2014) is to determine the radiation pattern. This step is often overlooked and approximations of 0.52 and 0.63 for the P-wave and S-wave respectively are commonly (values from Boore and Boatwright (1984)). Given that the focal mechanism of the seismic event is available from module 2, the formulation as described in Ou (2008) is used to calculate the radiation pattern.

Implementation stage 2: Seismic moment calculations

The data records used in the previous modules are measurements of particle velocity. The model in 6.27 is based on particle displacement measurements. So the first task conducted was to convert the particle velocity records into particle displacement records. This is conducted using the Seismic Analysis Code (SAC, Goldstein and Snoke (2005)). During this conversion, the seismographs instrumental response at low frequencies may interfere with this conversion. Using the provided poles and zeros file from the seismograph manufacturer, this effect, where possible, is dampened using the ‘transfer’ function in SAC.

With the data records converted to displacement and instrument effect handled, as advised by Stork et al. (2014), the data records are orientated into P, Sh and Sv directions. This is conducted by using the inclination and azimuth between the source and station and the method as described in Plesinger et al. (1986). The data was then moved to the frequency domain with a 500 ms time window padded up to 2 secs.

To ensure both code stability and automated processing, a predefined part of the spectra is used. This part of the spectra is defined from 5 Hz to 50 Hz, which covers the range of frequencies found in the data. A Brune model is then fitted to this part of the spectra for the P, Sh and Sv waves using the `fmincon` function in Matlab. This algorithm finds the minimum of a constrained nonlinear function, which in this situation is equation 6.27. In this module, the free parameters are the low-frequency asymptotic limit (A_0'), corner frequency (ω_c) and Q. This algorithm is constrained such that a solution is valid only if the output Q value is within the 95% quartile range as determined from the Q model. As only a Qp model was available, the range of Qs values matches the Qp model range.

The low-frequency asymptotic limit is now used with equation 6.26 together with the density as measured at that depth from the well log, the computed radiation pattern,

the velocity for that raypath and the distance between the source and station.

This process is carried out for all valid stations for the P and S waves. The seismic moments are converted into magnitude by,

$$M_w = (2/3 \text{Log}_{10}(M_0)) - 6.067. \quad (6.31)$$

Finally, the seismic moment and magnitudes are automatically added into a histogram and a normal distribution fitted, outputting a median value and the 95% quartile range.

Implementation stage 3: Energy flux and radiative energy ratio calculations

To calculate the energy flux, the method by Kwiatek and Ben-Zion (2013) requires particle velocity records. So the particle displacement records in the P, S_h and S_v orientations prepared in stage 2 are converted back into particle velocity and equation 6.29 used to calculate the energy flux J_c .

With the energy flux calculated, the radiative energy is calculated using 6.30, the ray velocity, the radiation pattern correction coefficient and the density. Similar to the seismic moment and magnitude calculations, the radiative energy values are placed into histograms and a normal distribution fitted, outputting a median radiative energy value for the P and S waves and a 95% quartile range.

Implementation: Flow chart

Overall, the implementation of this module is described in a flow chart in figure 6.16.

Seismic moment calculation and radiative energy ratios
 Method : Spectral analysis

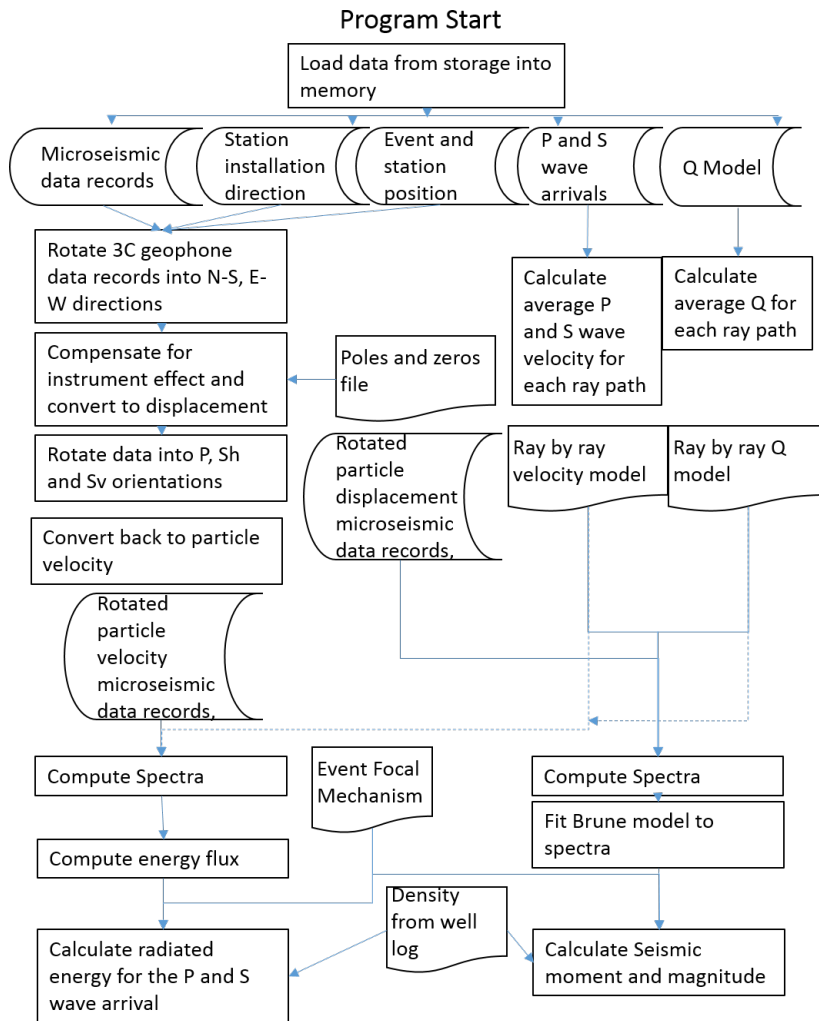


Figure 6.16: Flow chart for the implementation of the module

6.5.3 Testing

This module was split into two parts, calculation of the seismic moment and calculation of the radiative energy ratios. With regard to testing the first part of the module, as was alluded to in the opening for this section, calculating seismic moment is an established method and so the prototyping cycle in this instance was focussed on verifying there were no errors in the implementation of the method. Accordingly testing judgements for this part of the module were focussed on ensuring that the implementation of the automated process was running correctly. These judgements were: (1) modelled spectra with the Brune model matches the recorded spectra and (2) the resulting event magnitude is within a sensible range of the event magnitudes as determined from Contractor A and B. An example of the application of these judgements to the test event is shown as figure 6.17. In this test event, the magnitude computed was 0.69 and compares favourably to magnitude calculations by contractor B.

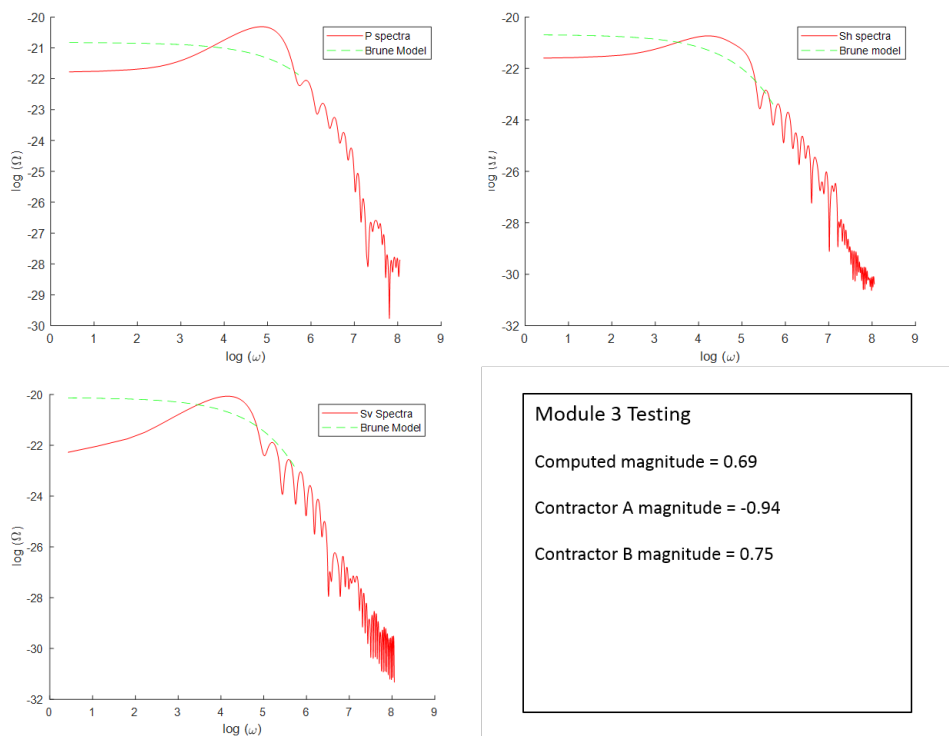


Figure 6.17: Results from applying the Brune model to station 92 for each of the 3 channels after rotation (P , S_h and S_v) and the output magnitude compared to the two contractors.

With regard to the second part of the module, this was an implementation of the method by Kwiatek and Ben-Zion (2013). Testing for this module was conducted to ensure that the implementation was successful. The judgement in this situation is based on the resulting radiative energy ratio are similar to the 539 events investigated in the study by Kwiatek and Ben-Zion. A histogram of the energy ratios computed in this study is shown as figure 6.18. For this test event, the energy ratio was 6.98 ± 2.94 which is within the distribution of the events analysed by Kwiatek and Ben-Zion, shown in figure 6.18. This result, according to Kwiatek and Ben-Zion’s criteria shows that the event is not purely a tensile event, agreeing with the moment tensor inversion results of a tensile angle of 15 degrees.

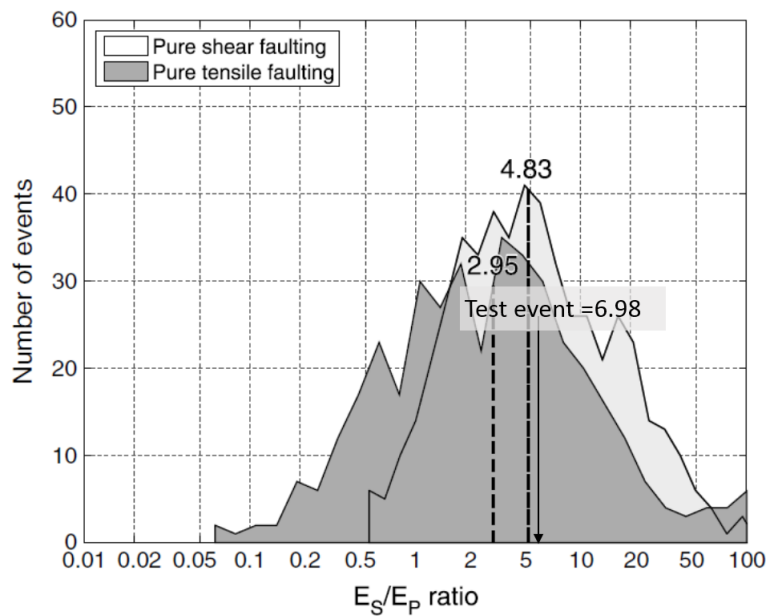


Figure 6.18: A histogram of the energy ratios computed by Kwiatek and Ben-Zion (2013) and where the test event’s radiative energy ratio places in this scale.

6.5.4 Evaluation

This module is successful in determining, automatically, the seismic moment and radiative seismic ratios for the P- and S-wave from a seismic event as determined from the established judgement criteria. This module required very few changes from the established methods by Eaton et al. (2014) for the seismic moment calculation and Kwiatek and Ben-Zion (2013) for the energy ratio to implement in an automated manner.

6.6 Software module 4: Coulomb stress transfer modelling

The final module of the software system to be developed concerns the modelling of the Coulomb stress transfer between seismic events. This module fulfils the second software system requirement to monitor for static stress transfers triggering seismic events.

The prototyping for this module differs from the other modules as the implementation required automatically preparing data files for input into an established software suite, Coulomb 3.3, and minimising the errors in this process. This section presents an overview of the design of the software package together with the required input parameters defined from the other modules. Although this software has been established in literature, this software is validated by comparing the output to a 2D fault model.

6.6.1 Design

The Coulomb 3.3 software package (Lin et al. (2011) and Toda et al. (2005)) has been chosen to model the Coulomb stress transfers between seismic events. This software can either model the Coulomb stress change on a specified fault given faulting within the area, a post-effect, or of more relevance to forecasting induced seismicity, a calculation of the change in stress along optimally orientated faults determined by the regional stress field which could trigger a seismic event.

The Coulomb 3.3 software upon input of the fault information (focal mechanism, position, regional stress tensor) calculates the displacement and strain from the fault with the specified focal mechanism for the principal and shear directions. This is modelled using the Okada (1992) model for a buried finite fault in a semi-infinite medium. The output from this process is a gridded displacement field (U_x, U_y, U_z) and the strain in the x, y and z directions (for example $\epsilon_{xx}, \epsilon_{xy}, \epsilon_{xz}$) based on the specified grid. This is converted into stress in the principal and shear directions by Hookes law, using the pre-defined Young's modulus (E) and Poisson's ratio (ν) for an isotopic material as,

$$\sigma_{xx} = \frac{E}{(1 + \nu)} \left(\frac{\nu V}{1 - 2\nu} + \epsilon_{xx} \right) \quad (6.32)$$

$$\sigma_{yy} = \frac{E}{(1 + \nu)} \left(\frac{\nu V}{1 - 2\nu} + \epsilon_{yy} \right) \quad (6.33)$$

$$\sigma_{zz} = \frac{E}{(1 + \nu)} \left(\frac{\nu V}{1 - 2\nu} + \epsilon_{zz} \right) \quad (6.34)$$

$$\tau_{xy} = \frac{E}{2(1 + \nu)} (\epsilon_{xy} + \epsilon_{yx}) \quad (6.35)$$

$$\tau_{xz} = \frac{E}{2(1 + \nu)} (\epsilon_{xz} + \epsilon_{zx}) \quad (6.36)$$

$$\tau_{yz} = \frac{E}{2(1 + \nu)} (\epsilon_{yz} + \epsilon_{zy}), \quad (6.37)$$

where ϵ_{ij} is the strain in the i by the j direction as specified and V is the sum of the strains in the three principal directions (xx,yy and zz).

The stress in the normal (σ_β) and shear (τ_β) directions are rotated according to either the input faults direction in a master-receiver fault configuration (as discussed in chapter 3, and King et al. (1994)) or as a range of strikes, dips and rakes in the optimally orientated fault configuration. The Coulomb stress change (σ_f) is then calculated by,

$$\sigma_f = \tau_\beta - \mu'(\sigma_\beta), \quad (6.38)$$

where τ_β is shear stress, σ_β is the normal stress, μ' is the effective coefficient of friction taking into account the pore pressure (equation 3.75) and is isotropic and constant for the entire site. For the optimally orientated fault configuration, the strike, dip and rake which results in the maximum Coulomb stress change are used as the optimally orientated fault direction.

With regard to validation of this method at the microseismic scale, the above method is based on fundamental equations (Hooke's law) which work at all scales so there should be no issues in using the above method for microseismic scale investigations.

6.6.2 Implementation

The implementation of this module involves setting up an input file from the outputs from modules 1 to 3 and imputing this file into Coulomb 3.3. For each event, the following data is required,

1. The slip distance
2. The dip angle of the seismic event
3. The rake angle of the seismic event
4. The starting position (x,y and z) of the fault
5. The ending position (x,y and z) of the fault

These parameters are summarised in figure 6.19 from the manual for Coulomb 3.3. In addition to these parameters for each fault, the Poisson's ratio, Young's modulus (bar) and the regional stress tensor (bar) are required. For this site, the regional stress tensor was detailed in chapter 4 taken from a study by Shen et al. (2019) and the parameters are shown in the table 6.3. The Poisson's ratio was calculated by

$$\nu = \frac{(Vp/Vs)^2 - 2}{2(Vp/Vs)^2 - 2} \quad (6.39)$$

where the Vp and Vs values were taken from the well log at the relevant depth.

Table 6.3: Regional stress tensor for the Waighan site

	Map direction (degrees)	Vertical direction (degrees)	Magnitude (bar)
SH	40	0	110
Sh	90	90	58
Sv	130	0	32

Positioning a fault in the Input file

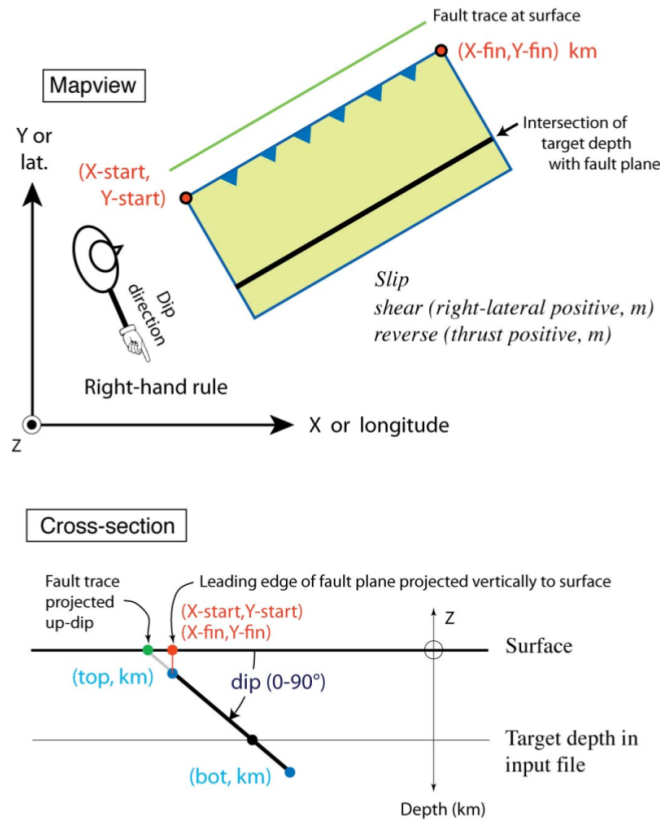


Figure 6.19: The parameters required for inputting a fault into the Coulomb software package

The fault parameters are taken from the operation of modules 1 to 3.

For item 1, the slip distance is taken from

$$M_0 = \mu D f L^2, \quad (6.40)$$

where D is the slip, M_0 is the seismic moment, μ is the lame parameter, f is the shape factor assumed to be 0.5 for a rectangle and L is the length of the fault. The length of the fault is taken from module 1 and the seismic moment is taken from module 3. For items 2 and 3, these items are based on the focal mechanism derived in module 2. There are two potential solutions for the focal mechanism. The solution used is confirmed from the fracture direction computed in module 1. For items 4 and 5, the length of fracture from module 1 is used with the position of the event.

With these items defined, the input file for Coulomb 3 is automatically filled and the

file can be used to generate a slice in depth of the change in Coulomb stress as each event is detected.

6.6.3 Testing

Coulomb 3 is an established software package in literature. To verify that the input file has been input correctly and the modelling of the strain field by the Okada model within Coulomb is implemented correctly, the strain modelling in Coulomb 3 is validated against an independent model. The model used for validation was a 2D model by Molnar (1983).

This model uses the relationship between the seismic moment and displacement Δu to calculate the strain change for a given volume. The relations for the four components are,

$$\epsilon_{yy} = \frac{M_0 \sin \phi \cos \phi}{\mu V} \quad (6.41)$$

$$\epsilon_{xy} = \frac{M_0 \sin^2 \phi}{\mu V} \quad (6.42)$$

$$\epsilon_{xx} = -\frac{M_0 \sin \phi \cos \theta}{\mu V} \quad (6.43)$$

$$\epsilon_{yx} = -\frac{M_0 \cos^2 \phi}{\mu V}, \quad (6.44)$$

where ϕ is the strike of the fault, μ is the shear modulus in Nm, M_0 is the seismic moment in Nm and V is the volume of the region bound by the fault surface where $V = L.W.h$. The model geometry as required for the previous equations are shown as figure 6.20 together with the dimensions for the test event.

As this is a 2D model, the dimensions and focal mechanism for the test event have been simplified for the purposes of testing. This means that the test event is modelled as a pure left-lateral strike-slip fault with a dip angle of 90 degrees and a rake angle of 0 degrees. The dimensions for this model are set from the operation of modules 1 to 3 with a fault length of 65 m, a strike of 93 degrees from the North and a seismic moment of 1.8×10^{10} Nm. The strain components, xx, yy, xy and yx for this model are 3.59×10^{-7} , -3.59×10^{-7} , 1.88×10^{-8} and 6.85×10^{-6} respectively.

In Coulomb, this fault was modelled and the strain components calculated. Maps of these strain components are shown as figure 6.21 and show that the average strain value calculated from the Molnar model compares favourably with the strain field

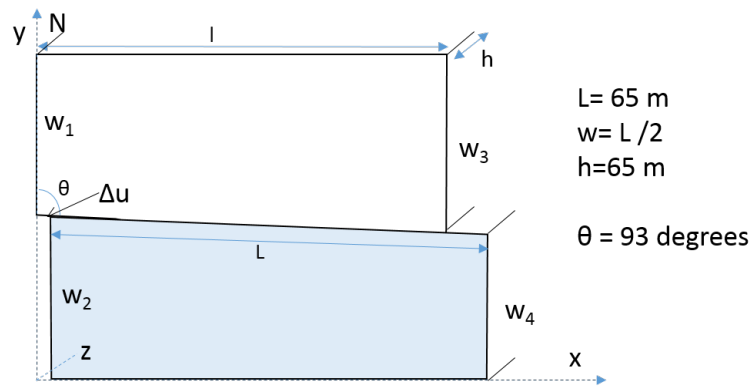


Figure 6.20: The Molnar model for a 2D fault with dimensions from the test event

components modelled in Coulomb as these averages are within 5 units of the maximum of the modelled strain fields.

With the strain field modelling verified by the independent 2D model, the Coulomb stress change for this test event is shown as figure 6.22. This shows that the test event produces a negative Coulomb stress change of 0.5 bar to the North and South.

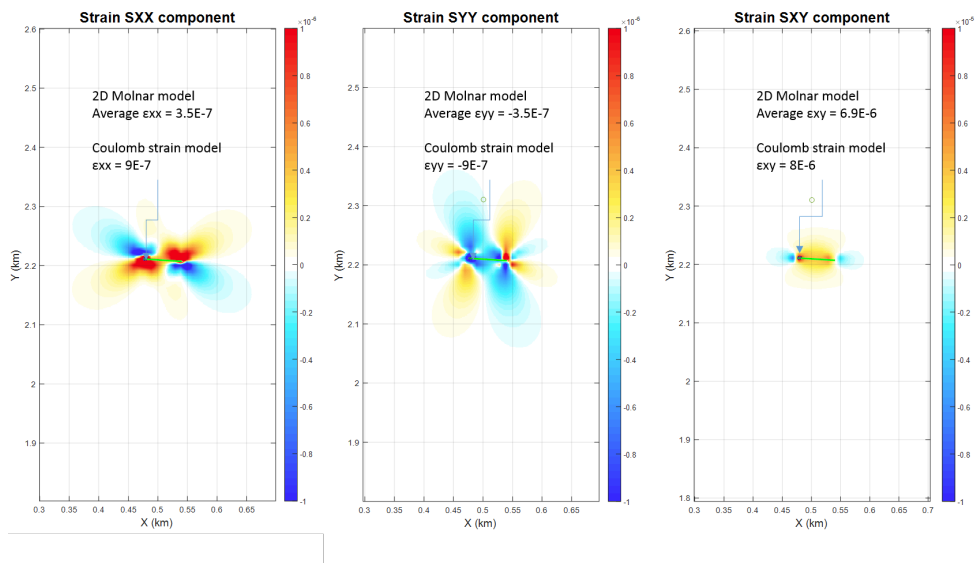


Figure 6.21: The strain components for the test event modelled by the Coulomb software compared to the average strain component values as calculated by the Molnar model.

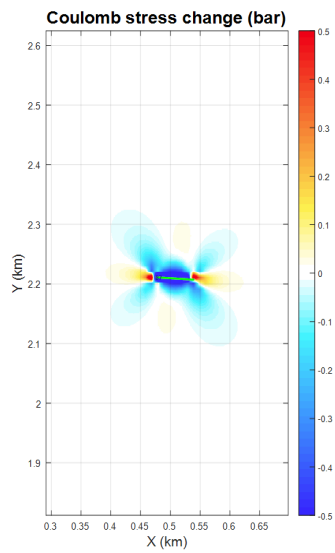


Figure 6.22: The Coulomb stress change for the strike-slip test event in bar.

6.6.4 Evaluation

This module is successful in determining the Coulomb stress change using the Coulomb 3.3 software for a set of faults with dimensions and focal mechanism as determined from the operation of modules 1 to 3. The implementation of Coulomb 3.3 and the data entry was validated against an independent 2D model which agreed with the strain fields modelled.

6.7 Software outputs: Map generation

With the data processing modules implemented and tested, the next stage of the software process is to produce the output maps. The two maps produced are a fracture map and a Coulomb stress change map. The Coulomb stress change map is produced from the Coulomb 3.3 software and no changes were made from the original scripts for this.

To produce the fracture map, the event is positioned and the fracture plane is placed on the centre of the event. The direction of the fracture plane is based on the strike results from moment tensor inversion module and validated by the direction of the fracture plane from the pulse directivity module. The fracture plane coloured represents the tensile angle between a 90-degree opening (yellow) and a 90-degree closure (blue) with shear slip as green. This tensile angle is taken from the moment tensor inversion module and validated using the radiated energy ratio and the criteria established in Kwiatek and Ben-Zion. The fracture and Coulomb stress change maps for the test event are shown as 6.23 and the output results used to generate this map are included in table 6.4.

Table 6.4: Output parameters from the operation of the software system on the test event

Event	ID			
	21			
Position	x (m)	y (m)	z (m)	
	102.19	808.7	2692.246	
Date/Time	Date	Time		
	12/01/16	05:20:58		
Geometry	Length (km)	Height (km)	Slip (m)	
	0.065±0.02	0.065±0.02	0.0002	
Focal mechanism	Strike (degrees)	Dip (degrees)	Rake (degrees)	Tensile (degrees)
	94	71	-29	15
Magnitude	M0 (Nm)	Mw		
	1.8E10	0.68		
Radiated energy	Ep (J)	Es (J)	Es/Ep	
	3.2E5	2.6E6	6.9	

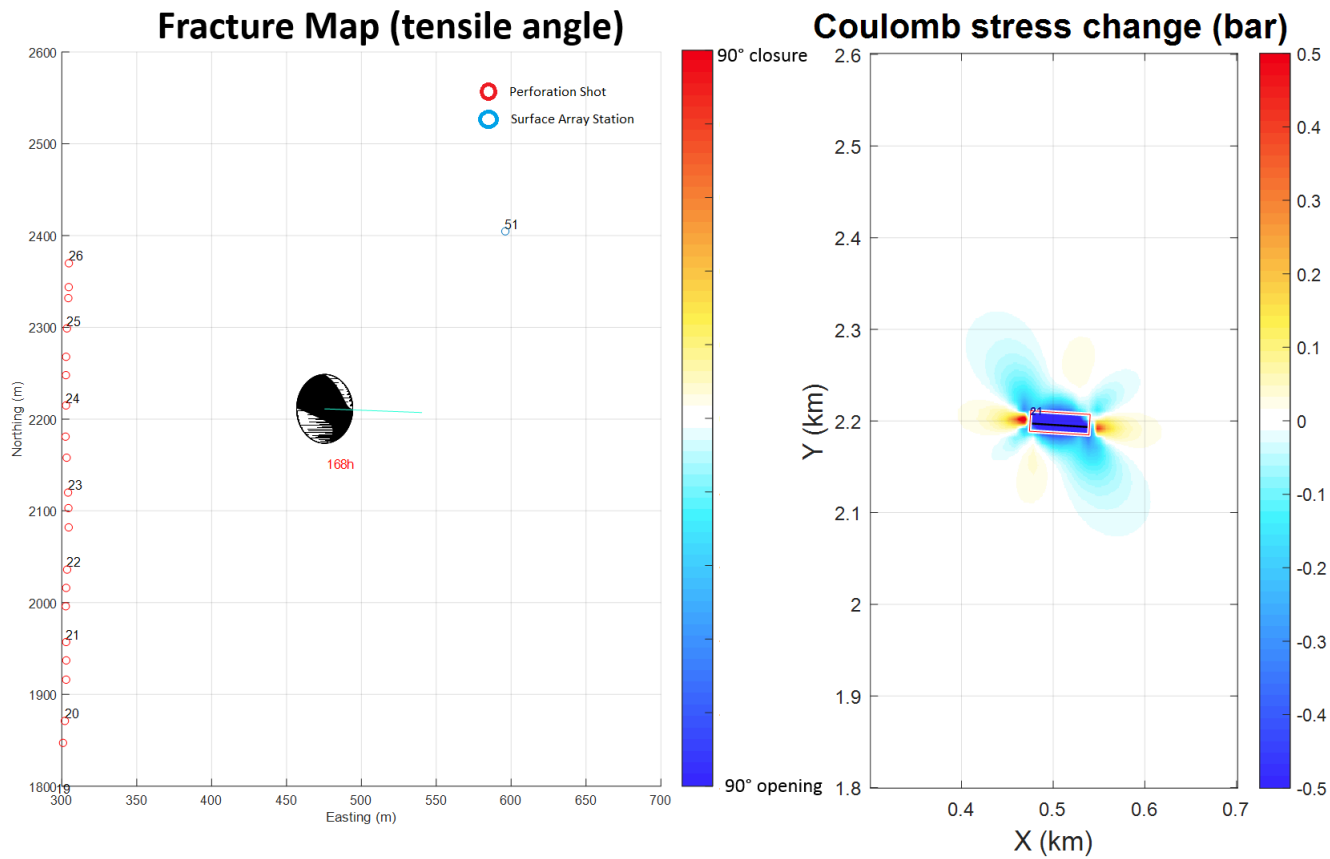


Figure 6.23: The left-hand map is a fracture map for the test event with the length of the fracture coloured by the tensile angle and the focal mechanism represented as a beachball. The right-hand side map is the Coulomb stress change in bar for the test event

6.8 Discussion

This chapter documents the software development process and the subsequent verification using a single microseismic event. Of the three programming requirements used to guide the development process, it is only possible to appraise the final requirement, the capability to run in real-time, at this point with testing a single microseismic event. Further testing will be carried out in the subsequent chapter using multiple events and a known induced seismic event to appraise the software performance for the first two requirements.

With regard to the third requirement, the software can be run in real-time but the current test data used precludes this. These reasons stem from the variability of the input data. Some of the data records have null channels or require a polarity reversal and checking for this variability requires user input. Secondly, the station design of geophones installed in a short borehole means the received signals are altered by local wave effects by the sides of the borehole stopping the automated algorithms from running correctly, meaning a manual process must be utilised. These manual processes are lengthy and currently stop the process from running in real-time.

Chapter 7

System Development: Testing with the industrial case study

7.1 Introduction

This chapter documents the final part of system development, testing of the software system using sets of events from the industrial case study to appraise the capability of the programming solution. The outputs from this testing process are compared to the software requirements in order to review the overall ability of the system to forecast induced seismicity from hydraulic fracture operations. In the previous chapter, the system was designed, implemented and tested using a single event to verify that such a system could monitor, in real-time, for the changes in the fracture network that could result in seismic activity induced from hydraulic fracture operations.

In this chapter, two sets of events from the industrial case study will be used to first test that the system has , the capability to monitor for the two mechanisms that induce seismicity as identified in the literature review (pore-pressure increases from hydraulic stimulation re-activating fault lines or static stress transfers triggering slip on fault planes) and secondly to consider if the software can be applied to forecast for seismicity caused by these two mechanisms.

To test the software systems monitoring capability robustly, the cause of the main event from the Wahigan dataset will be retrospectively analysed using the software system. Then with the cause diagnosed, the ability to forecast induced seismicity will be reviewed by comparing the output displays from the software system to the theoretical model established in chapter 2.

7.2 Analysis of the main event

Before analysis of the two mechanisms can begin, the parameters of the main event must be considered. The seismograph stations for this case-study were set-up to monitor for microscale events, and it is presumed not for events in the magnitude $M_w > 2.5$ range as the P- and S- wave arrivals for the main event have been clipped. Clipping of the data records affects module 1 and 2, the pulse directivity and full-waveform moment tensor inversion modules in the software system. This clipping issue means it is not possible to use the results from the software package for this event.

In order to see the endpoint of the evolving fracture network, analysis carried out by the two contractors and external academics are collated below in table 7.1 to see if a consensus can be found of the fault parameters.

Table 7.1: Main event parameters determined from the Contractors and academics

Source	Dataset	Strike	Dip	Rake	Magnitude
Contractor A	Microseismic array	15	84	63	2.9
Contractor B	Microseismic array	90	87	1	3.74
Schultz et al. (2017)	Regional seismograph stations	7	90		4.1
Wang et al. (2016)	Regional seismograph stations	5	86	-176	4.1

The analyse of the two academics using the regional dataset are relatively close and given that these values agree with Contractor A, an average of these three sources will be used as part of the analysis into the two mechanisms. To include the main event fault plane in the maps, an estimate of the fault length is required. This is estimated by using Maxwell (2013) presented as figure 7.1. Given the magnitude of the main event from 3.9 to 4, this corresponds to a fault length of approximately 1 km and a slip of 0.1 m.

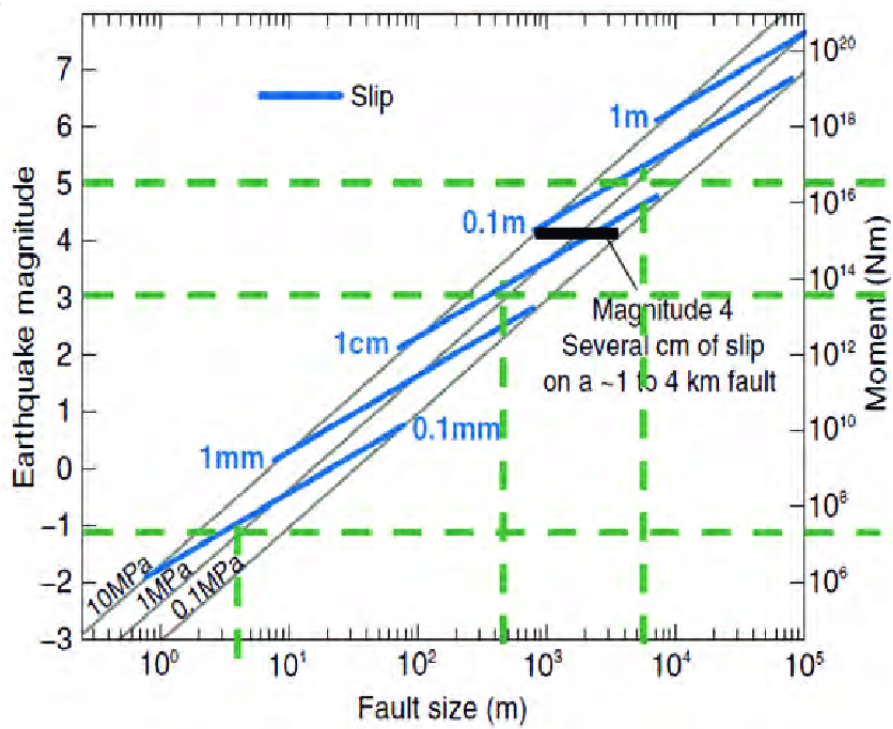


Figure 7.1: Graph showing the empirical relationships between the earthquake magnitude, fault size and seismic moment. Image from Maxwell (2013).

7.3 Mechanism 1, Hydraulic connection

The first programming requirement to be tested is that the software program is capable of monitoring for hydraulic connections between the well-bore and seismic activity associated with shear failure. This was tested by retrospectively analysing the events associated with this mechanism using the main event as the endpoint. The forecasting potential here is that by monitoring the evolving fracture network in time caused by the stimulation process, there should be a point in time when seismic activity associated with shear movement can be directly correlated to the activities at the well bore and a seismic event has an increased likelihood of occurring.

7.3.1 Mechanism 1, fault reactivation from hydraulic stimulation: Event set

To select the events that could contribute to a hydraulic connection between the well-bore and the main event, the events occurring from the stages closest to the main event were reviewed. These were stages 22 to 26. At each stage, the events which occurred within the pumping window were placed onto a map creating a time snapshot of the seismic activity occurring within that time window. These snapshots are shown as figure 7.2 to 7.6 with the position as given by velocity model A. The events were chosen from the positions using velocity model A. The event detection threshold for contractor A is lower than contractor B meaning there are more events available in-between the main event and the hydraulic fracture stages and the map position differences, as discussed in chapter 5, are on average 15 m for the Easting coordinate and 80 m for the Northing coordinate.

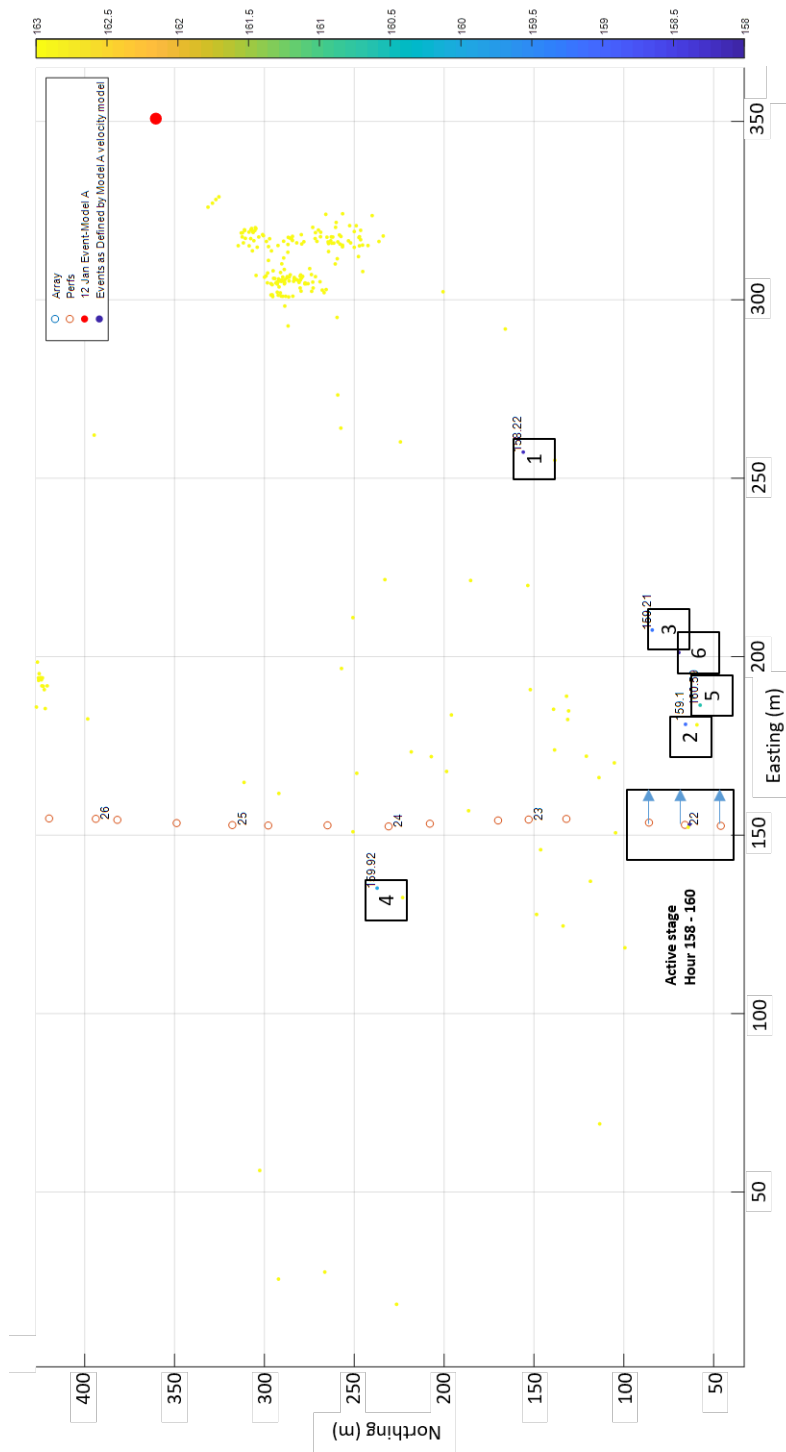


Figure 7.2: A map showing the events detected during stage 22 of the injection process calculated by velocity model A. These stages are part of the cause for an event which occurred on 12 January. This period of injection ran from the 12:25 – 15:06 on the 11 January and this map shows 6 events that occurred during this period. Of these 6 events, 4 events are possibly caused by the injection process. The other two events (1,4) are too far from the wellbore and occur too early to be linked to the injection activity.

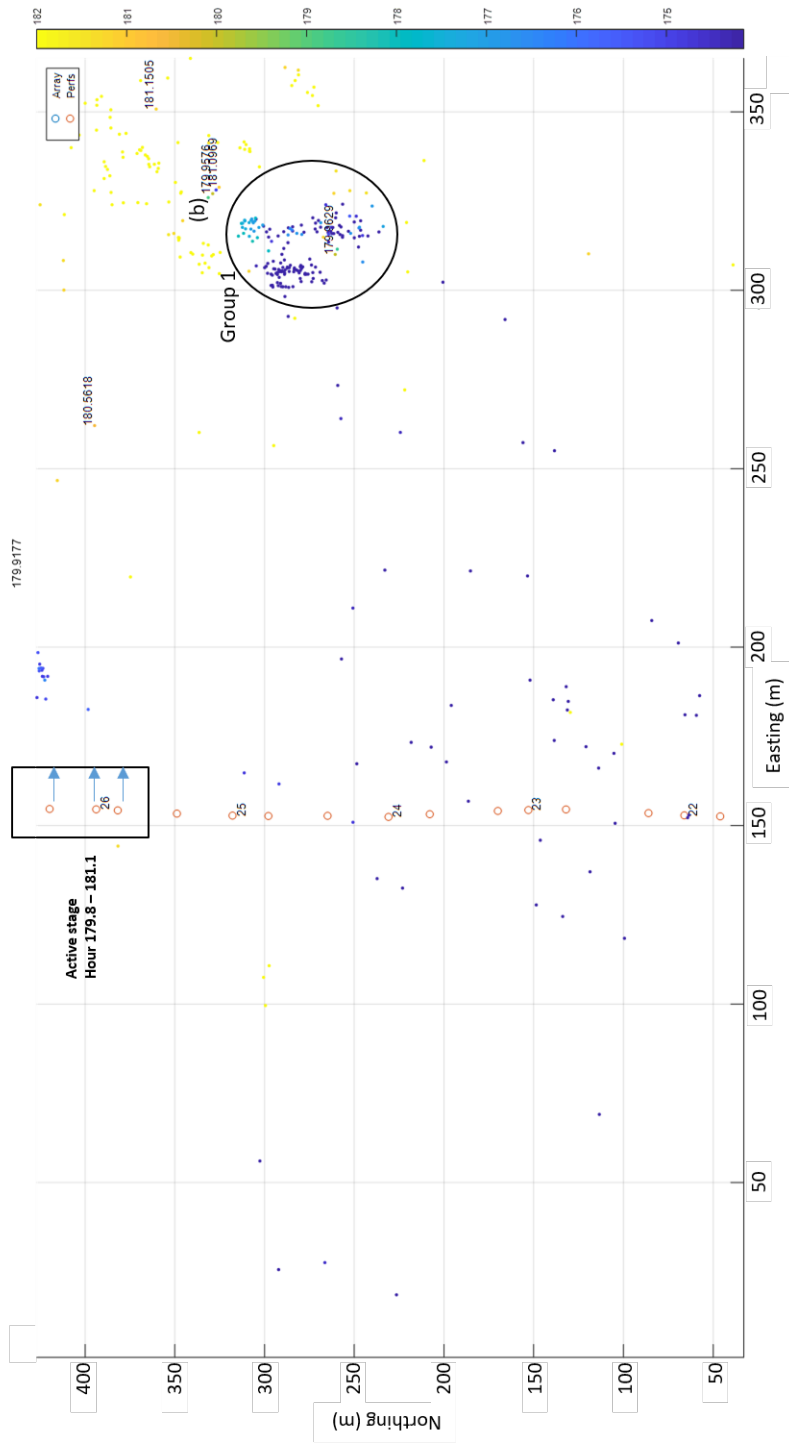
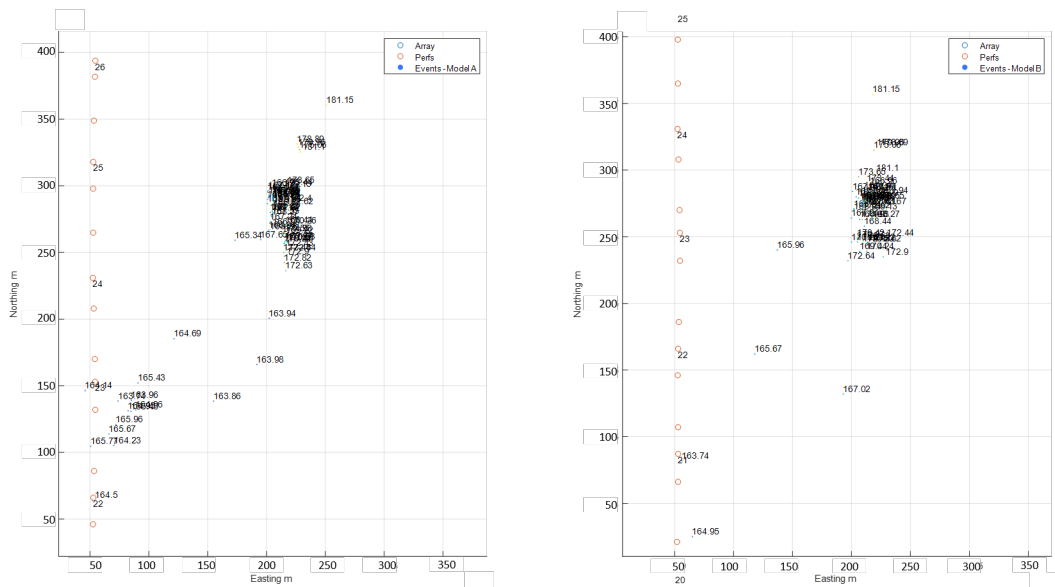


Figure 7.6: A map showing the events detected during stage 26 of the injection process calculated by velocity model A. These stages are part of the cause for an event which occurred on 12 January at 18:27. This period of injection ran from the 09:53– 11:21 on the 12 January and this map shows a number of events that occurred during this period. Within the events detected there are two events (b) occurring between the previous grouping and the main event possibly indicating fluid flow or movement towards the main event (red points) at hour 181 or 18:27. There are no events detected between the wellbore and the grouping in group 1.

By reviewing these time snapshots in figures 7.2 to 7.6 there were a number of trends that can be identified. These snapshots show that during stage 23 the number of events detected away from the wellbore increased compared to stage 22. These events can be grouped together (group 1 as annotated on the figures) and as the stages progress from stage 24 to 26 this grouping expands towards the hypocentre of the main event. During stage 25 to 26, there were four events detected to the north-west of the grouping which possibly indicates the hydraulic link to the area where the main event occurred. From stage 25 to 26 there are very few events detected in between the wellbore and area where the main event occurred.

There are 234 events that were detected by Contractor A between the start of the pumping at stage 23 and the main event failure. Of these 234, the majority of events are positioned within a grouping 150 m from the wellbore. To minimise the number of events to be processed and to ensure the process has the highest chance of success, 50 events with the greatest signal to noise ratios were used from this group. Any event which was positioned in a transect between stage 23 and the main event that does not place within this grouping was also added into the list to process. This brought the number of events to process up to 75. A map in figure 7.7 shows the chosen events positioned by velocity models A and B with the occurrence time annotated.



7.3.2 Mechanism 1, fault reactivation from hydraulic stimulation: Testing criteria

To confirm if fracture fluid transported via fracture flow from stage 23 is the cause of the slip at the main event, testing criteria, were established with the limitations that microseismic data analysis entails. These criteria are a hydraulic connection between the wellbore and the main event, and fracture aperture viability for the flow of frac fluids between the wellbore and the main event.

Testing criteria 1: Hydraulic connection between the wellbore and main event

The tests to be compared against are :

1. Events detected occurring between the wellbore and main event position within the viable time window
2. Information that shows the detected events are part of a fracture network between the wellbore and the main event

To test for point 1) the positions and accuracy of the events detected between stage 23 to the main event will be reviewed. To test for point 2) the fracture directions of each of the events detected will be reviewed to see if there is a network of fractures that can be traced from the wellbore to the main event confirming the hydraulic connection.

Testing criteria 2: Fracture aperture viability

The tests to be compared against are :

1. Information that shows the fluid can transport along the proposed fracture network
2. Information indicating any preferential pathways in the fracture network

To test for point 1) the failure mode of each event from the wellbore and main event will be reviewed to see if the fracture is opening, closing or is sliding (shear failure). To test for point 2) any trends of fracture failure modes will be traced to see if a preferential pathway can be found.

7.3.3 Mechanism 1: Monitoring capability tests

To test if the cause of the induced seismicity is from fracture fluid from stage 23 of the hydraulic fracture stimulation reactivating a fault plane causing fault slip, subset 1 of the events and the corresponding criteria discussed in section 7.3.2 will be used.

The methodology used was to firstly reposition the events in subset 1 using the final velocity model developed in chapter 5. With the events repositioned, the software system was then used, in exactly the same manner as the test event in chapter 6, for all of the available events in the subset to calculate the outputs required to generate the fracture map.

For the fracture map, the fracture lengths were calculated from the pulse directivity module and the direction of the fracture plane is calculated by the moment tensor inversion module and validated from the results from the pulse directivity module. Tensile angles were calculated from the moment tensor inversion module with the intention that the calculated radiated energy ratios could be used to verify these angles by comparing to the criteria established by Kwiitek and Ben-Zion (2013) i.e that an E_s/E_p ratio of less than 4.5 is indicative of an event with tensile forces. While the radiated energy ratio's for this subset of events were within the same reported range as those in Kwiitek and Ben-Zion (2013), there was no correlation between a fracture opening with a tensile force and the radiated energy ratio for this subset. The events where the tensile angle was greater than 30 degrees and the radiated energy ratio was greater than 4.5 were reviewed. This found that there was noise on the S-wave arrival and when combined with the exponential relationship, in chapter 6, this emphasises the higher frequencies where the noise resides biasing the result to a shear slip. For this reasoning, the radiated energy ratios were not utilised in this subset to verify the moment tensor inversion results.

Of the 75 events within this subset, it was not possible to reposition 7 of these events as the poor signal to noise ratio precluded the ability to identify any first arrivals for these events. Further details of the repositioning of these events were detailed in chapter 5.

Of the 68 events that were available after repositioning, 11 were unavailable to process in the software system. The signal to noise ratio for these events was too low (on average ~ 1.5) to have confidence in the output data. Examples of poor ($S/N \sim 1.5$) and excellent ($S/N \sim 5.5$) signal to noise ratio data records are shown as figure 7.8. The software solution was applied, following the same exact procedure as outlined in chapter 6, to these 58 events and used to judge against the established testing criteria outlined in section 7.3.2.

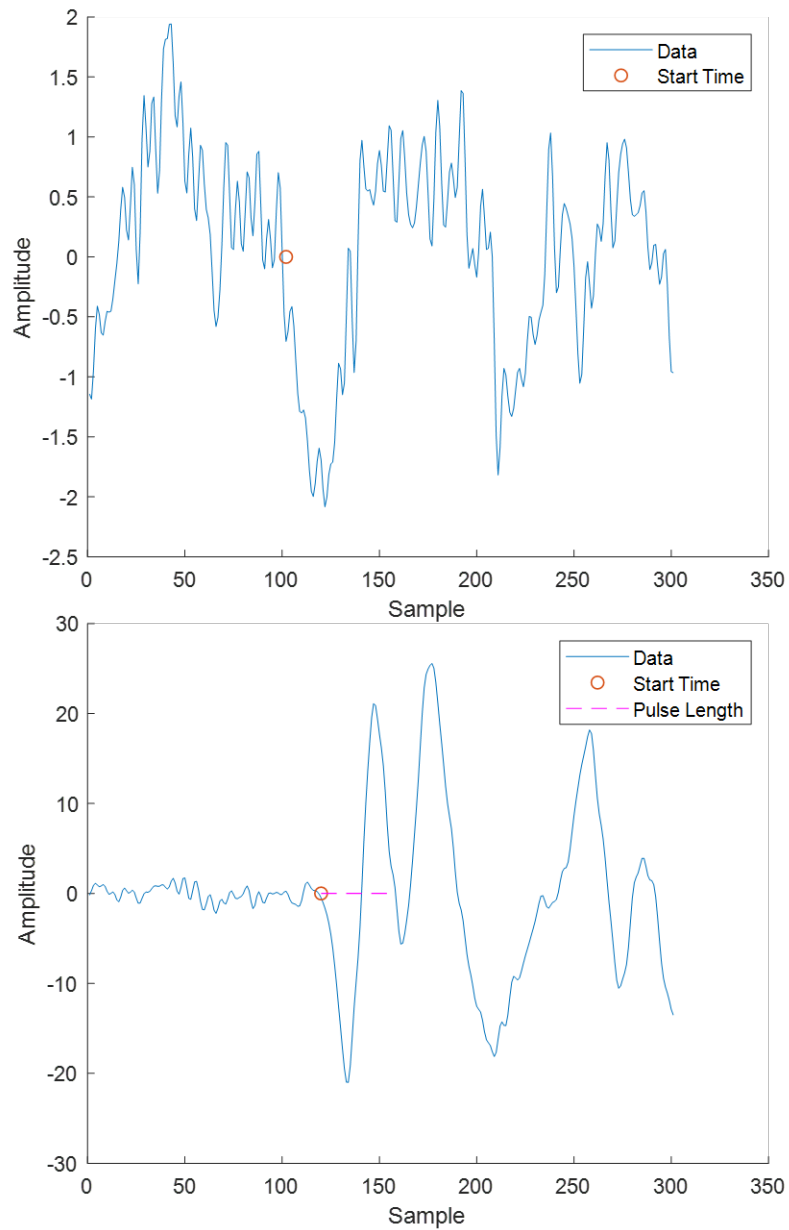


Figure 7.8: Comparison of a poor signal to noise ratio event (top) and a excellent signal to noise ratio event (bottom). The full extent of the first arrival wavelet is clear in the bottom image and a measurement of the pulse length can be made. This is in contrast to the top image where the high noise level does not allow a clear measurement of the pulse length.

Testing Criteria 1 - Hydraulic connection between the wellbore and main event

To test the first part of criteria 1, events detected occurring between the wellbore and main events position within a viable time window, the position and occurrence time of the events were considered. These repositioned events, together with a map accuracy estimate, are shown in map view as figure 7.9 to 7.11 coloured by the occurrence time and annotated with the Event ID used in the system.

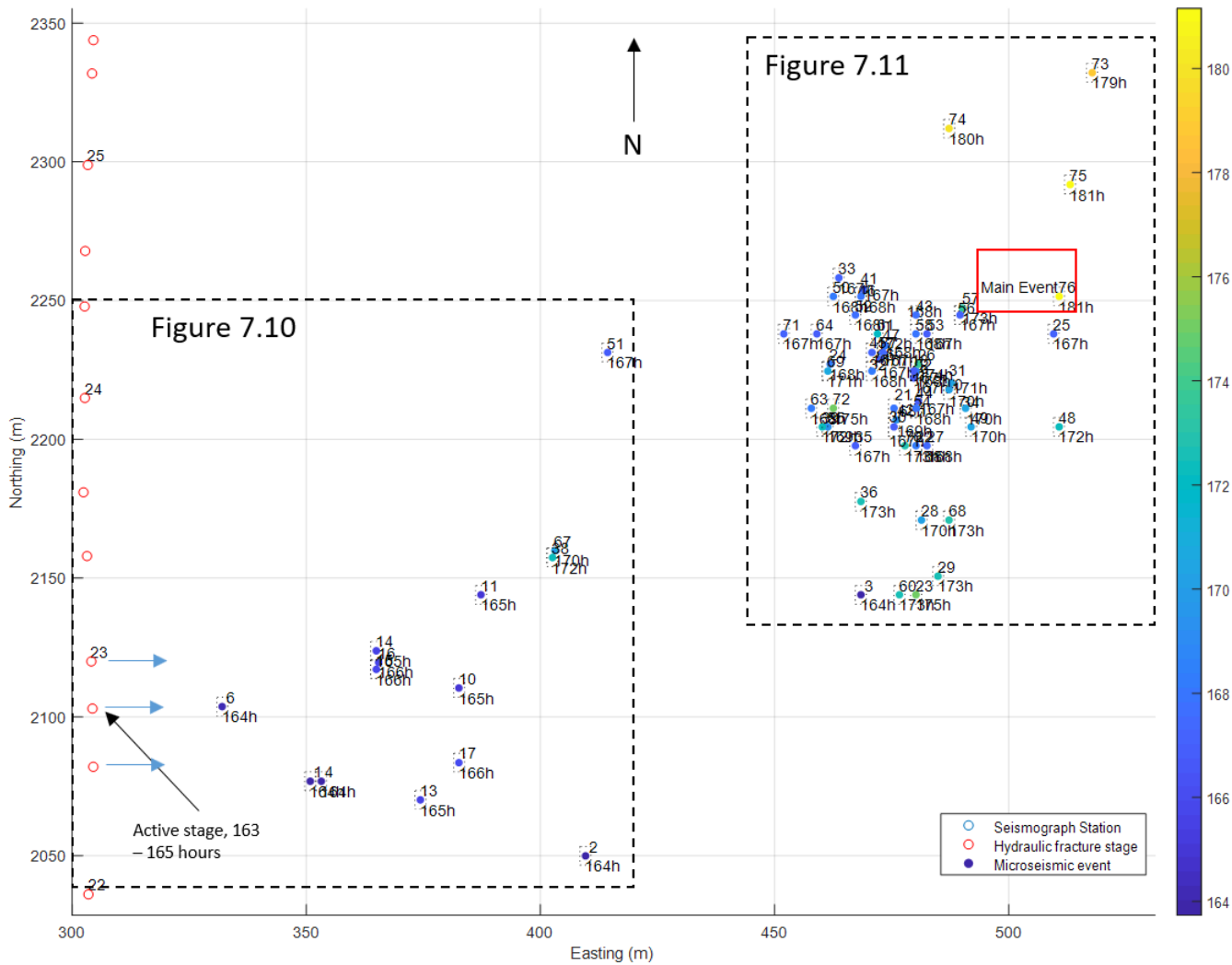


Figure 7.9: Map of all events from subset 1

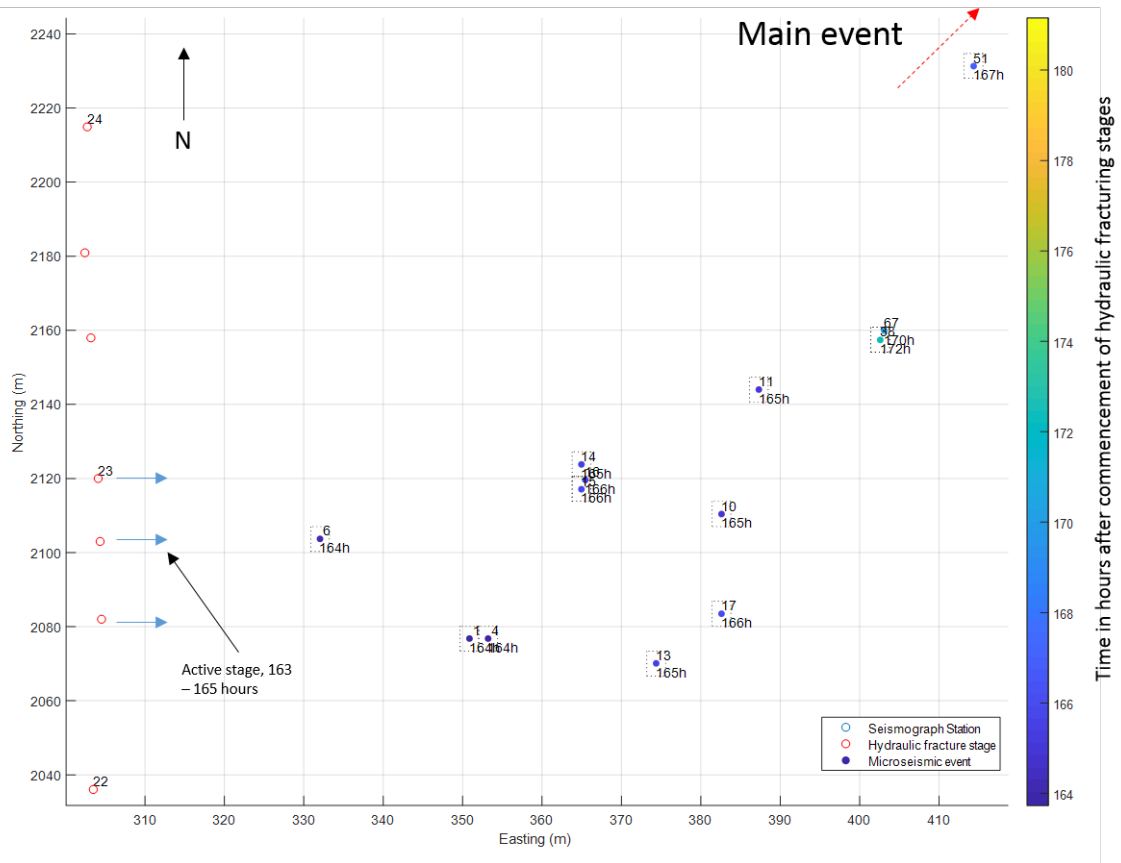


Figure 7.10: A smaller scale map of a selection of events from subset 1 where the boundaries of the plot are defined on figure 7.9.

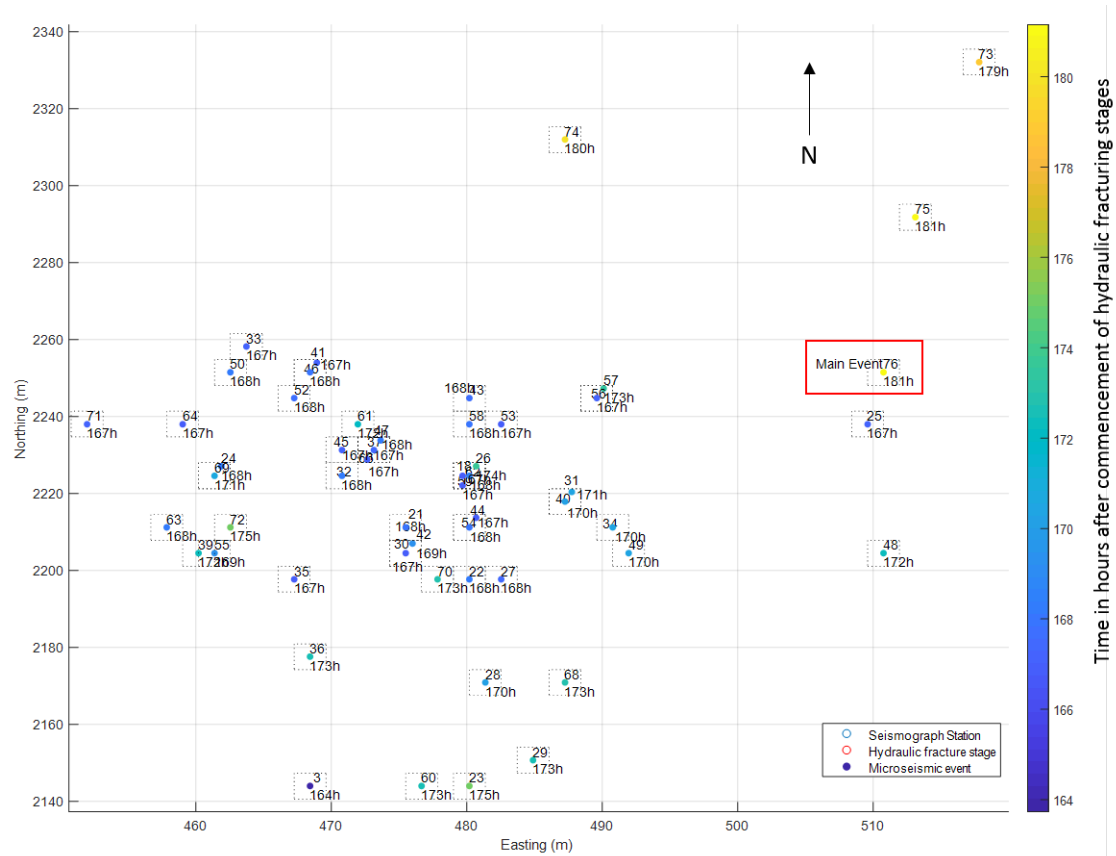


Figure 7.11: A smaller scale map of a selection of events from subset 1 where the boundaries of the plot are defined on figure 7.9.

The map views in Figures 7.9 to 7.11 show a clear trend of events with increasing origin time starting at the commencement of stage 23 of hydraulic fracturing at hour 163, from the beginning of the operation. In map view, it is clear that there are events detected in a direct line from the wellbore to the main event occurring between the start of the hydraulic fracturing stage at hour 163 and slip at the main event at hour 181. The depth variation of events between the wellbore and main event is considered by visualising figure 7.9 in depth in an E-W direction between stage 23 and the main event, as shown in figure 7.12. This figure shows that there are a few events in a direct line in depth between the wellbore and main event. The other events which are not on a direct path may occur along with other parts of the fault planes.

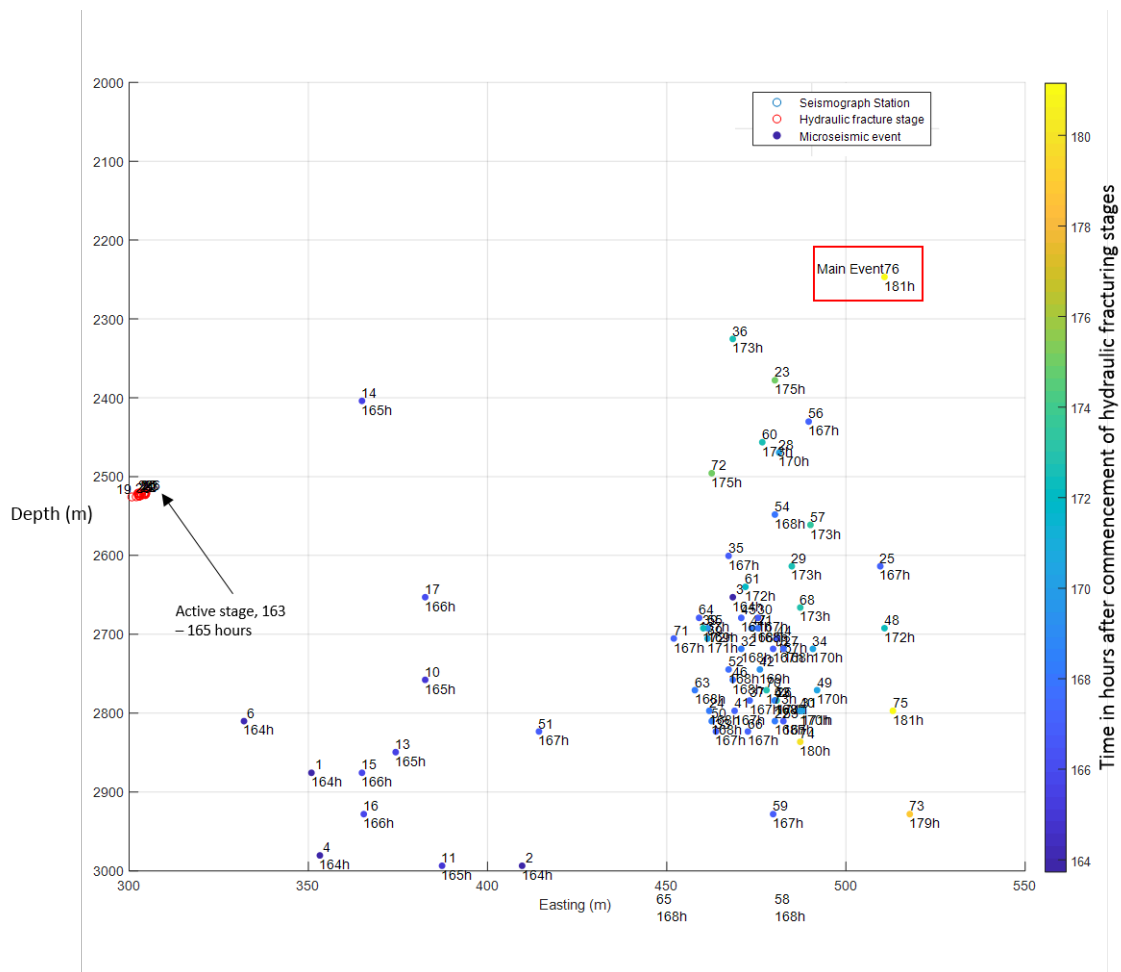


Figure 7.12: Map of all events from subset 1 viewed in-depth in an E-W direction

To test the second part of criteria 1, information that shows the detected events are

the location and fault plane of the main event. Signal strength issues prevented the link events from being analysed with the software so no fracture information is available for these. Of the events that were possible to be analysed, events 10,14,38 and 67, only event 38 is showing a fracture plane that links between the gap of the hydraulic fracture stage and the main event fault plane. The second area of interest is the grouping of events to the North-East, group 1, where there are fractures aligning in an SW-NE direction, towards the main event. This conclusion is clear from the overview map presented in figure 7.13, but further possible preferences of the evolution of the fracture network in time can be made when the origin time of the events are taken into account as shown in figure 7.14.

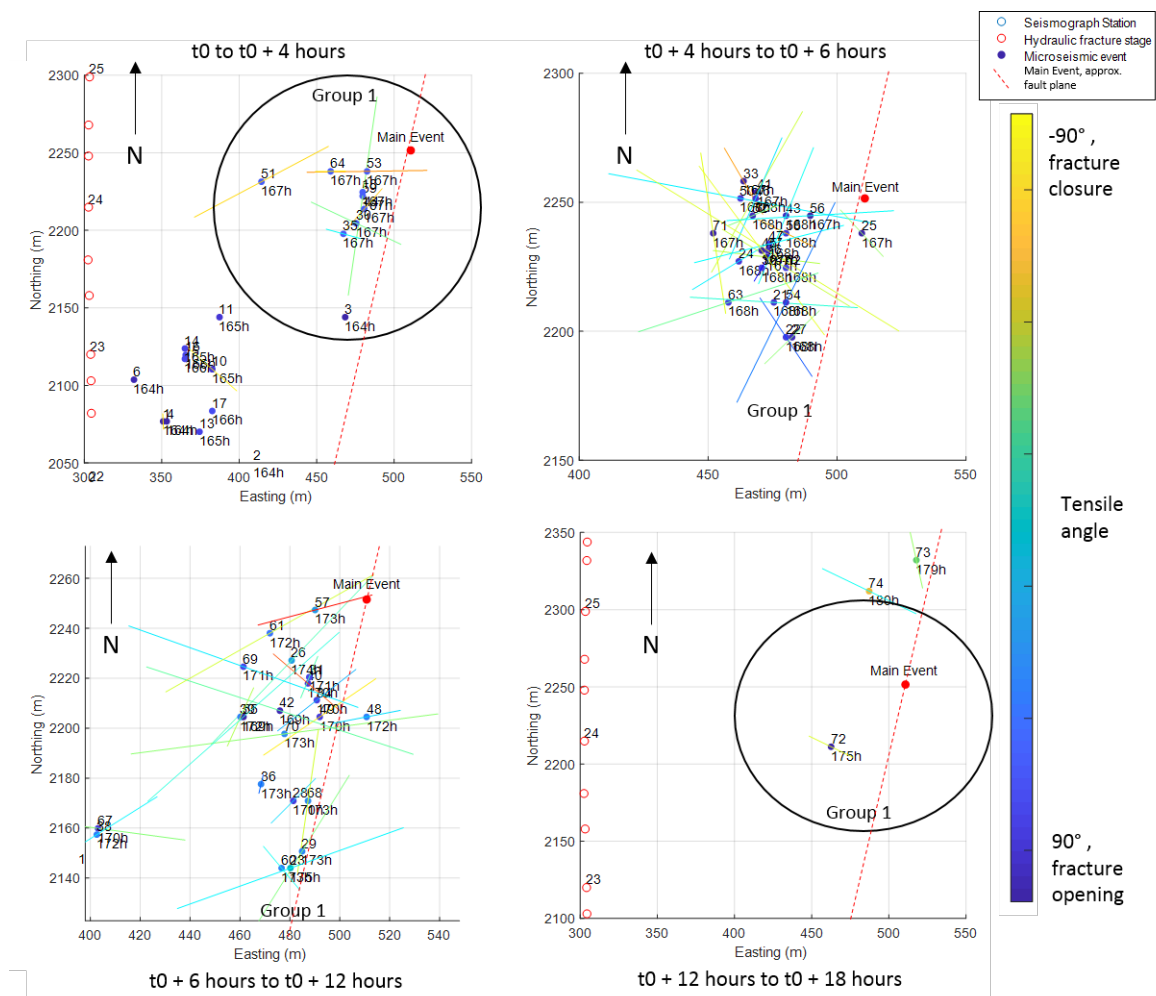


Figure 7.14: Evolution of the fracture network with time from the start of the hydraulic fracturing stage.

In figure 7.14 the evolution of the fracture network in time shows that a hydraulic connection between the wellbore is possible. From t_0 to $t_0 + 4$ hours, map (1) on figure 7.14, there are a number of events in the link between the wellbore and group 1 and within this group, there are a couple of events which align in an SW-NE direction. In the next 2 hours, map (2), a large number of events occur within group 1, with a wide range of fracture directions. The derived fracture planes extend over the approximate fault plane of the main event. In the following 6 hours, further fractures occur that overlap the main event's approximate fault plane. In addition, there is a fracture plane from event 38, that covers part of the link between the wellbore and group 1. In the final 4 hours before the main event slip, there are fewer events occurring within the area compared to the previous time segments. This is possibly linked to an increase in strain energy before slip occurs at the main event. This map shows that there is viability for a hydraulic connection between the wellbore and the main event from the map viewpoint.

If the data is viewed from a depth viewpoint, then the events in group 1 and the link events are positioned deeper than both the main event position and the wellbore. A hydraulic connection is possible between some of the events in group 1 (event 23, 28, 36 and 60) and the approximate extent of the fault plane (500 m width) for the main event. This is shown in figure 7.15 which shows a depth view following an E-W direction with the derived fracture planes and a approximate main event fault plane. Similar to viewing the data in map view, the lack of information regarding the link events means it is difficult to identify a hydraulic connection between the well-bore to group 1 from the depth viewpoint.

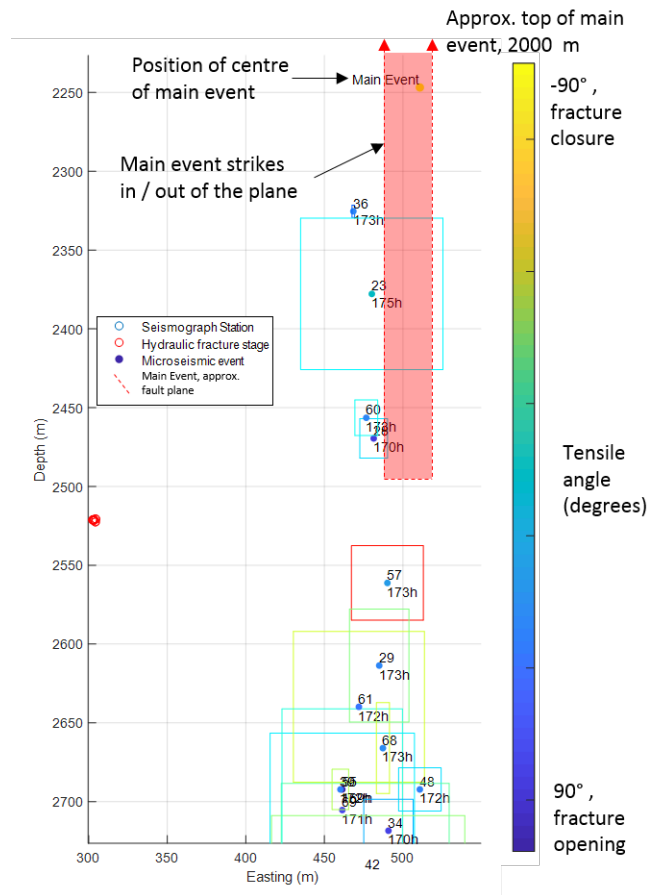


Figure 7.15: Depth view in an E-W direction of the fracture display output from the software package. This figure shows the fault planes for set 1 of the microseismic events coloured by the tensile angle and the approximate extent of the main event fault plane. There are two items of note in this display, (1) the lack of fracture information between the wellbore and the group of the microseismic events containing the main event location and (2) there are four microseismic events where the fracture planes coincide with the fault plane for the main event.

Testing Criteria 2 - Fracture aperture viability

To test the first part of criteria 2, information that shows that fracture fluid can transport through the proposed fracture network, the focal mechanism and in particular the tensile angles of the events in the fracture maps were considered. This is shown in figure 7.16 by categorising the tensile angle into two separate plots, tensile angles of 5 to 25 degrees and greater than 25 degrees. These plots show that there is a network of fractures which are opening towards the main event position allowing fluid to flow between the fractures.

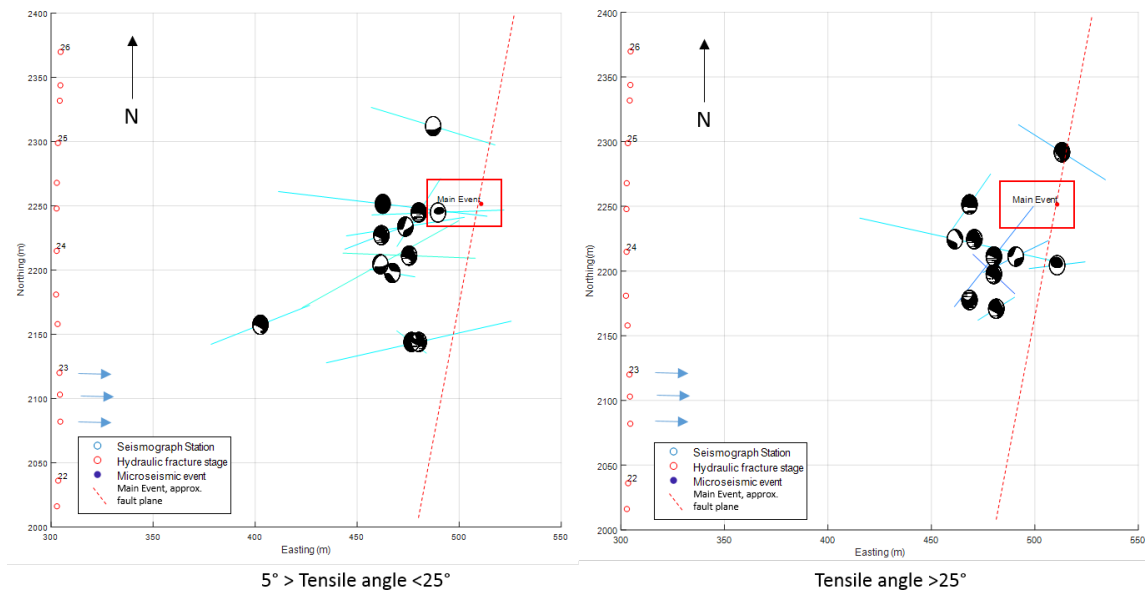


Figure 7.16: Maps of the microseismic events fracture planes, where the tensile angles are between 5 degrees and 25 degrees (left) and greater than 25 degrees (right).

To test the second part of criteria 2, information indicating any preferential fluid pathways in the fracture network, the focal mechanism for the faults are analysed to see if the slip is towards the main event. This is conducted by reviewing the rake direction from the focal mechanism. The rake angle shows the direction of the movement of the hanging wall, with angles of 0 and 180 degrees indicating strike-slip movement and 90 and -90 degrees indicating reverse and normal faults respectively. These different angles are shown in the diagram in figure 7.17. The rake directions are shown for the fractures with tensile angles greater than 5 degrees from a depth viewpoint, along an E-W direction as a directional vector. Figure 7.18 shows that fractures 23 and 60 are both moving upwards towards the main event diagonally

possibly showing a preferential pathway.

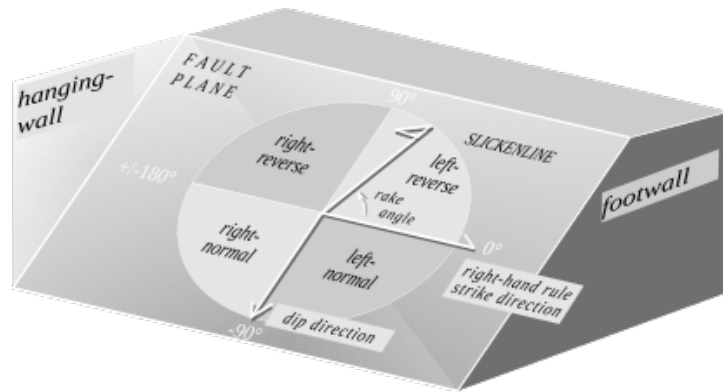


Figure 7.17: Relationship between the rake angle and the fault plane, image from Alberti (2005).

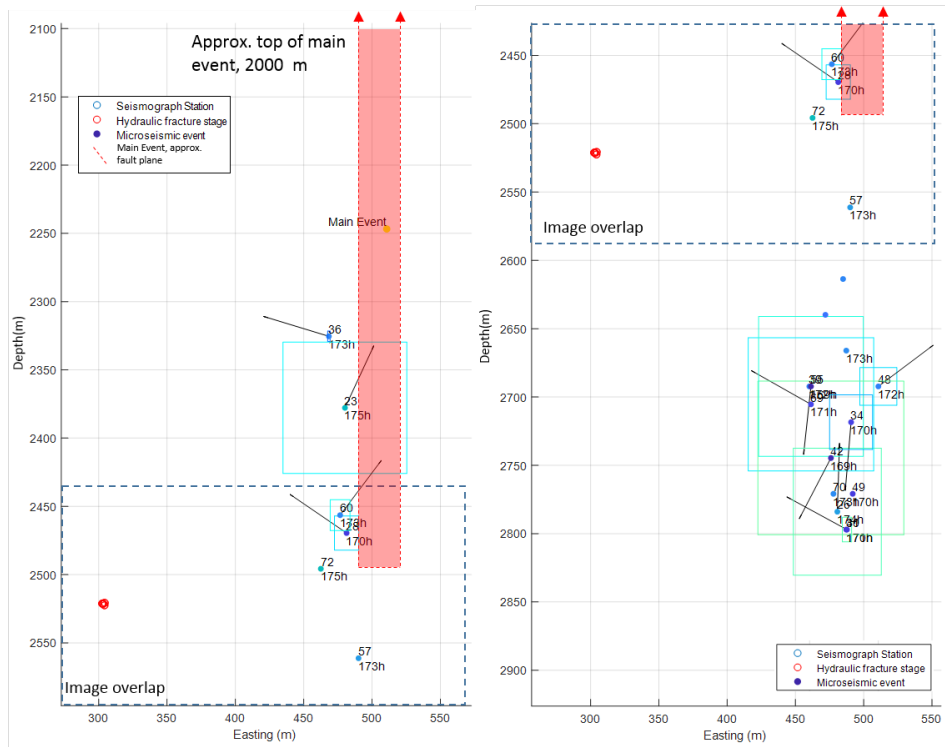


Figure 7.18: Depth view of the wellbore, main event and a set of microseismic events with tensile angles greater than 5 degrees. For each microseismic event, the fracture planes, coloured by the tensile angle and the rake angle is annotated. Of these events, events 23 and 60 show a slip direction towards the main events fault plane

In both of these comparisons to the testing criteria, the tensile angle is used as an analogue measure for fracture opening that would allow fluid flow. If a fracture aperture was calculated from the seismic events, this aperture would be smaller than the final aperture that fluid flows along, as the received seismic wave occurs at the point of maximum stress when the fracture initially opens. The fracture aperture then opens further with fluid flow post seismic. This part of the movement is not detectable at the distances in this case study, so any calculations of the aperture length would be a significant under-estimate. With regard to the testing criteria, figure 7.16 shows there are fractures opening under tensile conditions allowing fluid flow and figure 7.18 shows there is movement towards the main event position, highlighting a preferential pathway.

7.3.4 Conclusions, Mechanism 1

There were two sets of criteria used to judge if this mechanism is the cause of the main event. The result from each of these criteria is summarised below.

Testing criteria 1: Hydraulic connection between the wellbore and main event

1. Events detected occurring between the wellbore and main event position within the viable time window.

Criteria passed, Events detected occurring between the wellbore and main event during the 18 hour time window

2. Information that shows the detected events are part of a fracture network between the wellbore and the main event

Criteria partially passed, A fracture network appears to exist between the main event's fault plane and the fault planes from a group of microseismic events. The lack of signal strength for the microseismic events detected between the wellbore and this group of events stops these events from being investigated and a full hydraulic connection being resolved.

Testing criteria 2: Fracture aperture viability

The tests to be compared against are :

1. Information that shows the fluid can transport through the proposed fracture network

Criteria partially passed, within group 1 of the microseismic events, 26 of these events have tensile angles indicating the fracture is opening and the fluid could pass through. This information is not available for the link events between this group and the wellbore.

2. Information indicating any preferential pathways in the fracture network

Criteria passed, these fractures which are opening with a tensile force, two events show slip movement in the direction of the main events fault plane.

In conclusion, from the fracture map modelling of this set of 58 microseismic events, there is sufficient evidence to say that this mechanism was potentially the cause of the slip of the main event.

7.4 Mechanism 2, Stress transfer

The second programming requirement to be tested was that the software system is capable of monitoring for static stress transfers between seismic events. This was tested by retrospectively analysing the events associated with this mechanism with the main event as the endpoint. The forecasting potential here is that by monitoring the change in Coulomb stress in time during the stimulation activity, there should be a recognisable point in time when a seismic event is likely to be triggered from an increase in static stress.

7.4.1 Mechanism 2, static stress transfer from faults reactivated by hydraulic stimulation: Event set

There were over 5650 events that were detected by Contractor A that can be associated with a fault network running in an SW-NE direction. To minimise the number of events to be processed and to ensure the process has the highest chance of success, up to 10 events with the highest signal to noise ratios will be used from each of the 10 fault zones identified from figure 7.19. The events were chosen from the positions using velocity model A, as stated in the previous mechanism analysis, as the event detection threshold for contractor A is lower than contractor B.

Care was taken to ensure that the events chosen for processing extend over the full length of each individual fault zone so as to ensure that the Coulomb stress function modelled is an accurate representation of the changes in the stress field.

To check that the movement on these faults is due to the hydraulic stimulation activity at stage 1 and 2 and not just from background seismicity, 9 events were chosen which were positioned in-between stage 1 and 2 and the first fault zone. These events are highlighted in red on the figure 7.20. With these events and the events from the fault lines, the total number of events in subset 2 is 93.

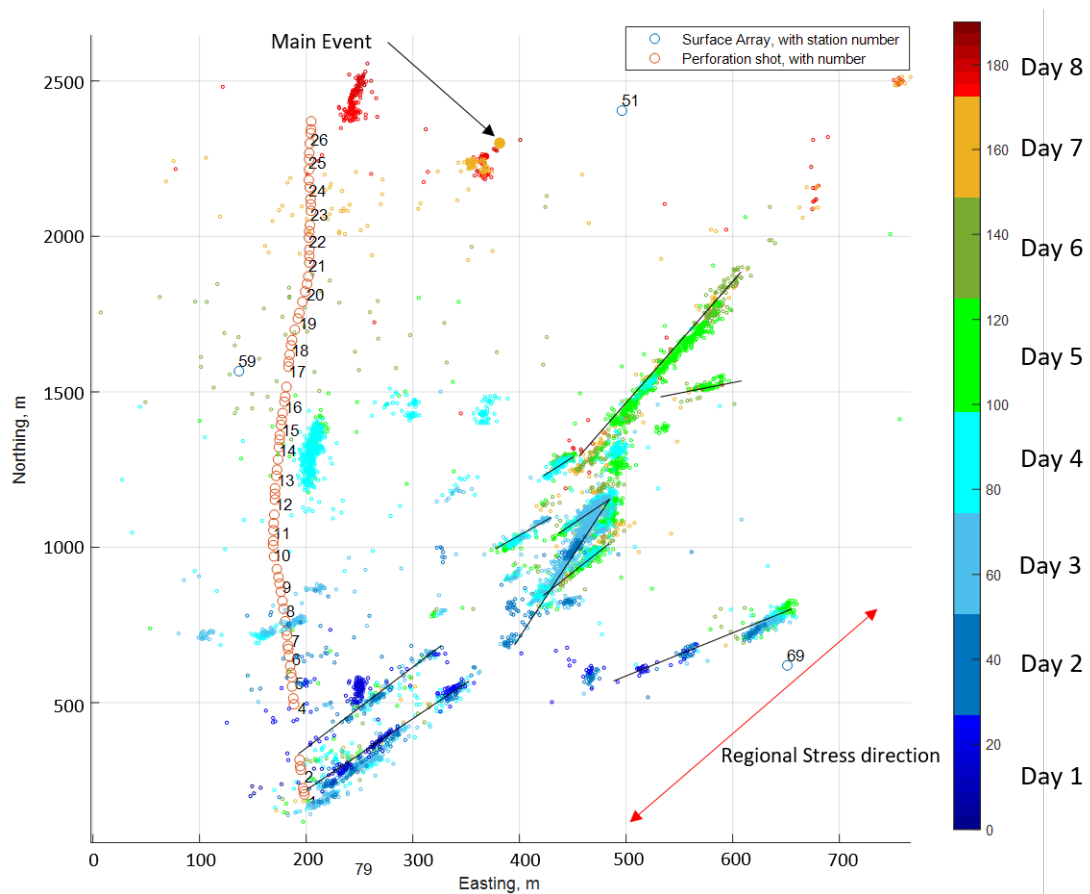


Figure 7.19: A map of all the events detected and positioned by velocity model A, coloured by occurrence day. Note the fault network running SW-NE, in-line with the regional stress direction.

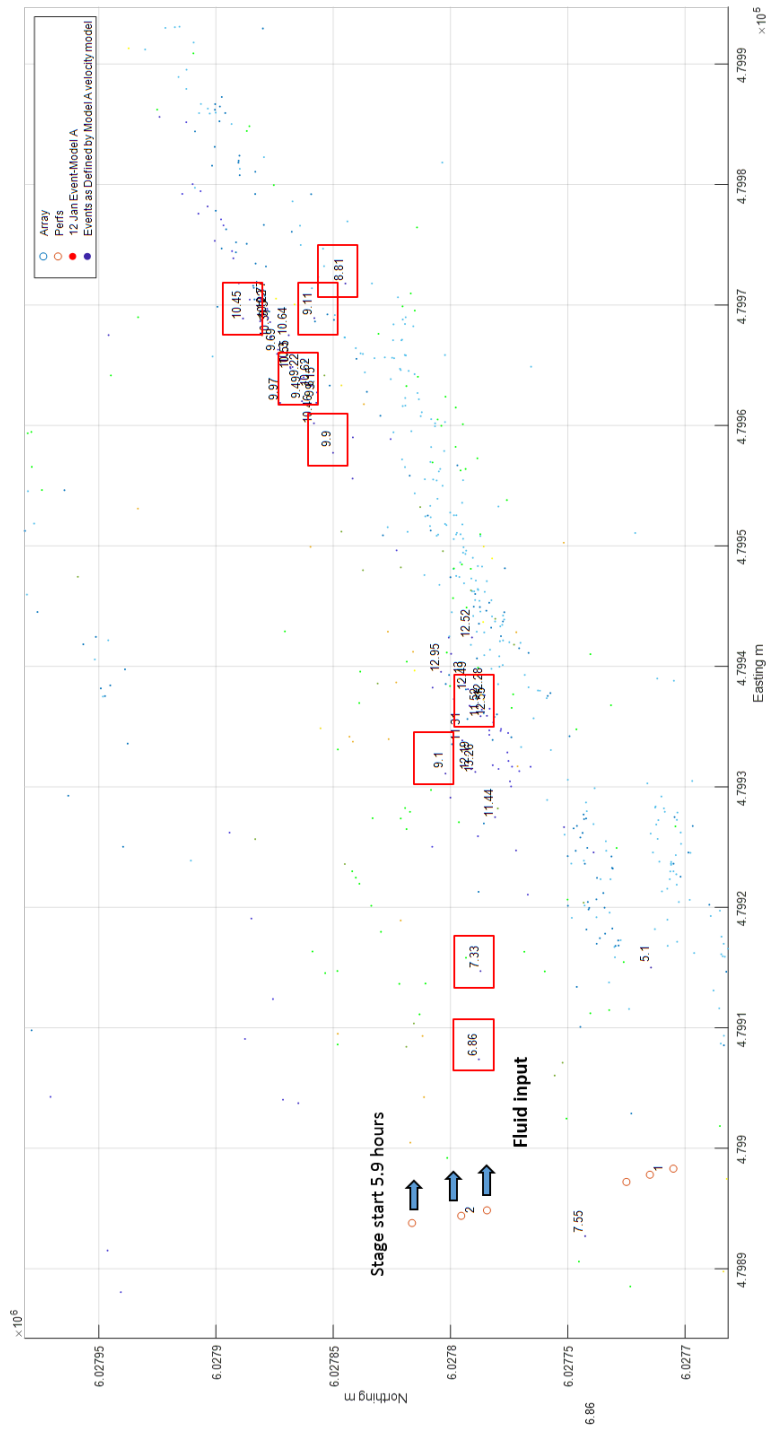


Figure 7.20: A map of the events positioned by velocity model A which occurred in the first 14 hours after the pumping routine started. The events highlighted in red were chosen for additional processing as the position and occurrence time implies a growing fracture network towards the start of the fault network

7.4.2 Mechanism 2, static stress transfer from faults reactivated by hydraulic stimulation: Testing criteria

To confirm if fracture fluid from stages 2 to 4 caused movement on the SW-NE fault network which then imparts a change to the stress field sufficient enough to trigger the main event, testing criteria, with the limitations that micro-seismic data analysis entails, were established. These criteria are a hydraulic connection between the wellbore and the nearest fault line to the wellbore and an increase in Coulomb stress change over the location of the main event.

Testing criteria 1: Hydraulic connection between the wellbore and the nearest fault line in the network

The tests to be compared against are :

1. Events detected occurring between the wellbore and the nearest fault line
2. Information that shows the detected events are part of a fracture network between the wellbore and the nearest fault line

To test for point 1) the positions and accuracy of the events detected between stage 2 to 4 to the nearest fault line will be reviewed. To test for point 2) the fracture directions of each of the events detected will be reviewed to see if there is a network of fractures that can be traced from the wellbore to the nearest fault line confirming the hydraulic connection using the developed software solution.

Testing criteria 2: Increase in Coulomb stress change over the location of the main event

The test to be compared against is :

1. An increase in Coulomb stress change over the location of the main event

To test for point 1) the Coulomb stress change will be modelled over the site by using the developed software package to look for a notable positive change in the Coulomb stress.

7.4.3 Mechanism 2: Monitoring capability tests

In this potential mechanism, the SW-NE fault system is firstly re-activated from fracture fluid from stage 1 and 2 of the hydraulic fracture operations. Fault planes slip along this network and this movement expands in a NE direction, transferring stress towards the main event. If this static stress change exceeds the strain limit for the fault plane of the main event, the event would then be triggered and slip. To consider this sequence of events, subset 2 of the events and the corresponding criteria discussed in section 7.4.2 will be utilised.

Similar to the first mechanism tested, the events were firstly re-positioned using the final velocity model. To analyse the potential for this mechanism the following maps were required,

1. A fracture map covering stage 1 and 2 of the hydraulic fracturing, to verify that this movement along this fault network was instigated by the hydraulic fracturing activities and not from background seismicity alone
2. A set of Coulomb stress change maps covering the SW-NE fault network over a series of depth slices that encapsulates the full extent of the main events fault plane.

To this end, the software system was used to generate the outputs for the fracture map and Coulomb stress change maps. The fracture map, similar to the first mechanism, required the fracture directions, lengths and mechanisms. Similar to the first mechanism the radiated energy ratio outputs were intended to verify the tensile angles of the events near to the well-bore. Comparing these two parameters, again similar to the results from the first mechanism, showed a lack of correlation and were once again not used to verify the tensile angles.

To use the Coulomb stress transfer module these parameters and in addition, the regional stress tension (calculated in chapter 4) and the slip of the recorded events were required. To calculate the slip of the recorded event, the magnitude of the event was calculated using the seismic moment module following the same procedure as established in chapter 6.

Of the 93 events within this subset, it was not possible to reposition 6 of these events, again due to the lack of signal strength compared to the background noise level. These 87 events were repositioned using the final velocity model ready for use with the software package. The software package was then applied to these events, following the established procedures outlined in chapter 6.

Testing Criteria 1 - Hydraulic connection between the wellbore and nearest fault line in the network

To test the first part of these criteria, events detected occurring between the wellbore and the nearest fault line, the position and occurrence time of subset 2 of the events were considered. While the hydraulic fracturing operation started on the 4/01/16 with a trial at stage 1, events were only logged from 05:00 on the 5/01/16 prior to the start of stage 2. To determine if the fracture fluid from stage 1 or 2 of the operations can enter, and re-activate the first fault of the SW-NE network the repositioned events in this area are reviewed. This is shown in figure 7.21 where 10 hours after the commencement of stage 2 of operation, there are two events (87 and 88) detected 100 m away from the wellbore. These events and three subsequent events, 95, 96 and 97 all align together into an SW-NE trend which continues towards the fault network. When viewed in-depth, these events are positioned deeper than the wellbore position as shown in figure 7.22.

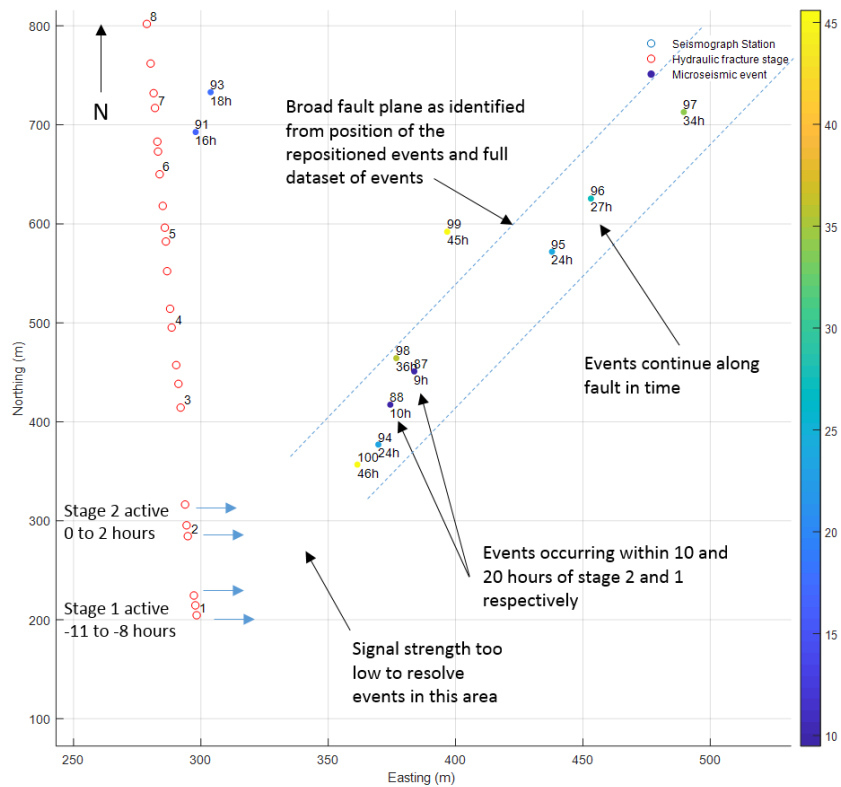


Figure 7.21: Map view of stage 1 and 2 of the hydraulic fracture operations and a set of microseismic events that are part of the SW-NE fault network

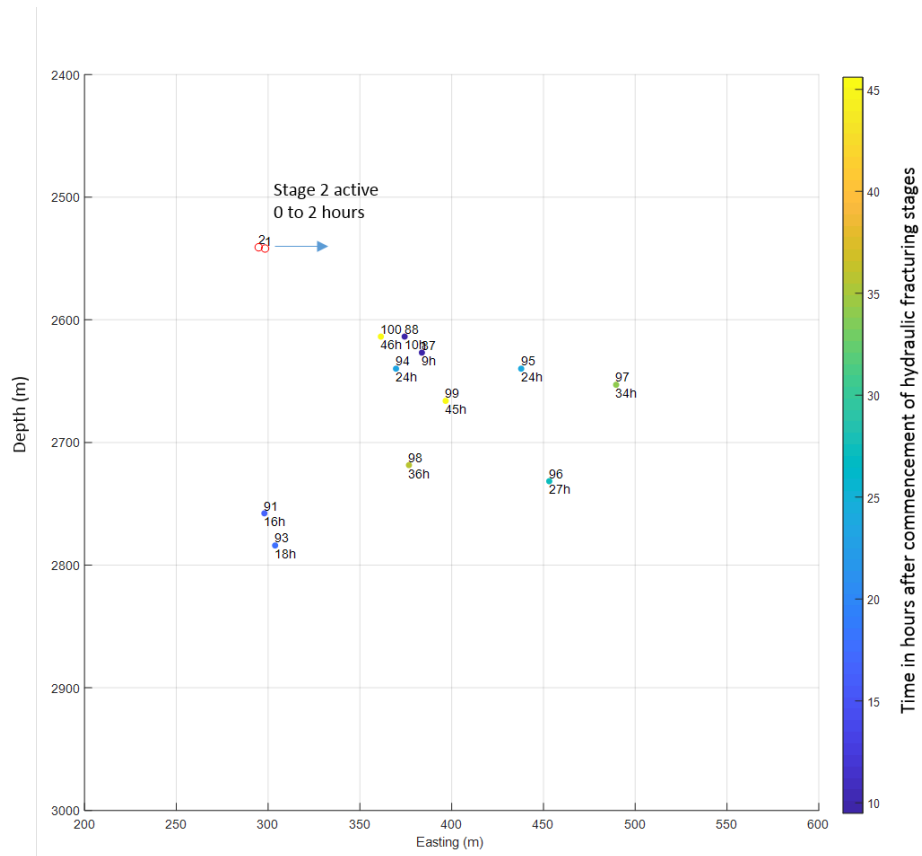


Figure 7.22: Depth view of stage 1 and 2 of the hydraulic fracture operations and a set of microseismic events that are part of the SW-NE fault network

To test the second part of this criteria, information that shows the detected events are part of a fracture network between the wellbore and the nearest fault line, the final fracture displays from the software were considered. This fracture display, shown as a map in figure 7.23, consists of the detected events (as points) near stage 1 and 2 of the hydraulic fracture operations with a map view of the fracture planes as calculated by the software package and coloured by the tensile angle, showing fracture opening or closure.

The fracture map shows that there is evidence of a fracture network linking the wellbore and fault 1, the start of the SW-NE fault network. Event 87 is the first event that could be repositioned and processed in the software and after analysis, this fracture opens with tensile forces. Subsequent events, 88, 95 - 97 are either shear dominated events or fracture closure implying that movement along this fault line started with the fluid input at event 87 and then continued with shear movement along the fault line. If these events are viewed in a depth view along the E-W direction, figure 7.24, there is overlap of the fracture plane for the tensile opening event, event 87 to the shear movement event, event 88. Event 100 also overlaps this event, further confirming that movement in the fault zone is instigated by fluid transfer. The first event identifiable in this sequence and within the fault zone is event 87 at 10 hours after the pumping of fracture fluid commenced. The other events chosen for subset 2 may have described the fracture network between the wellbore and fault 1 in the hours just after the start of the pumping operation unfortunately it was viable to reposition or process these events due to the poor signal to noise ratios.

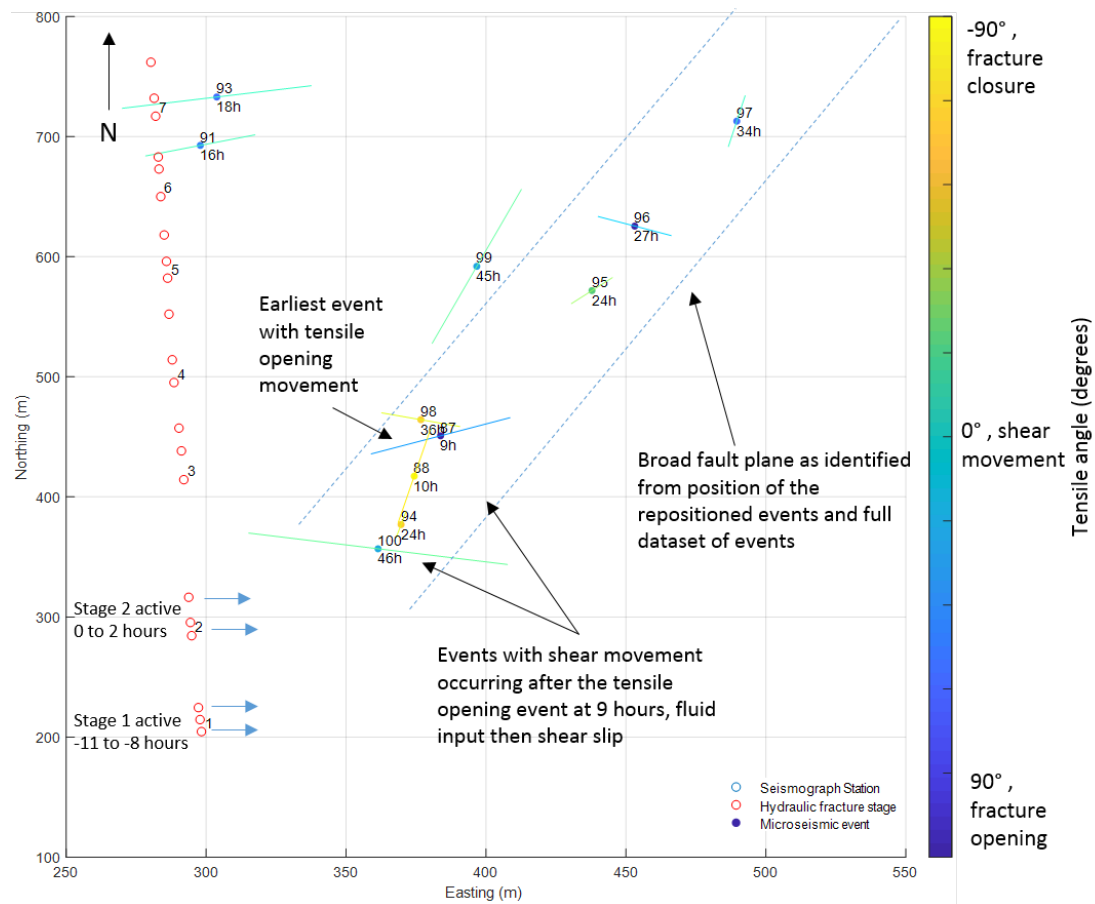


Figure 7.23: Fracture map generated from the software package. This map shows the detected events, with information regarding the occurrence time and ID number and a plan view representation of the fracture plane. This fracture plane is coloured according to the tensile angle with blue indicating a fracture opening under tensile forces. Additional annotations highlight the approximate fault plane of fault 1 of the SW-NE fault network. This map shows that there are few events which indicate that fluid flow from stage 1 and 2 start the movement of the SW-NE fault networks

Testing Criteria 2 - Increase in Coulomb stress change over the location of the main event

To test this criterion, the Coulomb stress change was modelled at depth slices from 2200 m to 2800 m depth. This range encapsulates the full extent of the potential fault plane for the main event and the wellbore target, the Duvernay. These slices are visualised as maps in figure 7.25 for 2200 m to 2400 m and figure 7.26 for 2600 m to 2800 m. These two figures show the Coulomb stress change imparted on the area from the SW-NE fault network. All of the slices show that the Coulomb stress change at the main event location does not exceed 3×10^{-4} bar. In comparison to the Coulomb stress change surrounding the microseismic events (± 1 bar), this is four orders of magnitude smaller, emphasising how small a change in stress is imparted on the site of the main event by this fault network. The required change in Coulomb stress to trigger an event is still an area of investigation within literature. A study by Stein (Stein, 1999) using aftershock information from the Landers - Big Bear earthquake on the San Andreas fault showed that 67% of the 10,000 $M_w > 1$ aftershocks positions were within regions where the Coulomb stress change was > 0.1 bar. Similar studies have been carried out by Kilb et al. (2002) on the same area and state a similar Coulomb stress change limit of 0.1 bar. There are no statistical studies similar to Stein (1999) that have been carried out on hydraulic fracturing projects.

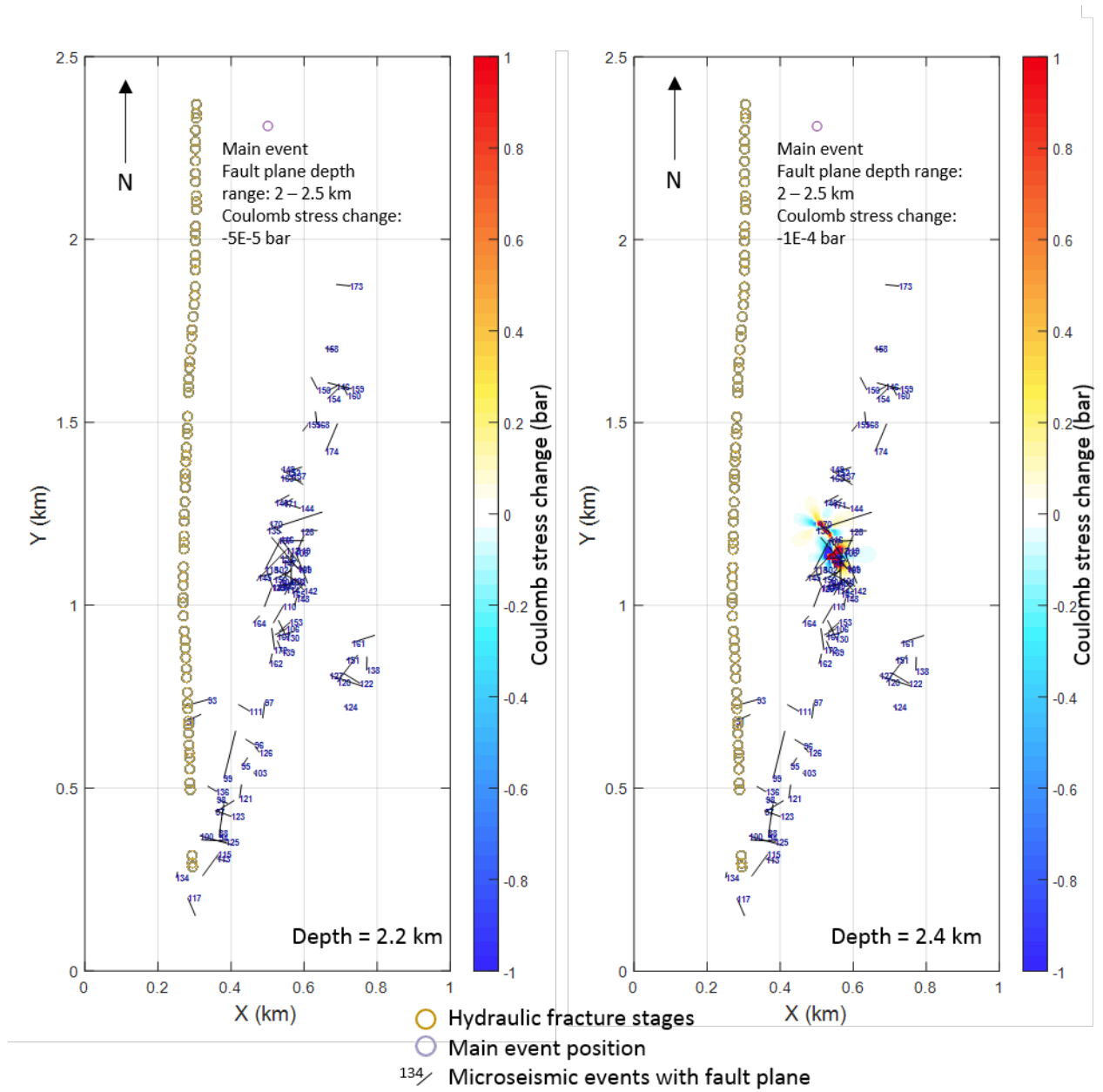


Figure 7.25: Coulomb stress change for the 2.2 km depth slice and 2.4 km depth slice

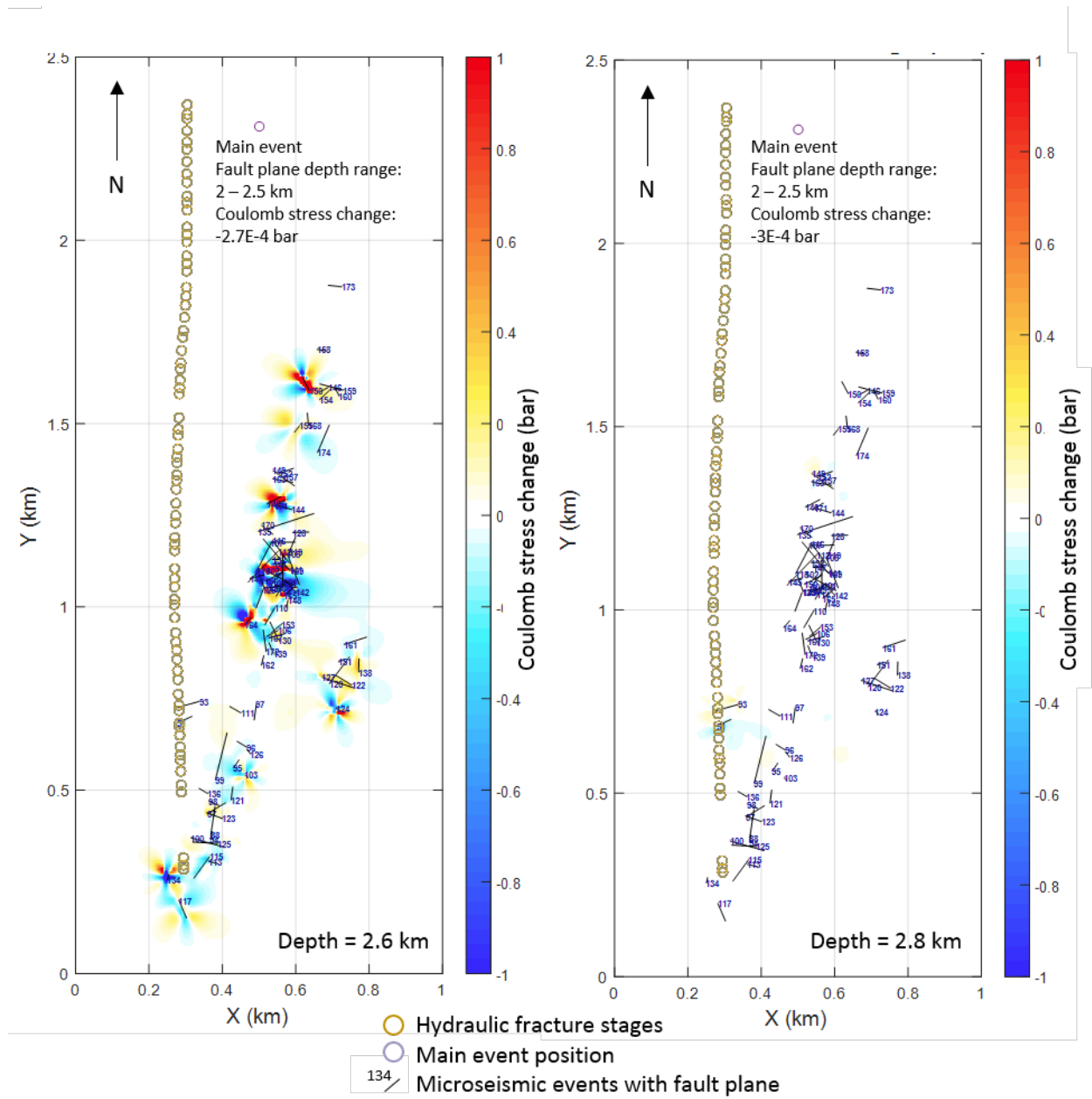


Figure 7.26: Coulomb stress change for the 2.6 km depth slice and 2.8 km depth slice

7.4.4 Conclusions, Mechanism 2

There were two sets of criteria used to judge if this mechanism is the cause of the main event. The result from each of these criteria is summarised below.

Testing Criteria 1 - Hydraulic connection between the wellbore and nearest fault line in the network

1. Events detected occurring between the wellbore and the nearest fault line of the SW-NE fault network

Criteria passed, Events detected occurring between the wellbore and the fault network

2. Information that shows the detected events are part of a fracture network between the wellbore and the nearest fault line

Criteria passed, Of these events there is evidence to show a hydraulic fluid connection, implying that movement along this fault network was instigated by the fluid transfer

Testing Criteria 2 - Increase in Coulomb stress change over the location of the main event

The tests to be compared against are :

1. A notable increase in Coulomb stress change over the location of the main event

Criteria failed, no notable increase in Coulomb stress change over the main event position.

In conclusion, from the Coulomb stress change modelled from this set of 88 micro-seismic events, this mechanism did not trigger slip at the main event.

7.5 Forecasting induced seismicity using the software package

In the previous two sections, the programming requirements of the software to monitor for the causes of induced seismicity were verified by diagnosing the cause of the main event slip. To address the overall aim of the thesis and the fifth objective, to evaluate the extent to which the developed software can be used to forecast induced seismicity, the sequence of events leading up to the slip at the main event was compared to the theoretical model developed in chapter 2.

The model developed from literature (figure 2.9) describes that there should be a point in time observable from the real-time monitoring of microseismic events when the evolving fracture network changes such that a seismic event is forecast to occur. For the first mechanism, this point is when there is a change in the direction of the fracture network and a change in the failure mode of the microseismic events from tensile opening to shear failure. For the second mechanism, this point is when the static stress transfers reach a critical point. The aim of this section is, using this case study, test if this model is valid as a means to test the overall ability of the software system to forecast seismic activity induced by hydraulic fracturing.

7.5.1 Mechanism 1: Forecasting induced events caused by pore-pressure changes instigated from hydraulic fracturing

To test if the software package developed can be used to forecast induced seismic events by the first mechanism, the final fracture displays in time increments from subset 1 of the events were compared to the model developed in chapter 2. The model for this mechanism is presented again as figure 7.27 and the fracture maps from the case study in time increments are presented as figure 7.28.

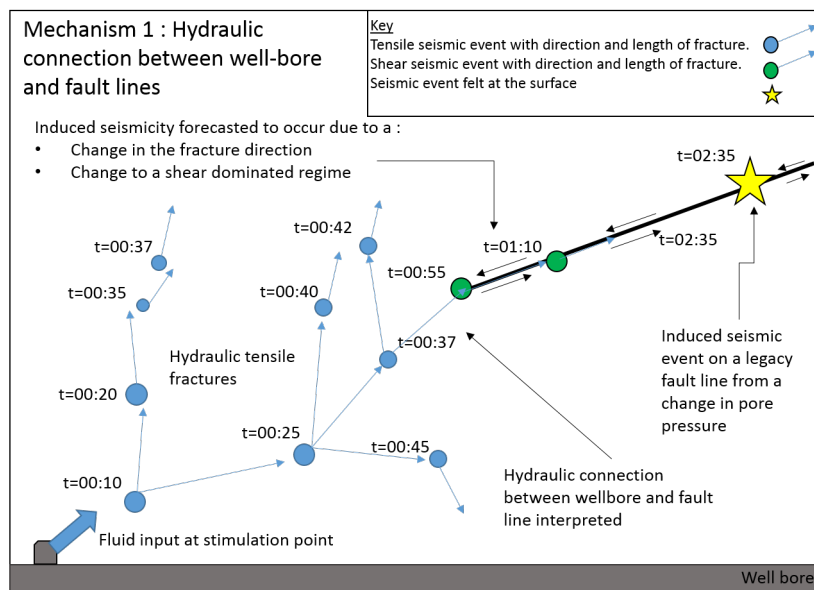


Figure 7.27: Data driven forecasting model for the first mechanism. A microseismic event should be observable where fluid enters the fault system. From this point onwards there is a higher likelihood of seismic event from occurring.

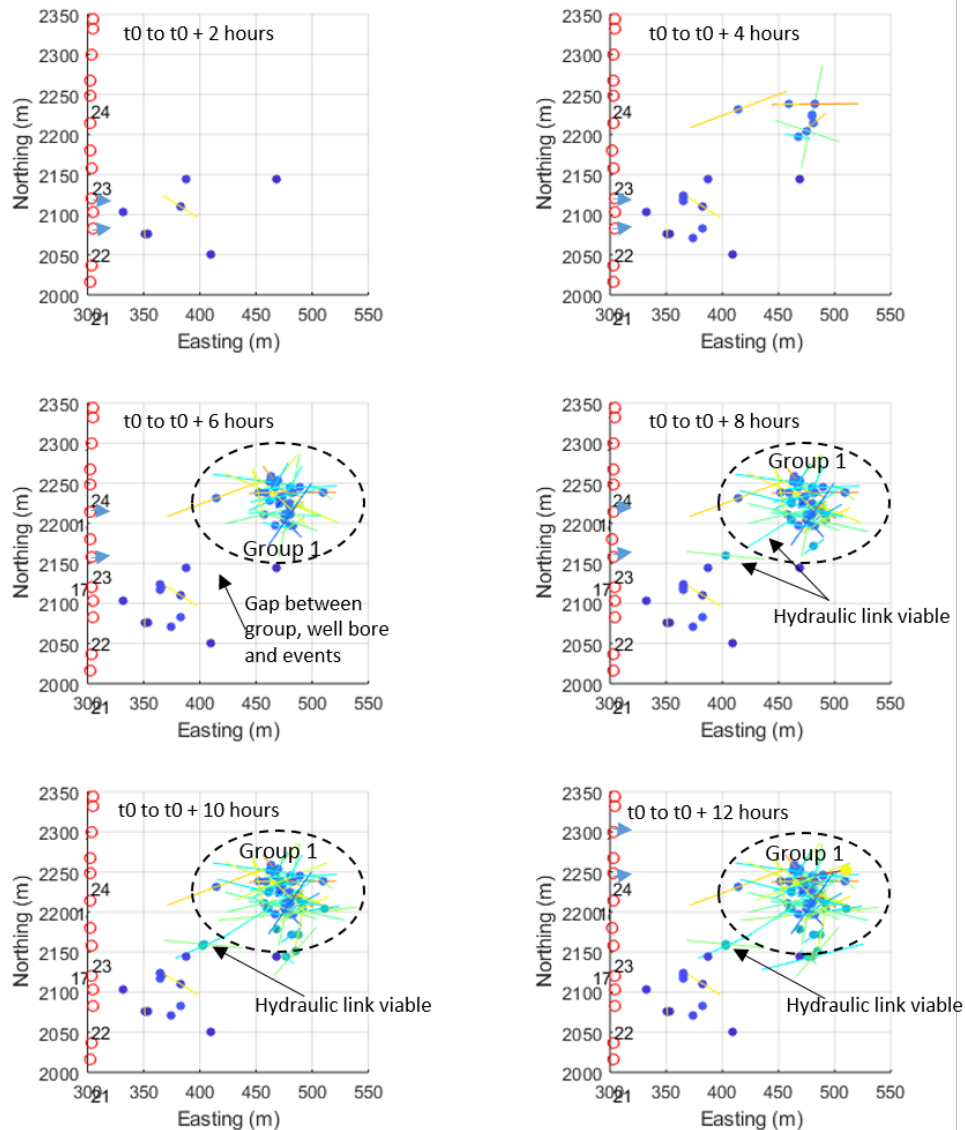


Figure 7.28: Fracture maps with time from the start of stage 23 of the hydraulic fracturing program (t_0) to 7 hours prior to the main event slip ($t_0 + 12$ hours). In the first maps from t_0 to $t_0 + 2$ hours only low signal to noise ratio events were detected which could only be positioned. In the second and third maps, t_0 to 4 hours and 6 hours, a number of events are detected in a grouping 100 m away from the wellbore. There is no established hydraulic link between the wellbore and this group at this point in time. In the next two images, $t_0 + 8$ hours and 10 hours, it is possible to interpret a hydraulic link between the well and this group.

Comparing the maps in figure 7.28 to the forecast model in figure 7.27 highlights the data processing challenges in this dataset. For the first 2 hours after the fluid injection started, only low signal to noise ratio events were detected, which were unable to be processed through the full sequence and could only be positioned. It is only after 2 hours when the first processable events are detected, in a group near where the main event eventually occurs, annotated on figure 7.28 as group 1. At no point in this sequence of events is there a clear transition from a set of tensile fractures next to the well bore to a shear dominated set of microseismic events as per the model in 7.27. The tensile fractures that are part of this model may be these low signal to noise events but this cannot be confirmed as it's not possible to process these events.

Reviewing the figures in 7.28 there is a point in time (from 8 hours after injection begins) when a transition can be interpreted from the fracture plane directions and tensile angles. This transition indicates that a hydraulic connection between the well-bore and group 1 has been established and that frac fluid is entering the fault system in question ultimately leading to the slip at the main event. This point in time could be utilised as when the forecast changes and the likelihood of an induced seismic event occurring increases, but because this is interpreted from retrospective knowledge without a clear transition (from tensile to shear events) this lacks independent objectivity. Moreover, while such an interpretation could be used to forecast that an induced seismic event is increasingly likely to occur in this group within the near future, using a criterion that differs from the forecast model may potentially miss the optimum moment for mitigatory measures to be enacted. To verify the forecast model, a case study where the monitoring array is situated closer to the events would allow this transition to be imaged with greater clarity.

7.5.2 Mechanism 2: Forecasting induced events triggered by static stress transfer from other microseismic events

To test if the software package developed can be used to forecast, in real-time, induced seismic events by the second mechanism, the Coulomb stress maps in time increments from both subset 1 and 2 of the events were reviewed to see if there is a point in time when an increase in Coulomb stress change exceeded 0.1 bar and then a high magnitude seismic event follows in sequence within the same area. This follows the model established in chapter 2, where if this criterion is exceeded a seismic event is likely to occur. Unlike the first mechanism, where the conditions leading up to the slip at the main event could be used as a case study, this mechanism was not the primary cause of the main event. This dataset was used to test the forecasting ability for this mechanism by reviewing other possible examples in subset 1 and 2.

To verify that the software system has this capability, the Coulomb stress change maps output from the software system were reviewed over the SW-NE fault network in time. These displays are calculated differently from the displays used in section 7.4.3 where the Coulomb stress change was modelled for the ‘receiver’ fault parameters of the main event. In this instance, the optimum fault parameters mode is used. To test this capability, areas where a higher magnitude seismic event occurs, were sought along the SW-NE fault network as a test to see if this event could be forecast from the Coulomb stress change. The faults occurring prior to this event are then used to calculate the Coulomb stress change maps to see if this chosen event is coincident in areas of increased Coulomb stress change, and associated increased risk of a seismic event occurring.

In figure 7.29 the 10 faults prior to two $M_w > 0.8$ events were utilised to calculate the Coulomb stress change map. Within 4 hours from when the events used as part of the calculation occurred, one of the $M_w > 0.8$ events is detected, coincident on an area of positive Coulomb stress change while the second $M_w > 0.8$ event is coincident on an area of negative Coulomb stress change. Although these two events originate closely in time (within 10 minutes of each other) and therefore the mechanisms involved in the events origin are unlikely to be purely due to a static stress change, it is not clear from this example if these two events could have been predicted from the Coulomb stress change maps as both events are not consistently located on an area of Coulomb stress change greater than 0.1 bar.

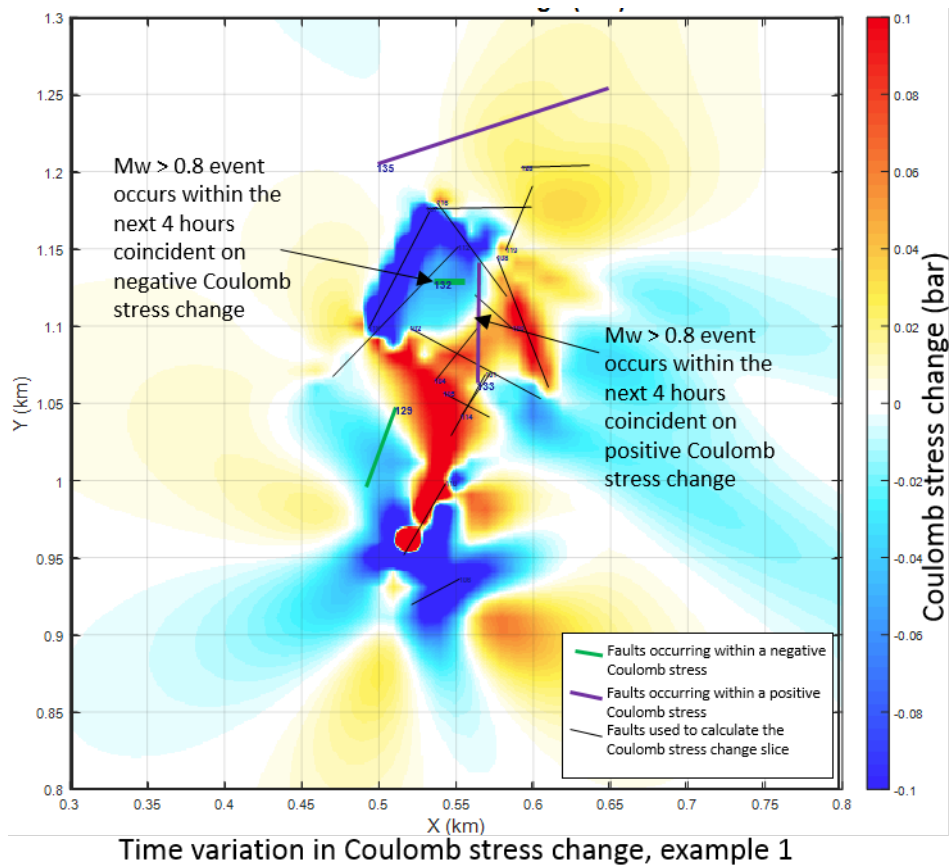


Figure 7.29: An example of the variation in Coulomb stress with time over part of the SW-NE fault network. In the example, the faults shown in black are used to calculate the Coulomb stress change. Over the next 4 hours, two faults are coincident on areas of positive Coulomb stress change again indicating these faults were in-part triggered by stress transfer, including one of the $M_w > 0.8$ events. There are also two faults which are coincident on areas of negative Coulomb stress change, where it should be less likely for faults to occur if static stress transfer is the sole cause of earthquake triggering.

7.6 Discussion

This chapter documents the final part of the software development process, testing the capability of the software system to monitor and forecast for the causes of the induced seismicity as per the objectives outlined at the beginning of the thesis.

The monitoring capability was trialled by diagnosing the cause of the main event from the Wahigan case study. This found that the main event was primarily caused by a change in pore-pressure on the fault plane, instigated by stimulation fluid travelling from stage 23 of the hydraulic fracturing program. This path is not imaged completely as there are a number of low signal to noise events that couldn't be processed in the path between the wellbore and the location of the main event. Although the path is not imaged completely, the microseismic events surrounding the main event line up to the wellbore and show tensile opening. This shows a hydraulic pathway from the wellbore allowing frac fluid to reach and re-activate the fault line ultimately causing slip and a disturbance on the surface. The other potential cause, static stress changes from an extensive SW-NE fault network triggering movement on the main event, was found to have a negligible effect. This is because the Coulomb stress over the position of the main event was four orders of magnitude lower than the required amount (as deemed from literature) to trigger an event.

The forecasting capability of the software system was trialled by comparing the outputs of the software to the forecast model developed in chapter 2. For the first mechanism, this was trialled by comparing the sequence of events leading up to the main event in time to the forecast model. This found no clear transition from tensile events near the wellbore to the shear events near the location of the main event. To verify this forecast model, other case studies would have to be examined where the monitoring array is situated closer to the event.

For the second mechanism, although it was not involved in the cause of the main event, a sequence of events was taken from the SW-NE fault network to see if a high magnitude event occurs within an area of greater than 0.1 bar Coulomb stress change. However, this dataset did not present a conclusive example where a high magnitude event was coincident on an area of positive Coulomb stress change from a set of events. This will require further testing with different datasets.

Overall, the issue of defining the correct moment to enact mitigatory measures given limited information and no knowledge of the final effect is the fundamental challenge for all reactive control methods such as traffic light systems and pre-defined fracture lengths. The advantage that this software package now allows is that greater information is available to interpret the point at which either a hydraulic connection has

been established, or when sufficient static stress change has been transferred, both of which may be used for improved forecasts of induced seismicity.

Chapter 8

Discussion and conclusions

8.1 Introduction

The work presented in this thesis aimed to establish the extent to which induced seismic activity from hydraulic fracturing can be forecast in real-time using micro-seismicity. This chapter reviews this aim and considers how the overall work in this thesis contributes to this aim. This chapter will review the objectives to the research project and highlight the key contributions and advancements along with commenting on the next stages of further work.

Recalling from the introduction given in chapter 1, the objectives were :

1. Review and critically evaluate the current approaches to forecast the seismicity associated with hydraulic fracturing.
2. Identify and review the primary mechanisms that induce seismicity from hydraulic fracturing operations.
3. Design and develop a software system to address the limitations associated with current forecast approaches.
4. Review and develop methods to appraise the positional accuracy of the geophysical models required in forecasting
5. Evaluate the extent to which the developed software can be used to forecast induced seismicity

8.2 Current state of forecasting induced seismicity

To consider the first objective a literature review was carried out to review the consequences of induced seismicity from hydraulic fracturing projects around the world and the methods employed to mitigate these causes. This highlighted that the majority of the industry utilise reactive control approaches as a means to minimise the level of induced seismicity. This approach, of which the well-known traffic light protocols are part, intends to use parameter(s) that once exceeding certain criteria to cause mitigation measures to be implemented, such as reducing the pressure from the hydraulic fracture stage or pausing injection. These reactive control approaches are therefore a means to forecast seismic events, as when these criteria are exceeded, a seismic event associated with the hydraulic fracture operations is judged to have a high probability of occurring.

The other forms of forecasting discussed in the literature review were probabilistic approaches using forecast models. These are a recent development within the industry and aim to supply a synthetic catalogue of induced seismic events that are to be expected in the future. While there was research into using forecast models to predict seismic events using case studies, these were all retrospective reviews and no system has yet been implemented to forecast in real-time during production. The only system that may be capable of this is the Adaptive Traffic Light System (ATLS) by the Swiss Seismological Service (SED). This system is a hybrid modelling approach that calculates the probabilistic seismic hazard in real-time and is currently (at the time of writing) being field-tested in Iceland. The limitations of both of these approaches were explored and the scope for a new forecasting system identified.

8.3 Design of a new forecasting approach and development of a software system

The literature review supported development for a new forecasting system that is an expansion of the reactive control approaches that consider the evolution of the fracture network with respect to the known mechanism of seismicity associated with hydraulic fracturing. A literature review of the mechanics that causes seismic events from hydraulic fracturing operations found two broad mechanisms that if monitored in real-time could be used to forecast if these seismic events are more likely to occur. This formed the basis of a forecast model. This model supposes that a point in time

is observable where for the first mechanism, there is a transition where the fracture fluid enters the legacy faults and for the second mechanism, the static stress transfers exceed a set amount.

Real-time monitoring for these two mechanisms, fault re-activation from an increase in pore pressure from a direct hydraulic connection and fault re-activation from the transfer of stress from other seismic events, was established as the central concept for the design of the software system. These requirements were used as the objectives to steer the system development and the geophysical analysis methods that could fulfil these requirements were researched (Chapter 3) and incorporated into the system design.

This review of methods identified five established geophysical analysis methods which when incorporated into one software system would fulfil the programming requirements to monitor the evolving fracture network. These methods were, pulse directivity, full-waveform moment tensor inversion, radiated energy ratio calculations, seismic moment calculations and Coulomb stress transfer modelling.

The overall intention of the software is that by monitoring for these two mechanisms in real-time there should exist a point in time when the observed fracture network can be interpreted as leading towards a higher probability of a notable seismic event occurring as identified in the forecast model. To validate this theory and verify the software system's ability to fulfil the processing requirements, an industrial case study was utilised.

8.4 Industrial case study

The case study was provided by an industrial partner from a shale gas production site in Fox Creek, Canada during January 2016. This well was targeting the Duvernay formation, a gas-rich shale formation, using a planned 30 stages of hydraulic fracturing. A 3.9 magnitude earthquake was felt at the well site on 12 January 2016 (named as the main event in the text) during stage 26, and in accordance with the traffic light protocols established by the AER (Alberta energy regulator) hydrofracture at the site was suspended. The dataset provided for analysis consisted of a surface array of 96 seismograph stations continuously recording microseismic events from prior to the commencement of the operations until 2 days after the main event was detected.

This dataset was the primary dataset for analysis in this thesis. This dataset had already been processed in 2016 by two different contractors and catalogues of detected events and velocity models were provided. The first challenge before this dataset

could be used to test the software system was to analyse the accuracy of the two velocity models and to solve the 350 m depth discrepancy between the two catalogued positions. This was the aim of the first part of chapter 5 using an objective function of the squared double-difference times between the modelled and observed arrival times of the first arrival (P-wave) from both a set of fixed-position events (the perforation shots) and variable position events (detected seismic arrivals from around the site). This quantitative analysis showed that velocity model A provided by the first contractor had a higher accuracy than velocity model B for the fixed position events but when the variable position events were considered, including the main event, the reverse was true and this was due to a fixed shift in the velocity model over-fitting the data to the fixed position events.

To finalise the final two required pre-requisites for the software system, first a new 1D velocity model was calculated using the fixed position events as input into a VFSA (very fast simulated annealing) algorithm. This velocity model was compared to the other velocity models using the variable position events and shown to be an improvement in positional accuracy compared to these models. The final pre-requisite, an attenuation model to remove the effect of attenuations on the path between source and receiver was calculated. This 2D model was calculated using a single seismic event detected near the centre of the array by the rise time method and verified using a second event.

8.5 Development and testing of the software system

With the dataset pre-requisites calculated, the software system was developed in a modular fashion while adhering to the three programming objectives. Testing for each module was provided by a single event from the dataset to facilitate rapid prototyping efforts. Despite attempts to use automated picking algorithms to identify the timing points required to calculate the rise and rupture times for the inversion in pulse directivity module, it was not possible on this dataset to identify automatically these points due to local interference on the received signal from the installation borehole. For this dataset, this nullifies the ability to work in real-time as these points had to be identified manually. During this development process discussed in chapter 6, the ability to use these methods at the scale lengths in question was verified and the outputs of each module were evaluated compared to empirical studies to ensure that the programming was completed competently.

With the software developed and tested using a single event, the testing schedule was

expanded to verify the software’s capability to complete the programming requirements (chapter 7). This was conducted by retrospectively determining the mechanism which contributed to the cause of 12 January seismic event (referred to as the main event). By using the software system in this manner validated that the software has the capability to monitor for the causes of induced seismicity outlined in chapter 2. Using two subsets of events that concerned each of the two potential mechanisms and a set of testing criteria, these two criteria were tested against the outputs from the software system. Judged against these criteria, it was deemed that the 12 January seismic event was caused by an increase in the pore-pressure reactivating the fault plane brought on by a hydraulic connection from stage 23 of the operations. There was no evidence as seen from the Coulomb stress change maps output from the software system that a series of microseismic events distributed as an SW-NE fault network transferred sufficient stress to the fault plane to solely cause re-activation.

This conclusion is in agreement with a recent report by Eyre et al. (2019) into the cause of the main event. This report details that while structurally the main event lies on a flower structure with the SW-NE fault network aligned on another strand of the structure, fractures from stage 23 of the operations may have activated this part of the fault structure from a change in the pore pressure.

With regard to the three programming requirements, it was demonstrated that the software system could monitor for the two potential mechanisms that induce seismic events from hydraulic fracturing operations. With regard to the third programming requirement, the capability to process in real-time, there were issues with running the autopicking routines on this dataset due to local interference altering the received wavelets.

8.6 Forecasting induced seismicity

To address the final objective and to consider if this type of software system could forecast induced seismic activity, the case study and the outputs from the software system were compared to the forecast model.

The forecast model for the first mechanism supposes that there should be a point in time when there is an observable transition in the fracture network from hydraulically connected tensile fractures to a shear fault. From this point onwards the likelihood of an induced seismic event occurring in the future in this area is raised. When this model was compared to the case study, there were a number of low signal to noise ratio events near the borehole which appeared to link to a grouping of events where the eventual fault line slipped. It wasn’t possible to validate this model fully with

this case study as the signal strength for these events precluded analysis through the software package.

The forecast model for the second mechanism supposes that if the Coulomb stress change exceeds 0.1 bar in an area then the likelihood of a seismic event increases. These criteria were set from the basis of three academic studies from the San Andreas fault where an increased aftershock density occurred in areas of a 0.1 bar Coulomb stress change. Unfortunately, as the static stress change towards the main event position was negligible, and after reviewing the interplay between other lower magnitude events there are no clear examples where this criterion was validated in this case study.

The extent to which this software system forecasts seismicity is by extending the reactive control approaches that currently utilise a single parameter (TLP's) to an interpretation, based on a forecast model, of two output maps. This forecast model is yet to be fully validated for both mechanisms and further case studies would have to be analysed using this system to see if this model is appropriate before this system could be trailed in real-time to forecast seismic activity induced by hydraulic fracturing operations.

8.7 Overall Conclusions

In terms of overall conclusions that can be drawn from the research performed, the following observations are presented:

1. A new induced seismic activity forecasting approach was devised that relies upon real-time monitoring of the mechanisms that induce seismic activity from hydraulic fracturing, removing modelling requirements used in current forecasting models.
2. A forecasting model that can determine when the likelihood of an induced seismic event increases was devised from a review of the mechanics of induced seismic activity and notable case studies.
3. The sensitivity of the positioning microseismic events from a case study was explored using a quantitative investigation method using an RMS objective function, and a seismic ray-tracer (Trabox) customised to function at this site scale and extended to run in a parallel processing environment.
4. The VFSA method used to derive a velocity model by Pei et al. (2009) using travel times from fixed positions was extended to include variations in the lay-

ering structure, refining the velocity model further than by using the original method by Pei et al. (2009)

5. A parallel processing grid search algorithm to reposition microseismic events was developed in order to reposition microseismic events.
6. A method to determine the installation angle of seismograph stations was devised and implemented using the amplitude of the P-wave arrivals
7. The pulse directivity method was, for the first time, applied to microseismicity scale wavelets to calculate the fracture length, velocity and direction by using both rise and rupture time measurements and models by Zollo and de Lorenzo (2001) and Cesca et al. (2011)
8. The 95% quartile range for the fracture parameters from the pulse length calculations were derived from a new technique in this field, orthogonal distance regression (ODR), to consider the error on both independent and dependent variables.
9. An automated moment tensor inversion system was developed, extended from full-waveform moment tensor inversion software by Křížová et al. (2013).
10. Using the outputs from the pulse directivity method it was possible to narrow down the two possible solutions from the full waveform moment tensor and remove the mathematical ambiguity.
11. The developed software package was used to investigate the cause of an induced seismic event from a hydraulic fracture site in Fox Creek, Canada and found that pore-pressure increases from stage 23 of the hydraulic fracturing operation were the prime cause
12. A comparison between the forecast model and the sequence of the events was made and found that the ability to process the low signal to noise ratio events is key for validating this model.

8.8 Suggestions for further work

The forecasting system developed in this thesis relies upon observing the point in time when the evolution of the fracture network changes to an increased likelihood of a seismic event occurring. While the software system is capable of monitoring for this change, the case study available for this study doesn't allow this change to be fully observed. This ultimately means that more case studies must be analysed with

this system to validate the forecast model before it is ready to be implemented in the field.

The problems with the analysis of microseismic events from this case study stem from the lack of any acquisition capability at depth. While the number and azimuthal distribution of the stations exceeded requirements for the analysis of microseismicity, the lack of geophones near the wellbore restricted the ability to confidently resolve, the depth of the microseismic events, and the attenuation structure of the subsurface. With an acquisition array at the same depth of the fluid injection, the velocity models could be refined further, removing the over-fitting considerations and improving the confidence in the depth coordinates of the microseismic events. By having an acquisition array at this depth, the attenuation structure could have been calculated in 3D using the spectral ratio method. While the rise time method was successful at determining an attenuation structure in 2D, there were challenges with this method as it makes an assumption that the source wavelet size is linearly related to the travel time and attenuation of the measured wavelet. Using the spectral ratio method would remove this assumption, reduce the error of the attenuation field and therefore the error of the fracture map parameters (length, rupture velocity and direction). Finally, with the acquisition array at the same level of the injection point, all of the tensile fractures opening from the injection could be analysed and the transition point towards the fault lines could be observed.

Ultimately this software system would be running in real-time during fluid injection. At the moment the system hasn't been verified to run in real-time as this case study's monitoring array precludes the automated timing identification systems from running correctly as scattering and interference from the monitoring boreholes alters the measured wavelet. Testing this software system on different case studies will allow this ability to be finally verified.

The output from the software package is currently two maps, the fracture map and the Coulomb stress change map. The Coulomb stress change is calculated under an assumption of constant pore-pressure. While this assumption is to a certain extent valid at this case study where the transfer of static stress was measured from the SW-NE fault network hydraulically separated from the 12 January event, it would be beneficial to combine the Coulomb stress change and the fracture map. This would simplify the forecasting maps as the Coulomb stress change would reflect both static stress transfers and pore pressure increases. Current methods which model the Coulomb stress change with variations in pore-pressure are extremely limited with only uniform variations of the pore-pressure via the Skempton coefficient being modelled recently by Kettlety et al. (2018). To correctly model the pore-pressure variations into the Coulomb stress change this would have to be a 3D varying value

at each grid cell with variations in time due to the injection of fluid.

Following a review and discussion of the text during the examination viva, the following additional areas could be considered in the development of this project. The first was the treatment of the Q-field, used extensively in the pulse length and moment tensor inversion modules. While the data limited the Q methods available, there are other methods which could confirm the choice of Q_p value in addition to the rise time method already chosen. For the Q_s field which was determined from a simple linear relationship between Q_p . There are empirical relationships between Q_p and Q_s which could have been considered. While the choice of Q_s had a limited effect with regard to the Green Function calculations within the chosen moment tensor inversion method, the use of a more realistic value of Q_s may lead to improvements in the fitting of the data to the Green Functions with more advanced modelling methods.

Appendix A

Appendix - Chapter 5

A.1 Modification to the ray-tracing software

The ray-tracing software was originally designed with large scale seismology in mind, so some modifications were made to make it work at this scale. The first modification was to use the interface between model 1 and 2 as the top of a basement rock formation with a set velocity greater than anything else in the model as a flat surface positioned at a depth of 5000 m. This ensures that if a ray path is incident on this surface, it will always reflect the ray back towards the surface. A cushion of 60 m is placed above this where if the ray path reaches this depth, the time step is adjusted iteratively until the ray path hits the 5000 m surface within an accuracy of 3 m. From this point, the subroutine calculates the reflected angle for the ray path via Snell's law and the ray continues to the surface. A schematic of this is shown as figure A.1 and A.2.

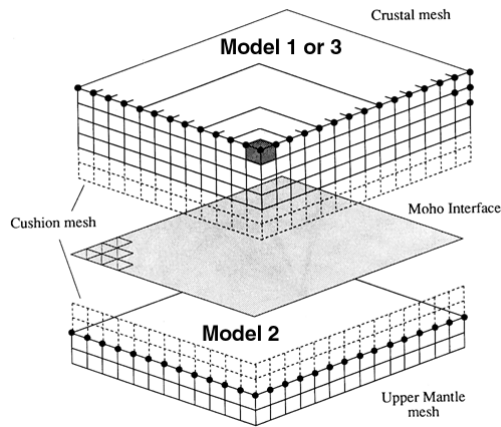


Figure A.1: The Trabox software velocity model arrangement

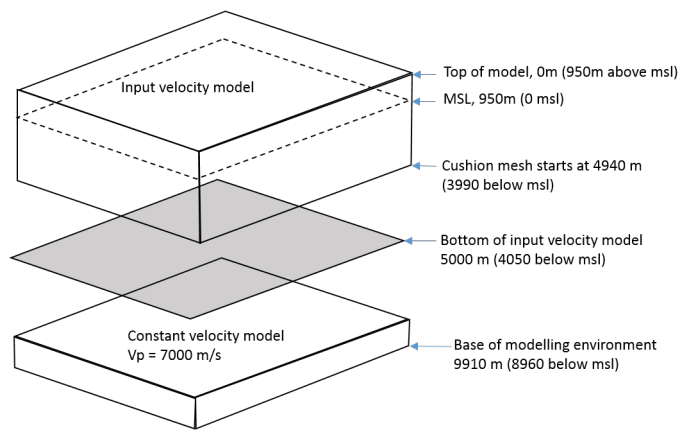


Figure A.2: The modified Trabox software velocity model arrangement for this site

The second modification made involves choosing the two starting angles, azimuth and declination for the ray path. For 1D models, the starting declination, angle is a key parameter for modelling the ray path. Trabox initially had a routine for calculating both the starting azimuth and declination angles to try and converge on the station coordinates. This routine calculated the partial derivatives of the endpoint with respect to the declination and azimuth and then takes the inverse matrix of these partial derivatives to result in a 2x2 matrix of adjustments to the starting angles of azimuth and declination. This method was found to be reliable only when the velocity model did not vary considerably, which for large scale seismology is fitting but not appropriate for the scale and variation in velocities that are involved at this site. A

new method was incorporated to ensure a more reliable convergence of the ray path to the station.

The first stage of this new method is to trace a swathe of ray paths starting vertically towards the surface, to the vertical towards the base of the model. If there is a change in polarity of two values Δx and Δy , the difference in meters in x and y from the end of the ray and the station coordinates then the correct starting declination for the station exists somewhere between these two ray paths with declinations, d_1 and d_2 . With this swathe, there may exist multiple paths to the surface so only the shortest path in time was considered in deciding d_1 and d_2 . Care was also taken to ensure that only raypaths which were a direct raypath (i.e. no intra-bed reflections, or reflections off the top of the basement) between the source and the surface are considered. If these raypaths are not discounted from this decision process than the ray-traced time would be considerably longer than for the direct path. It is highly likely that the arrival in the real data is from a direct ray path so considerable care is taken to ensure only direct ray paths are considered in this process. A schematic of the process involved is shown as figure A.3.

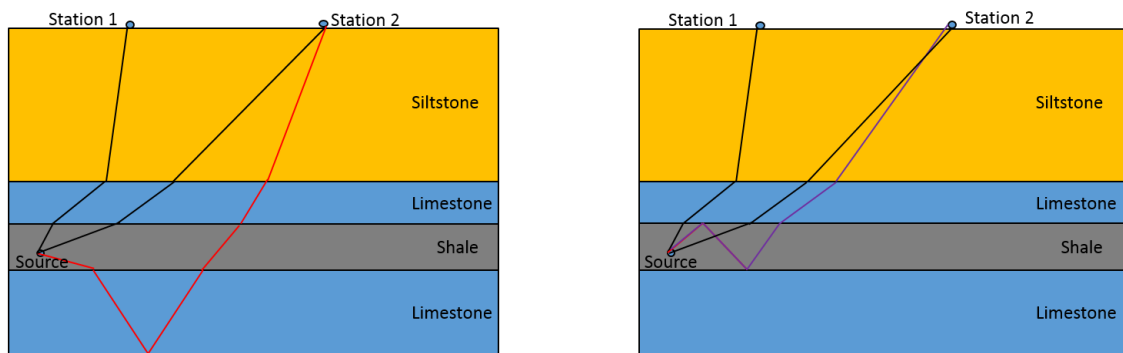


Figure A.3: The different raypaths possible in modelling in the Trabox software. The red and purple raypaths represent a reflection off the base of the model (or a basement layer) and an intrabed reflection respectively. These paths between the source and station 2 are possible but it would be notably slower than that of the direct ray path. In the real world it is likely there will always be a direct raypath between the source and station and so these paths are not used as the final converged solution but are used to find the converged raypath which may exist somewhere between a ray falling short of a station and one involving an intra-bed or base of model reflection.

With d_1 and d_2 decided, a swathe of 600 rays is traced but with declination angles between d_1 and d_2 . If the end of the ray path is less than the convergence accuracy defined by the user then the swathe between d_1 and d_2 is completed but the declination angle with the shortest distance to the station is saved as the final convergence

angle. Once this swathe is finished and a convergence angle recorded, the ray path is retraced with this angle and the ray trace for this station ends and the next station is considered. If a convergence angle is not found in this swathe, then angles d_3 and d_4 where a delta x and delta y change in polarity is found (which will always be less than d_1 and d_2) and another swathe of 600 rays are traced between this smaller range of angles. This is continued until an angle is found where the end-point of the ray is less than the convergence tolerance or the program exceeds the iteration limit of 3400. An iteration limit of 3400 was carefully chosen as at the end of this limit calculating an increment for the change in declination reaches the accuracy limit for 8 byte real numbers in Fortran. This method for 1D velocity models ensured a reliable result even with velocity models with large changes in velocity. A schematic of this method is shown as figure A.4.

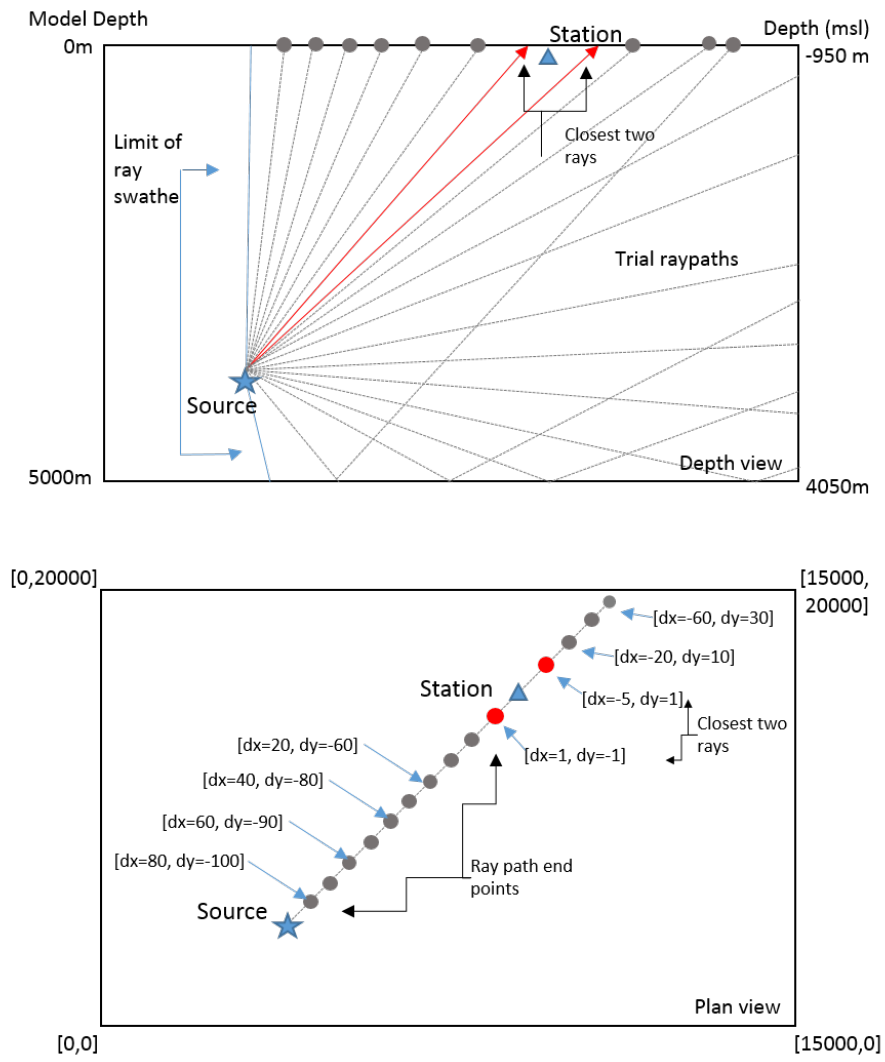


Figure A.4: The new method to calculate the starting declination angle

With these modifications there are only two reasons that the ray path doesn't reach convergence on the target. The first is if the velocity function means that for large source-station offsets the only path between source and station involves a reflection off a boundary, either the base of the model or in-between formations. The other reason and the most common reason is linked to the declination angle increment. When the separation between two angles is as small as the accuracy limit of 8 byte real numbers, the raypaths diverge on the path to the surface from refraction, landing either side of the target station and not reaching the convergence threshold.

A.2 First arrival identification for the perforation shots

All the seismic data were recorded continuously onto 30-second SEG-D records. There are records logging when the perforation shots were fired but these timings were from a 2 minute time window so cannot be used to time the event arrivals. The perforation shots in this site consisted of three explosive shots fired in quick succession through the casing.

The first step in processing this data was to convert the data from SEG-D to SEG-Y using the Seaseis software. The signal to noise ratio for the perforation shots is low and this makes identifying the arrival times from these sources a challenge. To improve the signal to noise ratio various signal processing methods were trailed. These included a bandpass filter to remove noise and an AGC (automatic gain control) to improve the signal level. A filter test showed that all the filters impacted the signal in some way and was of little benefit. This was confirmed in the spectral analysis shown in figure A.5.

The AGC while increasing the signal amplitude also increased the noise level meaning there was a risk of separating noise and signal from each other. An example of this is shown as figure A.6.

After testing these processes on a record with a clear perforation shot, the only methods applied were a whole trace equalisation to remove the differences in amplitude between station to station and a T^2 scalar to increase the amplitudes at the far offset. A before and after of the record is shown as figure A.7.

After signal processing, the SEG-Y records were loaded into Matlab and custom scripts were written to assist in picking the first arrivals. To assist in identifying the arrivals, all the traces at each station are used to improve the signal to noise

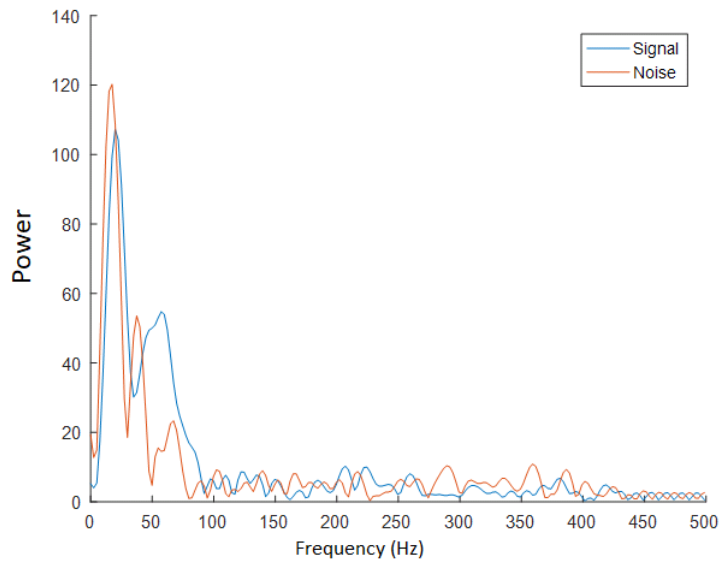


Figure A.5: Signal and noise spectrum of an example perforation shot. Signal taken using a fixed 2 second window centred around the received data. Noise spectrum produced from a 2 second window of a record before the injections started.

ratio. The majority of the 96 stations have two vertical geophones and a single 3-C geophone separated by 14 m in a string down a short 40 m borehole. The data provided by the industrial contact included dynamite shots set off at four stations to test station operation. By using these shots it was possible to calculate a clear timing shift between each geophone within the station. These timings allowed the traces to be corrected to the same depth level and then stacked together. Stacking these traces together results in 96 traces, one for each station. These 96 traces are then tripled and placed next to each other for visual identification purposes. This process allowed the arrivals for the smaller amplitude perforation shots to be identified and the signal to noise ratio improved via the stacking process: figure A.8 shows the record before and after this process.

Even with this process, it was still difficult to identify some of the perforation shots, so information provided by contractor A and a semblance method were used to narrow the search down. As the events are all recorded on a continuous recording system, a file is saved every 30 seconds. To narrow the search down to within a 30-second window contractor A provided, within the events catalogue, a file number where the perforation shot was identified.

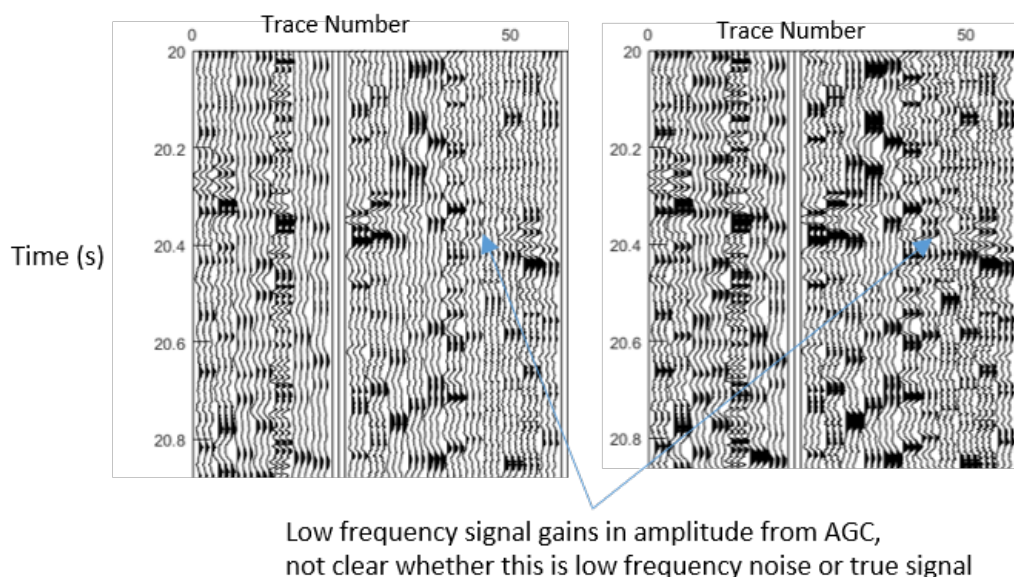


Figure A.6: Changes from the application of the AGC, increases the signal amplitude but also enhances low- frequency noise which could be interpreted as signal.

To narrow the search for a perforation shot event in the 30-second record down to a 2-second window, a semblance-based method was used. Semblance is a commonly used method in seismic reflection studies to determine velocity functions. By adjusting the timing of each trace by a single velocity value, events will align and stack with a higher coherency with the correct velocity value. If this coherency function is plotted against a range of velocity values as a contour plot then the velocity and observed time of the event can be identified. To enable this method in this dataset, the data was first sorted in increasing source-station offset. As the position of the perforation shot is known this means that the event should be observed in the record with an increasing time with an increase in offset. By applying semblance to a record meant it was possible to identify where in the 30-second record a coherently stacked event arrived. If an event arrived from a different source, and therein a different position, then the event arrivals will not increase with offset and when stacked would cancel out to zero. For these purposes, the velocity function observed in semblance will have little relevance to the overall velocity function of the model, as each ray path may have slightly different velocity functions, but at the scales of a 30 second window, this process allowed an observed event to be identified. An example of this process is shown as figure A.9 for perforation shot 20-1.

To ensure that this was a clear event and not just noise stacking in the semblance

display, the record was redefined as a 3D section with the axis of trace, time and amplitude as x,y and z respectively and rotated to look along the arrival to see the alignment. An example of this is shown as figure A.10.

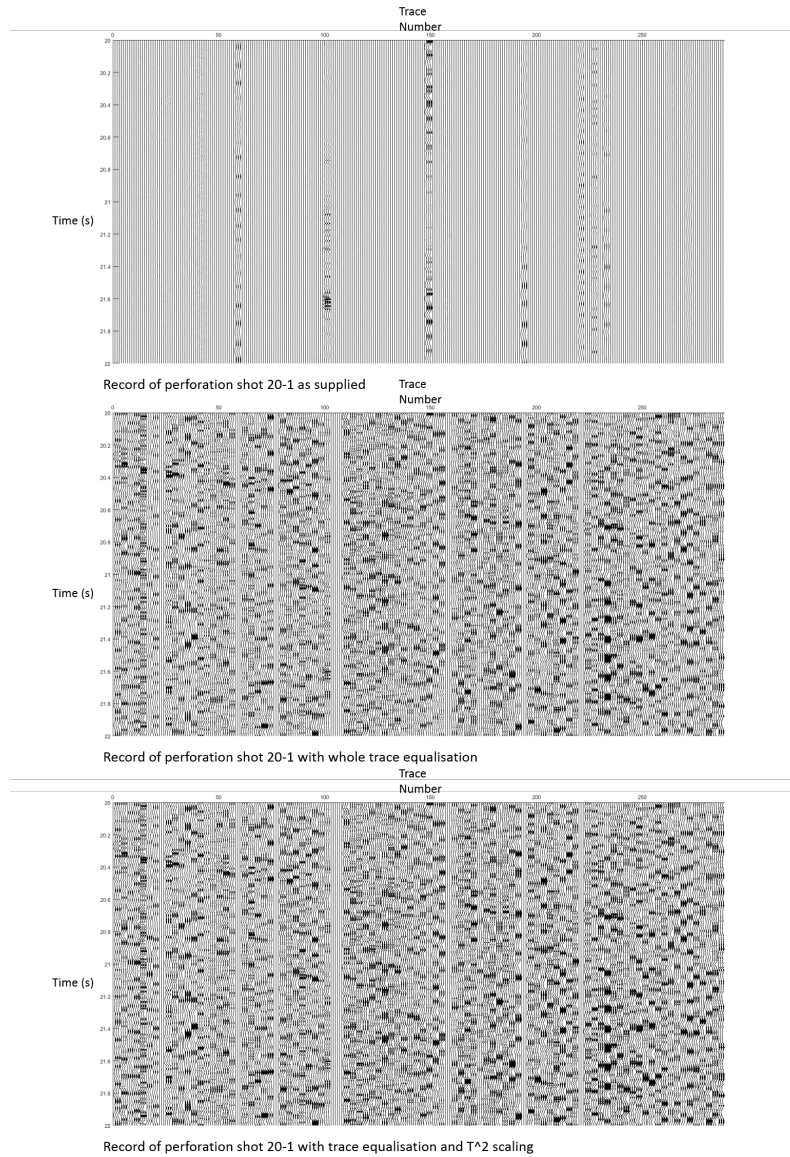


Figure A.7: Before and after application of the processing steps to a record containing a perforation shot

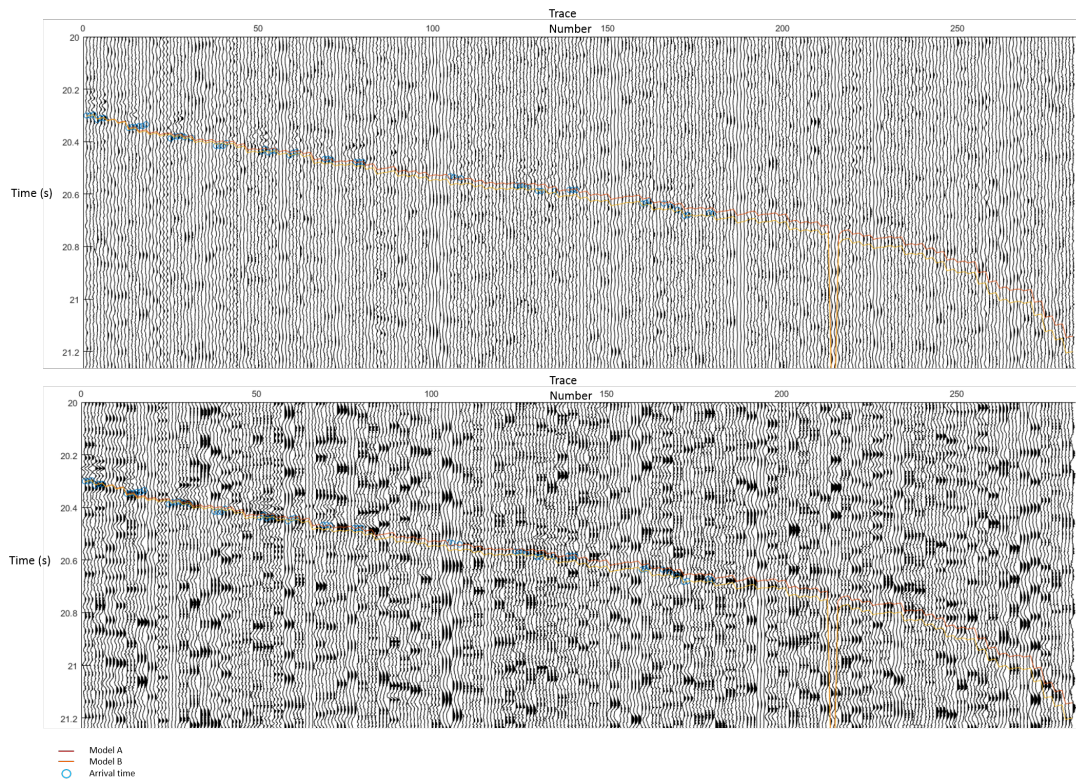


Figure A.8: The original record and the record after stacking all the traces in the station to form a single trace. These traces are then replicated three times for visual identification purposes

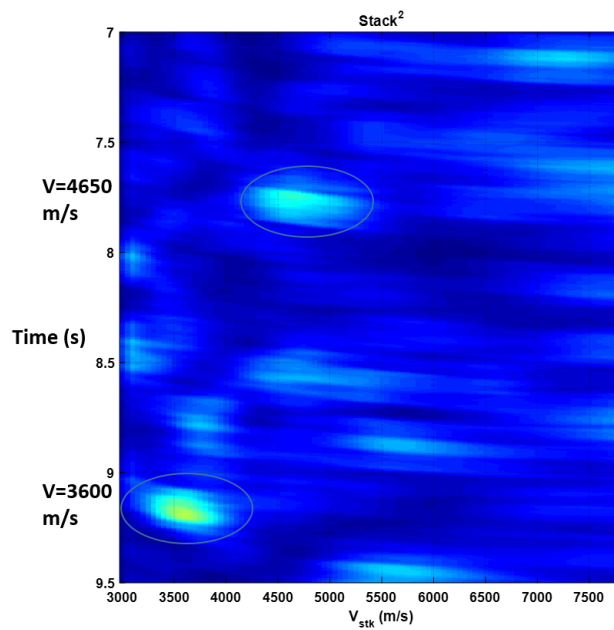


Figure A.9: Semblance plot for perforation shot 20-3. This shows two possible velocities (4650 m/s and 3600 m/s) which when applied as a linear move-out correction lead to a greater alignment for two possible events. This allows the user to narrow the search window from 30 seconds down to two possible events

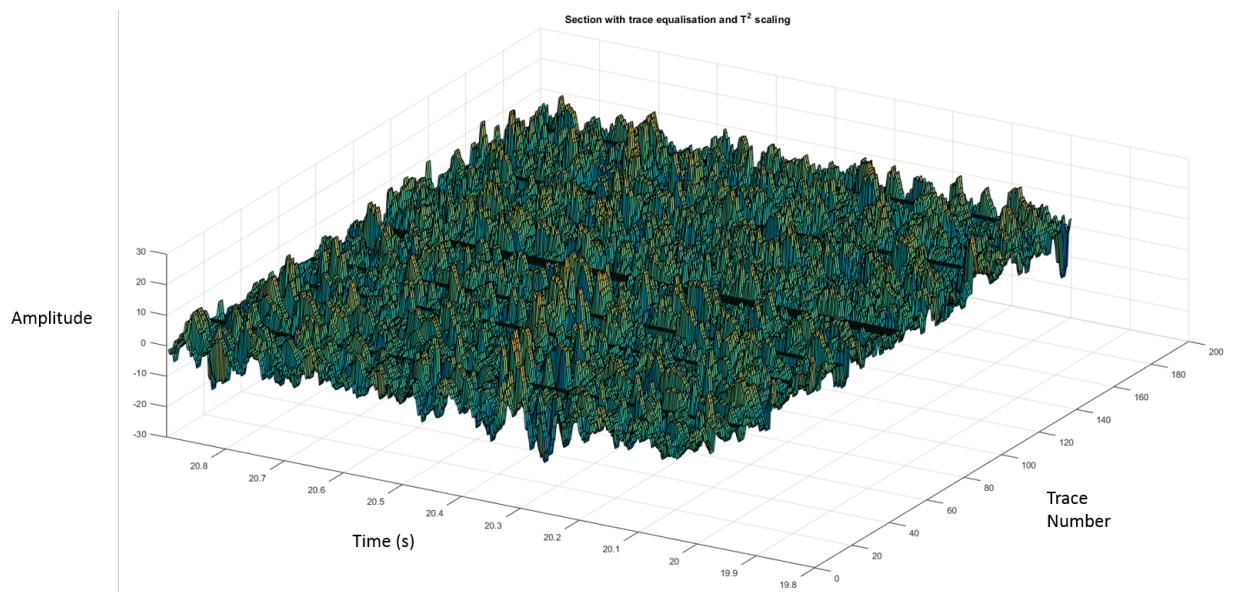


Figure A.10: Perforation shot 20-1, original record presented as a 3D Section with trace equalisation and T^2 scaling, note the perforation shot arrivals moving across the image

Once the observed arrival was narrowed down to around a 2 second time window the arrivals were identified manually for each perforation shot. This method differs than that of the contractors who rely on computer systems to adjust the timing of traces in order to find the highest coherency. Once a threshold of coherency is exceeded this is classified as an event and the timing of each trace and position of the event is noted. It is not usual for manual picks by an operator to be used. The advantage of this kind of system is that it is automated and can process many events efficiently, the downside is that while an event may exceed a set level of coherency there is no visual confirmation by an operator that this event is real or a noise train stacking in. Using these methods, of the 78 perforation shot fired through the casing, 69 were identified by the two contractors. Of these 69 it was possible for an operator to visually observe and manually pick 67 perforation shots in the records.

With the arrival times identified manually, there were concerns that there is a limit with regard to manual picking as it cannot distinguish between slight differences in the waveform at close distances. This is especially important when there might be a correct time pick half a waveform out that visually cannot be distinguished between each other. For this application, the pilot trace cross-correlation method was utilised as introduced by De Meersman et al. (2009). This stacks all the time corrected traces (so they events align at the same time) together to form a pilot trace and this is cross-correlated with every other trace. The lag times from each trace are then applied to the trace time and the set is stacked again to form a higher amplitude pilot trace. This process is conducted for a number of iterations as specified by the user. In this situation, the trace times were firstly adjusted by the interpolated arrival times (so as to ensure all traces align in time) from the manual picking and then form the pilot trace. Limits of the lag were placed so as to ensure the program doesn't latch on to a noise train away from the actual arrival and those which would defy a sensible travel time relationship. After testing these parameters, a limit of 5 iterations was decided upon with a cross-correlation window size of 0.015 s. Figure A.11 is an example of the pilot trace cross-correlation from the perforation shots in stage 17 together with an image of the record with the picks and picks altered by the cross-correlation process.

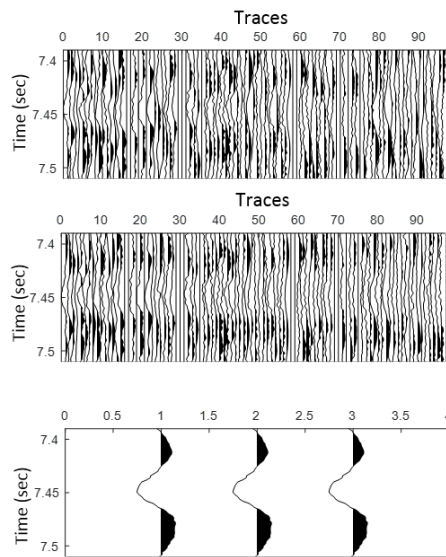


Figure A.11: Changes to event alignment with pilot trace cross-correlation for perforation 17-1. (Top) Shows the section where the event has been aligned using the picks identified by the manual process, the second record (middle) shows the section where this alignment has used the picks altered by pilot trace cross-correlation with a window range of 0.15 seconds. The bottom section shows the stack response after this process

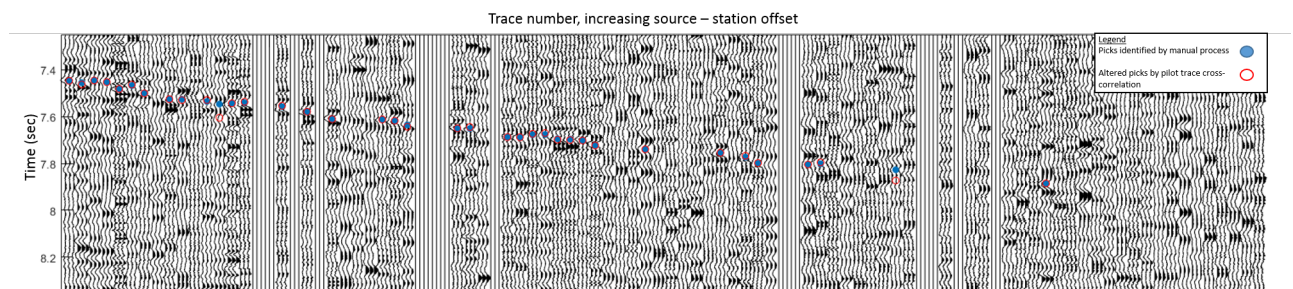


Figure A.12: Record of perforation shot 17-1 with each station trace reproduced three times for identification purposes with an increasing offset distance and overlay of the picks identified by the manual process of those altered by the pilot trace cross-correlation.

A.3 Raytracer software parameter decisions

With the software established, a number of modelling parameters had to be defined these were, the gridding size in the depth direction, the modelling ray tracing time step and any velocity smoothing applied to the model. These modelling parameters were determined by using response testing to establish modelling relationships.

A.3.1 Grid size, Z

The grid size in x and y is arbitrary when dealing with 1D velocity models but the Z-axis is a key parameter as the cardinal splines which determine the relationship between velocity and ray angle are calculated over 4 grid cells, so the number of grid cells will alter how the ray path is traced. There is also a cost with regard to processing time and memory limits.

The figures below (figure A.13 and A.14) show the variation in double-difference squared for a grid size of 5, 10, 20, 30, 40 and 50 m for both velocity models A and B.

For velocity model A, figure A.13 shows with a decrease in grid size from 40 m to 20 m there is a reduction in the squared double-difference value which eventually plateau. For velocity model B, this trend is not as clear, as there is a reduction in double-difference between 30 m to 5 m and 50 m to 40 m for perf 3. The reduction in double-difference from 30 m to 5 m is accompanied by a reduction in the number of source-station rays converging, implying that these results between 30 m to 5 m are the most stable. By using the double-difference squared value rather than the RMS error means the error to individual stations is not averaged out over multiple stations and clear changes to individual station response can be reviewed. When comparing the RMS error, some similar trends are seen as shown below as figure A.15 and A.16.

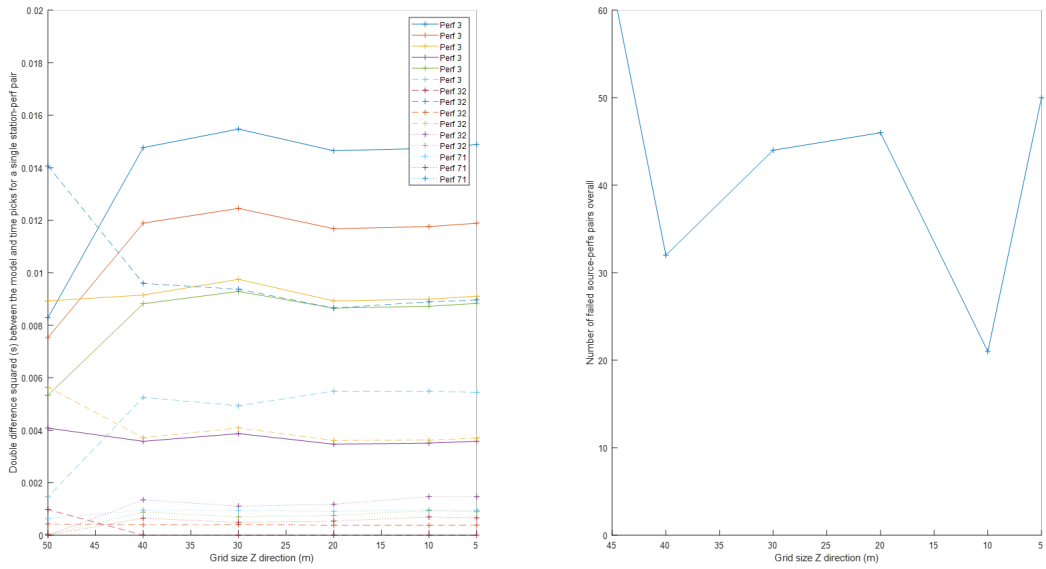


Figure A.13: A figure showing the variations in the modelling outputs with the grid size in the z-direction. The fixed modelling parameters for this are a 100x100 grid size in the x and y direction with velocity model A. On the left, shows the variation of double difference squared (s) with time step (ms). With a decreasing grid size, the variation of double difference reduces. On the right, shows an increase in source-station pairs which fail to converge with a decrease in grid size.

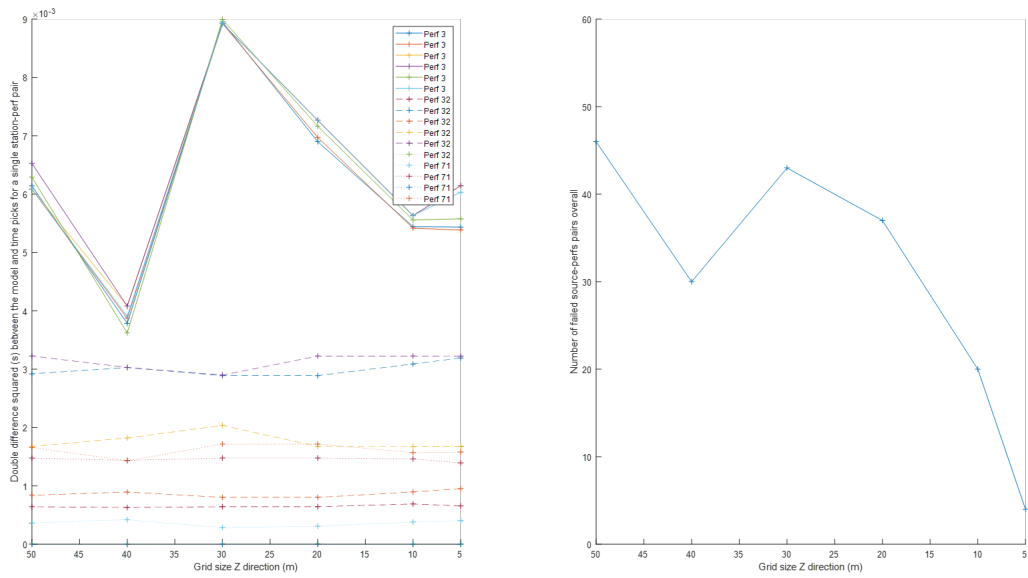


Figure A.14: A figure showing the variations in the modelling outputs with the grid size in the z direction. The fixed modelling parameters for this are a 100x100 grid size in the x and y direction with velocity model B. On the left, shows the variation of double difference squared (s) with time step (ms). With a decreasing grid size, the variation of double difference reduces. On the right, shows a decrease in source-station pairs which fail to converge with a decrease in grid size

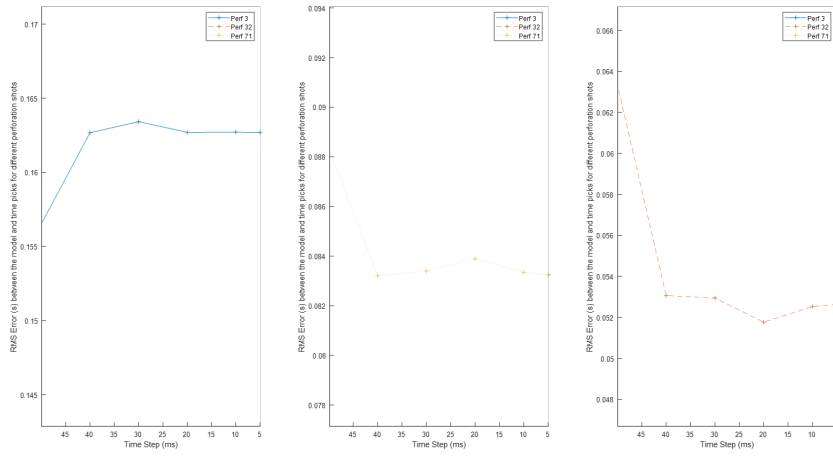


Figure A.15: A figure showing the variations in the modelling outputs with the grid size in the z-direction. The fixed modelling parameters for this are a 100x100 grid size in the x and y direction with velocity model A. Each panel shows the variation in RMS error for three perforation shots.

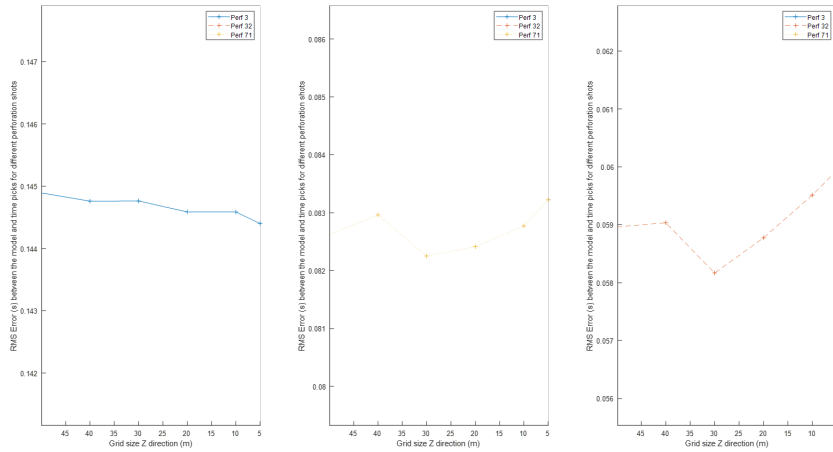


Figure A.16: A figure showing the variations in the modelling outputs with the grid size in the z-direction. The fixed modelling parameters for this are a 100x100 grid size in the x and y direction with velocity model B. Each panel shows the variation in RMS error for three perforation shots.

For velocity model A, a trend of reduced RMS error is observed with z grid size in perf 32. For perf 3 there is a single data point which is at a lower RMS compared the rest of the grid sizes. This point may be due to an increased number of failed source-station pairs not converging. If this point is discounted both this perf and perf 71 both exhibit a stable RMS change with grid size. For velocity model B a trend of reduced RMS error is observed for perf 3. For perf 32 and 71 this trend is increasing.

Using this test, it was decided to use a grid size of 10 m in the z-direction as the changes to double-difference squared and the RMS plateau at this size and the number of rays failing to converge on the station is at a minimum. Smaller than this and the number of rays failing to converge increases for Model A, and the improvement in double-difference squared and RMS error is minimal for both velocity models.

A.3.2 Time Step

The time step plays a crucial role in the ray trace: too small a time step and it will be influenced by multiple small changes in velocity function. If the time step is too long the resulting time will be influenced by a long average of the velocity function.

As before a series of tests were conducted, using the following fixed parameters, 100x100x10 m grid size, and a 10 m convergence accuracy. A series of time steps were tested from 2 ms to 60 ms. The tests are shown below as figure A.17 and A.18 for velocity models A and B with a variation in double-difference squared for a number of perforation shot sources and the RMS error for three perforation shots 3,32 and 71 as figures A.19 and A.20.

For Model B, with a reduction in time step, there is a clear reduction in double-difference squared and RMS error. This is most pronounced for the larger time step values of 60 ms to 30 ms. For Model A, the reduction is less pronounced for both the double-difference squared and RMS error. By starting the process at 2ms will ensure a high level of accuracy but by increasing the time step if no raypath is found ensures that convergence is met for all ray paths.

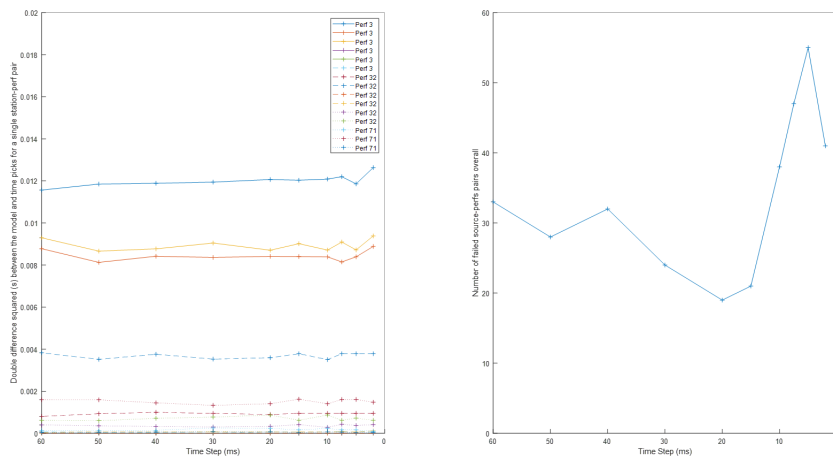


Figure A.17: A figure showing the variations in the modelling outputs with time step (ms), the fixed modelling parameters for this are a 100x100x10 grid size and convergence accuracy 10m with velocity model A. On the left, shows the variation of double difference squared (s) with time step (ms). With a decreasing time step the variation of double difference reduces. On the right, shows the increase in source-station pairs which fail to converge with time step.

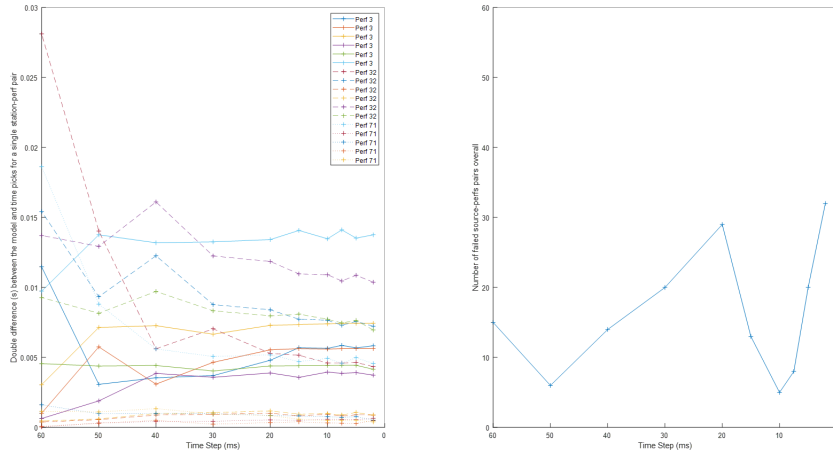


Figure A.18: A figure showing the variations in the modelling outputs with time step (ms), the fixed modelling parameters for this are a 100x100x10 grid size and convergence accuracy 10m with velocity model A. On the left, shows the variation of double difference squared (s) with time step (ms). With a decreasing time step the variation of double difference reduces. On the right, shows the increase in source-station pairs which fail to converge with time step.

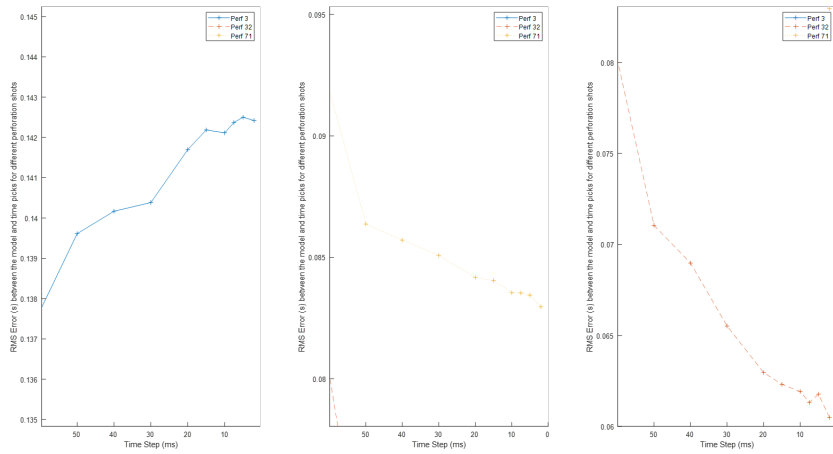


Figure A.19: A figure showing the variations in the modelling outputs with time step (ms). The fixed modelling parameters for this are a 100x100x10 grid size and a convergence accuracy 10m with velocity model A. Each panel shows the variation in RMS error for three perforation shots.

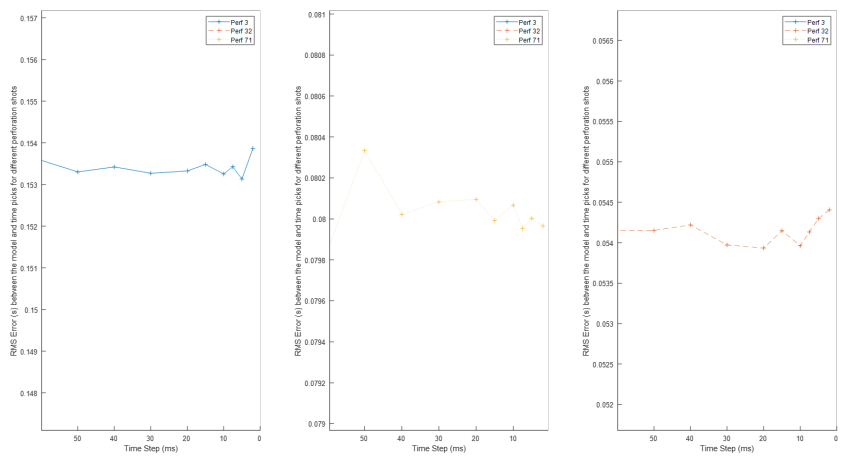


Figure A.20: A figure showing the variations in the modelling outputs with time step (ms). The fixed modelling parameters for this are a 100x100x10 grid size and a convergence accuracy 10m with velocity model A after applying a smoothing operator. Each panel shows the variation in RMS error for three perforation shots.

A.4 Geological Constraints for the velocity model

To calculate these constraints for each layer in the velocity model developed in chapter 5, a geological literature review was carried out for each formation to find relationships for velocity with respect to pressure, porosity, fluid and mineral content. Over the next sections, each formation and the constraints calculated are discussed.

Recent to Upper Cretaceous

This formation begins at the start of the well log until 1147 m (drilled depth). There is little information in the geological log regarding the lithology for this formation and for this reason no name has been given for this formation.

It is assumed to be Recent sands and silts from the Upper Cretaceous (the nominal geological age of the Lea Park formation) to Recent deposits. Given this lack of information, bounds were set from parameters for a sandstone from Mavko et al. (2009) with a velocity between 2000 to 3500 m/s.

Lea Park Formation

This formation extends to 1595 m (drilled depth). The Lea Park Formation was only included as a formation name in the log. No geological logging on this formation was included in the report. From Rosenthal (1984), the Lea Park formation sediments are predominantly fine-grained, consisting of dark grey to brown mudstone and siltstone.

To model the constraints, the Han's empirical relations Han et al. (1986) were used. These relate porosity and clay content to velocity for shaley sandstones by,

$$V_p = 5.77 - 6.94\phi - 1.73\sqrt{C} + 0.446(P_e - 1.0e^{-16.7P_e}). \quad (\text{A.1})$$

These relations relate clay content, porosity, fluid content and overburden pressure to velocity. It is assumed that the maximum depth this layer could potentially reach is when the next formation below is missing and this formation extends to 2218 m (drilled depth). The equivalent pressure for this depth is 40 MPa from the pressure log recorded during the petrophysical logging. Using an assumed maximum clay content of 50% and porosity range of 0.01 to 0.15 with a mixture between dry and fluid-filled formations the smallest velocity found by varying these variables was 3022 m/s at a porosity of 0.15 and clay component of 50% in a dry formation. The maximum

velocity found was 4430 m/s when the porosity equalled 0.05 with a clay content of 50% when the formation was water-filled.

Second White Speck Shale

This formation extends to 2218 m (drilled depth) and similar to the Lea Park Formation was only included as a formation name in the log. Meléndez-Martínez and Schmitt (2016) conducted a geomechanical investigation on this formation and show that the variation in velocity due to pressure is limited (300 m/s, for a 10 MPa increase in pressure) but that variation in velocity from horizontal transverse anisotropy is greater. These curves are shown as figure A.21. Using these curves the minimum velocity was set to 3450 m/s and the maximum velocity was set to 4200 m/s.

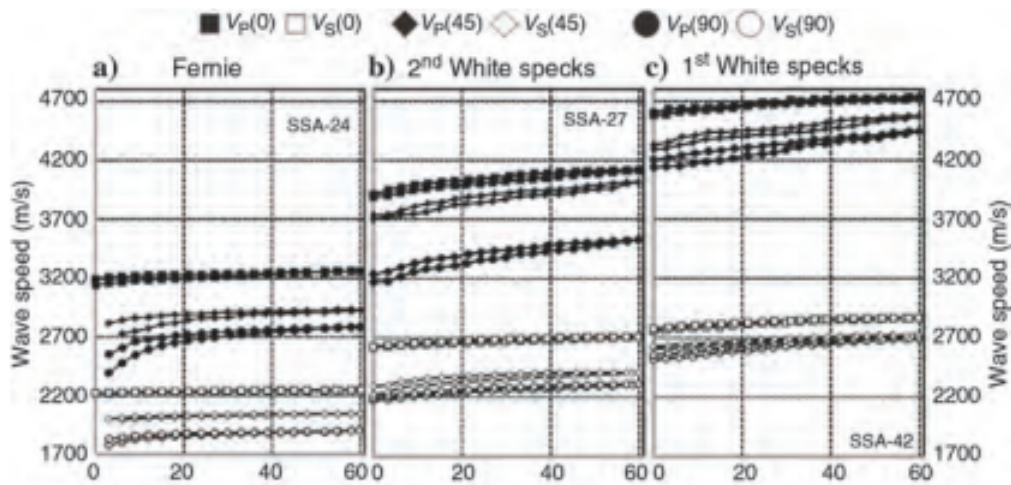


Figure A.21: The variation in wave speed (m/s) for three different formations in the Alberta province with a change in overburden pressure (MPa). Taken from Meléndez-Martínez and Schmitt (2016).

Fernie

This formation was logged in name only between 2218 - 2228 m (drilled depth). From the Geological Atlas of the Western Canada Sedimentary Basin, this is a grey silty shale (Mossop and Shetsen, 1994). The bounds for this formation were established by using the empirical relationship developed by Ong et al. (2016) as part of a study of the shale formations in the Alberta region.

Given a range of pressures from 55-60 MPa and the curves established by Ong et al. (2016) shown as figure A.22, a range of velocities was set to 3680 - 5700 m/s.

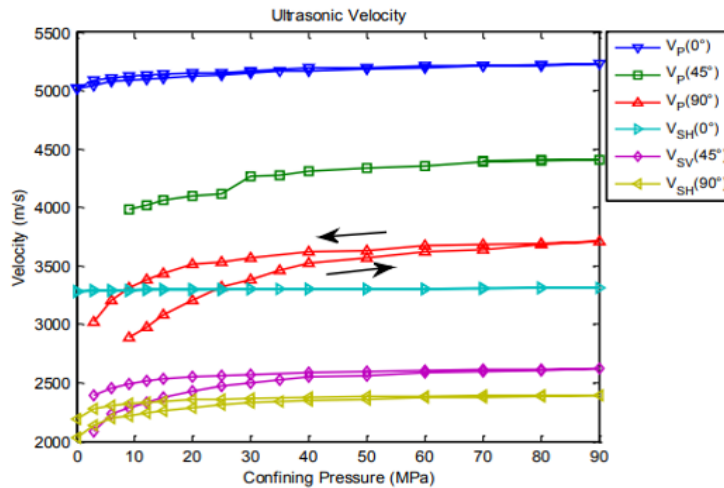


Figure A.22: Empirical relationship for the change in wave speed with pressure MPa for shales found in Alberta, Canada. Image from Ong et al. (2016).

Nordegg

This formation was logged in name only between 2228 - 2253 m (drilled depth). From the Lexicon of Canadian Geological Units, this formation is a dark grey to black, hard, platy to medium-bedded, cherty and phosphate limestone, with 40-90% chert occurring as layers exhibiting pinch and swell with lenticular beds and nodules. The chert is dark grey to black with blue tints. The constraints for this layer were derived from Fu's 2010 thesis which analysed different samples of chert from Texas and Canada. The constraints for this formation were taken from minimum and maximum velocities from the samples analysed from the well in Canada, in this case 3680 - 5780 m/s respectively.

Montney

This formation was logged between 2253 - 2352 m (drilled depth) and was logged as a siltstone, light to generally medium grey, slight medium brown grey, in part grading to lower very fine grained sandstone, sub angular to sub rounded, well sorted, quartz

and rare lithic grains, soft and bit damaged to locally moderately hard, trace to common dolomitic and siliceous with minor calcareous, minor to trace medium grey and medium brown clay, rare glauconite, estimate 2 to 4% porosity.

To determine the constraints for this formation the Han's empirical relationships were used again. Using the clay and porosity measures from the well log and a range of overburden pressure from 50 - 60 MPa this found the velocity range to be between 4070 - 4740 m/s.

Belloy

This formation was logged in name only between 2352 -2365 m (drilled depth). The Geological Atlas of Western Canada Sedimentary Basin splits this formation into three units

- Lower Belloy: Fine-grained, glauconitic, quartz arenites. Siltstone, and sandy, cherty, dolomitic limestones
- Middle Belloy: Two medium-grained, coarsening-upward, quartz arenite units
- Upper Belloy: Sandstone and carbonate (dolostone) units.

The atlas includes a series of interpreted sections and this site is close to one of these sections. The part that crosses this site is shown below as figure A.23 showing the Belloy split into the three units. For the purposes of defining constraints, two extremes are used, a clean arenite for the minimum velocity and a dolostone for the maximum velocity. The velocity for the arenite was determined by the Hans empirical relations with a 25% porosity. The dolostone velocity was determined from ultrasonic testing on limestone samples within Mavko et al. (2009). The constraints for this formation were set from 4900 - 7000 m/s.

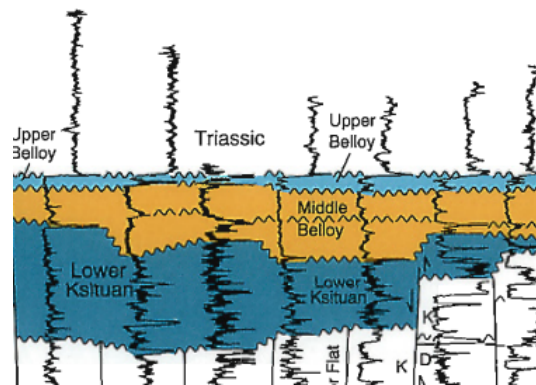


Figure A.23: The units within the Belly formation. Image from the geological atlas of Canada.

Mississippi age (Shunda and Pekisko units)

This formation was logged between 2365 - 2575 m (drilled depth) as limestone and shale beds. Work by Miller and Stewart (1990) reviewed the sonic velocity for a number of different samples from the Shunda and Pekisko units. To devise the constraints for this formation, the maximum and minimum velocities for these units as found in this review were used for the constraints: in this case a range between 4500 - 6347 m/s.

Banff

This formation was logged between 2575 - 2773 m (drilled depth) as a crystalline limestone beds. The constraints for this unit were defined from work conducted by Davies (1974) with a range between 5500 - 7000 m/s.

Wabamun

This formation was logged between 2773 - 3189 m (drilled depth) as a crystalline limestone beds. The constraints for this unit were defined from work conducted by Davies (1974) with a range between 5500 - 7000 m/s.

Ireton

This formation was logged between 3189 - 3366 m (drilled depth) as a dolomitic medium brown siltstone. The constraints for this unit were defined from work conducted by Davies (1974) with a range between 4600 - 6500 m/s.

Duvernay

This shale formation was the target for production and was logged between 3366 - 3420 m (drilled depth). The review of shale sample velocities by Ong et al. (2016), as shown in figure 4, derived a set of empirical relations between velocity and overburden pressure (MPa) for this formation in particular. These relations were used for an overburden pressure range of 80 - 90 MPa and result in a range of velocities between 3500 - 5250 m/s. Similar to the Second White Spec shale and the Fernie formations, the largest variation in velocities is as a result of anisotropic variation of velocity within the shale.

Majeau Lake

This shale formation was logged between 3420 - 3427 m (drilled depth). To determine the constraints for this formation the same relations were used for the Duvernay shale with an 80 - 90 MPa pressure range resulting in a range of velocities of between 3500 - 5250 m/s.

Top Carboniferous and Beaver Hill lake

This formation is the final formation logged in the well and extends from 3427 m (drilled depth) to the base of the well at 3465 m (drilled depth). This is a crystalline limestone formation and the constraints for this were defined from the same source as the Banff and Wabamun formations with a range between 5500 - 7000 m/s.

Appendix B

Appendix - Chapter 6

B.1 Problems with signal variation when attempting to use autopicking routines

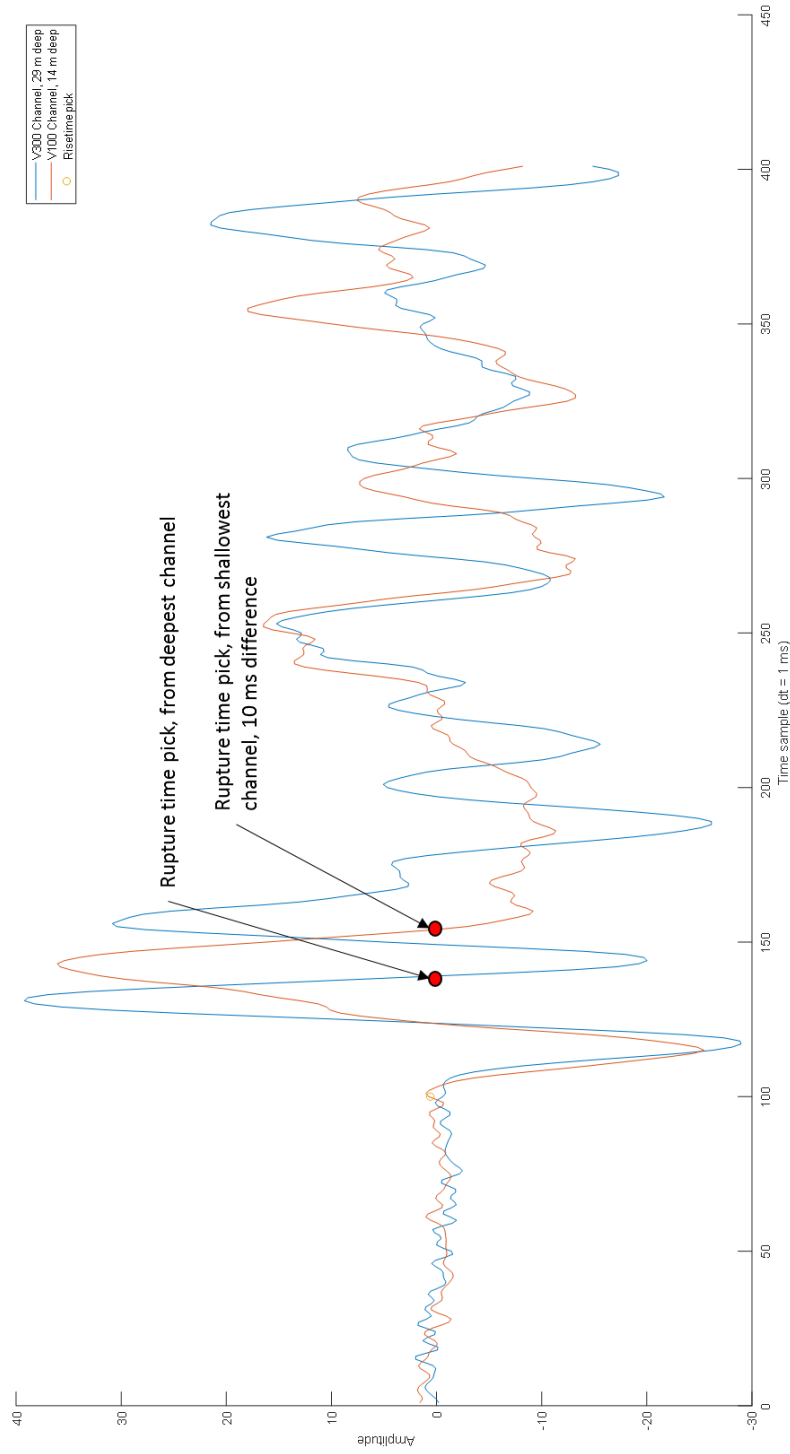


Figure B.1: Example of the received signals for the 14 m and 29 m geophone depths. The difference between the shallowest and deepest geophone rupture time is 10 ms. The signal from the deepest geophone is not affected by interference from the installation borehole to the same extent of the shallower geophone. For this reason only the deepest geophone is used in the analysis.

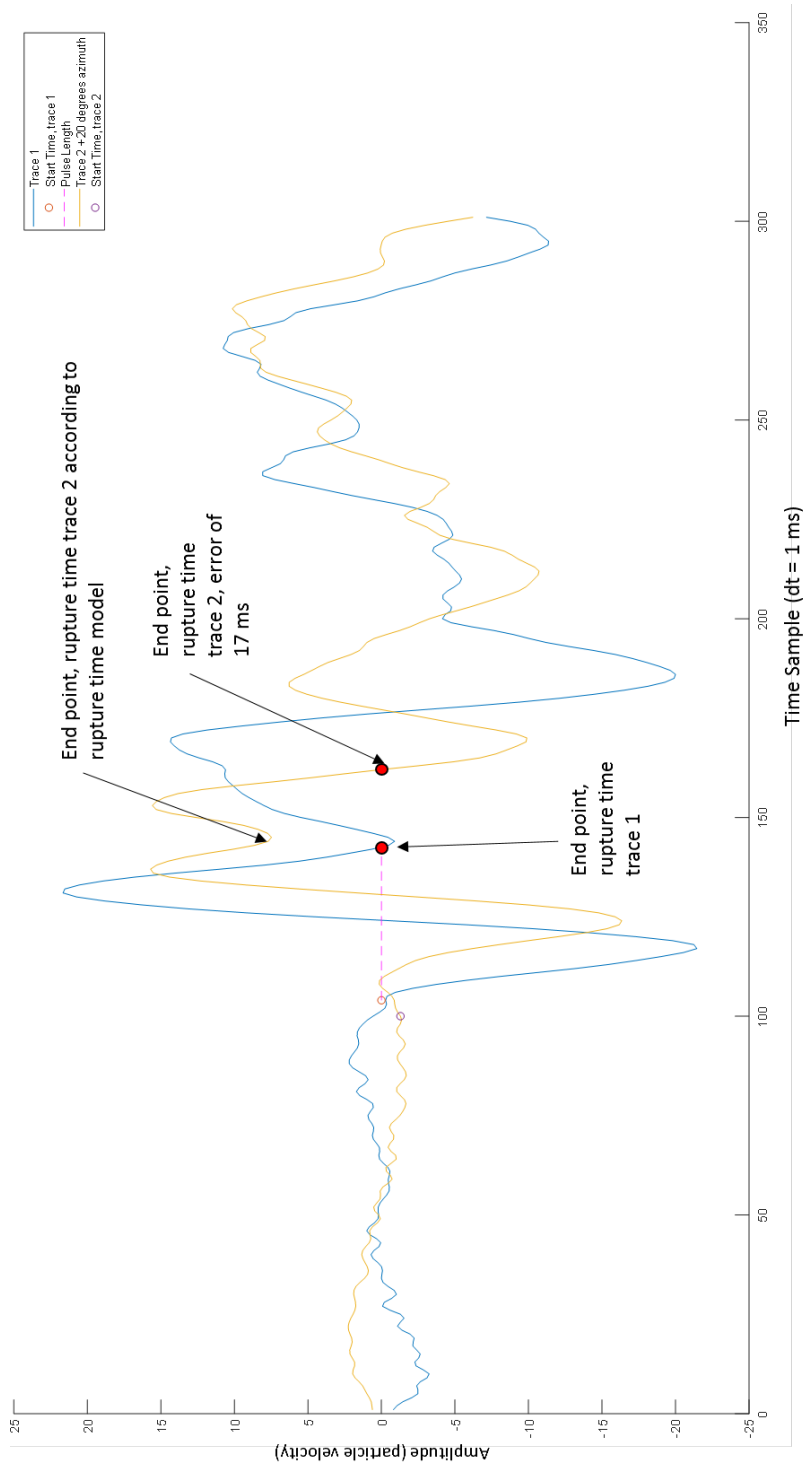


Figure B.2: Variation of the rupture time for a small change in azimuth of 20 degrees. The model definition states that the rupture time should be at 160 ms, at the second zero crossing, but the signal shows a dip towards the zero axis which matches the rupture time model. It is likely that this would be the second zero crossing if wasn't for interference from the borehole that the geophone is installed in.

B.2 Determining seismic stations installation angles

When a seismic array is installed, one or the other of the geophone axes (H1 and H2) may not point towards geographic north. This is especially important for the moment tensor inversion where if the installation axis does not match the geographic north, the angles of strike, dip and rake will then be incorrectly calculated. The installation angle for each station is not known, so a method was devised and implemented to determine the geographic angles for each station.

B.2.1 Method

The sensor polarity for the GS-ONE geophone is such that force to the back of sensor results in a negative amplitude on the record. Then if a seismic source is initiated at an azimuth of 90 degrees to the station, and the geophone axis of H1 is aligned to North, then the arrival at H2 should be a negative point and the arrival at H1 should be close to zero. If the seismic source azimuths compared to the station is known, then this model can be used by treating the amplitude at H1 and H2 as vector quantities and with trigonometry calculate the angle of H1 and H2.

B.2.2 Implementation

In this survey, there were four dynamite shots taken at stations 26, 42, 60 and 79. The location of these shots in relation to the rest of the survey stations is shown as figure B.3. These dynamite shots are analysed and the amplitude of the first arrival (P-wave) is picked on each of the H1 and H2 channels. For each of the four measured points, the angle at the principal direction is calculated with trigonometry and is graphed along with the measured points. These curves for each source station are compared to check there is a consistent angle for H1 between these four stations, and a median taken from the four sources. An example of this is shown in figure B.4.

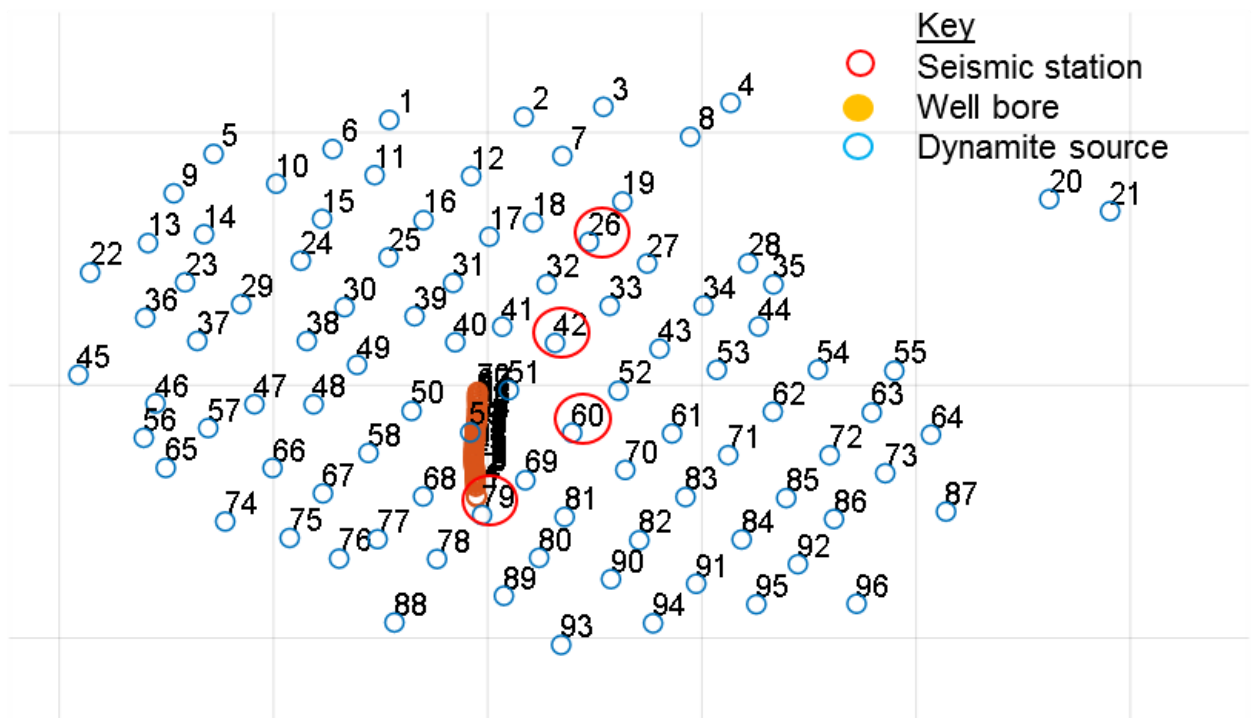


Figure B.3: Map of the seismic array and the positions of the dynamite shots used to test the array system during installation. In this instance, these dynamite sources are used to calculate the station azimuths

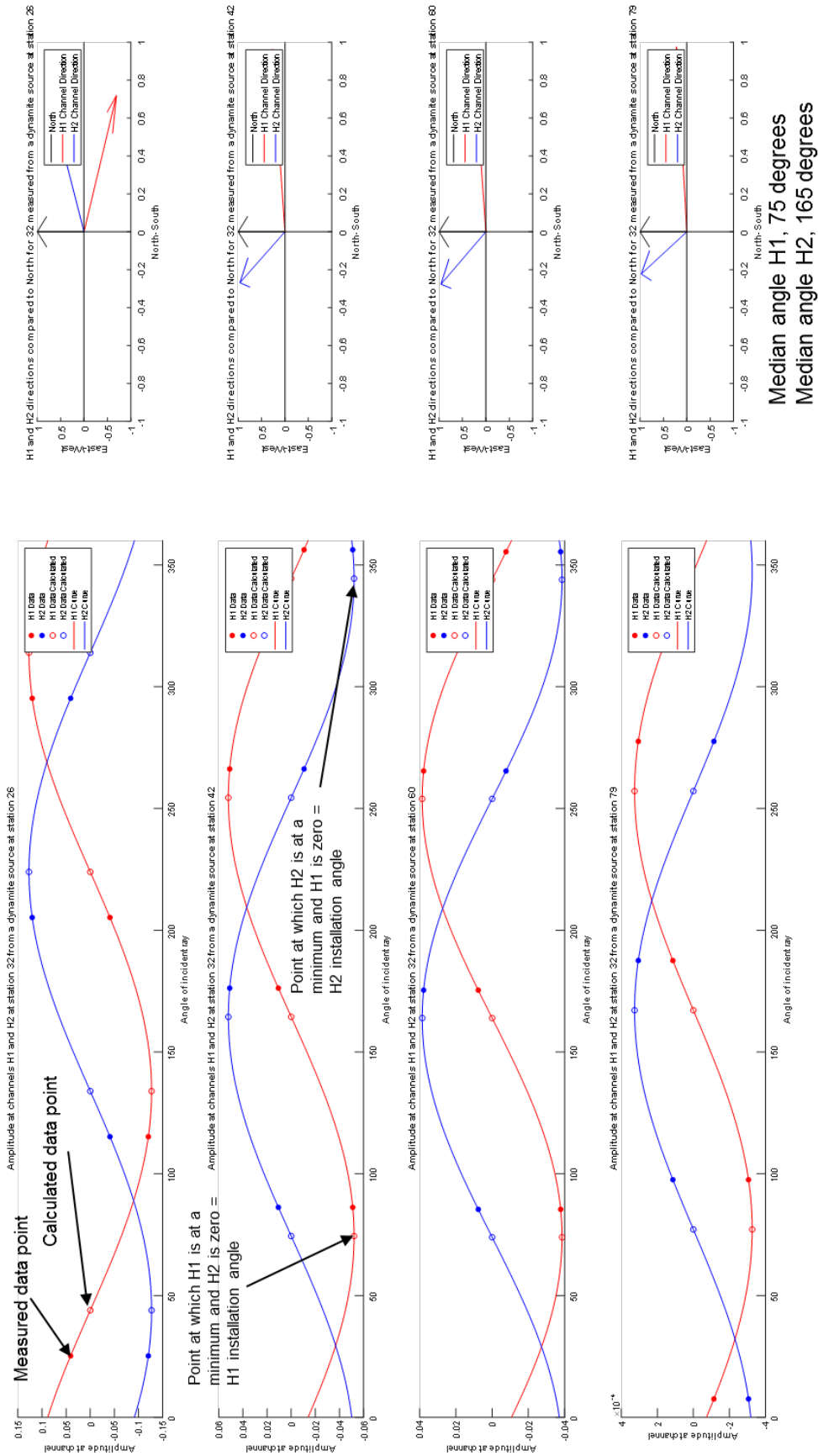


Figure B.4: Determining the rotation for the installation axis to geographic north. The amplitude at each channel (left hand images) is matched to a sinusoidal curve to predict the H1 installation angle. For this station, 32, four dynamic shots were used to calculate the installation angle. The images to the right hand side are the calculated installation angles to compare between sources

Bibliography

- Hans Agurto-Detzel, Marcelo Bianchi, Germán A Prieto, and Marcelo Assumpção. Earthquake source properties of a shallow induced seismic sequence in SE Brazil. *Journal of Geophysical Research: Solid Earth*, 122(4):2784–2797, 2017.
- Keiiti Aki and Paul G Richards. *Quantitative seismology*. University Science Books, 2002.
- Ian J Andrews. The carboniferous bowland shale gas study: geology and resource estimation. *British Geological Survey for Department of Energy and Climate Change*, 2013.
- Corinne E Bachmann, Stefan Wiemer, Jochen Woessner, and Sebastian Hainzl. Statistical analysis of the induced basel 2006 earthquake sequence: introducing a probability-based monitoring approach for enhanced geothermal systems. *Geophysical Journal International*, 186(2):793–807, 2011.
- T Bardainne, L Delmas, N Belayouni*, D Katz, and P-F Roux. Joint downhole and surface microseismic processing using 3c template relative migration. In *Unconventional Resources Technology Conference, San Antonio, Texas, 1-3 August 2016*, pages 1967–1977. Society of Exploration Geophysicists, American Association of Petroleum, 2016.
- NM Beeler, RW Simpson, SH Hickman, and DA Lockner. Pore fluid pressure, apparent friction, and coulomb failure. *Journal of Geophysical Research: Solid Earth*, 105(B11):25533–25542, 2000.
- Ari Ben-Menahem and Sarva Jit Singh. *Seismic waves and sources*. Springer Science & Business Media, 2012.
- Pascal Bernard and Aldo Zollo. Inversion of near-source s polarization for parameters of double-couple point sources. *Bulletin of the Seismological Society of America*, 79(6):1779–1809, 1989.

- John Boatwright. A spectral theory for circular seismic sources; simple estimates of source dimension, dynamic stress drop, and radiated seismic energy. *Bulletin of the Seismological Society of America*, 70(1):1–27, 1980.
- John Boatwright and Jon B Fletcher. The partition of radiated energy between p and s waves. *Bulletin of the Seismological Society of America*, 74(2):361–376, 1984.
- Paul T Boggs, Janet R Donaldson, Robert B Schnabel, et al. Algorithm 676: Odrpack: software for weighted orthogonal distance regression. *ACM Transactions on Mathematical Software (TOMS)*, 15(4):348–364, 1989.
- Julian J Bommer, Stephen Oates, José Mauricio Cepeda, Conrad Lindholm, Juliet Bird, Rodolfo Torres, Griselda Marroquin, and José Rivas. Control of hazard due to seismicity induced by a hot fractured rock geothermal project. *Engineering Geology*, 83(4):287–306, 2006.
- David M Boore and John Boatwright. Average body-wave radiation coefficients. *Bulletin of the Seismological Society of America*, 74(5):1615–1621, 1984.
- N Boroumand and D. W. Eaton. Comparing energy calculations-hydraulic fracturing and microseismic monitoring. *74th EAGE Conference and Exhibition incorporating EUROPEC*, 2012.
- Katherine Bosman, Adam Baig, Gisela Viegas, and Ted Urbancic. Towards an improved understanding of induced seismicity associated with hydraulic fracturing. *First Break*, 34(7):61–66, 2016.
- Michel Bouchon. A review of the discrete wavenumber method. *Pure and applied Geophysics*, 160(3-4):445–465, 2003.
- Michel Bouchon and Keiiti Aki. Discrete wave-number representation of seismic-source wave fields. *Bulletin of the Seismological Society of America*, 67(2):259–277, 1977.
- Michel Bouchon, Marie-Paule Bouin, Hayrullah Karabulut, M Nafi Toksöz, Michel Dietrich, and Ares J Rosakis. How fast is rupture during an earthquake? new insights from the 1999 turkey earthquakes. *Geophysical Research Letters*, 28(14):2723–2726, 2001.
- Heike Broichhausen, Roddy Muir, Colin Dunlop, and Euan Macaulay. Elastic dislocation modelling and coulomb stress change investigations. In *AAPG Annual Convention and Exhibition*, 2015.

- James N Brune. Tectonic stress and the spectra of seismic shear waves from earthquakes. *Journal of Geophysical Research*, 75(26):4997–5009, 1970.
- Michel Campillo, Michel Bouchon, and Bernard Massinon. Theoretical study of the excitation, spectral characteristics, and geometrical attenuation of regional seismic phases. *Bulletin of the Seismological Society of America*, 74(1):79–90, 1984.
- Flaminia Catalli, Men-Andrin Meier, and Stefan Wiemer. The role of Coulomb stress changes for injection-induced seismicity: The Basel enhanced geothermal system. *Geophysical Research Letters*, 40(1):72–77, 2013.
- Mathieu Causse and Seok Goo Song. Are stress drop and rupture velocity of earthquakes independent? insight from observed ground motion variability. *Geophysical Research Letters*, 42(18):7383–7389, 2015.
- Simone Cesca, Sebastian Heimann, Klaus Stammer, and Torsten Dahm. Automated procedure for point and kinematic source inversion at regional distances. *Journal of Geophysical Research: Solid Earth*, 115(B6), 2010.
- Simone Cesca, Sebastian Heimann, and Torsten Dahm. Rapid directivity detection by azimuthal amplitude spectra inversion. *Journal of seismology*, 15(1):147–164, 2011.
- Satinder Chopra, Ritesh Kumar Sharma, Amit Kumar Ray, Hossein Nemati, Ray Morin, Brian Schulte, and David D’Amico. Seismic reservoir characterization of duvernay shale with quantitative interpretation and induced seismicity considerations—a case study. *Interpretation*, 5(2):T185–T197, 2017.
- S Cianetti, C Giunchi, and M Cocco. Three-dimensional finite element modeling of stress interaction: An application to landers and hector mine fault systems. *Journal of Geophysical Research: Solid Earth*, 110(B5), 2005.
- Huw Clarke, Leo Eisner, Peter Styles, and Peter Turner. Felt seismicity associated with shale gas hydraulic fracturing: The first documented example in europe. *Geophysical Research Letters*, 41(23):8308–8314, 2014.
- Huw Clarke, James P Verdon, Tom Kettleby, Alan F Baird, and J-Michael Kendall. Real-time imaging, forecasting, and management of human-induced seismicity at Preston New Road, Lancashire, England. *Seismological Research Letters*, 90(5):1902–1915, 2019.
- Massimo Cocco and James R Rice. Pore pressure and poroelasticity effects in coulomb stress analysis of earthquake interactions. *Journal of Geophysical Research: Solid Earth*, 107(B2):ESE–2, 2002.

- O Coutant. Program of numerical simulation axitra, laboratoire de géophysique interne et tectonophysique report. *University of Joseph Fourier (in French)*, 1990.
- Cuadrilla. Hydraulic fracture plan, pnr 1z. *Cuadrilla Resources Ltd*, 2018.
- Richard Davies, Gillian Foulger, Annette Bindley, and Peter Styles. Induced seismicity and hydraulic fracturing for the recovery of hydrocarbons. *Marine and petroleum geology*, 45:171–185, 2013.
- Salvatore De Lorenzo and Aldo Zollo. Size and geometry of microearthquake seismic ruptures from p and s pulse width data. *Geophysical Journal International*, 155(2):422–442, 2003.
- Salvatore De Lorenzo, Giuseppe Di Grazia, Elisabetta Giampiccolo, Stefano Gresta, Horst Langer, Giuseppina Tusa, and Andrea Ursino. Source and qp parameters from pulse width inversion of microearthquake data in southeastern sicily, italy. *Journal of Geophysical Research: Solid Earth*, 109(B7), 2004.
- K De Meersman, J-M Kendall, and M Van der Baan. The 1998 valhall microseismic data set: An integrated study of relocated sources, seismic multiplets, and s-wave splitting. *Geophysics*, 74(5):B183–B195, 2009.
- Energy & Industrial Strategy Department for Business. Government ends support for fracking. November 2019a.
- Energy & Industrial Strategy Department for Business. Guidance on fracking: developing shale gas in the uk. November 2019b.
- Michel Dietrich and Michel Bouchon. Synthetic vertical seismic profiles in elastic media. *Geophysics*, 50(2):224–234, 1985.
- Katie Dyl. United States has been a net exporter of natural gas for more than 12 consecutive months, retrieved from . Technical report, Today in Energy, May 2019.
- David W Eaton and Farshid Forouhideh. Solid angles and the impact of receiver-array geometry on microseismic moment-tensor inversion. *Geophysics*, 76(6):WC77–WC85, 2011.
- David W Eaton, Mirko van der Baan, Brad Birkelo, and Jean-Baptiste Tary. Scaling relations and spectral characteristics of tensile microseisms: Evidence for opening/closing cracks during hydraulic fracturing. *Geophysical Journal International*, 196(3):1844–1857, 2014.

- David W Eaton, Nadine Igonin, Andrew Poulin, Ron Weir, Hongliang Zhang, Scott Pellegrino, and German Rodriguez. Induced seismicity characterization during hydraulic-fracture monitoring with a shallow-wellbore geophone array and broadband sensors. *Seismological Research Letters*, 89(5):1641–1651, 2018.
- William L Ellsworth. Injection-induced earthquakes. *Science*, 341(6142):1225942, 2013.
- Entrix. Hydraulic fracturing study pxp inglewood oil field, retrieved from . Technical report, Plains Exploration & Production Company, 2012.
- Tristan Euzen. Shale gas—an overview. Technical report, Technical report, IFP Technologies (Canada) Inc, 2011.
- Thomas S Eyre, David W Eaton, Megan Zecevic, David D’Amico, and Danylo Kolos. Microseismicity reveals fault activation before mw 4.1 hydraulic-fracturing induced earthquake. *Geophysical Journal International*, 218(1):534–546, 2019.
- Farshid Forouhideh and David W Eaton. Microseismic monitoring: insights from moment tensor inversion. *CREWES Research Report*, 2009.
- Wojciech Gajek, Michał Malinowski, and James P Verdon. Results of downhole microseismic monitoring at a pilot hydraulic fracturing site in Poland—Part 2: S-wave splitting analysis. *Interpretation*, 6(3):SH49–SH58, 2018.
- Emmanuel Gaucher, Martin Schoenball, Oliver Heidbach, Arno Zang, Peter A Fokker, Jan-Diederik van Wees, and Thomas Kohl. Induced seismicity in geothermal reservoirs: A review of forecasting approaches. *Renewable and Sustainable Energy Reviews*, 52:1473–1490, 2015.
- Valentin S Gischig and Stefan Wiemer. A stochastic model for induced seismicity based on non-linear pressure diffusion and irreversible permeability enhancement. *Geophysical Journal International*, 194(2):1229–1249, 2013.
- Michael T Gladwin and FD Stacey. Anelastic degradation of acoustic pulses in rock. *Physics of the Earth and Planetary Interiors*, 8(4):332–336, 1974.
- Paul Goldstein and A Snoke. Sac availability for the iris community. *Incorporated Research Institutions for Seismology Newsletter*, 7(UCRL-JRNL-211140), 2005.
- Christopher A Green, Peter Styles, and Brian J Baptie. Preese hall shale gas fracturing review and recommendations for induced seismic mitigation. *British Geological Survey*, 2012.

- De-hua Han, Amos Nur, and Dale Morgan. Effects of porosity and clay content on wave velocities in sandstones. *Geophysics*, 51(11):2093–2107, 1986.
- Nicholas B Harris, Julia M McMillan, Levi J Knapp, and Maria Mastalerz. Organic matter accumulation in the upper devonian duvernay formation, western canada sedimentary basin, from sequence stratigraphic analysis and geochemical proxies. *Sedimentary geology*, 376:185–203, 2018.
- Austin A Holland. Earthquakes triggered by hydraulic fracturing in south-central oklahoma. *Bulletin of the Seismological Society of America*, 103(3):1784–1792, 2013.
- Zuzana Jechumtálová and Leo Eisner. Seismic source mechanism inversion from a linear array of receivers reveals non-double-couple seismic events induced by hydraulic fracturing in sedimentary formation. *Tectonophysics*, 460(1-4):124–133, 2008.
- Hai-Yu Jiang, Zu-Bin Chen, Xiao-Xian Zeng, Hao Lv, and Xin Liu. Velocity calibration for microseismic event location using surface data. *Petroleum Science*, 13(2): 225–236, 2016.
- ML u Jost and RB Herrmann. A student’s guide to and review of moment tensors. *Seismological Research Letters*, 60(2):37–57, 1989.
- P.J. McLellan J.S. Bell, P.R. Price. In-situ stress in the western canada sedimentary basin. in *Geological Atlas of the Western Canada Sedimentary Basin, G.D. Mossop and I. Shetsen (comp.)*, Canadian Society of Petroleum Geologists and Alberta Research Council, 1994.
- Deborah L Kane, Deborah L Kilb, and Frank L Vernon. Selecting empirical green’s functions in regions of fault complexity: A study of data from the san jacinto fault zone, southern california. *Bulletin of the Seismological Society of America*, 103 (2A):641–650, 2013.
- Honn Kao and Shao-Ju Shan. The source-scanning algorithm: Mapping the distribution of seismic sources in time and space. *Geophysical Journal International*, 157 (2):589–594, 2004.
- Dimitrios C Karvounis, Valentin S Gischig, and Stefan Wiemer. Towards a real-time forecast of induced seismicity for enhanced geothermal systems. In *Shale Energy Engineering 2014: Technical Challenges, Environmental Issues, and Public Policy*, pages 246–255. 2014.

- J-M Kendall, S Pilidou, D Keir, ID Bastow, GW Stuart, and A Ayele. Mantle upwellings, melt migration and the rifting of africa: Insights from seismic anisotropy. *Geological Society, London, Special Publications*, 259(1):55–72, 2006.
- T Kettlety, JP Verdon, JM Kendall, and MJ Werner. Elastic coulomb stress transfer during injection induced seismicity. In *80th EAGE Conference and Exhibition 2018*, 2018.
- Debi Kilb, Joan Gomberg, and Paul Bodin. Aftershock triggering by complete coulomb stress changes. *Journal of Geophysical Research: Solid Earth*, 107(B4): ESE-2, 2002.
- Geoffrey CP King, Ross S Stein, and Jian Lin. Static stress changes and the triggering of earthquakes. *Bulletin of the Seismological Society of America*, 84(3):935–953, 1994.
- Eszter Király-Proag, J Douglas Zechar, Valentin Gischig, Stefan Wiemer, Dimitrios Karvounis, and Joseph Doetsch. Validating induced seismicity forecast models—induced seismicity test bench. *Journal of Geophysical Research: Solid Earth*, 121(8):6009–6029, 2016.
- Leon Knopoff and Michael John Randall. The compensated linear-vector dipole: A possible mechanism for deep earthquakes. *Journal of Geophysical Research*, 75(26): 4957–4963, 1970.
- Th Kohl and T Mégel. Predictive modeling of reservoir response to hydraulic stimulations at the european egs site soultz-sous-forêts. *International Journal of Rock Mechanics and Mining Sciences*, 44(8):1118–1131, 2007.
- Toni Kraft, Paul Martin Mai, Stefan Wiemer, Nicholas Deichmann, Johannes Ripperger, Philipp Kästli, Corinne Bachmann, Donat Fäh, Jochen Wössner, and Domenico Giardini. Enhanced geothermal systems: Mitigating risk in urban areas. *Eos, Transactions American Geophysical Union*, 90(32):273–274, 2009.
- Dana Křížová, Jiří Zahradník, and Anastasia Kiratzi. Resolvability of isotropic component in regional seismic moment tensor inversion. *Bulletin of the Seismological Society of America*, 103(4):2460–2473, 2013.
- Grzegorz Kwiatek and Yehuda Ben-Zion. Assessment of p and s wave energy radiated from very small shear-tensile seismic events in a deep south african mine. *Journal of Geophysical Research: Solid Earth*, 118(7):3630–3641, 2013.

- Alfred Lacazette and Peter Geiser. Comment on davies et al., 2012—hydraulic fractures: How far can they go? *Marine and Petroleum Geology*, 43:516–518, 2013.
- WS Leaney and CH Chapman. Microseismic sources in anisotropic media. In *72nd EAGE Conference and Exhibition incorporating SPE EUROPEC 2010*, 2010.
- Xinglin Lei, Dongjian Huang, Jinrong Su, Guomao Jiang, Xiaolong Wang, Hui Wang, Xin Guo, and Hong Fu. Fault reactivation and earthquakes with magnitudes of up to mw4.7 induced by shale-gas hydraulic fracturing in sichuan basin, china. *Scientific reports*, 7(1):7971, 2017.
- Jian Lin, Ross S Stein, Mustapha Meghraoui, Shinji Toda, Abdelhakim Ayadi, Catherine Dorbath, and Samir Belabbes. Stress transfer among en echelon and opposing thrusts and tear faults: Triggering caused by the 2003 mw= 6.9 zemmouri, algeria, earthquake. *Journal of Geophysical Research: Solid Earth*, 116(B3), 2011.
- LM Linzer. A relative moment tensor inversion technique applied to seismicity induced by mining. *Rock mechanics and rock engineering*, 38(2):81–104, 2005.
- Juan M Lorenzo, Trudy L Watkins, and Arash-Dahi Taleghani. Recommendations from error analysis of single well microseismic data with full-wavefield moment tensor inversion: A case study. In *Unconventional Resources Technology Conference, Austin, Texas, 24-26 July 2017*, pages 2767–2780. Society of Exploration Geophysicists, American Association of Petroleum, 2017.
- Raul Madariaga. Dynamics of an expanding circular fault. *Bulletin of the Seismological Society of America*, 66(3):639–666, 1976.
- K. Mageau. Resumption of hydraulic fracturing operations, sub-surface order no.2. retrived from . Technical report, AER, 2016.
- Gary Mavko, Tapan Mukerji, and Jack Dvorkin. *The rock physics handbook: Tools for seismic analysis of porous media*. Cambridge university press, 2009.
- SC Maxwell, M Jones, R Parker, S Miong, S Leaney, D Dorval, D D’Amico, J Logel, E Anderson, and K Hammermaster. Fault activation during hydraulic fracturing. In *SEG Technical Program Expanded Abstracts 2009*, pages 1552–1556. Society of Exploration Geophysicists, 2009.
- SC Maxwell, D Raymer, M Williams, and P Primiero. Tracking microseismic signals from the reservoir to surface. *The Leading Edge*, 31(11):1300–1308, 2012.

- Shawn Maxwell. Unintentional seismicity induced by hydraulic fracturing. *CSEG Rec*, 38(8):40–49, 2013.
- A McGarr, David Simpson, L Seeber, and William Lee. Case histories of induced and triggered seismicity. *International Geophysics Series*, 81(A):647–664, 2002.
- Jaime Meléndez-Martínez and Douglas R Schmitt. A comparative study of the anisotropic dynamic and static elastic moduli of unconventional reservoir shales: Implication for geomechanical investigations. *Geophysics*, 81(3):D245–D261, 2016.
- Susan LM Miller and Robert R Stewart. Effects of lithology, porosity and shaliness on p-and s-wave velocities from sonic logs. *Canadian Journal of Exploration Geophysics*, 26(1-2):94–103, 1990.
- Peter Molnar. Average regional strain due to slip on numerous faults of different orientations. *Journal of Geophysical Research: Solid Earth*, 88(B8):6430–6432, 1983.
- G Mossop and I Shetsen. Introduction to the geological atlas of the western canada sedimentary basin. *Geological Atlas of the Western Canadian Sedimentary Basin. Compiled by GD Mossop and I. Shetson. Canadian Society of Petroleum Geologists and Alberta Research Council, Calgary, Alberta*, pages 1–12, 1994.
- Masaru Nakano and Hiroyuki Kumagai. Waveform inversion of volcano-seismic signals assuming possible source geometries. *Geophysical research letters*, 32(12), 2005.
- Richard C Nolen-Hoeksema and Larry J Ruff. Moment tensor inversion of microseisms from the b-sand propped hydrofracture, m-site, colorado. *Tectonophysics*, 336(1-4): 163–181, 2001.
- OGA. Consolidated onshore guidance, retrieved from . Technical report, Oil and Gas Authority, 2018.
- OGA. Interim report of the scientific analysis of data gathered from cuadrilla’s operations at preston new road. Technical report, Oil and Gas Authority, 2019.
- Yosihiko Ogata. Statistical models for earthquake occurrences and residual analysis for point processes. *Journal of the American Statistical association*, 83(401):9–27, 1988.
- Masayasu Ohtsu. Simplified moment tensor analysis and unified decomposition of acoustic emission source: application to in situ hydrofracturing test. *Journal of Geophysical Research: Solid Earth*, 96(B4):6211–6221, 1991.

- Yoshimitsu Okada. Internal deformation due to shear and tensile faults in a half-space. *Bulletin of the seismological society of America*, 82(2):1018–1040, 1992.
- Taro Okamoto. Full waveform moment tensor inversion by reciprocal finite difference green’s function. *Earth, planets and space*, 54(6):715–720, 2002.
- Oliver N Ong, Douglas R Schmitt, Randolph S Kofman, and Kristine Haug. Static and dynamic pressure sensitivity anisotropy of a calcareous shale. *Geophysical Prospecting*, 64(4):875–897, 2016.
- B Orlecka-Sikora. The role of static stress transfer in mining induced seismic events occurrence, a case study of the rudna mine in the legnica-glogow copper district in poland. *Geophysical Journal International*, 182(2):1087–1095, 2010.
- Gwo-Bin Ou. Seismological studies for tensile faults. *TAO: Terrestrial, Atmospheric and Oceanic Sciences*, 19(5):4, 2008.
- Volker Oye, Hilmar Bungum, and Michael Roth. Source parameters and scaling relations for mining-related seismicity within the Pyhasalmi ore mine, Finland. *Bulletin of the Seismological Society of America*, 95(3):1011–1026, 2005.
- K Parks, T Byrnes, and P Johnston. Subsurface order no.2, retrieved from . Technical report, AER, 2015.
- Donghong Pei, John A Quirein, Bruce E Cornish, Dan Quinn, and Norman R Warpin-ski. Velocity calibration for microseismic monitoring: A very fast simulated annealing (vfsa) approach for joint-objective optimization. *Geophysics*, 74(6):WCB47–WCB55, 2009.
- A Plesinger, M Hellweg, and D Seidl. Interactive high-resolution polarization analysis of broad-band seismograms. *J. Geophys*, 59:129–139, 1986.
- A Preston, G Garner, K Beavis, O Sadiq, and S Stricker. Duvernay reserves and resources report, retrieved from . Technical report, AER, 2016.
- BC Richards, JE Barclay, KG Osadetz, FH Trollope, and A Hartling. Carboniferous strata of the western canada sedimentary basin. *Bulletin of Canadian Petroleum Geology*, 38(1):178–178, 1990.
- Lorne RP Rosenthal. *The stratigraphy, sedimentology and petrography of the Upper Cretaceous Wapiabi and Belly River formations in southwestern Alberta*. PhD thesis, 1984.

- James T Rutledge and W Scott Phillips. Hydraulic stimulation of natural fractures as revealed by induced microearthquakes, carthage cotton valley gas field, east texashydraulic stimulation of natural fractures. *Geophysics*, 68(2):441–452, 2003.
- Jonny Rutqvist, Antonio P Rinaldi, Frédéric Cappa, and George J Moridis. Modeling of fault activation and seismicity by injection directly into a fault zone associated with hydraulic fracturing of shale-gas reservoirs. *Journal of Petroleum Science and Engineering*, 127:377–386, 2015.
- MS Sambridge and BLN Kennett. Boundary value ray tracing in a heterogeneous medium: a simple and versatile algorithm. *Geophysical Journal International*, 101(1):157–168, 1990.
- Tamao Sato. A note on body wave radiation from wxpanding tension crack. *Science reports of the Tohoku University. Ser. 5, Geophysics*, 25(1):1–10, 1978.
- Tamao Sato and Tomowo Hirasawa. Body wave spectra from propagating shear cracks. *Journal of Physics of the Earth*, 21(4):415–431, 1973.
- Martin Schoenball, Clément Baujard, Thomas Kohl, and Louis Dorbath. The role of triggering by static stress transfer during geothermal reservoir stimulation. *Journal of Geophysical Research: Solid Earth*, 117(B9), 2012.
- Ryan Schultz, Ruijia Wang, Yu Jeffrey Gu, Kristine Haug, and Gail Atkinson. A seismological overview of the induced earthquakes in the duvernay play near fox creek, alberta. *Journal of Geophysical Research: Solid Earth*, 122(1):492–505, 2017.
- Luyi W Shen, Douglas R Schmitt, and Kristine Haug. Quantitative constraints to the complete state of stress from the combined borehole and focal mechanism inversions: Fox creek, alberta. *Tectonophysics*, 764:110–123, 2019.
- Thomas Smith. Is shale gas bringing independence? 2012.
- David Smythe. Submission to the appg on the impact of shale gas: The traffic light system to be held on 2 april 2019. 2019.
- Fuxian Song and M Nafi Toksöz. Full-waveform based complete moment tensor inversion and source parameter estimation from downhole microseismic data for hydrofracture monitoring. *Geophysics*, 76(6):WC103–WC116, 2011.
- F Stanek and L Eisner. New model explaining inverted source mechanisms of microseismic events induced by hydraulic fracturing: 83rd annual international meeting, seg, expanded abstracts, 2201–2205. *Reply to the discussion X25*, 2013.

- Ross S Stein. The role of stress transfer in earthquake occurrence. *Nature*, 402(6762): 605, 1999.
- Ross S Stein, Geoffrey CP King, and Jian Lin. Change in failure stress on the southern san andreas fault system caused by the 1992 magnitude= 7.4 landers earthquake. *Science*, 258(5086):1328–1332, 1992.
- Stein Steith. Michael wysession. 2003. an introduction to seismology, earthquakes, and earth structure, 2003.
- Michael H Stephenson. Shale gas in north america and europe. *Energy Science & Engineering*, 4(1):4–13, 2016.
- FA Stoakes and S Creaney. Sedimentology of a carbonate source rock: the duvernay formation of central alberta. 1984.
- AL Stork, JP Verdon, and J-M Kendall. The robustness of seismic moment and magnitudes estimated using spectral analysis. *Geophysical Prospecting*, 62(4):862–878, 2014.
- Brian W Stump and Lane R Johnson. The determination of source properties by the linear inversion of seismograms. *Bulletin of the Seismological Society of America*, 67(6):1489–1502, 1977.
- SB Switzer, WG Holland, DS Christie, GC Graf, AS Hedinger, RJ McAuley, RA Wierzbicki, JJ Packard, GD Mossop, and I Shetsen. Devonian woodbend-winterburn strata of the western canada sedimentary basin. *Geological Atlas of the Western Canada Sedimentary Basin: Canadian Society of Petroleum Geologists and Alberta Research Council*, pages 165–202, 1994.
- Jan ter Heege and Holger Cremer. M4shalegas-measuring, monitoring, mitigating and managing the environmental impact of shale gas. 2017.
- Shinji Toda, Ross S Stein, Keith Richards-Dinger, and Serkan B Bozkurt. Forecasting the evolution of seismicity in southern california: Animations built on earthquake stress transfer. *Journal of Geophysical Research: Solid Earth*, 110(B5), 2005.
- J Tomic, RE Abercrombie, and AF Do Nascimento. Source parameters and rupture velocity of small $m \leq 2.1$ reservoir induced earthquakes. *Geophysical Journal International*, 179(2):1013–1023, 2009.
- Rainer Tonn. The determination of the seismic quality factor q from vsp data: A comparison of different computational methods. *Geophysical Prospecting*, 39(1): 1–27, 1991.

- G-A Tselentis, Paraskevas Paraskevopoulos, and Nikos Martakis. Intrinsic q p seismic attenuation from the rise time of microearthquakes: a local scale application at rio-antirrio, western greece. *Geophysical prospecting*, 58(5):845–859, 2010.
- UN. Paris agreement, 2016. URL https://treaties.un.org/pages/ViewDetails.aspx?src=TREATY&mtdsg_no=XXVII-7-d&chapter=27&clang=_en.
- Václav Vavryčuk. Inversion for parameters of tensile earthquakes. *Journal of Geophysical Research: Solid Earth*, 106(B8):16339–16355, 2001.
- Václav Vavryčuk. Focal mechanisms in anisotropic media. *Geophysical Journal International*, 161(2):334–346, 2005.
- Václav Vavryčuk. On the retrieval of moment tensors from borehole data. *Geophysical Prospecting*, 55(3):381–391, 2007.
- James Verdon and David Harrison. Hydraulic fracture plan for well km-8. *Third Energy*, 2017.
- James P Verdon. Comments on the scientific basis, or lack thereof, for hydraulic fracturing fault respect distances, 2018.
- James P Verdon and J-Michael Kendall. Detection of multiple fracture sets using observations of shear-wave splitting in microseismic data. *Geophysical Prospecting*, 59(4):593–608, 2011.
- JP Verdon, J-M Kendall, and A Wüstefeld. Imaging fractures and sedimentary fabrics using shear wave splitting measurements made on passive seismic data. *Geophysical Journal International*, 179(2):1245–1254, 2009.
- William R Walter and James N Brune. Spectra of seismic radiation from a tensile crack. *Journal of Geophysical Research: Solid Earth*, 98(B3):4449–4459, 1993.
- Ruijia Wang, Yu Jeffrey Gu, Ryan Schultz, Ahyi Kim, and Gail Atkinson. Source analysis of a potential hydraulic-fracturing-induced earthquake near fox creek, alberta. *Geophysical Research Letters*, 43(2):564–573, 2016.
- Simon N Weides, Inga S Moeck, Douglas R Schmitt, and Jacek A Majorowicz. An integrative geothermal resource assessment study for the siliciclastic granite wash unit, northwestern alberta (canada). *Environmental earth sciences*, 72(10):4141–4154, 2014.
- Rob Westaway and Neil M Burnside. Fault “corrosion” by fluid injection: A potential cause of the november 2017 5.5 korean earthquake. *Geofluids*, 2019, 2019.

- Rachel F Westwood, Samuel M Toon, Peter Styles, and Nigel J Cassidy. Horizontal respect distance for hydraulic fracturing in the vicinity of existing faults in deep geological reservoirs: a review and modelling study. *Geomechanics and geophysics for geo-energy and geo-resources*, 3(4):379–391, 2017.
- Patrick Whitelaw, Clement N Uguna, Lee A Stevens, Will Meredith, Colin E Snape, Christopher H Vane, Vicky Moss-Hayes, and Andrew D Carr. Shale gas reserve evaluation by laboratory pyrolysis and gas holding capacity consistent with field data. *Nature communications*, 10(1):1–10, 2019.
- Stefan Wiemer, Toni Kraft, Evelina Trutnevyte, and Philippe Roth. “good practice” guide for managing induced seismicity in deep geothermal energy projects in switzerland. *Swiss Seismological Service (SED)*, 2017.
- Chong Xu and Xiwei Xu. Comment on “spatial distribution analysis of landslides triggered by 2008.5. 12 wenchuan earthquake, china” by shengwen qi, qiang xu, hengxing lan, bing zhang, jianyou liu [engineering geology 116 (2010) 95–108]. *Engineering Geology*, 133:40–42, 2012.
- Han Yue, Thorne Lay, Jeffrey T Freymueller, Kaihua Ding, Luis Rivera, Natalia A Ruppert, and Keith D Koper. Supershear rupture of the 5 january 2013 craig, alaska (mw 7.5) earthquake. *Journal of Geophysical Research: Solid Earth*, 118(11):5903–5919, 2013.
- X Zhang, M Holland, W Van Der Zee, D Moos, et al. Microseismic estimates of stimulated rock volume using a detection-range bias correction: Theory and case study. In *SPE Hydraulic Fracturing Technology Conference*. Society of Petroleum Engineers, 2014.
- Aldo Zollo and Salvatore de Lorenzo. Source parameters and three-dimensional attenuation structure from the inversion of microearthquake pulse width data: Method and synthetic tests. *Journal of Geophysical Research: Solid Earth*, 106(B8):16287–16306, 2001.